Modelling embankment breaching due to overflow

Myron van Damme
Wolfson college

Ocean and Coastal Engineering and Water Resources Group
Department of Engineering Science
University of Oxford

Hilary term 2014

Modelling embankment breaching due to overflow

Thesis submitted in fulfilment for the degree of Doctor of Philosophy
at the University of Oxford, Hilary term 2014.

Myron van Damme
Wolfson College
University of Oxford

Abstract

Correct modelling of embankment breach formation is essential for an accurate assessment of the associated flood risk. Modelling breach formation due to overflow requires a thorough understanding of the geotechnical processes in unsaturated soils as well as erosion processes under supercritical flow conditions. This thesis describes 1D slope stability analysis performed for unsaturated soils whose moisture content changes with time. The analysis performed shows that sediment-laden gravity flows play an important role in the erosion behaviour of embankments. The thesis also describes a practical, fast breach model based on a simplified description of the physical processes that can be used in modelling and decision support frameworks for flooding. To predict the breach hydrograph, the rapid model distinguishes between breach formation due to headcut erosion and surface erosion in the case of failure due to overflow. The model also predicts the breach hydrograph in the case of failure due to piping. The assumptions with respect to breach flow modelling are reviewed, and result in a new set of breadth-integrated Navier–Stokes equations, that account for wall shear stresses and a variable breadth geometry. The vertical 2D flow field described by the equations can be used to calculate accurately the stresses on the embankment during the early stages of breach formation. Pressure-correction methods are given for solving the 2D Navier–Stokes equations for a variable breadth, and good agreement is found when validating the flow model against analytical solutions.

Acknowledgments

I foremost would like to thank my departmental supervisors, Alistair Borthwick and Chris Martin for giving me freedom in choosing my own approach during my DPhil, while maintaining a sincere interest in my progress and warning me, whenever I became too ambitious. I would like to thank Alistair Borthwick for continuing his supervision after moving to University of Cork, and Chris Martin for taking over his role as my local supervisor.

I also would like to thank Mark Morris and Mohamed Hassan from HR Wallingford for supervising my work on the development of the simplified breach model, for sharing their knowledge in the field of embankment breach modelling, and for their meticulous approach in checking my work.

I also like to thank Richard Soulsby for helping me edit parts of this thesis and for his supervision and expertise in discussing the erosion mechanisms of embankments. The development of a correct physical description of embankment erosion is a true challenge and I felt grateful to have access to his knowledge of Richard Soulsby when I needed some feedback.

Furthermore I would like to thank Daniel Corbett for his advice. I am grateful for the help he provided in further improving my understanding of the Navier–Stokes equations, and the means of solving them.

I would like to thank Mark Morris and Peter Stansby and the Flood Risk Management Research Consortium for providing me with funding for the duration of my studies.

Last but not least I would like to thank Mohamed Haniffah, Ton van den Bremer, Jana Orszaghova, Pawel Kozlowski for being so supportive throughout my time at Oxford.

Contents

List of Figures

List of Tables

Chapter 1

Introduction

History shows that the consequences of flood events can be severe. The flooding of the South-West of the Netherlands and South-East of England in 1953 resulted in a large number of fatalities and substantial economic losses. More recent examples of floods with large economic damage are the flooding of New Orleans in August 2005 (Seed et al., 2006) , and that of Queensland Australia in January 2011 (ABC news, 2011). Between 1998 and 2009, 213 floods occurred in Europe which caused for economic, social, and environmental damage, and 1126 deaths (European Environment Agency, 2010). As an attempt to improve flood risk management the EU Floods Directive 2007/60/EC was developed and published in October 2007 (Parliament, 2007). The aim of the EU Floods directive is to reduce and manage flood risk with respect to public health, environment, cultural heritage, and economic activity. EU member states are required to perform a preliminary assessment of areas at risk of flooding. Flood risk maps will have to be completed for these areas by 2013, and prevention, protection and preparedness plans have to be developed for these areas by 2015 (Parliament, 2007). To assess the areas at risk of flooding and the possible severity of floods, flood spreading models have been developed and included into river flow models and coastal models. For accurate modelling of the spreading of a flood, the flow rate of water entering a flood area needs to be accurately predicted. When failure of an embankment causes an area to flood, the flow rate of inflowing water is determined by the size of the breach, and the growth rate of the breach with respect to the rate of change of the water level in the river. Empirical breach relationships have been developed using available data on breaches (Verheij and Van der Knaap, 2002). However the large variety in loading

conditions on embankments, embankment design, and failure modes, combined with limited data available on failed embankments, make empirical models highly inaccurate. Unfortunately developers of empirical models often do not comment on the inherent inaccuracy of the models. Hence some studies related to the uncertainty in flood risk (see e.g. De Moel (2012)) ignore the inherent inaccuracy of breach models and focus solely on the impact of variation in input parameters on the accuracy of output values. This then leads to the erroneous conclusion that breach models make only a small contribution to the overall inaccuracy in flood risk, whereas the opposite could be true. Although more accurate predictions of flood volumes could be obtained from process-based breach models, it should be noted that model inaccuracies nevertheless arise from a lack of understanding of the breach processes. This thesis focuses on the development of process-based breach models. As a starting point, the next section reviews the limits in understanding of breach processes and the way these processes are currently modelled.

1.1 Limits in knowledge

Process-based models simulate reality by closely approximating the physical processes. To produce an accurate model it is essential that model approximations are understood and that the model is not applied outside sensible parameter limits. Nowadays, nearly all breach models describe breach processes according to the simplified steps of breach formation described by Morris et al. (2009a) and Visser (1998). Figure 1.1 shows a typical breach hydrograph for embankment failures by overflow. In discussing the stages, the embankment is described as having a waterside slope, a crest, and a landside slope. The waterside slope is defined as the sloping face of the embankment at the side of the river or coastal water. The landside slope is defined as the sloping face of the embankment at the inland side. The following stages occur, with the possible exception of Stage 3:

1. Embankment is stable and functions well. T_0-T_1

2. Embankment starts to overflow and water percolates into the embankment. Material is progressively removed and the landside slope retreats towards the waterside slope. T_1-T_2

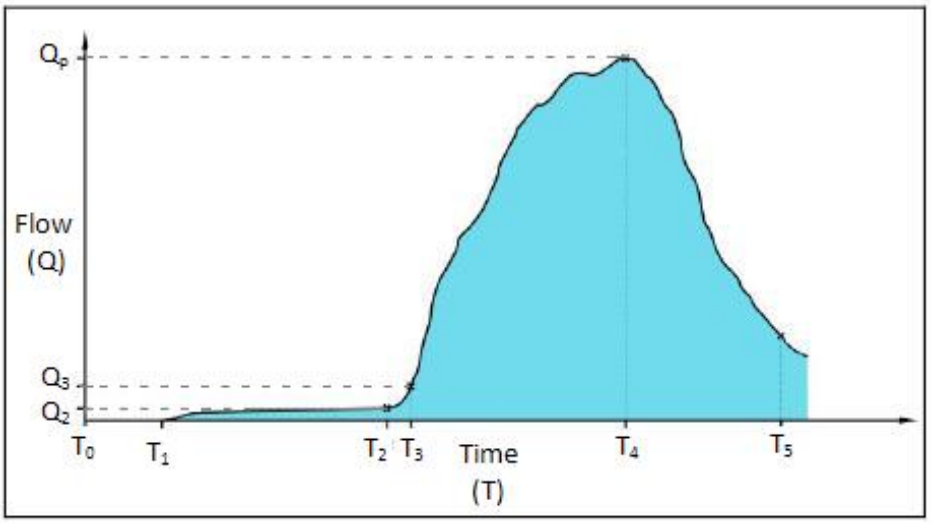

Figure 1.1: Generic breach hydrograph (After Morris et al. (2009b))

3. Erosion of the landside slope reaches the waterside slope and the flow slowly starts to increase. The increased hydraulic head over the embankment leads to higher flow velocities through the breach, and an increased horizontal flow contraction besides the already present vertical flow contraction. T_2-T_3

4. Rapid increase in flow velocity with erosion of the waterside slope and simultaneous widening of the breach. Flow velocities are supercritical. T_3-T_4

5. Breach flow becomes affected by the rise of the downstream water level, and/or the fall of the upstream water level, and the breach flow starts to decrease to the point that the flow velocities become so small that the erosion process stops. T_4-T_5

These stages have been observed in several large- and small-scale breach experiments (Morris et al., 2008). However, differences in breach behaviour have been found in the rate, and manner of breach formation. The limits in knowledge relate to the lack of complete understanding of why these differences occur as is exemplified by considering the simple case of breach formation due to overflow of a trapezoidal-shaped flood embankment protected by a grass layer. Water starts to overflow the embankment when the level of water against the embankment exceeds the crest level. Grass protection prevents erosion of the embankment soil for a period of time, during which the water level may decrease again. To fully assess the breach process as a function of time, it is thus necessary to understand how and when a grass protection layer fails.

In The Netherlands, the Expert Network on Water Safety (ENW) performed several tests on grass erosion under wave attack. ENW (Muijs, 1999) reported that evenly distributed and healthy grass provides a cover layer that is highly resistant to erosion. ENW found that grass strength is greatly influenced by the strength of the turf layer. Grass roots of barely-fertilized grass were found to be more erosion resistant than well fertilized grass. However no explanation is given by ENW on how grass erodes. Nezu and Okamoto (2010) studied the profiles of flow over a grass layer, and found that the vertical and horizontal turbulence intensities near the roots were minute, indicating a negligibly small shear stress at the bed. Over the height of the stems, the cumulative shear stress causes a normal tensile force in the stem which is transferred to the soil. This could have a two-fold effect on erosion. First, the tension could cause the stem to snap at the roots leading to a less protected bed. Second, the tension could pull the roots out of the bed. Fluctuations in bed shear stress may thereby loosen the turf layer. Pollen (2006) studied root reinforcement of streambanks. Pollen measured the tensile strength and pull-out forces of grass roots and found that for small diameter roots the breaking forces exceeded the pull-out forces. Larger diameter roots were more likely to be pulled out of the soil. The threshold between the two depends on the shear strength of the soil, the frictional bonds between the root and the soil grains, and the plant-specific tensile strength. Pollen also found that the tensile strength of roots is largely independent of soil moisture content. However, the moisture content of the soil did have an effect on the threshold between roots being pulled out of the soil and breaking of roots. It was observed that as the soil dried, the frictional bonds between roots and soil became stronger because the apparent cohesion increased with the matric suction of the soil, where matric suction is defined as the suction present in the unsaturated soil matrix due the capillary effects of groundwater. Pollen (2006) found that the root reinforcement by grass was lowest when the soil moisture content was high and the soil shear strength was low. Richards (1931) found a relationship between soil pore pressure and moisture content. When a soil dries out, its pore pressure becomes progressively negative as the moisture content decreases, positively affecting soil stability. The capillary effect of the soil matrix causes water to flow from regions of high water content (or low matric suction) to regions of lower water content (high matric suction). From the study by Pollen (2006) it is possible to conclude that the matric suction of the soil directly affects the erodibility of grass. When an embankment overflows, water percolates into the embankment, increasing the

moisture content of the soil. The resistance of grass to erosion is therefore expected to be dependent on time as well as grass quality. For accurate modelling of the breaching of a grass-covered embankment it is not only necessary to address when the grass cover fails but also where along the embankment perimeter it fails. Both the load on the grass cover and the grass quality vary along the perimeter of the embankment, and so the grass cover does not fail everywhere at once. The order in which the grass cover fails influences the erosion process and hence the breach hydrograph profiles.

After failure of the grass cover, Stage 2 continues whereby two types of soil erosion processes can occur. The first is surface erosion, the second headcut erosion (Morris et al., 2009a). With surface erosion, the embankment erodes gradually, whereby sharp gradients in the embankment profile are smoothed out. This behaviour was also found by Sametz (1981) who performed scale overflow experiments on an embankment of $0.365m$ high and made out of non-cohesive material. The time stepping results are given in Figure 1.2, which clearly shows the reduction in gradients in the embankment profile. Headcut erosion is defined by Zhu et al. (2008) as "... a vertical or near vertical

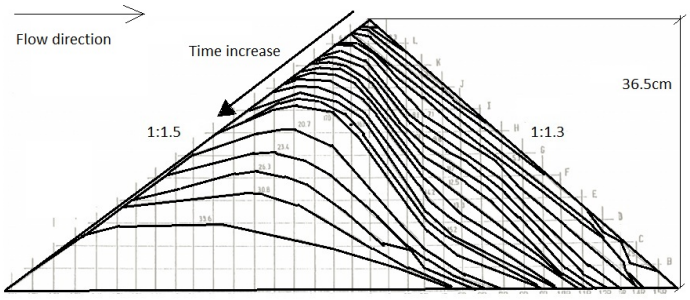

Figure 1.2: Dam profile development with time for a homogeneous scale embankment consisting of non-cohesive material (After Broich (1996)).

drop in elevation occurring in rill, gully earth spillway and overtopped embankments". Zhu et al. (2011) performed scale experiments to breaching of embankments made up out of a range of cohesive soils. Figure 1.3 shows the embankment profile development with time for the erosion due to overflow of the test embankment constructed of the most cohesive soil. The figure shows a much steeper landside slope gradient for the cohesive embankment as is expected in the case of headcut erosion. Although many studies have examined the physics behind headcut erosion, an understanding of the dynamics of headcut erosion is still inadequate. Zhu et al. (2008) explain the formation of headcuts as follows. When the decrease in crest height causes the flow over the

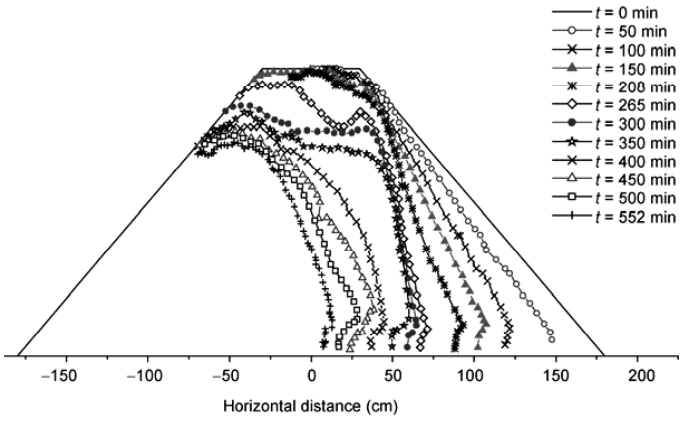

Figure 1.3: Dam profile development with time for a homogeneous scale embankment consisting of cohesive material (Flow direction is from left to right) (After Zhu et al., 2011)

embankment to increase, the flow overshoots at the transition between the crest and the landside slope, and forms an impinging jet. At the reattachment point of the jet with the embankment, scour erosion processes cause the slope to steepen and a step to form. The step formation process is repeated further along the landside slope due to transitions between step bases and the landside slope (see figure 1.4). With increasing

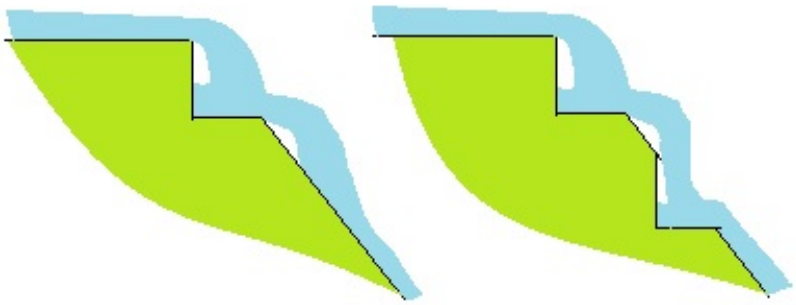

Figure 1.4: Schematised headcut growth process

flow velocity and continuation of erosion of the headcuts, the step sizes increase until the jet overshoots all steps. Scour under the landside slope then causes the embankment to fail.

Why surface erosion prevails over headcut erosion, or vice versa, is explained by studying the flow dynamics, sediment transport processes, and soil mechanics. When an embankment overflows it acts as a broad-crested weir. Conservation of energy over

the crest gives a lower water level over the crest, compared to the upstream water level, and leads to correspondingly higher flow velocities. When the flow reaches the landside end of the crest the sudden drop in channel bed causes the flow to behave according to one of the following three flow types (See Figure 1.5).

1. The flow forms a free nappe when the pressure just after the landside end of the crest is atmospheric.

2. A recirculating flow pattern arises under the main flow to the point where the flow reattaches to the embankment.

3. The change in bed level is mild and the flow does not separate from the bed.

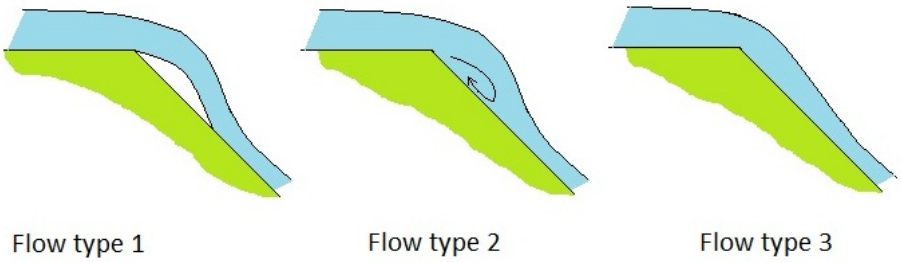

Figure 1.5: Three possible types of flow behaviour

From a hydraulic point of view, each of the flow types results in a different erosion behaviour. With flow type 1, the stresses along the landside slope are focused where the free nappe reattaches to the embankment. The localized stresses lead to headcut erosion. Where the cascade flow impacts on the embankment surface, the flow disperses and undercuts the embankment. The local erosion rate depends upon the energy with which the flow hits the soil, and hence on the height of the cascades. Similarly flow type 3 leads to surface erosion since the flow remains fully attached to the embankment surface. For flow type 2 it is more difficult to predict the process by which the embankment erodes since some erosion occurs before the reattachment point, while the stresses are focused at the reattachment point (see Figure 1.5). The flow-induced stresses on the embankment between the separation and the reattachment point determine the type of erosion process from a flow perspective. Depending on the embankment geometry, more than one flow type could occur simultaneously at different locations, causing the embankment to erode according to a combination of erosion types. For example, in the case of a horizontal berm halfway down the landside slope, the flow has more

time to accelerate alongside the landside slope before reaching the berm. Separation and reattachment of the flow after the berm would lead to flow type 1 irrespective of how the flow behaves at the end of the crest.

Transport of embankment material is governed by sediment transport processes. The flow accelerates along the landside slope and is thereby predominantly supercritical. For most embankments, the landside slope is not sufficiently long for equilibrium flow conditions to be reached. Under the accelerating flow conditions, no equilibrium transport conditions are obtained and the breach erodes due to live scour effects. To the author's knowledge, no transport equations have been developed that describe live bed scour under supercritical flow conditions, and hence a practicable approximation was instead established. Yang (2006) mentions shear stress and streampower to be useful parameters by which to describe the erosion rate, since both parameters represent the forces along the bed. The shear stress approach relates the erosion rate of sediment to the shear stress acting on the bed. The streampower approach relates the erosion rate to energy dissipated by turbulence. The shear stress based erosion equation for the erosion rate, as used in breach models and rill erosion models, is given by

$$E = K_e \left(\tau - \tau_c\right)^m \tag{1.1}$$

where E is the erosion rate, τ the bed shear stress, τ_c the critical bed shear stress needed for the initiation of motion, K_e is the soil erodibility factor, and m a power index related to efficiency. When using the erosion equation, it is inherently assumed that the flow dynamics are not influenced by the concentration of suspended sediment present (Govindaraju and Kavvas, 1991). Besides this limitation, the erosion equation is limited to subcritical flow conditions (Smith, 2006).

Unlike the shear stress approach, the streampower approach is also valid under supercritical flow conditions. In developing the streampower approach Bagnold (1966) related the transport rate of material to the rate of energy used in transporting materials. Bagnold's relationship that relates streampower to the sediment transport rate is given by

$$\frac{\gamma_s - \gamma}{\gamma} E \tan\alpha = \tau V e_b, \tag{1.2}$$

where γ_s and γ are respectively the specific weight of sediment and water, $\tan\alpha$ is the ratio of the tangential to normal force, V is the average flow velocity, and e_b is an

efficiency coefficient. Unlike Bagnold, who applied the streampower concept to a unit bed area, Yang (1979) applied the power to the unit weight of water used to transport sediment (Yang, 2006), thus directly relating the total sediment concentration or total bed material load to streampower. Between these equations the unit streampower equations developed by Yang are less sensitive to a variation in Froude number and are applicable to subcritical, transitional, and supercritical flow regimes (Smith, 2006). Despite being valid for an extensive range of flow velocities, the sediment transport equations based on the streampower approach are derived for equilibrium sediment transport conditions. However, due to the continuous accelerating flow along the embankment perimeter, equilibrium sediment transport conditions are not reached in practice. Comparison between the erosion equation and the streampower relationship shows that the erosion equation is a function of the shear stress τ, and the streampower equation is a function of the shear stress τ multiplied by the mean velocity V. With the shear stress approximated as a function of the velocity squared, the erosion equation becomes similar to the streampower equation when a power of efficiency of 1.5 is applied. Hence the erosion equation is assumed to give a reasonably good approximation under supercritical flow conditions for $m = 1.5$. Cohesive sediments have a lower degree of erodibility than non-cohesive sediments. Hence most of the energy dissipated by turbulence is not used to transport sediment particles and a lower value for the power m is expected. The power in the erosion equation is thus expected to vary between 1 and 1.5, with a value of 1 more applicable to cohesive sediments, and 1.5 more applicable to loose sediment. Both the streampower based method and the shear stress based method use a factor of proportionality to calculate the actual erosion rate as a function of soil erodibility, and hence location. In a homogeneous soil, differences in erodibility are caused by compaction and the occurrence of negative pore pressures. Sidorchuk (2002) stochastically modelled soil erosion and soil deposition using five characteristic stochastic variables: flow velocity, soil cohesion, aggregate size of both native and deposited sediment, and soil consolidation. Sidorchuk (2002) found a relatively low increase in erosion rate with respect to the flow velocity, when the driving forces exceeded the stabilizing forces considerably. The influence of the variability of soil properties like cohesion, aggregate size and soil consolidation was also found to be less important in determining the erosion rate at high flow energy events. These conclusions are valid for saturated soil conditions, and correspond with the Shields Theory (Van Rijn, 1993). Shields showed that the dimensionless shear

stress became independent of the particle Reynolds number for high particle Reynolds numbers corresponding to high flow velocities or large particle sizes. The flow of water in and out of the embankment affects the lift force on the particles and could therefore influence surface erosion. Butt et al. (2001) studied the influence of swash infiltration and exfiltration on beach sediment transport. They hypothesized that the outflow of water from the beach causes fluidization of the top soil layer and hence increases beach erosion. Although Butt et al. (2001) discovered that the pressures in the beach were not high enough for fluidization to occur, they did observe a small increase in sediment transport. This was linked to the outflow of water: (1) increasing the lift force on the particles making them more susceptible to erosion, and (2) enhancing the thickness of the laminar boundary layer, thus decreasing the shear forces on the particles. Butt et al. (2001) found a decrease of 10.5% in wave uprush transport because of infiltration and an increase of 4.5% in transport caused by exfiltration during downrush. From the literature to date (and to the author's knowledge), it is evident that the effects of inflow and outflow on sediment erodibility and the erodibility of unsaturated soils are still poorly understood. Thus far the analysis of erosion types has been restricted to the possible effects of erosion due to flow. Due to an increase in flow velocities along the slope in combination with non-equilibrium transport conditions, the embankment slope is theoretically expected to steepen even if the flow does not separate from the bed. A continuous steepening embankment slope leads to a geotechnically unstable embankment shape. This is unrealistic for full scale embankments, especially when the embankment is constructed from non-cohesive materials. Hence geotechnical failures are expected to have a large impact on the overall erosion behaviour.

Based on visual observations of embankment breaches, micro-geotechnical failures appear to dominate over the macro-geotechnical failures in limiting the landside slope gradient. The matric suction inside unsaturated embankment soil increases the stability of the embankment and contributes to preventing major geotechnical failures from occurring (Nearing et al., 1988). Initiation of groundwater flows parallel to an overflowing landside embankment slope was the main cause of failure of embankments with steep slopes in the 1953 flooding in the South-West of the Netherlands (Verruijt, 2001). Groundwater flows parallel to steep slopes initiate sediment-laden gravity flows that prevent the slopes from steepening (Takahashi, 2009; Iverson et al., 1997). Hence this could play an important role in breach formation. For an embankment constructed of non-cohesive material, and with slopes sufficiently long to allow for a 1D analysis for

the stability, the stability of the embankment slope is determined by the safety factor F_s given by

$$F_s = \frac{\tan\phi}{\tan\alpha}, \tag{1.3}$$

where $\tan\phi$ is the gradient of internal friction of the soil, and $\tan\alpha$ the gradient of the embankment slope. The safety factor F_s reduces by (approximately) 50% in the case of groundwater flow parallel to the embankment slope (Takahashi, 1981; Verruijt, 2001). Sediment-laden gravity flows increase the apparent erosion of the slope and reduce the internal friction angle of the soil. A shear stress exerted by a flow over the landside slope further reduces this factor of safety. Fox et al. (2007) found a strong correlation between seepage flow and the occurrence of headcuts. Hence it is assumed that headcuts only occur when (1) the cohesive properties of the soil under saturated conditions prevent small-scale slope instabilities, or (2) the unsaturated soil properties for the duration of the erosion process prevent sediment-laden gravity flows. In the latter case, the embankment soil must have a low permeability. In cases where sediment-laden gravity flows occur, their apparent smoothening effect by redistribution of the embankment soil prevents the formation of headcuts. Hence embankments made of non-cohesive and relatively porous material erode according to the surface erosion process irrespective of the flow type. Even when small-scale slope failures are prevented, the flow velocity over the crest must be high enough for a concentration of shear stresses to occur at the landside slope in order for the headcut erosion process to initiate.

In the case of headcut erosion, the flow rate increases sharply when the retrograde erosion of the landside slope reaches the waterside slope, leading to Stage 3 and subsequently Stage 4. In the case of surface erosion, sediment-laden gravity flows in combination with erosion lead to a smoothed embankment profile and Stage 3 becomes less distinguishable. Stage 4 initiates when the smoothed profile starts to affect the waterside slope. Horizontal flow contraction causes a reduced pressure on the side walls and this can result in flow separation from the side walls. When the flow separates, the strong turbulent motions cause an increase in shear stress and lateral erosion. Changes in the lateral breach dimensions are discontinuous in nature, and governed by a combination of erosion and geotechnical failure mechanisms. Two distinguishable geotechnical failure processes contribute to the shape of the breach sides (see Figure 1.6). The first failure mechanism is initiated by downward erosion of the breach invert level. When the embankment soil is reasonably permeable, the phreatic water level in

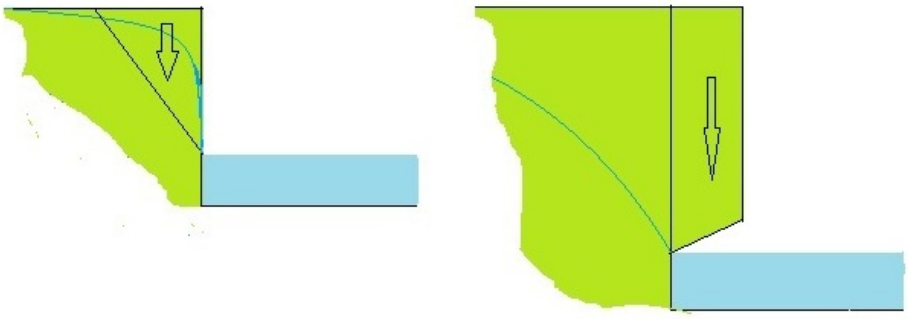

Figure 1.6: Types of breach side slope failure

the embankment lowers progressively along with the water level in the breach. In the case of less permeable embankment material, the rate at which pore pressures reach a new equilibrium is assumed to be smaller than the downward erosion rate of the breach invert level. Groundwater flow from the breach side walls into the breach causes embankment material to become unstable and to slump into the breach, narrowing the breach (Rinaldi and Casagli, 1999). However the high flow velocity and transport capacity of the flow lead to rapid removal of the slumped material. Increased flow velocities through the breach can initiate a second failure mechanism whereby the breach flow undercuts the embankment at the breach sides. The undercut sections slump into the breach when their weight exceeds the stabilizing forces (Mohamed, 2002). The rate at which the flow undercuts the side slopes is determined by the flow through the breach and the degree of horizontal contraction. The breach continues to grow laterally until the end of Stage 5 at which the breach flow is so small that the erosion process stops.

1.2 Current methods for breach modelling

As explained in the previous section, the failure of a grass cover depends on time, location, grass type, grass quality, and geotechnical properties such as the soil type and pore pressure. Current breach models often simplify the failure process of a grass cover by assuming instantaneous failure of the entire grass cover provided certain conditions are met, making the failure of the cover independent of the location. The duration of resistance against failure of a grass cover under certain flow conditions can be estimated using the design chart from Technical Note 71 (Whitehead et al., 1976), as presented in

Figure 1.7 . The given relationships are not presented as functions of the soil properties

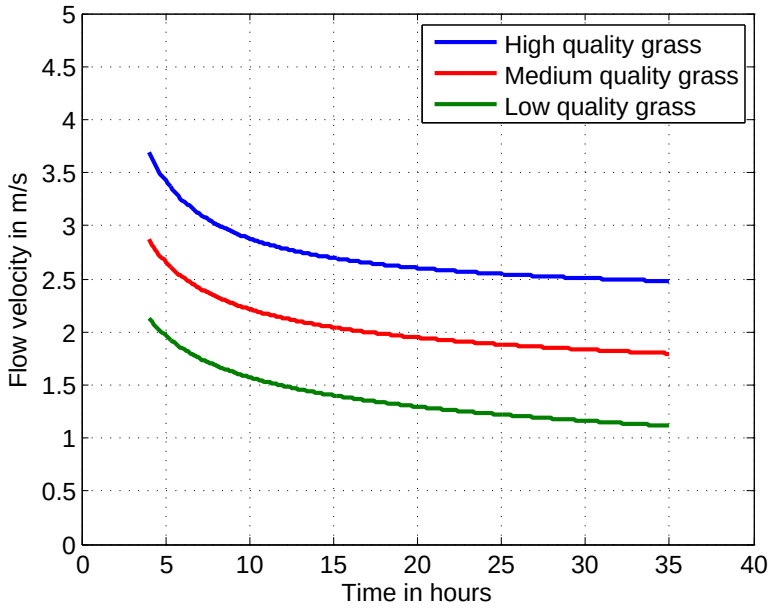

Figure 1.7: Critical velocities versus time to failure for 3 quality types of grass covers (After Whitehead et al. (1976))

and hence the error bars corresponding to each of the relationships are expected to be quite large (though are not provided in Technical Note 71). After failure of the grass cover the actual breach model sets in. Extensive reviews of the history of breach models are given by Morris et al. (2009a) , Mohamed (2002), and Visser (1998). Mohamed classified breach models into non-physics based methods (data-based models), semi-physics based methods (empirical models), and physics based methods. Mohamed and Morris reported that the early physics based models by Cristofano (1965), Harris and Wagner (1967), and Brown and Rogers (1981) used a broad-crested weir formula with a fixed weir coefficient to calculate the flow over the embankment. Each of these physics based models assumed a constant breach shape, which continuously grew to simulate breach development. A shift in modelling strategy occurred during 1981 to 1984, when the flow prediction was made using the shallow water equations with sediment movement modelled using separate transport equations. These models were deficient in assuming that no lateral erosion would occur after the peak outflow (Mohamed, 2002). From 1984 to 1989 the modelling of breach flows reverted to use of the weir equation with the erosion rate determined by sediment transport equations. Up to this time, models used pre-defined breach shapes to account for the effects of geotechnical failures. Over time, breach models became better able to predict the peak discharge and the moment when this occurred, however they remained inaccurate in predicting breach

dimensions. Mohamed reported that these models overestimated the lateral growth of the breach. From 1989 to 1998, the models under development did not account for side slope stability. However advances were made in the use of different sediment transport formulae and in the development of empirical formulae for the erosion rate based on data from small-scale experiments. For example, Visser (1998) used a combination of 4 sediment transport formulae for the BRES model. Broich (1998) developed the DEICH_N1 and DEICH_N2 models in which the flow was modelled using the one-dimension and 2D shallow water equations and sediment transport was calculated using a combination of empirical formulae. This model still assumed a standardized breach shape. After 1998, the primary goal of model development remained a proper representation of the sediment transport rate. For this reason, further experiments were performed on embankments constructed from cohesive and non-cohesive soils in order to create a larger dataset for model validation. In recent years, breach modelling has involved calibrating soil erodibility by finding the best fit to various different sediment transport formulae, and typically the flow through the breach is modelled using the broad-crested weir equation given by

$$\overline{\widetilde{u}} = c_w \sqrt{2g\Delta H}, \tag{1.4}$$

where $\overline{\widetilde{u}}$ is the depth and breadth-averaged flow velocity through the breach as defined in Chapter 4, c_w is the weir coefficient, g is the acceleration due to gravity, and ΔH is the head difference. Mohamed (2002) noted that the weir equation might perform better than the 1D shallow water equations because it is possible to take flow curvature into account by calibrating the weir coefficient in the broad-crested weir equation. The problem however is that the weir coefficient c_w does not have a constant value in the case of embankment breaching. Because of the changing shape of the embankment during the breach, the weir coefficient should be constantly recalibrated. For an idealised flow with minimum energy losses because of friction and contraction, the weir coefficient has a value of 1 (Ackers et al., 1978; Nortier and De Koning, 1991). For situations where high energy losses occur, such as at a long weir, this value can become as low as 0.7 (Ackers et al., 1978; Nortier and De Koning, 1991). When the downstream slope has eroded away and the resulting breach geometry corresponds to a short weir,

the streamlines contract. The pressure distribution becomes lower than hydrostatic, leading to increased flow discharge and velocity. In this case, the maximum increase in the weir coefficient is 40% (Nortier and De Koning, 1991). The error in flow discharge and hence velocity may therefore also be up to 40%. In practice, this problem is still relatively small because the weir coefficient can be calibrated in such a way as to compensate for the systematic error in estimating the discharge. However, the error made in the estimate of sediment transport rate is more serious. In the case of a shear stress based approach, the error in the calculated erosion rate is linearly dependent on the error made in the calculation of the shear stress, which is approximately quadratically dependent on the flow velocity u. When the streampower method is used, any error made in the calculation of the flow velocity is enhanced to a third power in the calculation of the erosion rate.

As becomes clear from this brief historical review, the sophistication and predictive capability of breach models has improved over the past half a century, although such models still contain numerous assumptions with corresponding uncertainties. The performance of breach models is often misinterpreted (Morris et al., 2009a). Morris et al. (2008) mention that models are usually developed and calibrated against a single dataset because of the lack of high quality datasets available for calibration purposes, hence the ability of the model to reproduce the results of the dataset is inherently quite good. Moreover, the assessment of model performance by comparing predicted and measured flood hydrographs is also misleading because the flood volume is not solely controlled by the rate and size of the breach growth. Currently models are able to predict the peak discharge to within an accuracy of 25-30%. Model inaccuracy in predicting the time at which the peak discharge takes place is even worse. In the early stages of its development, the HR BREACH model (Mohamed, 2002) used a constant weir coefficient. Nowadays, HR BREACH incorporates a changing weir coefficient, based on the global shape of the embankment, the aim being to obtain a more accurate calculation of the flow. Morris (2010) found that use of a variable, instead of a constant weir coefficient led to a slight improvement in accuracy, but concluded that

the primary source of error lay in the calibration of the soil erodibility, which was solely dependent on the soil properties. Morris et al. (2009a) observed that material texture, moisture content, and degree of compaction all influence soil erodibility. Of these, material texture and compaction are both difficult to assess and model. However the influence of moisture content can be modelled reasonably well. Techniques for modelling the effects of rainfall on the development of pore pressures in slopes can be used to simulate the development of pore pressures in embankments. Recently Morris (2010) further observed that the effects of the pore water pressure and other soil properties should not be neglected when breach processes are modelled; however this is the case in many existing breach models.

The conclusions that can be drawn from the previous sections are

- Five stages can be identified in breach formation. In Stage 1, the embankment functions well. In Stage 2, the landside slope retreats towards the waterside slope, In Stage 3, the landside slope reaches the waterside slope and the flow increases, In Stage 4, the flow rapidly increases with widening of the breach and further erosion of the waterside slope. In Stage 5, the flow velocities decrease to the point that the erosion process stops.

- The strength of a grass protection layer depends on the frictional forces between the soil and the roots, and the tensile strength of the roots. The frictional forces are a function of the moisture content of the soil. Hence the strength of a grass protection layer is dependent on the soil parameters, grass characteristics, and time. Failure relationships used in breach models to determine the failure of a grass protection layer are expected to have large bands of uncertainty.

- Whether an embankment erodes due to surface erosion or headcut erosion depends on the flow dynamics, sediment transport processes under supercritical flow velocities, and the stabilizing and destabilizing processes in the embankment soil. Soil erosion under continuous accelerating supercritical flow velocities

is best represented by

$$E = K_e \left(\tau - \tau_c\right)^m , \tag{1.5}$$

where $m = 1.5$ in the case of surface erosion and $m = 1$ in the case of headcut erosion.

- The matric suction in unsaturated soils strongly influences the soil stability and hence should be accounted for when determining the stability of a slope. Groundwater flows parallel to the slope reduce the stability of the slope and induce sediment-laden gravity flows.

- In the past, breach models have modelled flows with depth integrated flow models. In some breach models flow contraction is accounted for by means of contraction factors. Instead of improving the accuracy with which the flow is modelled, recently the focus has been on improving the calculation of sediment transport rates.

- The small number of good quality datasets available has caused misinterpretations in the performance of breach models.

1.3 Aims and objectives

Breach predictions form a key part in predicting the quantity of flood water released, the rate at which it is released, the size of the breach, and the timing of the breach. The quantity of flood water and the rate at which it is released are both used in flood spreading models to assess the damage rising from a flood event. The size of the breach and timing of the maximum breach discharge are used in the development of evacuation plans and to assess the available time for emergency repairs. Ideally a breach model needs to give a highly accurate, rapid breach assessment to form the basis of the statistical analysis. Unfortunately model accuracy comes at a cost of model speed. Whether the requirement of the model is speed or accuracy, the model should also be able to simulate failure by surface erosion or headcut erosion correctly.

1.3.1 Influence of geotechnical processes

Section 1.1 notes that groundwater flow parallel to the landside slope reduces the maximum achievable slope angle of the soil by approximately 50%. A flow over the landside slope further reduces the maximum achievable slope angle and induces sedment-laden gravity flows (Takahashi, 1981). For sediment-laden gravity flows, the instability in the bed is not caused by the hydrodynamic forces of the fluid but because of a static disequilibrium of the soil. When the failed material is distributed uniformly over the depth of the fluid flow, a sediment-laden gravity flow is called a debris flow. In the case of embankment failures this distinction is however of minor importance. What is of importance is whether the occurrence of a sediment-laden gravity flow contributes to the erosion process of an embankment. Insight into static disequilibrium of the landside embankment slope under overflow conditions could improve the understanding of how the landside slope erodes and retreats through the embankment. The first aim of this thesis is to develop some understanding of how geotechnical processes influence embankment breaching, and how to model their effects.

Objectives

In order to achieve this aim, the following objectives were set:

- To analyse the processes of saturation of an overflowing landside embankment slope.
- To describe the process of saturation mathematically.
- To use the relationship between moisture content and matric suction to derive how the pore pressures change during saturation of the soil.
- To derive a time dependent stability condition for a slope of unsaturated soil with increasing moisture content.

1.3.2 Rapid breach prediction

In the U.K. the research project Risk Assessment for flood and coastal defence for Strategic Planning (RASP) (HR, Wallingford and University of Bristol, 2004) developed a framework for undertaking risk analysis. Within this framework, the performance (reliability) of the system of flood defences is represented using fragility curves that describe the likelihood of structural failure (breaching) under given hydraulic loading conditions. This framework was adopted by the Environment Agency and has been used to underpin its National Flood Risk Assessment (NaFRA) (Hall et al., 2003), (Environment Agency, 2009). This method was further developed by Gouldby et al. (2010), and then implemented within the Environment Agencys Modelling Decision and Support framework (MDSF2).

Within NaFRA, and more recently MDSF2, breach size and flood volume is predicted using a simplified calculation based on crude assumptions (Hall et al., 2003). Any error in predicting breach formation translates to an error in predicting the risk of flooding of downstream areas. An improved method for predicting the flood volume through a breach is needed for a more reliable assessment of different flood scenarios. The flood volume prediction method needs to be fast since system risk approaches (as used in MDSF2) require the calculations to be repeated numerous times with slightly different parameters. The problem with breach predictions are that the hydrograph shape depends on the river hydrograph, flood area, embankment shape, embankment materials, and embankment protection type. Each of these parameters varies strongly between embankment sections. Furthermore, the influence of each of these parameters is different throughout the duration of the breach formation and describe often discontinuous processes. An almost infinite number of combinations of breach conditions is possible, and limited data are available on embankment breaches. Consequently statistical methods and the use of equations to predict breach size, breach volume, and the timing of a breach event, are highly inaccurate. The second main aim of this thesis is to develop a fast, accurate embankment breach prediction tool for incorporation in the system risk modelling strategy, capable of predicting both the flood volume and breach

size. This model is referred to as AREBA (A Rapid Embankment Breach Assessment).

Objectives

In order to achieve this second aim, the following objectives are set:

- To describe the effects of the flow, and geotechnical properties, in a simplified way.
- To develop analytical equations for calculating the rate of breach growth based on the simplified description of the flow.
- To incorporate a simplified description of the geotechnical failures when solving the equations
- To combine the different analytical equations in a rapid model
- To benchmark the AREBA model against HR BREACH
- To validate AREBA model against field data

1.3.3 New methods for modelling breach development

The mechanics of erosion of an embankment due to overflow is presently not fully understood. The complex interactions of geotechnical and hydrodynamic processes provide a challenge to modelling the formation of an embankment breach (Morris et al., 2008). Only by accurate modelling of the interacting physical processes can a better understanding of the breach behaviour be obtained.

State-of-the-art breach models use either a 1D or a depth-averaged 2D description of breach flow. The inherent assumption of hydrostatic pressure limits these models in their ability to model breach flow accurately. Due to averaging of the flow over the depth and width, (1) the effects of turbulent motions on the erosion and energy balance are ignored, and (2) the effects of non-hydrostatic pressures due to flow contraction are either not, or incorrectly, accounted for. Inaccuracies in the description of the flow are

amplified in the calculation of the bed shear stresses. Together with assumptions concerning the erodibility of the soil, this provides an inaccurate prediction of the erosion rate and hence the erosion behaviour of the embankment. Below, for breach Stages 2-5

Figure 1.8: Illustration of the three phases in breach flows (Photo's by M. Morris (2004))

methods are proposed for an accurate description of the flow and the physics. Figure 1.8a shows Stage 2 of a breach flow during which the embankment protection fails and the landside slope retreats towards the waterside slope. During Stage 2, flow accelerations are negligible in the horizontal direction transverse to the main flow direction. The pressure distribution is non-hydrostatic where the flow contracts vertically over the crest and accelerates along the landside slope. The start of Stage 3 is characterised by both horizontal and vertical contracting streamlines, as is depicted in Figure 1.8b. The horizontal contraction of the streamlines indicates that the horizontal flow accelerations normal to the main flow direction may no longer be neglected. In Stage 4, depicted in Figure 1.8c, the embankment erodes over its full height and the streamlines contract both horizontally and vertically until the breach has grown over the full height of the embankment. From that moment in Stage 4 onwards, including Stage 5, the effects of vertical flow accelerations can be neglected. An important aspect is the period of time during which the embankment is able to withstand the erosional forces in Stage 2 in relation to the timing of the high water event. When the time scale of the river hydrograph is smaller than the time scale of Stage 2, then Stage 3 is never reached and the damage remains small. Hence the processes during Stage 2 determine whether a full breach stage is reached or not. Once a full breach has been formed, the flow velocities increase rapidly. The accuracy with which Stages 3-5 are modelled

has a small impact on the overall flood volume released through the breach, though it is important for an accurate calculation of the peak discharge. Since the processes during Stage 2 determine whether a large breach forms and whether actions could be taken to prevent this, the third main aim of this thesis is to develop methods for a more accurate physical description of the failure processes operating during Stage 2.

Objectives

In order to achieve this aim, the following objectives were set:

- Derive a reduced set of equations that give an accurate description of the flow
- Develop a method to solve the reduced set of equations
- Validate the method against several test cases

1.4 Synopsis

In Chapter 2, a 1D analysis is given of how the stability of an overflowing slope changes over time due to changes in matric suction with saturation of the embankment. A time dependent safety factor is derived to arrive at an artificial erosion rate due to sediment-laden gravity flows. In Chapter 3, constitutive equations are given for a rapid breach model that has been developed to improve upon the calculation of flood volumes through breach formation performed in the national flood risk assessment (NaFRA) and applied in the modelling decision and support framework (MDSF2) (HR, Wallingford and University of Bristol, 2004). Chapter 3 gives the modelling methodologies for failure by both headcut erosion and surface erosion. The rapid model is benchmarked against the breach model HR BREACH, and validated against experimental data from the EU IMPACT project, under which extreme flood processes and uncertainties were investigated, and data from the experiments performed by the US Department of Agriculture-Agricultural Research Services (USDA-ARS). The model results are compared against the method used in NaFRA and MDSF2. Chapter 4 presents

the process of breadth integration applied to the Reynolds-Averaged Navier–Stokes equations for incompressible flows, pressure Poisson equations, and eddy viscosity relationship, to arrive at a new set of equations for a variable breadth flow geometry. The resulting equations can be used to calculate the flow field in a vertical 2D plain for flows with negligible horizontal contraction though with a varying breadth geometry. In Chapter 5 several pressure correction methods are given which can be used to solve the system of equations. The solution method for each of the different equations is provided for one of the pressure correction methods. Results of the validation tests used to test the equations and the solver are given in Chapter 6. In Chapter 7 both the rapid breach model and the vertical 2D flow model are discussed. Conclusions and recommendations are given in Chapter 8. A nomenclature can be found in the back of the thesis.

Chapter 2

Slope stability analysis

Sediment-laden gravity flows and debris flows belong to the category of landslides, which are defined here as the mass movement of material or debris down a slope. Theoretical models predict the susceptibility of landslides by studying the conditions of static disequilibrium of an infinitely long slope using the effective stress principle (Iverson, 2000). For example Takahashi (1981) analysed conditions for the mobilization of a sediment-laden gravity flow by accounting for surface shear stresses in the soil stability analysis, assuming the soil to be fully saturated. To study time dependent changes of the (dis)equilibrium of a landside embankment slope under overflow conditions, a similar analysis is performed here to that undertaken by Takahashi (1981), while accounting for unsaturated soil conditions.

2.1 Problem description

As the starting point of the analysis, the landside embankment slope is idealised as an infinitely long slope of uniform non-cohesive material over which water flows with depth equal to the normal depth. This assumption of normal water depth is not entirely correct. However in most cases, the effect of uncertainty due to limited knowledge of the influence of local soil properties on the static equilibrium of the embankment is expected to outweigh the effects of the slight error in the hydrodynamic boundary

conditions. The static balance equation for an infinite slope is given by

$$\frac{\partial \sigma'_{\varepsilon\varepsilon}}{\partial \varepsilon} + \frac{\partial \tau'_{\varepsilon\zeta}}{\partial \zeta} + \frac{\partial P_p}{\partial \varepsilon} + \gamma_s \sin\alpha = 0, \tag{2.1}$$

$$\text{and} \qquad \frac{\partial \tau'_{\varepsilon\zeta}}{\partial \varepsilon} + \frac{\partial \sigma'_{\zeta\zeta}}{\partial \zeta} + \frac{\partial P_p}{\partial \zeta} + \gamma_s \cos\alpha = 0,$$

where ε is a distance in the $\hat{\varepsilon}$-coordinate direction parallel to the slope, ζ is the distance in the $\hat{\zeta}$-coordinate direction normal to the landside slope into the soil, γ_s is the specific weight of the soil, and α is the angle between the $\hat{z}$ Cartesian coordinate direction (pointing vertically upwards) and the $\hat{\zeta}$-coordinate direction (see Figure 2.1). σ' refers to the effective normal stress, τ' to the effective shear stress and P_p to the local pore pressure. The soil is assumed to be unsaturated when the flow over the slope first

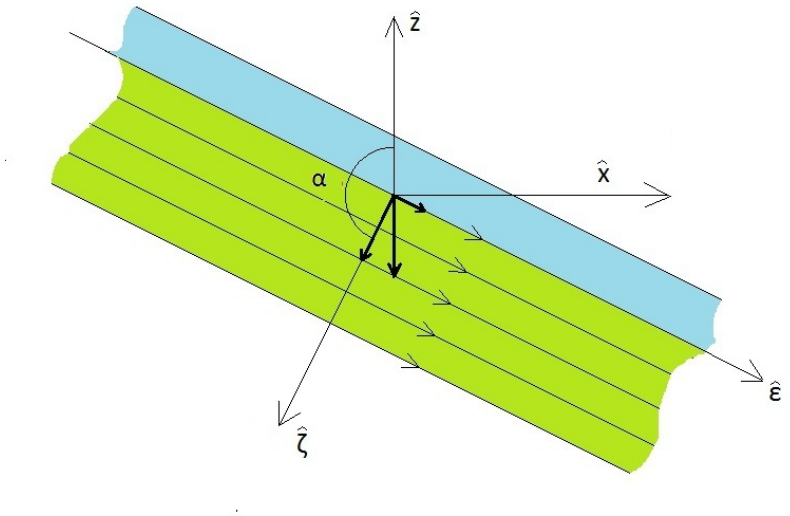

Figure 2.1: Definition sketch for the coordinate system used in describing the flow over and through the landside slope.

occurs. Capillary action in unsaturated soil causes a matric suction that enhances the stability of the embankment, but reduces with time with saturation of the soil. Richards (1931) studied the capillary behaviour of liquids in porous media. By combining the continuity equation with Darcy's law and by defining a capillary potential, Richards (1931) mathematically described how the soil moisture content changes with time. In the analysis that follows, the Richards equation is used in combination with Equation

(2.1) to derive an expression for the stability of the slope, expressed as a safety factor F_s, as a function of time, soil properties, and slope geometry.

2.2 Saturation of the soil

The time-dependent storage equation for the pore water concentration θ is given by

$$\frac{\partial \theta}{\partial t} + \frac{\partial \theta u_\varepsilon}{\partial \varepsilon} + \frac{\partial \theta w_\zeta}{\partial \zeta} = 0, \tag{2.2}$$

where w_ζ is the flow velocity in the $\hat{\zeta}$-direction, u_ε is the flow velocity in the $\hat{\varepsilon}$-direction, and t is time (See Figure (2.1)). It is assumed that the filling rate of the pores is independent of the $\hat{\varepsilon}$-coordinate direction leading to the 1D storage equation given by

$$\frac{\partial \theta}{\partial t} + \frac{\partial \theta w_\zeta}{\partial \zeta} = 0. \tag{2.3}$$

With a constant value for the concentration of saturated soil (θ_s), and by assuming a constant value for the residual water content θ_r, Equation (2.3) is rewritten in terms of the normalised water content Θ as

$$\frac{\partial \Theta}{\partial t} + \frac{\partial \Theta w_\zeta}{\partial \zeta} = 0, \tag{2.4}$$

where

$$\Theta = \frac{\theta - \theta_r}{\theta_s - \theta_r}. \tag{2.5}$$

McKee and Bumb (1984) suggested an exponential relationship between the normalised water content Θ and matric suction Ψ near maximum desaturation or close to fully saturated conditions. For positive suction the relationship is (Fredlund and Xing, 1994)

$$\Theta = \frac{1}{1 + e^{(-\Psi - a)/b}}. \tag{2.6}$$

For the intermediate range of saturation McKee and Bumb (1984) suggested

$$\Theta = \frac{1}{e^{(-\Psi - a)/b}}, \tag{2.7}$$

where a and b are curve fitting parameters used to fit the relationship to the soil-water characteristic curve. Rewriting the pressure as a function of the normalised water content gives

$$\Psi = -b\ln\left(\frac{1}{\Theta} - 1\right) + a. \tag{2.8}$$

For fully saturated conditions $\Theta = 1$ and the capillary suction Ψ should be 0. To fulfill this condition, the pressure is expressed in terms of the normalised water content according to Equation (2.7) instead of (2.6), leading to

$$\Psi = -b\ln\left(\Theta\right) + a. \tag{2.9}$$

Figure (2.2) illustrates a possible pressure plot between the normalised water content and the matric suction for a fine graded sandy soil for which $a = 10$, and $b = 100$ (Fredlund and Xing, 1994). In the case of finer soils the same moisture content gives a higher matric suction and a and b increase. Similarly a and b decrease for a coarser grained soil (Fredlund and Xing, 1994). An expression for the flow velocity w_ζ is found by reformulating Darcy's law in terms of capillary suction, leading to

$$w_\zeta = -\frac{K}{\rho_w g}\left(-\frac{\partial \Psi}{\partial \zeta} + \rho_w g \cos\alpha\right), \tag{2.10}$$

where the degree of suction Ψ is positive, K is the hydraulic conductivity of the soil, ρ_w is the density of water, and g is the acceleration due to gravity. In the case of a fully saturated soil, $w_\zeta = 0$ and

$$\Psi = \int \rho_w g \cos\alpha d\zeta = \rho_w g \zeta \cos\alpha + C \tag{2.11}$$

where C is an arbitrary constant which is given by the boundary conditions. The

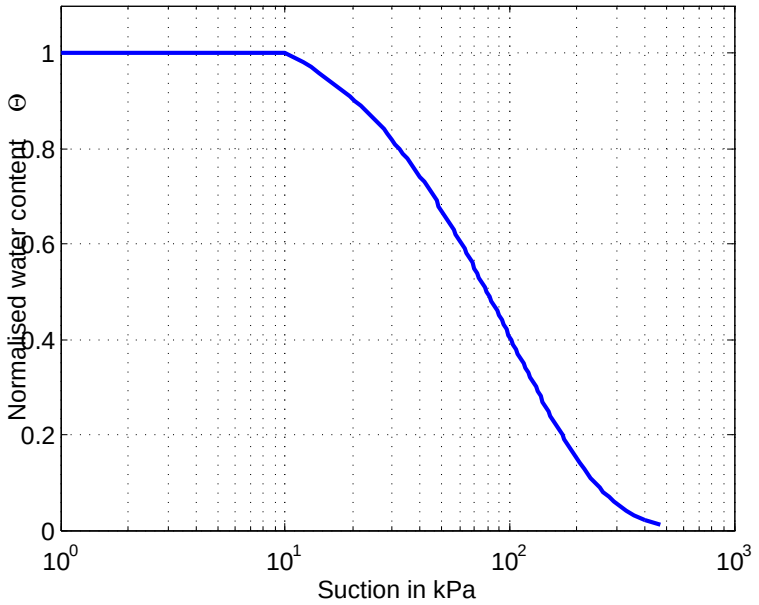

Figure 2.2: Relationship between the capillary suction (Ψ) and the normalised water content (Θ), for a fine graded sandy soil for which $a = 10$ and $b = 100$ (After McKee and Bumb (1984))

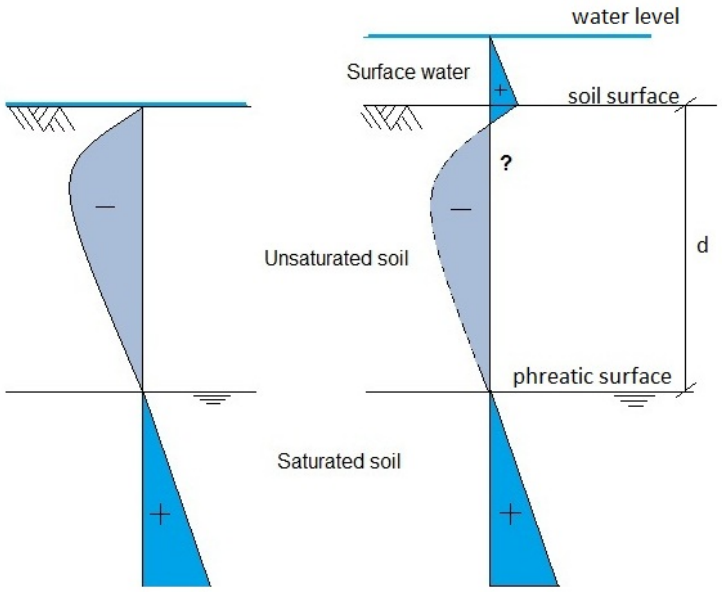

Figure 2.3: Two different initial suction profiles for unsaturated soils

left illustration in Figure 2.3 shows a possible pressure profile for an unsaturated soil stratum lying above a saturated soil stratum with a negligibly thin layer of water flowing over the soil surface. With the uppermost layer of the soil saturated, the suction pressure in the soil becomes zero and Equation (2.9) is valid. However in

the right illustration, the depth of water on the soil is significant. Since the water infiltrates into the soil with a constant velocity w, the surface water on the soil does not experience vertical acceleration and the pressure distribution of the water on the soil is hydrostatic. However it is not possible to account for the hydrostatic pressure on the soil by adding a constant pressure to the relationship between the water content and the suction to satisfy the boundary condition at the soil surface for the case when $\Theta = 0$, since this violates the boundary condition at the interface between the saturated and unsaturated soils, given by $\Psi|_{\zeta=d} = 0$. In order to satisfy the boundary condition due to the hydrostatic pressure at the soil surface as well as the condition of zero pressure at the interface between the saturated and unsaturated soils, the relationship between the moisture content and the pressure is modified as

$$\Psi_m = -b\ln\Theta + \Psi|_{\zeta=0} - \zeta\frac{\Psi|_{\zeta=0}}{d_{ph}} \tag{2.12}$$

for $d_{ph} > 0$, and

$$\Psi_m = -b\ln\Theta + \Psi|_{\zeta=0} \tag{2.13}$$

for $d_{ph} = 0$, where d_{ph} is the distance below the landside slope at which the phreatic surface is located, Ψ_m indicates the modified equation, and $\Psi|_{\zeta=0}$ is the hydrostatic pressure boundary condition at the soil surface where $\zeta = 0$. The assumed linear increase in pore suction (or decrease in pore pressure), indicated by the last term in Equation (2.12), was based on the reasoning that w_ζ must remain constant between $\zeta = 0$ and $\zeta = d$ to satisfy continuity. Inserting Equation (2.10) in terms of Ψ_m in Equation (2.4) leads to

$$\frac{\partial\Theta}{\partial t} - \frac{\partial}{\partial\zeta}\left[\frac{\Theta K}{\rho_w g}\left(-\frac{\partial\Psi_m}{\partial\zeta} + \rho_w g\cos\alpha\right)\right] = 0, \tag{2.14}$$

or

$$\frac{\partial\Theta}{\partial t} - \frac{\partial}{\partial\zeta}\left[\frac{\Theta K}{\rho_w g}\left(-\frac{\partial\Psi}{\partial\zeta} + \rho_w g\cos\alpha + \frac{\Psi|_{\zeta=0}}{d_{ph}}\right)\right] = 0, \tag{2.15}$$

where α is the angle that the $\hat{\zeta}$-coordinate direction makes with the vertically upward $\hat{z}$-coordinate direction (See Figure 2.1). This partial differential equation contains both Ψ and Θ and cannot be solved directly. With

$$-\frac{\partial \Psi_m}{\partial \zeta} = b\frac{\partial \left(\ln\Theta\right)}{\partial \Theta}\frac{\partial \Theta}{\partial \zeta} + \frac{\Psi|_{\zeta=0}}{d_{ph}}, \tag{2.16}$$

Equation (2.15) gives for K and b constant, and $\Psi|_{\zeta=0} = \rho_w g d_n \cos\alpha$

$$\frac{\partial \Theta}{\partial t} - \frac{Kb}{\rho_w g}\frac{\partial^2 \Theta}{\partial \zeta^2} - K\cos\alpha\left(1 + \frac{d_n}{d_{ph}}\right)\frac{\partial}{\partial \zeta}\Theta = 0. \tag{2.17}$$

2.3 Solution of the 1D storage equation

Assuming that a flow over the embankment initiates at $t = t_0$ with a depth equal to the normal depth d_n, an analytical solution of Equation (2.17) is developed using Laplace transforms.

2.3.1 Solution by Laplace transforms

The general Laplace transform is given by

$$F(s) = \int_0^\infty e^{-st} f(t) dt, \tag{2.18}$$

where $f(t)$ is defined in the domain $t > 0$. Outside the domain $f(t) = 0$. The Laplace transform gives the following expression for a derivative

$$\begin{aligned}\int_0^\infty e^{-st}\frac{\partial f}{\partial t}dt = \int_0^\infty e^{-st}df = \int_0^\infty d\left(e^{-st}f\right) - \int_0^\infty f de^{-st} = \\ -f\left(0^t\right) + s\int_0^\infty e^{-st}f dt = sF(s) - f\left(0^t\right).\end{aligned} \tag{2.19}$$

Let

$$\hat{\Theta} = \int_0^\infty \Theta e^{-st} dt, \tag{2.20}$$

then using Laplace transforms, Equation (2.17) is recast as giving the corresponding ordinary differential equation

$$-\frac{Kb}{\rho_w g}\frac{d^2\hat{\Theta}}{d\zeta^2} - K\cos\alpha\left(1+\frac{d_n}{d}\right)\frac{d\hat{\Theta}}{d\zeta} + s\hat{\Theta} - \Theta_0 = 0. \tag{2.21}$$

The particular solution of this ordinary differential equation is $\hat{\Theta} = \frac{\Theta_0}{s}$. Assuming that $\hat{\Theta} = e^{\lambda\zeta}$, the differential equation gives

$$-\frac{Kb}{\rho_w g}\lambda^2 - K\cos\alpha\left(1+\frac{d_n}{d}\right)\lambda + s = 0. \tag{2.22}$$

Solving for λ gives

$$\lambda_1 = \rho_w g\frac{K\cos\alpha\left(1+\frac{d_n}{d_{ph}}\right) + \sqrt{\left(K\cos\alpha\left(1+\frac{d_n}{d_{ph}}\right)\right)^2 + 4\frac{Kb}{\rho_w g}s}}{-2Kb}, \tag{2.23}$$

$$\text{and} \qquad \lambda_2 = \rho_w g\frac{K\cos\alpha\left(1+\frac{d_n}{d_{ph}}\right) - \sqrt{\left(K\cos\alpha\left(1+\frac{d_n}{d_{ph}}\right)\right)^2 + 4\frac{Kb}{\rho_w g}s}}{-2Kb}.$$

The sum of the homogeneous and particular solutions of the ordinary differential equation gives the general solution

$$\hat{\Theta} = \frac{\Theta_0}{s} + c_1 e^{\zeta\lambda_1} + c_2 e^{\zeta\lambda_2}. \tag{2.24}$$

To find the initial condition, the steady state solution is solved for an assumed groundwater flow with the phreatic surface parallel to the landside slope at a depth d_{ph}. For the initial condition the embankment surface is assumed dry and hence $d_n = 0$. This gives the boundary conditions

$$\hat{\Theta}|_{\zeta=0} = \frac{A}{s}, \tag{2.25}$$

$$\text{and} \qquad \hat{\Theta}|_{\zeta=d_{ph}} = \frac{1}{s},$$

where A is an arbitrary water concentration in the soil at the boundary, and subscript d_{ph} refers to the boundary condition at an arbitrary depth at which the soil is fully saturated. Solving for c_1 and c_2 in Equation (2.24) for this set of boundary conditions gives

$$\begin{aligned}
&\zeta = 0 \rightarrow \hat{\Theta} = \frac{A}{s} = \frac{(A-\Theta_0)}{s} + c_1 + c_2 \rightarrow c_1 = -\frac{\Theta_0}{s} - c_2, \\
&\zeta = d_{ph} \rightarrow \hat{\Theta} = \frac{1}{s} = \frac{\Theta_0}{s} + c_1 e^{d_{ph}\lambda_1} + c_2 e^{d_{ph}\lambda_2}, \\
&c_1 = \left[\frac{(1-\Theta_0)}{s} + \frac{\Theta_0 - A}{s} e^{d_{ph}\lambda_2}\right] / \left(e^{d_{ph}\lambda_1} - e^{d_{ph}\lambda_2}\right), \\
\text{and} \qquad &c_2 = \frac{(A-\Theta_0)}{s} - \left[\frac{(1-\Theta_0)}{s} + \frac{(\Theta_0 - A)}{s} e^{d_{ph}\lambda_2}\right] / \left(e^{d_{ph}\lambda_1} - e^{d_{ph}\lambda_2}\right).
\end{aligned} \tag{2.26}$$

The solution is found by solving the inverse Laplace transform given by

$$f(t) = \frac{1}{2\pi i} \int_{c-i\infty}^{c+i\infty} e^{st} F(s) ds. \tag{2.27}$$

Since this requires a complex integral to be solved. Due to the serious computational challenge associated with solving this complex integral, the solution has been approached by multiplying Equation (2.24) with s, and afterwards replacing any s with $\frac{1}{2t}$ (Barends and Uffink, 2003). The solution is given by

$$\begin{aligned}
\Theta = &\Theta_0 + \overbrace{\frac{(1-\Theta_0) + (\Theta_0 - A)\, e^{d_{ph}\lambda_2}}{e^{d_{ph}\lambda_1} - e^{d_{ph}\lambda_2}}}^{c_1} e^{\zeta\lambda_1} + \\
&\overbrace{\left((A-\Theta_0) - \frac{(1-\Theta_0) + (\Theta_0 - A)\, e^{d_{ph}\lambda_2}}{e^{d_{ph}\lambda_1} - e^{d_{ph}\lambda_2}}\right)}^{c_2} e^{\zeta\lambda_2},
\end{aligned} \tag{2.28}$$

with

$$\lambda_1 = \rho_w g \frac{K\cos\alpha + \sqrt{(K\cos\alpha)^2 + 4\frac{Kb}{2t\rho_w g}}}{-2Kb}, \tag{2.29}$$

and

$$\lambda_2 = \rho_w g \frac{K\cos\alpha - \sqrt{(K\cos\alpha)^2 + 4\frac{Kb}{2t\rho_w g}}}{-2Kb}.$$

The steady state solution of Equation (2.28), forms the initial condition for Equation (2.22) with c_1 and c_2 given by Equation (2.26). The steady state solution is found for $\lim_{t\to\infty}$ for which $\lambda_2 = 0$, and

$$\lambda_1 = -\rho_w g \frac{\cos\alpha}{b}. \tag{2.30}$$

Substituting the expressions for λ_1 and λ_2 in Equation (2.28) gives

$$\Theta = \Theta_0 + \left(\frac{1-A}{e^{-\frac{\rho_w g d_{ph}\cos\alpha}{b}} - 1}\right) e^{-\zeta\frac{\rho_w g\cos\alpha}{b}} + (A - \Theta_0) - \left(\frac{1-A}{e^{-\frac{\rho_w g d_{ph}\cos\alpha}{b}} - 1}\right), \tag{2.31}$$

ot

$$\Theta = A - \left(\frac{1-A}{e^{-\frac{\rho_w g d_{ph}\cos\alpha}{b}} - 1}\right)\left(e^{-\zeta\frac{\rho_w g\cos\alpha}{b}} - 1\right). \tag{2.32}$$

For $b = 100$, $a = 0$, and the initial steady state boundary conditions

$$\begin{aligned} \Theta|_{\zeta=0} &= 0.2, \\ \Theta|_{\zeta=1} &= 1, \end{aligned} \tag{2.33}$$

the initial condition is depicted in Figure 2.4. The figure clearly shows the limited effect of the matric suction on the vertical uprise of water close to the phreatic surface. After the initial condition is found, the boundary conditions describe the situation of the phreatic surface at a depth d for groundwater flow parallel to the landside slope, and flow over the embankment surface. The boundary conditions that need to be satisfied

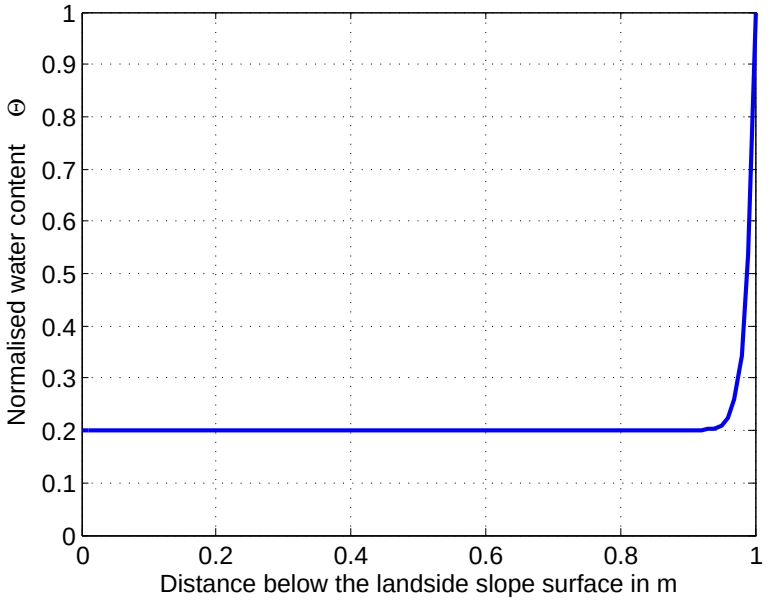

Figure 2.4: Initial condition for calculating the change in water content Θ with time t.

are

$$\hat{\Theta}|_{\zeta=0} = \frac{1}{s}, \qquad (2.34)$$
$$\text{and} \qquad \hat{\Theta}|_{\zeta=d} = \frac{1}{s}.$$

Solving the values of c_1 and c_2 for the second set of boundary conditions gives

$$\zeta = 0 \rightarrow \hat{\Theta} = \frac{1}{s} = \frac{\Theta_0}{s} + c_1 + c_2 \rightarrow c_2 = \frac{1-\Theta_0}{s} - c_1, \qquad (2.35)$$
$$\zeta = d_{ph} \rightarrow \hat{\Theta} = \frac{1}{s} = \frac{\Theta_0}{s} + c_1 e^{d_{ph}\lambda_1} + c_2 e^{d_{ph}\lambda_2},$$
$$c_1 = \left[\frac{(1-\Theta_0)}{s}\left(1 - e^{d\lambda_2}\right)\right] / \left(e^{d_{ph}\lambda_1} - e^{d_{ph}\lambda_2}\right),$$
$$\text{and} \qquad c_2 = \frac{1-\Theta_0}{s} - \left[\frac{(1-\Theta_0)}{s}\left(1 - e^{d_{ph}\lambda_2}\right)\right] / \left(e^{d_{ph}\lambda_1} - e^{d_{ph}\lambda_2}\right).$$

Substitution of the expressions for c_1 and c_2 from Equation (2.35) into Equation (2.22), and carrying out the approximation to the inverse Laplace transform gives

$$\Theta = \Theta_0 + \overbrace{\left[\frac{(1-\Theta_0)\left(1 - e^{d_{ph}\lambda_2}\right)}{\left(e^{d_{ph}\lambda_1} - e^{d_{ph}\lambda_2}\right)}\right]}^{c_1} e^{\zeta\lambda_1} + \overbrace{\left[1 - \Theta_0 - \frac{(1-\Theta_0)\left(1 - e^{d_{ph}\lambda_2}\right)}{\left(e^{d_{ph}\lambda_1} - e^{d_{ph}\lambda_2}\right)}\right]}^{c_2} e^{\zeta\lambda_2}, \qquad (2.36)$$

with

$$\lambda_1 = \rho_w g \frac{K\cos\alpha\left(1+\frac{d_n}{d_{ph}}\right) + \sqrt{\left(K\cos\alpha\left(1+\frac{d_n}{d_{ph}}\right)\right)^2 + 4\frac{Kb}{2\rho_w g t}}}{-2Kb}, \tag{2.37}$$

and $$\lambda_2 = \rho_w g \frac{K\cos\alpha\left(1+\frac{d_n}{d_{ph}}\right) - \sqrt{\left(K\cos\alpha\left(1+\frac{d_n}{d_{ph}}\right)\right)^2 + 4\frac{Kb}{2\rho_w g t}}}{-2Kb}.$$

For the boundary conditions given by $\Theta|_{\zeta=0} = \Theta|_{\zeta=1} = 1$, $d_n = 0$, and the initial condition depicted in Figure 2.4, the change in water content with time is depicted in Figure 2.5. One would expect a saturation front to move through the soil whereby

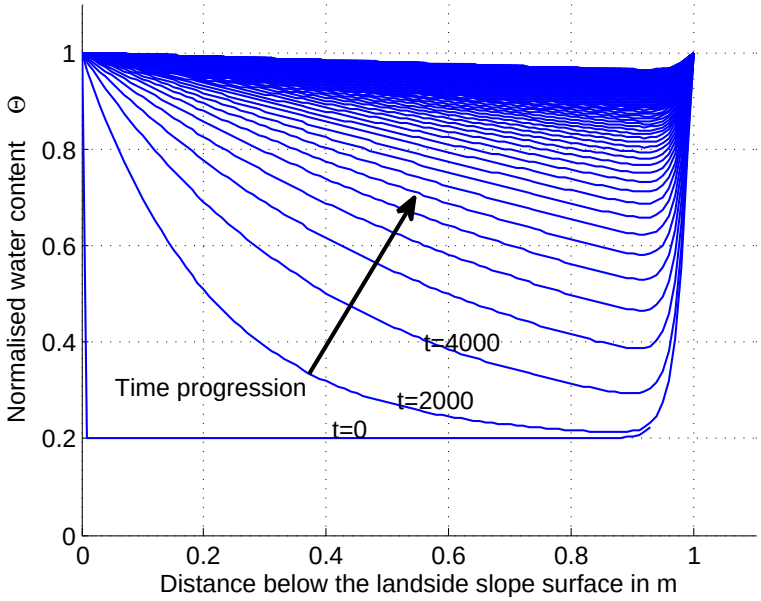

Figure 2.5: Change in water content with time for $K = 0.0001$ m/s,$\Delta t = 2000$ s, $b = 100$, and $a = 0$

the gradient in saturation at the front becomes more diffusive with increasing depth. However this behaviour is not well represented by the analytical solution that follows from the Laplace transform under the boundary conditions applied. Despite further diffusion of the saturation front with the depth, volume should be conserved and equal to the volume of water entering the soil at the boundary. At the phreatic surface at a depth d in the soil, the soil is fully saturated, and $\Theta = 1$. The effect of this boundary condition is that no more water can enter the soil at that depth. Hence the flow of

water at the downstream boundary stops, causing an increase in the saturation rate of the soil close to the downstream boundary. This description of the processes is used below to arrive at a mass conservative analytical solution of the saturation of the soil using error functions.

2.3.2 Solution by means of error functions

A general solution of the 1D diffusion equation

$$\frac{\partial c}{\partial t} - D\frac{\partial^2 c}{\partial x^2} = 0 \tag{2.38}$$

is given by the Gaussian distribution function

$$c(x,t) = \sqrt{\frac{t_0}{t}}\exp\left(\frac{-x^2}{4Dt}\right), \tag{2.39}$$

which describes a Gaussian shape which broadens and decreases in height in such a way that the mass under the graph is preserved. In a similar way the cumulative distribution function corresponding to the Gaussian shape describes a diffusing front (Barends and Uffink, 2003). When moving with a front of value 1 from left to right, the diffusion of the front is given by Equation 2.38 to which the analytical solution is

$$c(x,t) = \frac{1}{2}\mathrm{erfc}\left(\frac{x}{\sqrt{4Dt}}\right), \tag{2.40}$$

where erfc is the complementary error function. Figure (2.40) presents the close match between the analytical and numerical solution of a diffusing front whereby the volume under the graph is preserved. In an Eulerian representation of the passing front, the diffusion equation becomes an advection diffusion equation given by

$$\frac{\partial c}{\partial t} + u\frac{\partial c}{\partial x} - D\frac{\partial^2 c}{\partial x^2} = 0. \tag{2.41}$$

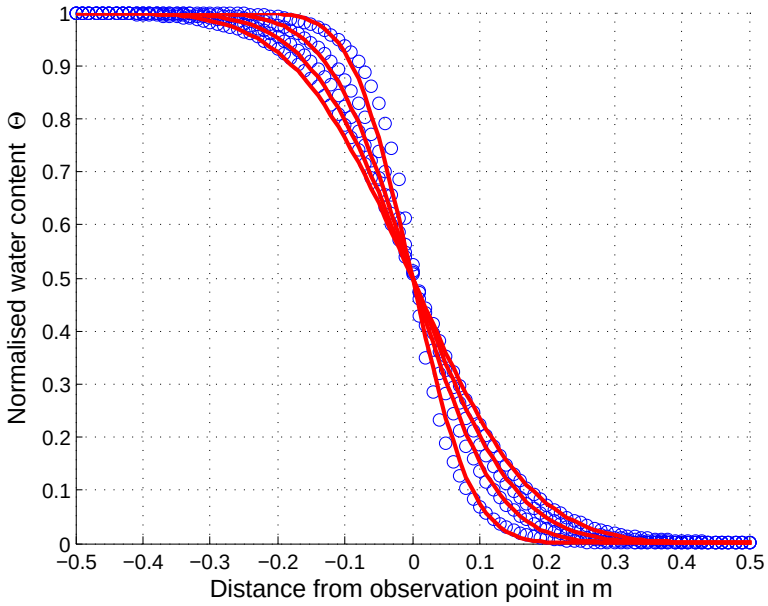

Figure 2.6: Comparison of the analytical solution of the diffusion equation (red line) with the numerical solution (blue dots)

Since advection is solely responsible for the movement of the front towards the right and does not influence the shape of the front, the analytical solution follows from accounting for change in location of the front with the speed u, and is given by

$$c(x,t) = \frac{1}{2}\mathrm{erfc}\left(\frac{x-ut}{\sqrt{4Dt}}\right). \tag{2.42}$$

The individual derivatives in Equation 2.41 are now given by

$$\frac{1}{2}\frac{\partial}{\partial t}\left[\mathrm{erfc}\left(\frac{x-ut}{\sqrt{4Dt}}\right)\right] = \frac{D\,(ut+x)\,e^{-\frac{(x-ut)^2}{4Dt}}}{2\sqrt{\pi}\,(Dt)^{3/2}}, \tag{2.43}$$

$$u\frac{1}{2}\frac{\partial}{\partial x}\left[\mathrm{erfc}\left(\frac{x-ut}{\sqrt{4Dt}}\right)\right] = \frac{2uDt\,(ut+x)\,e^{-\frac{(x-ut)^2}{4Dt}}}{2\sqrt{\pi}\,(Dt)^{3/2}}, \tag{2.44}$$

$$\text{and} \qquad -D\frac{1}{2}\frac{\partial^2}{\partial x^2}\left[\mathrm{erfc}\left(\frac{x-ut}{\sqrt{4Dt}}\right)\right] = -D\frac{(x-ut)\,e^{-\frac{(x-ut)^2}{4Dt}}}{2\sqrt{\pi}\,(Dt)^{3/2}}. \tag{2.45}$$

Adding (2.43), (2.44), and (2.45) gives 0, proving that Equation (2.42) is a solution of the advection diffusion equation. The specific solution for the saturation of the soil is

found by defining

$$u = -K\cos\alpha\left(1 + \frac{d_n}{d_{ph}}\right), \tag{2.46}$$

and

$$D = \frac{Kb}{\rho_w g}, \tag{2.47}$$

leading to

$$\Theta(\zeta, t) = \frac{1}{2}\mathrm{erfc}\left(\frac{\zeta + K\cos\alpha\left(1 + \frac{d_n}{d_{ph}}\right)t}{\sqrt{4\frac{Kb}{\rho_w g}t}}\right), \tag{2.48}$$

in which d_n is the water depth on the soil, and d is the depth of the phreatic surface. When the front reaches the part of the soil that is already saturated, the transmissivity of the fluid through the soil becomes equal to zero and

$$\frac{\partial\Theta}{\partial\zeta} = 0. \tag{2.49}$$

The erfc function does not satisfy this condition at the phreatic surface at $d = 1$. A solution is however found by mirroring of the erfc function across the location of the phreatic surface giving

$$\Theta(\zeta, t) = \Theta_0 + \frac{1}{2}(1 - \Theta_0)\,\mathrm{erfc}\left(\frac{\zeta + K\cos\alpha\left(1 + \frac{d_n}{d_{ph}}\right)t}{\sqrt{4\frac{Kb}{\rho_w g}t}}\right) + \tag{2.50}$$

$$\frac{1}{2}(1 - \Theta_0)\,\mathrm{erf}\left(\frac{\zeta - K\cos\alpha\left(1 + \frac{d_n}{d_{ph}}\right)t - 2d_{ph}}{\sqrt{4\frac{Kb}{\rho_w g}t}}\right)$$

where $d_n\cos\alpha$ is the water depth on the embankment, d_{ph} is the distance below the slope surface at which the phreatic surface is located, and Θ_0 is independent of ζ. With Θ_0 constant in time and space, Equation (2.50) does not account for an initial partial saturation of the soil. However the initial water content profile only varies spatially close to the phreatic surface (see Figure 2.4). Hence the error caused by ignoring a spatially varying initial water content is negligible when studying the effects of water

infiltration into the soil following the initial occurrence of a sediment-laden gravity flow. A typical solution, for $\Theta_0 = 0.2$, is given in Figure (2.7)

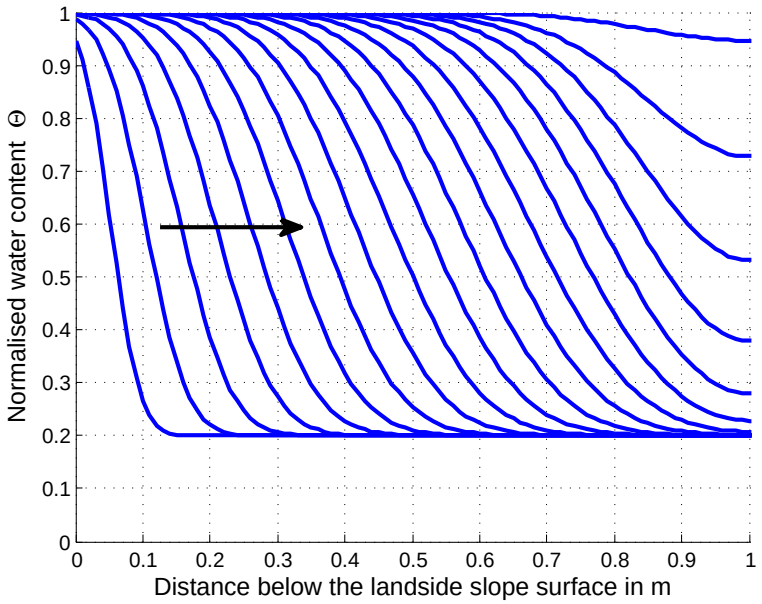

Figure 2.7: Results of the analytical solution for the change in normalised water content Θ due to infiltration for $\alpha = 150$, $\Delta t = 100$ s, $b = 100$ and $K = 0.0006$ m/s. The arrow indicates the progression of time.

2.4 Unsteady solution for the matric suction

Substituting the resulting expression for $\Theta(\zeta, t)$ in the modified distribution (Equation (2.12)), as suggested for the relationship between the normalized water content and suction, gives

$$\Psi(\zeta,t) = -b\ln\left[\Theta_0 + \frac{1}{2}(1-\Theta_0)\,\mathrm{erfc}\left(\frac{\zeta - ut}{\sqrt{4Dt}}\right) + \frac{1}{2}(1-\Theta_0)\,\mathrm{erf}\left(\frac{\zeta + ut - 2d_{ph}}{\sqrt{4Dt}}\right)\right] + \Psi|_{\zeta=0} - \frac{\Psi|_{\zeta=0}}{d_{ph}}\zeta \tag{2.51}$$

with

$$u = -K\cos\alpha\left(1+\frac{d_n}{d_{ph}}\right), \tag{2.52}$$

$$\text{and} \qquad D = \frac{Kb}{\rho_w g}.$$

The boundary condition for the pore pressure is given by the hydrostatic pressure on the slope surface at $\zeta = 0$, given by

$$\Psi|_{\zeta=0} = \gamma_w d_n \cos\alpha. \tag{2.53}$$

An additional condition is that under fully saturated conditions $w_\zeta = 0$. The equation for the flow in the $\hat{\zeta}$-coordinate direction is given by

$$\frac{K}{\rho_w g}\left(\frac{\partial\Psi}{\partial\zeta} - \rho_w g\cos\alpha\right) = 0. \tag{2.54}$$

At the moment the soil is fully saturated, $w_\zeta = 0$, $d_{ph} = 0$ and hence

$$\Psi = \rho_w g\zeta\cos\alpha + \Psi|_{\zeta=0}. \tag{2.55}$$

Figure 2.8 shows the change in capillary suction with time at a distance of 0.5 m below the landside embankment slope surface, for $d_n = 0$, $b = 100$, $a = 0$, and the relationship between the pressure and water content given by Figure 2.2. The figure clearly shows how the suction correctly tends to 0 as the soil becomes saturated.

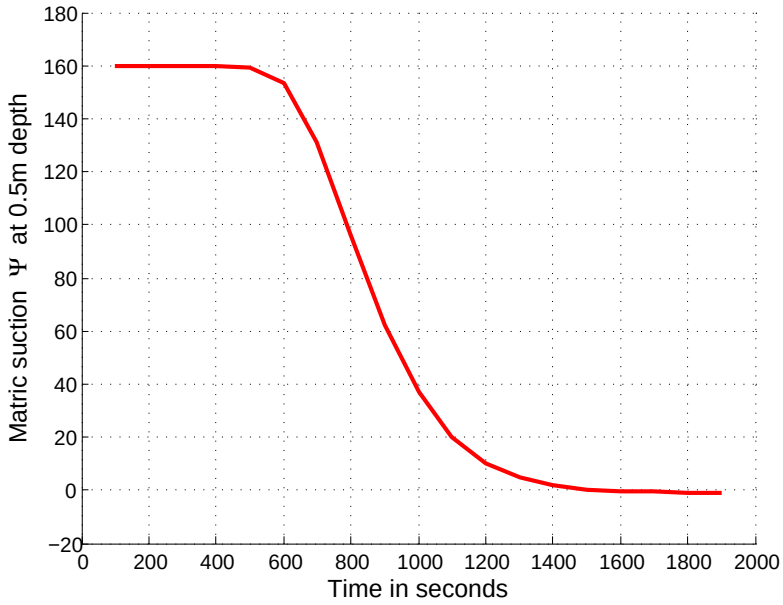

Figure 2.8: Change in matric suction Ψ over time at a depth of $0.5m$ for $K = 0.0006m/s$, $b = 100$, and $a = 0$

2.5 Slope stability analysis for unsaturated soils

The Terzaghi stress principle gives that total stresses σ are related to effective stresses σ' by $\sigma_{\zeta\zeta} = \sigma'_{\zeta\zeta} - \Psi$, and $\sigma_{\varepsilon\varepsilon} = \sigma'_{\varepsilon\varepsilon} - \Psi$. The resulting expression for the pressure is substituted in the balance equation for the effective stresses given by

$$\begin{aligned} &\frac{\partial \sigma'_{\varepsilon\varepsilon}}{\partial \varepsilon} + \frac{\partial \tau'_{\varepsilon\zeta}}{\partial \zeta} - \frac{\partial \Psi}{\partial \varepsilon} - \gamma_s \sin\alpha = 0, \\ \text{and} \qquad &\frac{\partial \tau'_{\varepsilon\zeta}}{\partial \varepsilon} + \frac{\partial \sigma'_{\zeta\zeta}}{\partial \zeta} - \frac{\partial \Psi}{\partial \zeta} + \gamma_s \cos\alpha = 0. \end{aligned} \tag{2.56}$$

With the pressure independent of the $\hat{\varepsilon}$-coordinate direction, the balance equations become

$$\begin{aligned} &\frac{\partial \tau'_{\varepsilon\zeta}}{\partial \zeta} - \gamma_s \sin\alpha = 0 \\ \text{and} \qquad &\frac{\partial \sigma'_{\zeta\zeta}}{\partial \zeta} - \frac{\partial \Psi}{\partial \zeta} + \gamma_s \cos\alpha = 0, \end{aligned} \tag{2.57}$$

or

$$\tau'_{\varepsilon\zeta} = \int (\gamma_s \sin\alpha)\, \mathrm{d}\zeta, \tag{2.58}$$

$$\text{and} \qquad \sigma'_{\zeta\zeta} = \int \frac{\partial \Psi}{\partial \zeta} d\zeta - \int (\gamma_s \cos\alpha)\, \mathrm{d}\zeta.$$

Under equilibrium flow conditions, the pressure gradient driving the flow balances the bed shear stress. Hence the shear stress boundary condition at the embankment surface is

$$\tau'_{\varepsilon\zeta}|_{\zeta=0} = \gamma_w d_n \sin\alpha = \tau_w, \tag{2.59}$$

and the solution of the shear stress $\tau'_{\varepsilon\zeta}$ becomes

$$\tau'_{\varepsilon\zeta} = \gamma_s \zeta \sin\alpha + \gamma_w d_n \sin\alpha. \tag{2.60}$$

When accounting for hydrostatic pressures on the embankment slope, the total stress in the $\hat{\zeta}$-coordinate direction is given by

$$\sigma_{\zeta\zeta} = -\gamma_s \zeta \cos\alpha - \gamma_w d_n \cos\alpha. \tag{2.61}$$

The effective stresses are given by $\sigma' = \sigma + \Psi$, with Ψ being the degree of suction. With $\Psi|_{\zeta=0} = \gamma_w d_n \cos\alpha$, the effective stresses are now given by

$$\sigma'_{\zeta\zeta}(\zeta, t) = -b \ln\left[\Theta_0 + \frac{1}{2}(1-\Theta_0)\,\mathrm{erfc}\left(\frac{\zeta - ut}{\sqrt{4Dt}}\right) + \frac{1}{2}(1-\Theta_0)\,\mathrm{erf}\left(\frac{\zeta + ut - 2d_{ph}}{\sqrt{4Dt}}\right)\right] - \frac{\Psi|_{\zeta=0}}{d_{ph}}\zeta - \gamma_s \zeta \cos\alpha \tag{2.62}$$

with $u = -K\cos\alpha\left(1 + \frac{d_n}{d_{ph}}\right)$, $D = \frac{Kb}{\rho_w g}$, $\cos\alpha < 0$, $\gamma_s = \rho_s g$, and $\gamma_w = \rho_w g$. Coulomb discovered that a critical shear stress τ_f could be defined as a function of the internal friction angle of the soil ϕ and the cohesive forces c according to (Verruijt, 2001)

$$\tau_f = c + \sigma' \tan\phi. \tag{2.63}$$

whereby a slope stability factor F_s can be defined, given by the ratio of the strength and the load, as (Verruijt, 2001)

$$F_s = \frac{|\tau'_{\varepsilon\zeta}/\sigma'_{\zeta\zeta}|_{max}}{|\tau'_{\varepsilon\zeta}/\sigma'_{\zeta\zeta}|}. \tag{2.64}$$

For the flow of water over a slope with unsaturated soil, the stability factor F_s is given by

$$F_s = \frac{|\left[-\gamma_s\zeta\cos\alpha - \frac{\Psi|_{\zeta=0}}{d_{ph}}\zeta - b\ln\left(\Theta(\zeta,t)\right)\right]\tan\phi|}{|(\gamma_s\zeta + \gamma_w d_n)\sin\alpha|}, \tag{2.65}$$

where Φ is the internal friction angle of the soil, and the normalized water content $\Theta(\zeta,t)$ is given by Equation (2.50), and

$$\Theta = \frac{\theta - \theta_r}{\theta_s - \theta_r}, \tag{2.66}$$

in which θ_r is the residual water content and θ_s is the saturated water content. Failure is indicated when $F_s < 1$. By incorporating the water depth at the embankment slope surface and shear stress over this surface, the failure depth becomes a function of the slope angle α. The condition for failure is given by

$$1 > \frac{|\left[-\gamma_s\zeta\cos\alpha - \frac{\Psi|_{\zeta=0}}{d_{ph}}\zeta - b\ln\left(\Theta(\zeta,t)\right)\right]\tan\phi|}{|(\gamma_s\zeta + \gamma_w d_n)\sin\alpha|}, \tag{2.67}$$

where γ_w is the specific weight of water, and γ_s the specific weight of the soil. Figure 2.9 shows how the safety factor changes with time at varying depths compared with the condition of failure indicated by the horizontal (red) line. Figure 2.9 clearly shows the progression in failure depth with time. It should however be noted that in reality the failure depth progresses faster since each time the stability limit is reached the top layer of the soil will slide off, leading to a faster rate of saturation of the remaining soil.

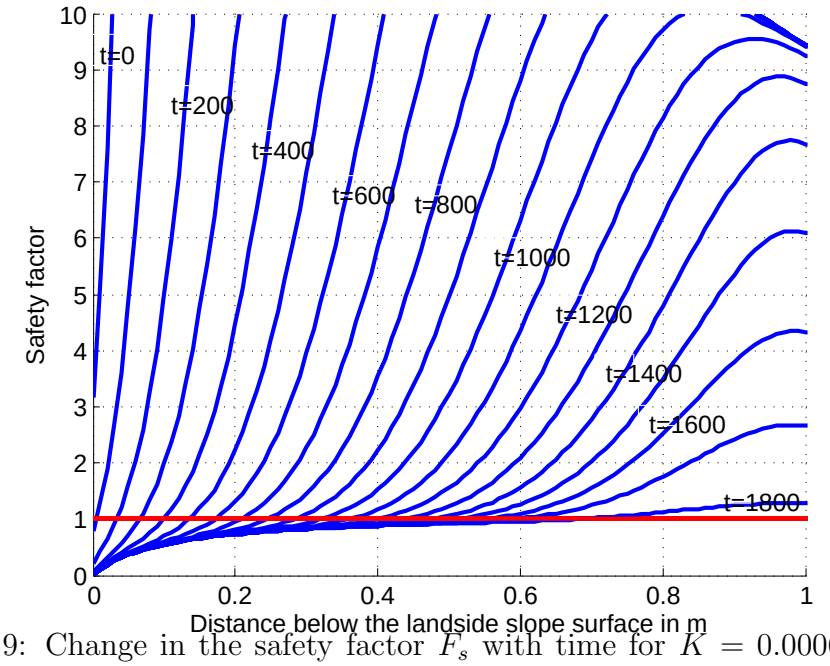

Figure 2.9: Change in the safety factor F_s with time for $K = 0.0006$ m/s, $b = 100$, $d_n = 0.2$ m, $\Delta t = 100$s and $a = 0$ (blue), compared with the condition for failure (red). The arrow indicates the progression of time

2.6 Sediment-laden gravity flows

With the specific weight of the soil γ_s given by

$$\gamma_s = g\left(c_*\left(\rho_p - \rho_w\right) + \rho_w\right), \tag{2.68}$$

where g is the gravitational constant, ρ_p the density of a soil particle, ρ_w the density of water, and c_* the grain concentration, then for $t \to \infty$ and $d_n = 0$, Equation (2.67) reduces to Equation (2.69), which is the condition for the occurrence of a sediment gravity flow under fully saturated conditions as found by Takahashi (2009)

$$1 > \frac{c_*\left(\rho_p - \rho_w\right)}{c_*\left(\rho_p - \rho_w\right) + \rho_w}\frac{\tan\phi}{\tan\alpha} \tag{2.69}$$

For $\rho_s \approx 2000\text{kg/m}^3$, $\rho_w \approx 1000\text{kg/m}^3$, $\phi \approx 30^0$, Equation (2.69) indicates that slope gradients larger than 15^0 are unstable, leading to sediment gravity flows. Since embankment slopes with larger slope gradients exist, sediment gravity flow processes are likely to contribute to the manner in which non-cohesive embankments erode. Based on the assumption that the operating shear stress and resisting shear stress are distributed

linearly, as depicted in Figure 2.10, Takahashi (1981) obtains

$$1 > \frac{c_* \left(\rho_s - \rho_w\right)}{c_* \left(\rho_s - \rho_w\right) + \rho_w \left(1 + d_n a_l^{-1}\right)} \frac{\tan\phi}{\tan\alpha} \tag{2.70}$$

where a_l is the depth at which the slope will fail. By replacing ζ with a_l in Equation (2.67) the failure depth is given as a function of time. Using a similar approach to how

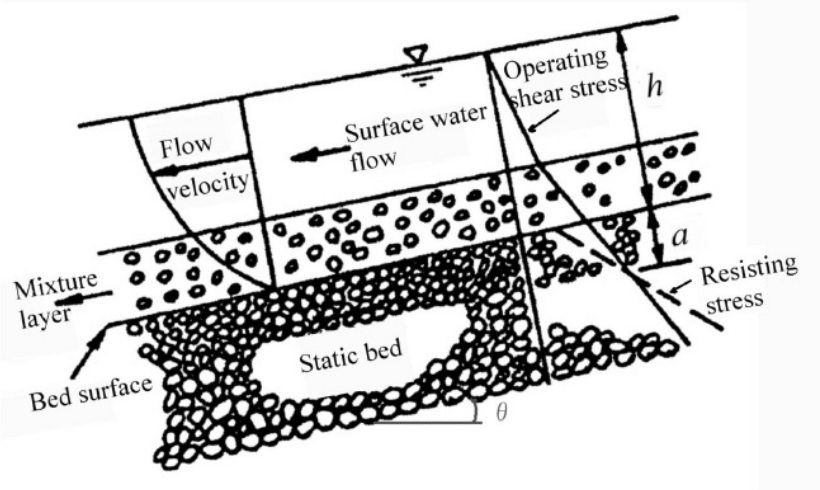

Figure 2.10: Occurrence of debris flow (Takahashi, 1981)

Takahashi calculated the conditions for sediment-laden gravity flows under saturated soil conditions, the same conditions have been derived as a function of time for unsaturated soil conditions using Equation (2.67). From the corresponding Figure 2.9, the predicted variation of failure depth with time is derived as presented in Figure 2.11, which in turn can be used to derive an artificial erosion rate. For the chosen parameters the artificial erosion rate is given by 0.3 mm/s. This is for a hydraulic conductivity K of 0.0006 m/s. Alyamani and Sen (1993) found the empirical relationship between the grain distribution and Hydraulic conductivity given by

$$K = 0.015 \left[I_0 + 25 \left(d_{50} - d_{10}\right)\right]^2 \tag{2.71}$$

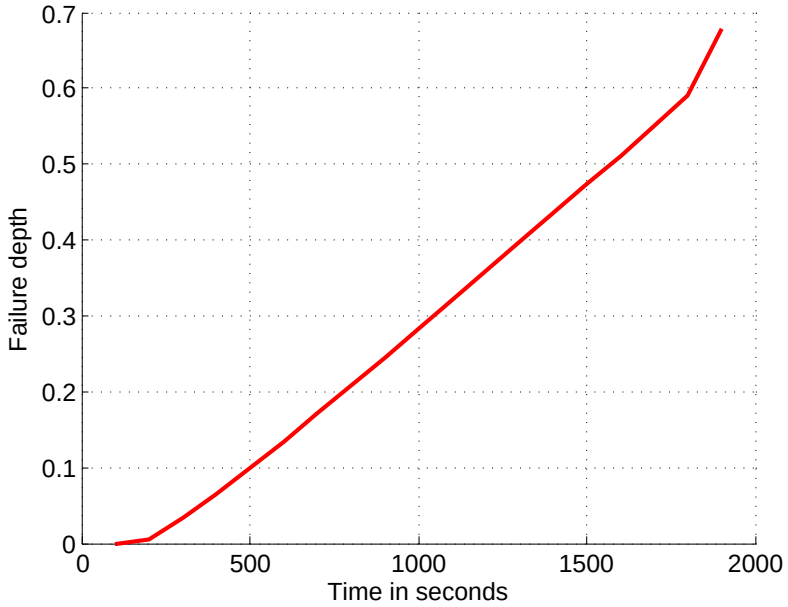

Figure 2.11: Change in failure depth with time for $K = 0.0006$ m/s, $b = 100$, $d_n = 0.2$ m and $a = 0$

where $I_0 \approx D_{10}$, D_{10} is the grain diameter, which is exceeded by 90% of the grain sizes in the grain distribution, and D_{50} is the median grain diameter. All diameters are in m, and K is in m/s. A K-value of 6×10^{-4} m/s corresponds with $D_{50} = 0.5$ mm, and $D_{10} \approx 0.2$ mm. This would indicate a moderately erodible soil. The erosion equation given by Nearing et al. (1988) is

$$E = K_e \left(\tau_w - \tau_c\right)^m \tag{2.72}$$

where E is the erosion rate in m/s, K_e is the soil erodibility in m^3/Ns, τ_c is the critical bed shear stress needed for the initiation of motion in $\mathrm{N/m}^2$. With $\tau >> \tau_c$, τ_w given by Equation (2.59), and for $K_e = 1.7 \times 10 - 7$ m^3/Ns for a moderately erodible soil, the erosion equation gives an erosion rate of 0.26 mm/s ($m = 1$). This is of the same order of magnitude as the artificial erosion rate found using the theory of sediment-laden gravity flows developed above, which could indicate that the occurrence of sediment-laden gravity flows might have been mistaken for erosion. However unlike the erosion rate theory, the sediment-laden gravity flow theory explains how the landside slope of an embankment is limited in steepness. The theory of sediment-laden gravity flows can also be used to derive the hydraulic conductivity, and/or cohesive properties needed for

the occurrence of headcut erosion. Although the 1D analysis performed here provides insight into the role of sediment-laden gravity flows in embankment breach formation, it is insufficient for practical modelling applications and hence it is necessary to extend the analysis to two dimensions. In further analysis of the role of sediment-laden gravity flows it is recommended to incorporate the effects of micro-scale slope failures as well. The moment a slope failure occurs, a new soil surface is formed at which the soil is fully saturated, which might speed up the saturation rate of the remaining soil and hence cause higher values of the artificial erosion rate.

Chapter 3

The simplified breach model AREBA

3.1 Modelling simplifications

The simplified breach model AREBA (A Rapid Embankment Breach Assessment) calculates a breach hydrograph shape for failure of an embankment due to overflow, or internal erosion. The methodology used for modelling internal erosion failures has been adopted from HR BREACH and is discussed in Appendix 1. The present chapter focuses on the approach used for modelling breach formation due to overflow. As an initial simplification the embankment geometry is assumed to be trapezoidal and protected by a grass cover. Furthermore the breach is assumed to form according to the different breach stages as identified in section 1.1.

As was mentioned in section 1.1 grass failure depends on time, geotechnical properties of the soil, and location. Despite there being an understanding of the reasons for grass failure, a model has yet to be developed for rapid prediction of localized grass failures. Hence for the purpose of modelling grass failure in AREBA, the grass cover of the embankment is assumed to fail simultaneously everywhere when the critical flow conditions are reached (as defined by Technical Note 71 (Whitehead et al., 1976)). Whitehead et al. (1976) give relationships for the time to failure of three different

quality grass covers as a function of the flow velocity. The flow velocity becomes maximum along the landside slope where the depth approaches the normal depth. Hence for simplicity the flow velocity corresponding to the normal depth is used to determine the moment of failure of the grass cover. This flow velocity is given by

$$\overline{\widetilde{u}}_n = \frac{d_n^{\frac{2}{3}} i_{bi}^{\frac{1}{2}}}{n} \tag{3.1}$$

where $\overline{\widetilde{u}}_n$ is the breadth-averaged and depth-averaged flow velocity corresponding with the normal depth, i_{bi} is the embankment's landside slope gradient, d_n is the normal depth in m, and n is the Manning coefficient in $\mathrm{s/m^{1/3}}$ (Nortier and De Koning, 1991). Assuming a relatively shallow breach flow with a breadth b much larger than the depth d, the normal depth follows from

$$d_n = \left(\frac{\widetilde{q}^2 n^2}{i_{bi}} \right)^{0.3} \tag{3.2}$$

where $\overline{q}$ is the breadth-averaged overflow discharge in $\mathrm{m^2/s}$. The critical flow velocity for grass failure follows from

$$\begin{aligned} \overline{\widetilde{u}}_{g1} =& 2.385 - 0.0167 \ln(T) + \frac{5.333}{T} \\ \overline{\widetilde{u}}_{g2} =& 2.161 - 0.131 \ln(T) + \frac{3.551}{T} \\ \overline{\widetilde{u}}_{g3} =& 1.889 - 0.236 \ln(T) + \frac{2.2767}{T} \end{aligned} \tag{3.3}$$

which are empirical fits to data given by Whitehead et al. (1976), with $\overline{\widetilde{u}}_g$ being the breadth-averaged and depth-averaged velocity in m/s at which the grass cover fails at time T in hours. The subscripts $1, 2$, and 3 are quality indicators of the grass cover, with indicator 1 referring to a high quality grass cover, indicator 2 to a medium quality grass cover, and indicator 3 to a low quality grass cover (See Figure 1.7). A presence of a clay outer layer on the embankment may both influence the critical velocities for grass failure and influence the failure rate of the embankment. Further analysis in the effects of a clay protection layer on the initiation of failure is recommended. When the grass

cover fails, the embankment erosion process initiates. The embankment acts as a broad weir. Flow velocities over the embankment largely exceed the infiltration rate of water into the embankment; hence infiltration of water into the embankment is ignored in the mass balance equation. The characteristic flow velocities U over the embankment and, during a later stage, through the breach, are of the order of 1 m/s. Overflow over an embankment is caused by extreme events with characteristic time scales T of the order of hours. During the flow through the breach, the boundary conditions do not vary in time due to the small characteristic length scale of the breach L_b. Because $UT >> L_b$, the influence of local accelerations is neglected leading to a quasi-steady state approach. The mass conservation equation for the flow down the landside slope is given by

$$\frac{\partial Q_b}{\partial \varepsilon} = 0 \tag{3.4}$$

where ε is a coordinate in the $\hat{\varepsilon}$-coordinate direction parallel to the landside the slope as indicated in Figure 3.1, and Q_b is the breach discharge in m^3/s, which follows from the broad weir equation given by

$$Q_b = c_w b h_2 \sqrt{2g(H - h_2)} \tag{3.5}$$

where c_w is the weir coefficient, b the breadth of the flow in m, h_2 the water level over the crest in m, and H the height difference between the upstream water level and the crest level in m. h_2 is assumed to be equal to $\frac{2}{3}H$ for a non-drowning weir flow, and equal to the difference between the downstream water level and the crest level for a drowning weir flow (Nortier and De Koning, 1991). In Stage 2, during which the landside slope erodes towards the waterside slope, the weir coefficient accounts for the effects of vertical flow contraction. After the retrograde erosion reaches the waterside slope, the weir coefficient accounts for both vertical and horizontal flow contraction. Once the invert level reaches the foundation level of the embankment, the effects of horizontal contraction are solely accounted for by the weir coefficient. Flow velocities along the breach perimeter are calculated from the discharge, breadth, and local depth.

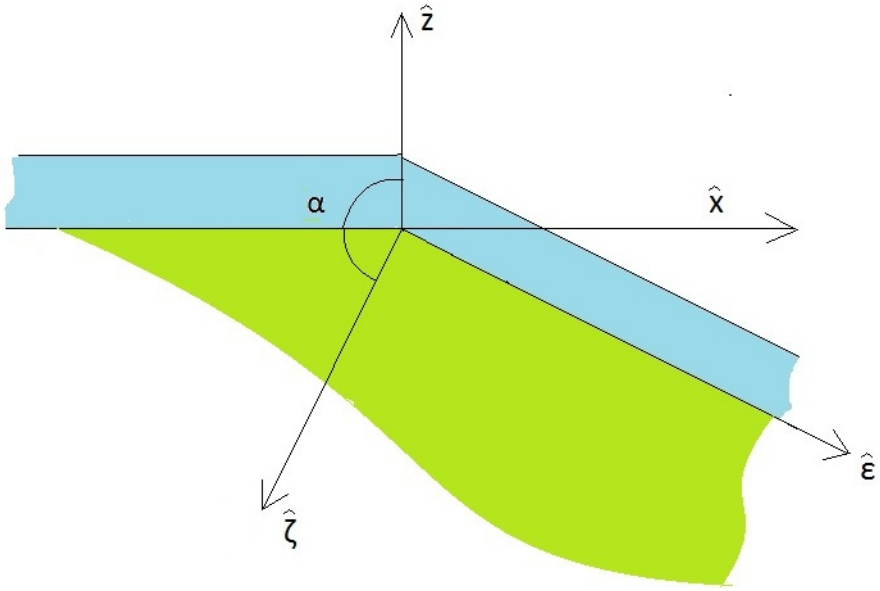

Figure 3.1: Definition sketch for the coordinate system

The flow depth is assumed to be equal to the critical depth d_c at the transition from the crest to the landside slope and to approach the normal depth d_n along the landside slope. The hydraulic radius of the flow along the landside slope is approximated by the normal depth. With this the critical depth d_c follows from

$$d_c = \left(\frac{\widetilde{q}^2}{g}\right)^{\frac{1}{3}} \tag{3.6}$$

where $\widetilde{q}$ is the breadth-averaged discharge over the embankment in m^2/s (Nortier and De Koning, 1991). The breadth of the breach is assumed as spatially constant. Once the water level in the breach falls below the crest level of the embankment stretch adjacent to the breach, the breach grows laterally and the breadth depends on the degree of lateral erosion and the effects of the material slumping into the breach. Any erosion below the foundation level of the embankment has not been accounted for in AREBA since the effects on the breach hydrograph are negligible. Over the past, most breach models have dealt with the lateral breach growth processes by assuming a predefined breach shape which is rectangular, triangular, trapezoidal, or parabolic (Mohamed, 2002). The eventual breach geometry follows from the breach depth, and pre-defined

breach shape. Other models deal with breach side slope stability in a simplified fashion. Either the rate of lateral erosion is calculated and combined with a maximum slope angle (BRES model, 1998) (Visser, 1998), or a simplified slope stability analysis is made where it is assumed that the undercut soil volume is being transported instantaneously when failure occurs (HR Breach 2002)(Mohamed, 2002). Matric suction of the soil allows for slope angles on both sides of the breach to become larger than the corresponding internal friction angle of the embankment soil. In AREBA the side slope instability has been dealt with by assuming vertical breach sides which erode in lateral direction as a function of the mean flow velocity. Since the breadth is assumed as spatially constant, the flow over landside slope is assumed to be bounded by the same rectangular profile as the breach.

The breach hydrograph shape is controlled by changes to the dimensions of the hydraulic control and the water levels given by the boundary conditions. The height of the hydraulic control is given by the breach invert level, here defined as the maximum height of the breach profile relative to the embankment's foundation, and is assumed to be located where the crest meets the landside slope. Changes in the dimensions of the hydraulic control depend on whether the embankment erodes according to surface erosion or headcut erosion. Due to simplifications made in describing the flow, information with regard to the flow type is lost and it is no longer possible to assess which failure mechanism is dominant. Hence the failure mechanism is user-defined. The change in dimensions of the hydraulic control is given below for both surface erosion and headcut erosion

3.1.1 Surface erosion

Before the retrograde erosion of the landside slope reaches the waterside slope the change in invert level follows from downward erosion of the crest. Once retrograde erosion of the landside slope reaches the waterside slope, the rate at which the invert level lowers, increases. Hence the timing of when the landside slope reaches the waterside slope is of importance for an accurate breach hydrograph prediction. The

erosion of the landside slope is affected by sediment laden gravity flows which limit the steepness of the landside slope. The effects of sediment laden gravity flows are accounted for by assuming that the gradient of the landside slope remains equal to its initial value whereby the rate of the retreat is dependent on the average value for the shear stresses along the landside slope. This assumption is based on a 1D slope stability analysis under the assumption of an infinitely long slope, and improvement of this assumption through a multi-dimensional analysis of the unsaturated soil mechanics is recommended. The rate of retreat of the landside slope under its initial angle is calculated with the erosion equation. Below, an analytical equation is derived for the shear stress along the landside slope.

Assuming a constant breach width, a straight landside slope, and a critical depth at the top of the landside slope, the depth profile along the landside slope follows from the Bélanger equation (Battjes, 2002), given by

$$\Delta d(\varepsilon) = \Delta d_0 e^{(\varepsilon-\varepsilon_0)/L}. \tag{3.7}$$

where Δd is the difference between the normal depth and the local water depth in m, Δd_0 is the difference between the critical depth and the normal depth in m, e is the base of the natural logarithm, ε the distance along the landside slope from the origin given at the end of the crest to where the depth is calculated, ε_0 is the offset from the origin, and L is the adaptation length in m, defined as the length along the slope where Δd is equal to $\Delta d_0/e$. L follows from (Battjes, 2002)

$$L = \left(\frac{1}{3i_{bi}} - \frac{d_n^{\frac{1}{3}}}{3gn^2} \right) d_n. \tag{3.8}$$

This relationship is valid for variations from the normal depth. The ratio of the local depth over the critical depth is

$$\frac{d(\varepsilon)}{d_c} = \frac{d_n + (d_c - d_n)\, e^{(\varepsilon-\varepsilon_0)/L}}{d_c}, \tag{3.9}$$

where d_c is the critical depth and d_n the normal depth. For a constant breadth, mass conservation gives that the increase in flow velocity along the landside slope is inversely proportional to the increase in depth. The breadth-averaged and depth-averaged flow velocity $\overline{\widetilde{u}}$ as a function of the distance along the landside slope ε becomes

$$\overline{\widetilde{u}}(\varepsilon) = \frac{1}{\frac{d_n}{d_c} + e^{\frac{\varepsilon-\varepsilon_0}{L}} - \frac{d_n}{d_c} e^{\frac{\varepsilon-\varepsilon_0}{L}}} \overline{\widetilde{u}}_c, \tag{3.10}$$

where $\overline{\widetilde{u}}_c$ is the breadth-averaged and depth-averaged flow velocity corresponding to the critical depth. The relationship between the flow velocity u in m/s and the shear stress τ is

$$\tau = \rho_w \overline{\widetilde{u}}^2 \frac{n^2 g}{d_n^{\frac{1}{3}}}, \tag{3.11}$$

where d_n replaces the value of the hydraulic radius, and ρ_w is the density of water in kg/m^3. Substituting Equation (3.10) into Equation (3.11) leads to the following expression for the shear stress as a function of ε, given by

$$\tau(\varepsilon) = \rho_w \left[\frac{1}{\left(-a e^{\frac{\varepsilon-\varepsilon_0}{L}} + a + e^{\frac{\varepsilon-\varepsilon_0}{L}} \right)^2} \right] \overline{\widetilde{u}}_c^2 \frac{n^2 g}{d_n^{\frac{1}{3}}}, \tag{3.12}$$

where a follows from

$$a = \frac{g^{\frac{1}{3}} n^{\frac{2}{3}}}{d_n^{\frac{1}{9}} i_{bi}^{\frac{1}{3}}}. \tag{3.13}$$

The erosion rate is calculated with

$$E = K_e \left(\tau - \tau_c \right)^m \tag{3.14}$$

where τ is the bed shear stress in N/m^2, τ_c the critical shear stress in N/m^2, K_e the erodibility coefficient in m^3/Ns, ^{m} a coefficient of efficiency, and E the erosion rate in m/s (Nearing et al., 1988). The coefficient of efficiency (m) was set to 1 for two reasons

1. The erosion equation is used to describe the rate of retreat of the slope due to sediment-laden gravity flows. Under a constant slope angle, the slope fails

when at a certain depth a degree of saturation is reached. Figure 2.7 in Chapter 2 shows that the rate with which the moisture content increases with depth is mostly constant for a constant hydraulic conductivity. This indicates a linear relationship between the shear stress and the erosion rate, and hence a coefficient of efficiency of 1.

2. The erosion equation with a power of 1 is applied in the breach model HR BREACH which is used for benchmarking the rapid model. HR BREACH has been extensively tested and calibrated.

Substituting Equation (3.12) into Equation (3.14) gives the erosion rate as a function of the distance along the landside slope ε. The assumption that the gradient of the landside slope remains equal to its initial value requires averaging of the erosion rate along the landside slope. The mean erosion rate is obtained numerically from Equations (3.12) and (3.14) because no analytical solution is available. The landside slope erodes in the $\hat{\zeta}$-coordinate direction normal to the embankment slope surface. By accounting for the landside slope angle, the rate at which the crest width reduces (R_c) is given by

$$R_c = \overline{E}\sqrt{\left(\frac{1}{i_{bi}}\right)^2 + 1}, \tag{3.15}$$

where $\overline{E}$ is the numerical averaged erosion rate of the landside slope, and i_{bi} is the landside slope gradient. The instant the landside slope reaches the waterside slope the rate at which the invert level lowers is given by

$$R_c = \frac{1}{i_{bo}^{-1} + i_{bi}^{-1}}\overline{E}\sqrt{\left(\frac{1}{i_{bi}}\right)^2 + 1}, \tag{3.16}$$

where i_{bo} is the waterside slope gradient. Before the retreat of the landside slope reaches the waterside slope, downward crest erosion reduces the net rate of retreat of the landside slope towards the waterside slope. The rate at which the invert level lowers is given by

$$E = K_e\left(\rho_w \widetilde{\overline{u}}^2 \frac{n^2 g}{d^{\frac{1}{3}}} - \tau_c\right), \tag{3.17}$$

where E is the rate of lowering of the invert level, and the velocity over the invert level $\overline{\widetilde{u}}$ follows from

$$\overline{\widetilde{u}} = c_w \sqrt{2g\,(H - h_2)}, \tag{3.18}$$

where c_w is the weir coefficient. The net reduction in the rate with which the crest width reduces is obtained after accounting for the effects of the slope gradients by multiplying the downward erosion rate (3.17) with the factor f_S given by

$$f_S = \frac{1}{i_{bi}} + \frac{1}{i_{bo}}. \tag{3.19}$$

Vertical erosion of the embankment soil is assumed to stop once the invert level reaches the foundation level of the embankment since further lowering of the invert level has negligible effect on the breach discharge. The breadth is assumed not to vary along the centre line of the breach. The lateral erosion rates are assumed to depend solely on the mean flow velocities. With the downward erosion rate a function of the mean flow velocity, it is reasonable to assume that the lateral erosion rate is a function of the downward erosion rate. The breach widening rate is calculated with the empirical relationship applied in HR BREACH, which states that the breach widening rate is 1.4 times the rate at which the crest lowers. When the invert level equals the embankment's foundation level, the rate of breach widening follows from

$$E_w = 1.4 K_e \left(\rho_w \overline{\widetilde{u}}^2 \frac{n^2 g}{h_2^{\frac{1}{3}}} - \tau_c \right), \tag{3.20}$$

where E_w is the breach widening rate.

3.1.2 Headcut erosion

Headcuts are formed under conditions of relatively high flow velocities over the crest and an embankment soil with cohesive properties which prevents sediment laden gravity flows from occurring. Due to flow overshoots a cascading flow forms which impacts on the embankment surface, disperses, and undercuts the embankment soil. The local

erosion rate depends upon the energy with which the flow hits the soil and therefore on the height of the cascades. Once erosion causes the cascades to reach the waterside slope, the flow rate increases rapidly due to the lowering of the invert level and an increase in the horizontal contraction of the flow. Increase in flow leads to an increase in the energy with which the flow impacts the soil. At the same time a reduction in crest height reduces the height over which the flow drops before impacting on the soil and reduces the flow energy. In AREBA, the headcut failure is modelled using the method described by Temple et al. (2005). This method is based on observations of large-scale breach experiments of cohesive clay embankments. The following assumptions made by Temple et al. (2005) regarding the overall erosion process have been adopted for the development of AREBA.

1. The crest level does not lower before the headcut has reached the upstream slope.
2. The cross-sectional breach shape is rectangular.
3. The foundation of the embankment is not erodible
4. Headcut initiates at the top of the landside slope.

The first assumption is valid when the downward erosion rate of the crest level is negligibly small. Hence either the soil erodibility is very small, or the critical shear stress exceeds the shear stress exerted by the flow over the crest. Under other circumstances the assumption made may lead to an inaccurate prediction of the flood hydrograph since any downward erosion of the crest lowers the invert level and increases the breach flow. However as mentioned above, field observations led Temple et al. (2005) to assume that the downward erosion of the crest is negligible during the retreat of the headcuts across the embankment. The observations can be explained by the effect of cohesion on the critical shear stress of the soil or by the effects of a grass cover present on the soil. Although it is assumed that a grass cover fails instantaneously, the grass cover is likely to fail sooner where the headcut initiates. Headcuts could therefore grow and move through the embankment while the remainder of the grass over at the crest

prevents the invert level from falling. The second and third model assumptions have been discussed in section 3.1.1. With regard to the fourth assumption; as discussed in section 1.1 the bed slope transition where the crest meets the landside slope could cause a free nappe to form or the flow to separate, leading to the headcut erosion process when the soil properties prevent any geotechnical failures. However the flow accelerates along the landside slope. Irregularities, present along the landside slope could cause the flow to separate at a later stage and initiate headcut formation at any location along the landside slope.

Temple et al. (2005) developed a simplified headcut erosion model (SIMBA) based on empirical equations for the erosion rate and a 1D flow description. The headcut erosion modelling technique was later also added to HR BREACH. In HR BREACH the headcut is allowed to initiate at any location along the landside slope. Also the effects of multiple headcuts are modelled by HR BREACH. In AREBA the headcut is assumed to start where the crest meets the landside slope since the growth and progression of this headcut determines the change in invert level when it reaches the waterside slope. The effects of the formation and progression of other headcuts are therefore neglected in AREBA leading to a faster model. Temple et al. (2005) identified the following four stages in the headcut breach process:

- Stage A: Headcut formation on the downward slope
- Stage B: Headcut advance through the embankment crest
- Stage C: Breach formation as the headcut enters the reservoir
- Stage D: Breach expansion during reservoir drawdown

During Stages A and B the invert level does not significantly decrease. In AREBA, the erosion rate E is calculated with Equation (3.14). Temple et al. (2005) calculate the shear stress along the landside slope with

$$\tau = \rho_w g d_n S, \tag{3.21}$$

where S is the embankment slope defined as the *Sine* of the angle of the landside slope with the horizontal, and d_n is the normal depth obtained from Equation (3.2). Stage A ends when the calculated erosion depth exceeds the critical depth. During Stage B, the headcut overfall height increases to a maximum of the embankment height relative to its foundation level, while the headcut retreats through the embankment crest. Temple et al. (2005) express the rate of headcut retreat by

$$\frac{dx}{dt} = -C\left(\widetilde{q}h_{hc}\right)^{\frac{1}{3}}, \tag{3.22}$$

where x is a distance from the origin in the $\hat{x}$-direction as indicated in Figure 3.1, C is the headcut parameter, q is the breadth-averaged discharge in m^2/s, h_{hc} is the step height of the headcut in m, which when multiplied with $\widetilde{q}$ represents the dissipation of energy by the water landing on the headcut base. The downward erosion of the headcut base is calculated using Equation (3.14), whereby τ is given by the maximum of the values following from Equations (3.21) and

$$\tau = \rho_w g d_c 0.011 \left(\frac{h_{hc}}{d_c}\right)^{0.582}. \tag{3.23}$$

Equation (3.21) is the relation for the shear stress due to flow down a slope, and (3.23) is the relation for a plunging jet under the assumption of low tailwater (Temple et al., 2005). During Stages A and B the hydraulic control, located at the most upstream section of the crest, is not affected. When the headcut retreat reaches the waterside slope Stages C and D commence and the breach erosion affects the hydraulic control. The rate of change in invert level h_c during Stage C follows from multiplying Equation (3.22) with the negative of the waterside slope gradient and is given by

$$\frac{dh_c}{dt} = i_{bo} C\left(\widetilde{q}h_{hc}\right)^{\frac{1}{3}}, \tag{3.24}$$

where i_{bo} is the waterside slope gradient. The increase in width of the hydraulic control is assumed to be equal to the decrease in height (Temple et al., 2005). Once the invert

level relative to the embankment's foundation becomes smaller than the critical depth, the headcut progress stops and the rate of change in crest height follows from

$$\frac{dh_c}{dt} = -K_e \left(\tau - \tau_c\right), \tag{3.25}$$

where K_e is the erodibility coefficient, τ_c the critical bed shear stress, and the bed shear stress τ is now obtained from

$$\tau = \frac{\rho_w g^2 n^2 \left(h_1 - h_2\right)}{h_2^{\frac{1}{3}}}. \tag{3.26}$$

The lateral growth rate of the breach is proportional to the rate at which the crest lowers by a factor of 1.4 (Temple et al., 2005). Once the waterside slope has fully eroded, the breach only grows laterally because a non-erodible embankment foundation is assumed. The lateral growth rate is however still calculated with Equations (3.25) and (3.26) but no new invert level is calculated.

3.2 Testing of AREBA

3.2.1 Benchmark tests

AREBA has been benchmarked against HR BREACH, which, together with SIMBA, was selected by the Dam Safety Interest Group (DSIG) breach modelling project as a model with potential for further development for industry use (Wahl et al., 2008). Validation of HR BREACH against different datasets led to the incorporation of a calibration coefficient of 1.6 for the downward erosion rate. This factor was based on model performance for a range of material and structure types. To enable proper comparison between AREBA and HR BREACH the same coefficient has been adopted in AREBA. Table 3.2.1 lists the input parameters kept constant for all verification runs with HR BREACH, and Table 3.2.1 lists the input parameters that were varied, where *Slope* refers to the landside slope gradient. A box shaped reservoir with continuous

inflow was chosen for the upstream boundary condition. The reservoir's initial water level was taken as 0.30 m below the crest level h_{crest}. The initial breach depth was assumed to be 0.25 m. Although the initial water level in the reservoir is below the invert level of the breach, the inflow in the reservoir causes the reservoir level to rise until a flow through the initial breach notch initiates (see Figure 3.2). An infinitely large floodplain was chosen for the downstream boundary condition to eliminate the effects of drowning and to facilitate a clear comparison between the two models.

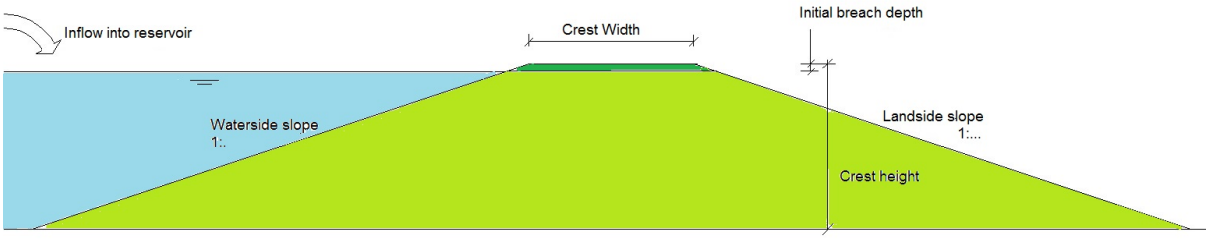

Figure 3.2: Initial condition for benchmark tests

Parameter	Present in AREBA	Value	Unit
Breach level	✓	$h_{crest} - 0.3$	m
Crest width	✓	6	m
Discharge into reservoir	✓	1	m^3/s
Surface area reservoir	✓	30000	m^2
Initial breach depth	✓	0.25	m
Crest length	✓	200	m
Soil cohesion	✓	1×10^{-5}	kN/m^2
Soil tension strength	-	1×10^{-5}	kN/m^2
Friction angle	-	30	degrees
Porosity	-	0.2	-
Dry unit weight	✓	16.8	kN/m^3
Critical shear stress	✓	1×10^{-5}	N/m^2
Manning coefficient	✓	0.035	s/m^3
Weir coefficient	✓	1	-
Erosion rate factor	✓	1.6	-

Table 3.1: Fixed input parameters HR BREACH benchmark tests

In AREBA's surface erosion mode, the landside slope gradient remains equal to its initial value while it retreats towards the waterside slope. In HR BREACH unrealistic landside slope gradients are prevented by averaging the erosion rate over the crest

Run no.	Erodibility coefficient (K_e) (m^3/Ns)	Crest height h_{crest} (m)	Slope m/m
1	5×10^{-6}	12	1/3
2	5×10^{-6}	6	1/3
3	5×10^{-6}	9	1/6
4	5×10^{-6}	9	1/2

Table 3.2: Variable input parameters HR BREACH benchmark tests

and erosion rate near the top of the landside slope, and by averaging the erosion rate near the bottom of the slope with the erosion rate of the embankment's foundation. The different approach to preventing unrealistic landside slope gradients is expected to lead to different model outcomes. Figure 3.3 shows the results of Run 1, and Figure 3.4 shows the results of Run 2. As is shown, the results from HR BREACH and

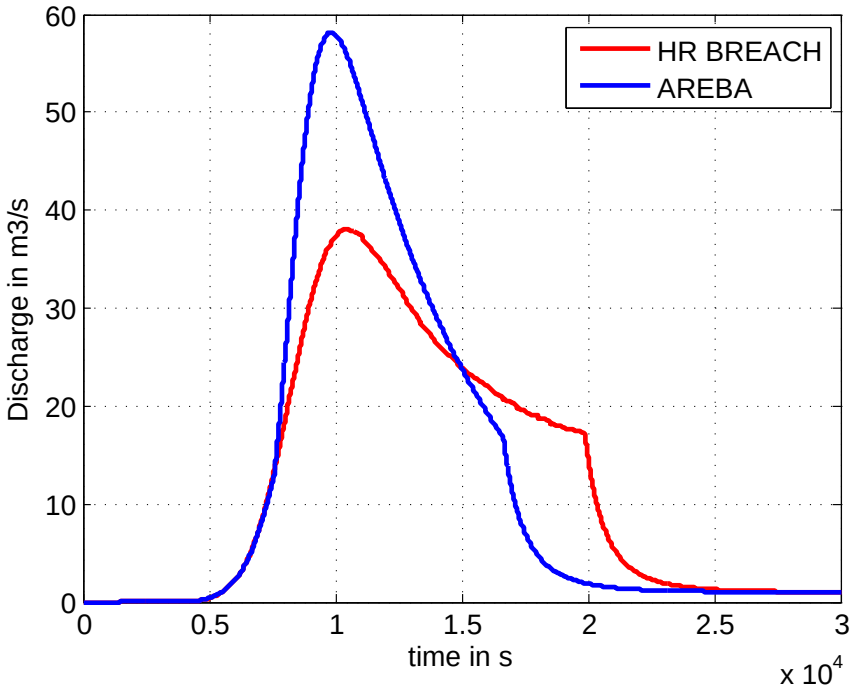

Figure 3.3: Hydrograph output HR BREACH and AREBA: Run 1

AREBA are almost identical for Run 2. The input of Run 2 differs from that of Run 1 in the ratio of the crest height over the crest width. In AREBA, the invert level is assumed to erode downwards while the landside slope retreats towards the waterside slope. For relatively high ratios of the crest width to the crest height, or

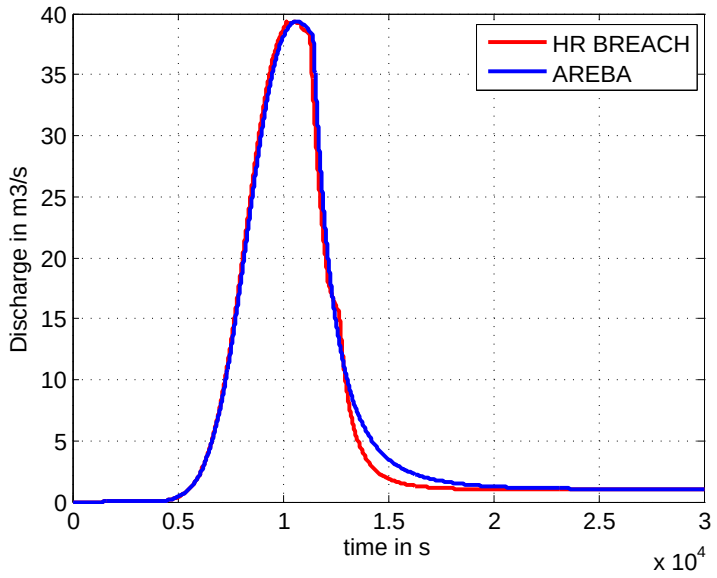

Figure 3.4: Hydrograph output HR BREACH and AREBA: Run 2

relatively high values for the erodibility, the downward eroding invert level reaches the foundation level before the retreat of the landside slope reaches the waterside slope. The approach used in HR BREACH for the prevention of unrealistic steep slopes is empirical. In AREBA the approach is based on a 1D analysis of the unsaturated soil mechanics. However due to limited validation data available, and without a full 2D analysis of the soil processes, it is not possible to state which assumption has the lowest impact on the accuracy to which the physical process is represented. The different approaches in limiting the steepness of the landside slope lead to differences in model outcomes. These are evident by comparing the results from Runs 3 and 4, which only differ in the steepness of the landside slope (see Figures 3.5 and 3.6). Figure 3.6 shows a close fit between HR BREACH and AREBA for a landside slope of $1:2$. Figure 3.5 shows a worse comparison for a landside slope of $1:6$. The model outcomes of AREBA are identical for the two landside slope gradients because the downward erosion of the invert level reaches the embankment's foundation before the landside slope retreat reaches the waterside slope. Despite a discrepancy in the value for the peak discharge, AREBA and HR BREACH do provide results that agree on the overall shape of the hydrograph and the time of the peak discharge. To get a better

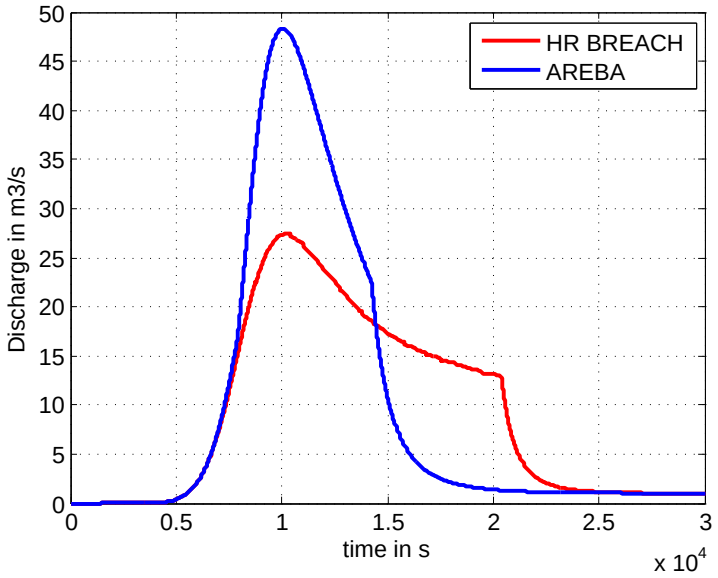

Figure 3.5: Hydrograph output HR BREACH and AREBA: Run 3

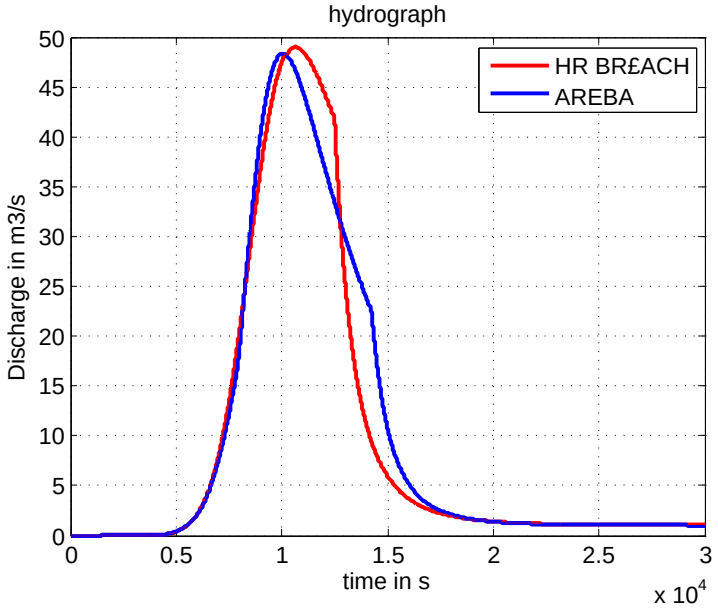

Figure 3.6: Hydrograph output HR BREACH and AREBA: Run 4

estimate of the impact of the assumptions, AREBA has been validated against the EU IMPACT project field experiments (IMPACT project, 2005) and the experiments performed by the Agricultural Research Services of the US Department of Agriculture (USDA-ARS)(Wahl, 2007).

3.2.2 Validation tests

A problem with validating embankment breach models is the overall lack in availability of quality datasets. Consequently it is often the case that there are more unknown model input values than validation data available. Several combinations of input parameters can be found that give a near perfect match with the validation data. This does however not mean that the model represents the physical processes correctly. Therefore, instead of calibrating the unknown model parameters to fit the experimental data, upper and lower limits are estimated for the input parameters based on the data, reports, and empirical relationships. These limits form the boundaries of a uniform distribution from which input values are drawn. It is the strength of AREBA to be able to rapidly perform these statistical analyses. A run time of the order of 0.1s per run keeps the overall run time of the model low while providing a more extensive analysis of the problem. After running AREBA 500 times for different combinations of input parameters, envelopes are obtained between which the experimental results are expected to lie. This gives the impact of the degree of uncertainty on the accuracy of the prediction. After completing one run, the same process is repeated for half the range of input values while maintaining the same mean value. The boundaries of the full range are referred to a Lower bound and Upper bound. The boundaries of half this range are referred to as Lower bound half and Upper bound half. The range in values for the input parameters of the Manning coefficient, and weir coefficients were the same in all validation cases. Nortier and De Koning (1991) provide a range of Manning coefficients based on different hydraulic conditions. The lowest Manning coefficient to be used in case of a straight natural channel with good material conditions is 0.025 $s/m^{1/3}$. The maximum value given for a curved natural channel with different depths is

0.045 s/m$^{1/3}$. These values are used as respectively the lower bound and upper bound. The choice in weir coefficients also influences the erosion rate. AREBA requires the input of three weir coefficients. The first weir coefficient, represents the influence of the vertical contraction and friction and has an upper bound of 1.1 and a lower bound of 0.9. The second weir coefficient is taken into account when the landside slope of the embankment reaches the waterside slope. At this stage the combined horizontal and vertical contraction leads to a higher weir coefficient with a maximum increase in discharge coefficient of 40% for practical purposes (Nortier and De Koning, 1991). Since horizontal contraction only influences the discharge positively, a lower bound of 1 and an upper bound of 1.4 are used. The third weir coefficient replaces the first and second one when the invert level reaches the foundation level of the embankment. At this stage the breach has already widened considerably. With all test cases the shapes of the reservoir behind the embankment were longer than they were wide. The ratio in breach width over reservoir width was considered to be insignificant to account for horizontal contraction once the foundation level is reached, and the third weir coefficient was kept at a value of 1. This leads to the range in values of the Manning coefficient and weir coefficients as given in Table 3.3. AREBA was validated against the EU IM-

-	**Lower bound**	**Lower bound half**	**Mean**	**Upper bound half**	**Upper bound**
Manning coefficient s/m$^{1/3}$	0.025	0.03	0.035	0.04	0.045
Weir coefficient 1	0.9	0.95	1	1.05	1.1
Weir coefficient 2	1	1.1	1.2	1.3	1.4

Table 3.3: Range of input parameters AREBA for all validation cases

PACT experiments and the USDA-ARS experiments. Data for all the validation cases used here can be found in the report by Van Damme et al. (2012). The embankment constructed for the EU IMPACT experiments had no grass cover. The embankment tested in USDA-ARS experiments had a cover of young grass of very low quality and Hanson (2012) recommended to ignore the presence of this grass cover for validation purposes. Hence for both cases no grass was accounted for. The density of water was

kept at 1000kg/m^3 for all test cases.

EU IMPACT minimum cohesive embankment validation case

Hassan and Morris (2009) studied the accuracy of the input and output values of the EU IMPACT project field experiments and reported on inaccuracies in the data. Besides present uncertainties in the values to use as input and output, several model input parameters of AREBA were undefined and needed to be estimated. Table 3.4 gives the input values which were kept constant during the different runs. The input hydrograph followed directly from the data of the EU IMPACT experiment (Van Damme et al., 2012). Besides the variation in Manning coefficient and weir coefficients, a range in

crest length	39 m
crest width	2 m
base width	18 m
crest height	5 m
initial breach width	2 m

Table 3.4: Fixed input parameters embankment geometry for testing against the EU IMPACT minimum cohesive embankment experiment

critical shear stress was estimated from actual sediment sizes and the Shields relation. Hassan and Morris (2009) recommends the use of a D_{50} of 4.75 mm for the mean grain size. Since a coarsely graded soil was used, a variation in grain size between 2 and 8 mm is assumed. A grain size of 4.75 mm gives a critical shear stress of $4.2N/m^2$. Similarly grain sizes of 2 mm and 8 mm give critical shear stresses of 1.78 N/m^2 and 7.12 N/m^2. Estimation of the erosion coefficient is more difficult to do. The IMPACT test embankment was poorly constructed leading to a relatively high erosion coefficient (Hassan and Morris, 2009). The lack of any further information regarding the erodibility leads to a relatively large range in uncertainty. The HR BREACH support file provides an approximate erosion coefficient based on the degree of erodibility. A maximum value for the erodibility of 18×10^{-6} m^3/Ns (for very erodible soil) and a minimum value of 0.18×10^{-6} m^3/Ns (for moderately erodible soil) are chosen. Figure 3.7 displays the maximum and minimum values of the discharge found per run, whereby

-	**Lower bound**	**Lower bound half**	**Mean**	**Upper bound half**	**Upper bound**
Critical shear stress (N/m^2)	1.8	3	4.2	5.6	7.1
Erodibility coefficient (m^3/Ns)	1.8×10^{-7}	4.6×10^{-6}	9×10^{-6}	1.35×10^{-5}	1.8×10^{-5}
Waterside slope gradient	1/1.7	1/1.75	1/1.8	1/1.85	1/1.9
Landside slope gradient	1/1.6	1/1.62	1/1.65	1/1.68	1/1.7
Initial breach depth ((m))	0.1	0.105	0.11	0.115	0.12

Table 3.5: Range of input parameters AREBA for testing against the EU IMPACT minimum cohesive embankment experiment.

for each run new variables are selected from a uniform distribution with the bounds given by Tables 3.3 and 3.5. In the Figures Upper bound and Lower bound refer to respectively the maximum and minimum value found for the discharge over 500 runs. Figure 3.8 presents the bounds for the growth in breadth of the breach.

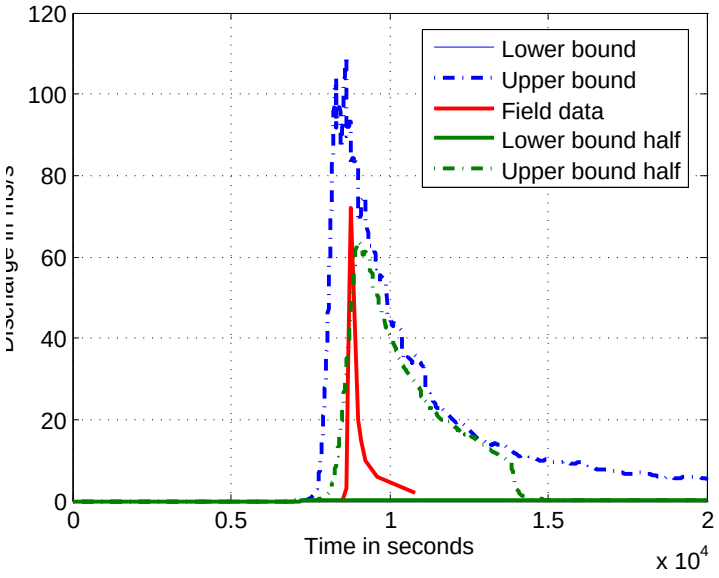

Figure 3.7: Maximum and minimum discharge (per time step) predicted by AREBA for 500 runs, compared with the IMPACT surface erosion field data. The lower bound, and Lower bound half values coincide with the x-axis.

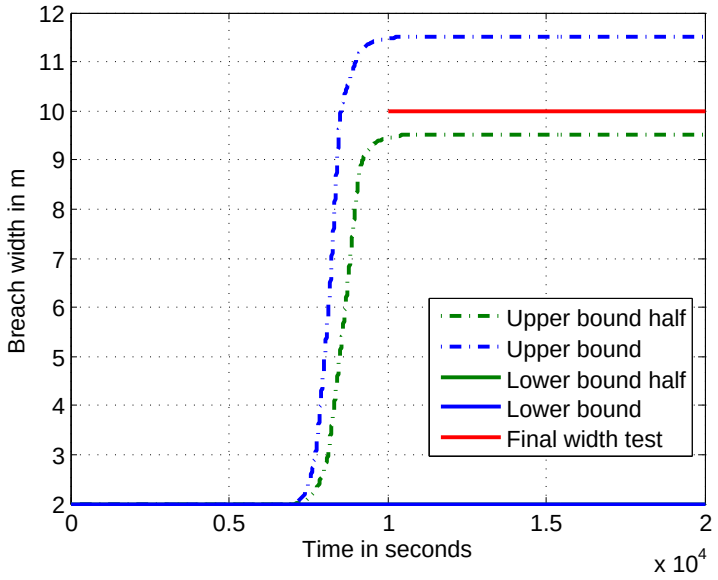

Figure 3.8: Maximum and minimum breach width (per time step) predicted by AREBA for 500 runs compared with the IMPACT surface erosion field data. The lower bound, and Lower bound half values coincide with the x-axis.

IMPACT 'maximum cohesive' embankment validation case

The clay embankment overflow experiment performed under the EU IMPACT project forms one of the two breach experiments used to validate the headcut failure mode in AREBA. A similar analysis of the input parameters as described under the previous section was performed for validation of AREBA's headcut failure mode. The fixed input parameters of the embankment geometry are given in Table 3.6. The input hydrograph was taken directly from the dataset. The headcut coefficient (C) in ($s^{-2/3}$)

crest length	39 m
crest width	2 m
base width	29.4 m
crest height	5.9 m

Table 3.6: Fixed input parameters embankment geometry for testing against the EU IMPACT 'maximum cohesive' embankment experiment.

was added to the analysis since this also influence the erosion rate in the case of headcut erosion. The headcut coefficient followed from Equation 3.27 and the extreme values

for the erodibility factor (K) of 1.7s$^{-2/3}$ and 18s$^{-2/3}$ such that

$$C = 2.46 \times 10^{-4} K \tag{3.27}$$

The value 2.46×10^{-4} follows from converting the given correlation in the HR BREACH help file to SI standards and has units $\frac{\mathrm{Ns}^{1/3}}{\mathrm{m}^3}$. Since the Shields curve does not account for cohesive effects, the critical shear stress was estimated from the model assumption that no downward crest erosion takes place due to flow over the crest (Temple et al., 2005). For this assumption to be true, the critical shear stress should be higher than the shear stress exerted by the flow on the structure. A hydraulic head of 0.2 m was assumed to calculate the flow velocity over the crest. Extreme values for the critical shear stress were calculated from the flow velocity and the upper and lower bound of the Manning coefficient. This resulted in a critical shear stress of 20 N/m^2 as a lower bound and a critical shear stress of 65 N/m^2 as an upper bound. Table 3.7 lists the ranges of all input parameters used for validation. Figures 3.9, 3.10, and 3.11 present the model outcomes together with the experimental data.

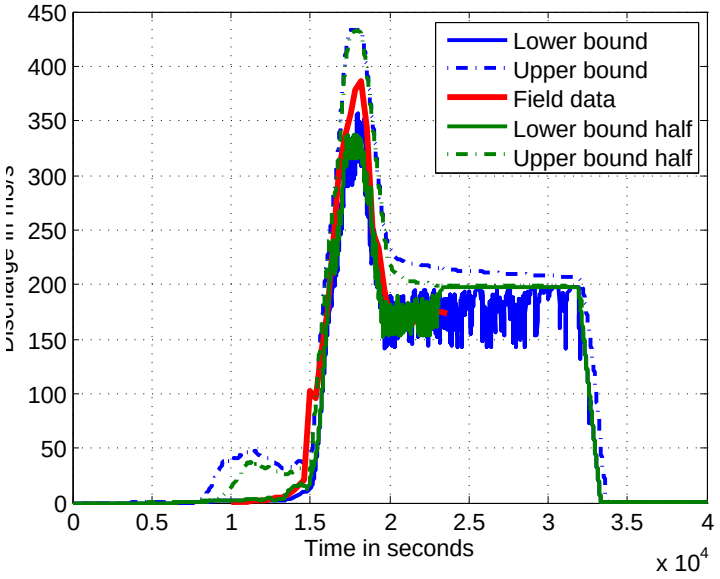

Figure 3.9: Maximum and minimum discharge (per time step) predicted by AREBA for 500 runs and compared with IMPACT surface headcut field data

-	**Lower bound**	**Lower bound half**	**Mean**	**Upper bound half**	**Upper bound**
Critical shear stress $(N/m)^2$	1.7	5.775	9.85	13.925	18
Erodibility coefficient (m^3/Ns)	1.7×10^{-6}	5.775×10^{-6}	9.85×10^{-6}	1.393×10^{-5}	1.8×10^{-5}
Headcut coefficient ($s^{-2/3}$)	1.335×10^{-4}	4.536×10^{-4}	7.735×10^{-4}	1.1×10^{-3}	1.4×10^{-3}
Waterside slope gradient	1/2	1/2.1	1/2.2	1/2.3	1/2.4
Landside slope gradient	1/2	1/2.0625	1/2.125	1/2.1875	1/2.25
Initial breach depth (m)	0.4	0.425	0.45	0.475	0.5
Initial breach width (m)	5.4	6.05	6.7	7.35	8
Crest height (m)	5.9	5.925	5.95	5.975	6

Table 3.7: Range of input parameters AREBA for testing against the EU IMPACT maximum cohesive embankment experiment.

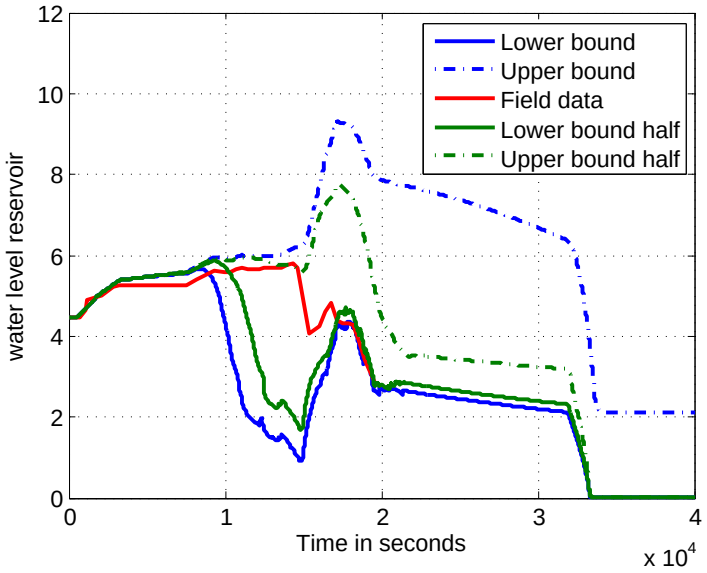

Figure 3.10: Maximum and minimum water depth in the reservoir (per time step) predicted by AREBA for 500 runs and compared with the IMPACT headcut erosion field data

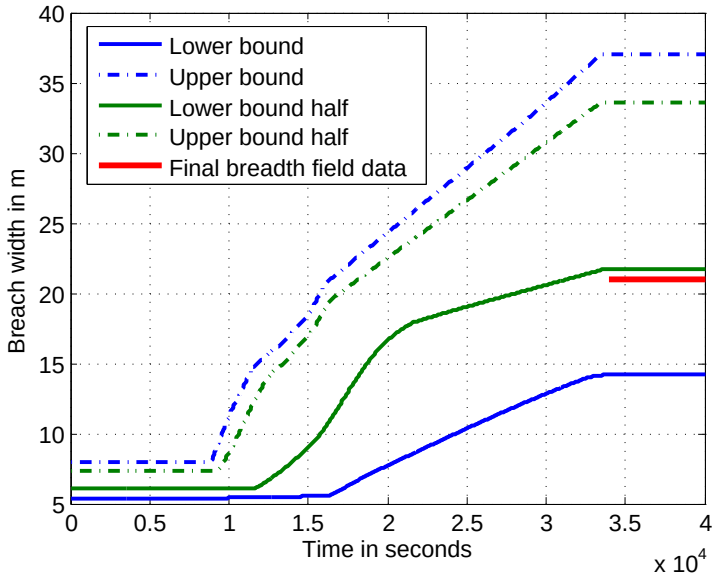

Figure 3.11: Maximum and minimum breach widths (per time step) predicted by AREBA for 500 runs compared with the IMPACT surface headcut field data

USDA-ARS1 validation case

The fixed values used in AREBA for the test embankment constructed for the first USDA-ARS experiment are given in Table 3.8. The reservoir storage parameters were obtained from the dataset provided. The initial breach was trapezoidal in shape with

crest length	7.3 m
crest width	1.83 m
base width	15.24 m
crest height	2.225 m
Slope gradients	1/3
Initial breach depth	0.46 m

Table 3.8: Fixed input parameters embankment geometry USDA-ARS1 experiment

side slopes of 1/3. Since AREBA assumes a square breach shape, the input values for the initial breach width have been varied. From the given headcut advance rate the headcut coefficient was estimated using Equation 3.24. The overfall height h_{hc} was approximated with the crest height. The outflow hydrograph of the experiment gave two values for the discharge, 0.56 m^3/s and 1.12 m^3/s. From the discharges and overfall height the headcut coefficients were estimated as presented in Table 3.9. In turn the

derived headcut coefficient was used to obtain a range for the erodibility coefficients using Equation 3.27. A 10% confidence interval was assumed when determining the upper and lower bounds. The critical shear stress was set as a fixed value of 45 N/m^2. Figures 3.12, 3.13, and 3.14 present the match found between the model runs and the

-	**Lower bound**	**Lower bound half**	**Mean**	**Upper bound half**	**Upper bound**
Cohesion (kN/m^2)	20	31.25	42.5	53.75	65
Critical shear stress (N/m^2)	1.7	5.775	9.85	13.925	18
Erodibility coefficient (m^3/Ns)	1.7×10^{-6}	5.775×10^{-6}	9.85×10^{-6}	1.393×10^{-5}	1.8×10^{-5}
Headcut coefficient ($s^{-2/3}$)	1.335×10^{-4}	4.536×10^{-4}	7.735×10^{-4}	1.1×10^{-3}	1.4×10^{-3}
Initial breach width (m)	1.8288	2.501	3.20	3.8860	4.572

Table 3.9: Range of input parameters AREBA for USDA-ARS1 headcut erosion validation case

field data.

USDA-ARS2 validation case

The parameters kept constant during validation against the second experiment performed by the Agricultural Research Services of the US Department of Agriculture are given in Table 3.10. Table 3.11 lists the input parameters which were varied and their range in variation. The range of values in Table (3.11) have been derived according

crest length	7.3 m
crest width	1.83 m
base width	15.54 m
crest height	2.225 m
Slope gradients	1/3
Initial breach depth	0.46 m

Table 3.10: Fixed input parameters embankment geometry USDA-ARS2 experiment

to the same process as used for validating AREBA against the first ARS experiment.

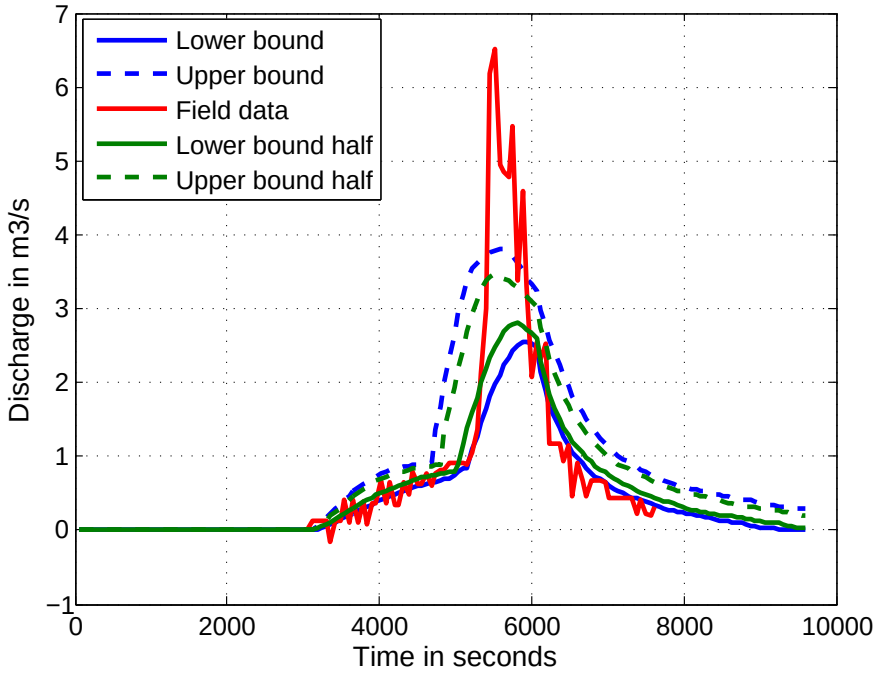

Figure 3.12: Maximum and minimum discharge (per time step) predicted by AREBA for 500 runs and compared with the field data of the USDA-ARS1 experiment

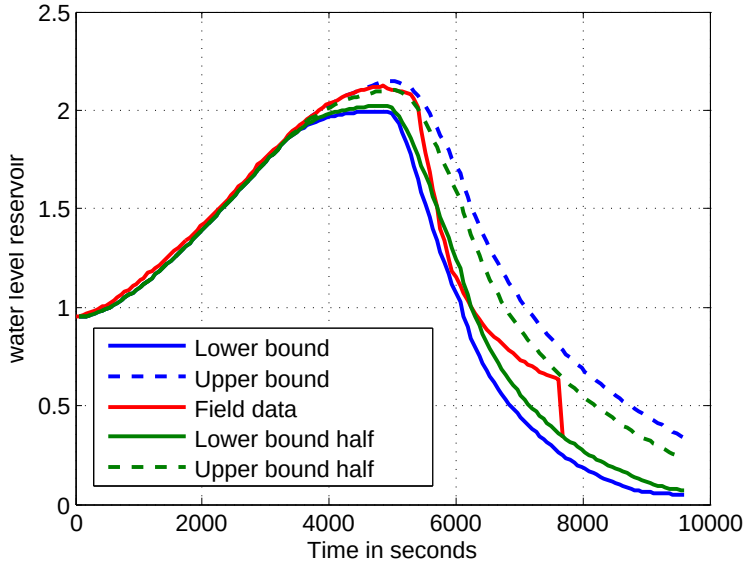

Figure 3.13: Maximum and minimum water depth in the reservoir (per time step) predicted by AREBA for 500 runs and compared with the field data of the USDA-ARS1 experiment

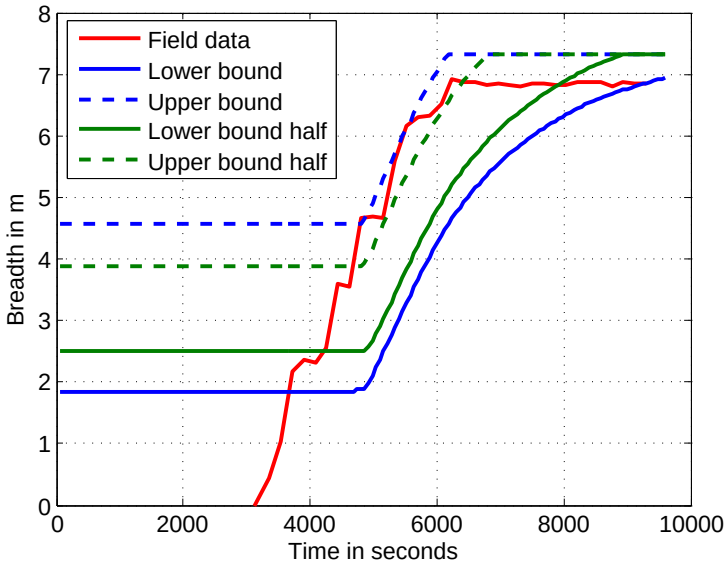

Figure 3.14: : Maximum and minimum breach width (per time step) predicted by AREBA for 500 runs and compared with the field data (red line) of the USDA-ARS1 experiment

Since the embankment did not fail, no difference was found for the overflow discharge

-	**Lower bound**	**Lower bound half**	**Mean**	**Upper bound half**	**Upper bound**
Cohesion (kN/m^2)	4	4.5	5	5.5	6
Critical shear stress (N/m^2)	12.5	13.25	14	14.75	15.5
Erodibility coefficient (m^3/Ns)	2×10^{-8}	2.1×10^{-8}	2.2×10^{-6}	0.023×10^{-8}	2.4×10^{-8}
Headcut coefficient ($s^{-2/3}$)	3.25×10^{-5}	3.3×10^{-5}	3.35×10^{-5}	3.4×10^{-5}	3.45×10^{-5}
Initial breach width (m)	1.8288	2.501	3.20	3.8860	4.572

Table 3.11: Range of input parameters AREBA for USDA-ARS1 Headcut erosion validation case

between the upper and lower bound. For this reason only the overlapping outcome for the range between Upper bound and Lower bound (Large range) has been given in Figures 3.15 and 3.16.

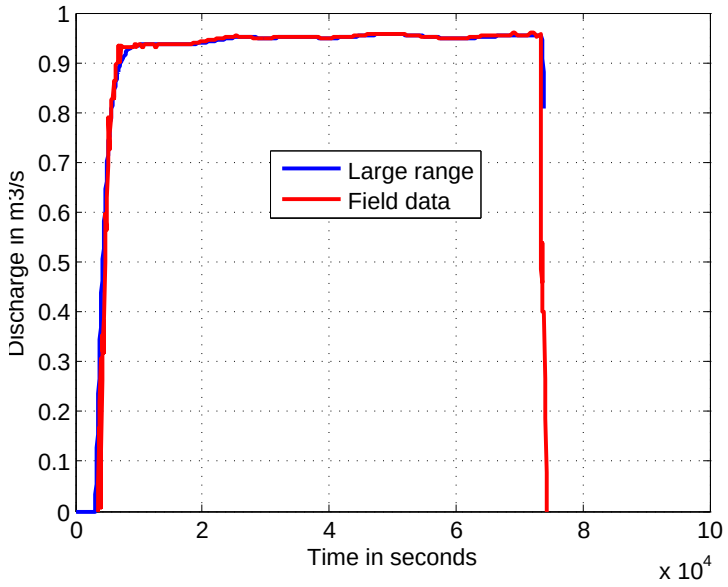

Figure 3.15: Maximum and minimum discharge (per time step) predicted by AREBA for 500 runs and compared with the field data of the USDA-ARS2 experiment

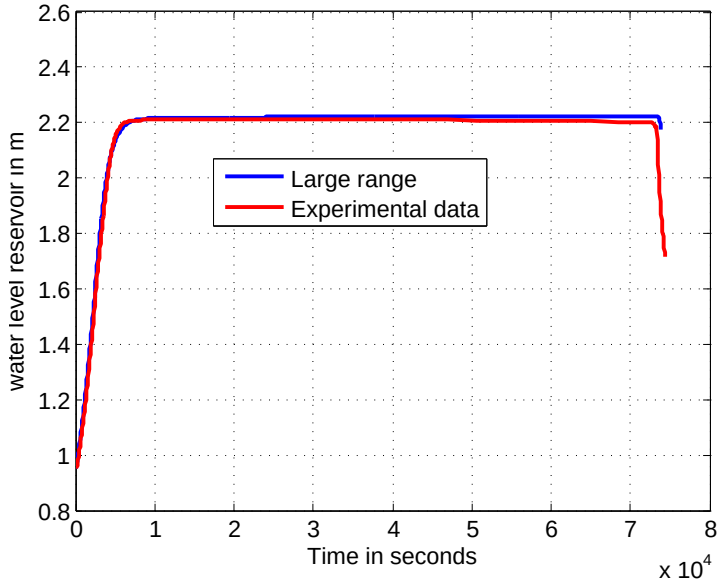

Figure 3.16: Maximum and minimum water depth in the reservoir (per time step) predicted by AREBA for 500 runs and compared with the field data of the USDA-ARS2 experiment

3.3 Comparison of AREBA with the MDSF2 method

In the U.K. the research project Risk Assessment for flood and coastal defence for Strategic Planning (RASP) developed a framework for undertaking risk analysis (HR, Wallingford and University of Bristol, 2004) . Within this framework, the performance of the system of flood defences is represented using fragility curves that describe the likelihood of structural failure (breaching) under given hydraulic loading conditions. The framework has been adopted by the Environment Agency and used to underpin its National Flood Risk Assessment (NaFRA) (Hall et al., 2003). This method was further developed and implemented within the Environment Agencys MDSF2 software system (Mc. Gahey et al., 2011). Within NaFRA, and more recently MDSF2, breach size and flood volume are predicted using a simplified calculation based on coarse assumptions (Mc. Gahey et al., 2011). Any error in predicting breach formation translates to an error in predicting the risk of flooding of downstream areas. AREBA has been developed to improve the method for predicting the flood volume through a breach in order to obtain a more reliable assessment of different flood scenarios. In this section a comparison of the AREBA model with the method applied in NaFRA and MDSF2 is presented.

The equations used by MDSF2 for calculating breach dimensions and associated volumes are detailed in Mc. Gahey et al. (2011) and summarised below. In NaFRA and MDSF2 the volume entering the floodplain via a single asset follows from

$$V = 3600 \cdot \mathit{Hydmult} \cdot \widetilde{q} \cdot b \cdot T, \tag{3.28}$$

where V is the volume of water in m^3 entering the floodplain, *Hydmult* is a hydrograph multiplier with a value of 0.55, $\widetilde{q}$ is the breadth-averaged discharge in m^2/s, b is the breadth of the discharge in m, and T, is the duration of the flow across the asset in hours. An asset is here defined as an artificial or natural structure that works as a flood defence. The discharge $\widetilde{q}$, in Equation (3.28) follows from the broad weir equation

$$\widetilde{q} = \sqrt{\frac{gh^3}{3.35}}, \tag{3.29}$$

where g is the acceleration due to gravity, and h the head difference. If the asset is in an overflow state, then $h = swl - cl$, where swl is the still water level, and cl is the crest level. If the asset is in a breached state, then h is approximated with

$$h = c_h\sqrt{L_x} + swl - cl. \tag{3.30}$$

However, if $\left(c_h\sqrt{L_x}\right) > (cl - gl)$, then

$$h = swl - gl, \tag{3.31}$$

where c_h is a head constant of 0.5 m, L_x the ratio between the return period of the extreme event and the standard of protection of the asset, and gl the ground level immediately landward of the asset. When the asset overflows, the flow breadth b is given by the length of the asset. In a breached state, for any extreme event that is smaller than the standard of protection of the asset, b is given by

$$b = c_b L_{def}, \tag{3.32}$$

where L_{def} is the defence length, and c_b a breach constant with a value of 0.1 for hard assets and a value of 0.2 for soft assets. If the return period of the breach event exceeds the standard of protection of the asset, then the flow breadth b is in accordance with the ratio of the load limited to the length of the asset, or

$$\text{if} \qquad c_b\frac{RP}{SoP} < 1 \text{ then} \tag{3.33}$$

$$b = \min\left(c_b\frac{RP}{SoP}L_{def}, L_{def}\right)$$

where RP is the return period of the loading even in years, and SoP the standard of

protection of the asset in years. The duration T is for fluvial assets given by

$$T = \sqrt{L_x} A_{ca}^{0.25} c_T, \tag{3.34}$$

and for coastal assets given by

$$T = \sqrt{(L_x)} c_T, \tag{3.35}$$

where A_{ca} is the size of the catchment area upstream of the asset in km^2 and c_T a duration constant following from Table 3.12. A test case is used to study the impact

Type	Fluvial Shallow	Fluvial Average	Fluvial Steep	Tidal and Coastal
Definition	Gradients less than 1 : 5000	Gradients ranging from 1:1000 to 1:5000	Gradients greater than 1:1000	Based on semi-diurnal tidal cycle
c_T for $RP \leq 50$	0.6	0.4	0.6	3
c_T for $RP > 50$	1.2	0.8	1.2	3

Table 3.12: Values for the duration constant c_T

of applying the AREBA model over the existing breach assumptions discussed above. The embankment used for the test case has a crest length of 2233.9 m, a crest level of 218.0 m and a ground level of 214.6 m. The other input parameters for AREBA were provided by a calibrated input file from HR BREACH and are listed in Table 3.13. The floodplain characteristics and river hydrograph used in the comparison are given in Figure 3.17. The outcomes given by AREBA and the method from MDSF2 have been compared for a range of return periods. For each return period, a peak water level was provided. Since these peak water levels did not correspond with the peak water level given by the river hydrograph from Figure 3.17, the river hydrograph was scaled to the peak water levels given per return period. If the peak water level was smaller than the crest level, then AREBA was run in Piping mode (See Appendix A), otherwise AREBA was run in Surface erosion mode. Table 3.14 gives the flood volumes found with AREBA and the method used in MDSF2 for a range of return periods and peak water levels. In all cases, the volume outputs from AREBA are

Grass quality	medium
Crest width	8.9 m
Initial breach width	2 m
Initial breach height	0.2 m
Waterside slope gradient	1/6.5
Landside slope gradient	1/7
Pipe level	0.3 m above foundation level
Initial pipe diameter	0.3 m
Cohesion embankment soil	4.79kN/m^2
Manning coefficient	0.02s/m^3
D_{50} soil	0.6 mm
Critical shear stress	5 N/mm^2
Erodibility soil	$1.768 \text{cm}^3/\text{s}$
All weir coefficients	1
Time step	300s

Table 3.13: Input parameters AREBA for comparison with the MDSF2 method

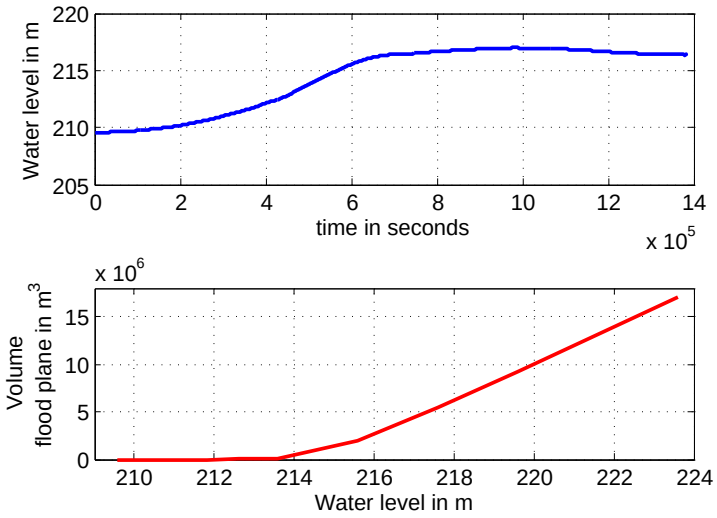

Figure 3.17: River hydrograph and flood plain characteristics test case

Return period (years)	Peak water level (m AD)	AREBA Volumes in m^3	MDFS2 Volumes in m^3
45	214.73	4.41×10^2	0
50	214.82	2.77×10^3	0
60	214.98	1.024×10^4	0
70	215.11	1.10×10^4	0
80	215.23	1.52×10^4	0
90	215.33	2.04×10^4	0
100	215.42	2.80×10^4	0
125	215.60	9.80×10^5	0
150	215.74	1.02×10^6	0
175	215.87	104×10^6	0
200	215.98	1.04×10^6	0
250	216.16	1.04×10^6	0
500	216.72	1.09×10^6	0
750	216.89	1.10×10^6	0
1000	217.02	1.11×10^6	0
2500	217.51	1.12×10^6	0
5000	218.01	2.79×10^8	6.86×10^6
7500	218.31	6.87×10^8	5.43×10^7
10000	218.52	1.21×10^9	1.25×10^8
20000	219.03	3.01×10^9	4.34×10^8

Table 3.14: Flood volumes calculated with AREBA and MDSF2 for a range of return periods and peak water levels.

quite different from those performed within the MDSF2 calculation. Within flood risk analysis models these differences translate into different flood extents and depths and hence ultimately flood risk. Given the simplistic nature of the existing MDSF2 breach volume calculations and the favourable comparison of the AREBA model with field data, a significant improvement in the accuracy of the risk calculations can be made when using AREBA for the calculation of breach volumes.

Chapter 4

Modelling breach flow

In Section 1.3.3 the breach flow characteristics during Stage 2, Stage 3, and Stage 4 have been discussed. During Stage 2, an accurate flow field can be obtained while neglecting the horizontal momentum exchange normal to the main flow direction. To simulate non-hydrostatic pressures and possible flow separation during Stage 2, a vertical 2D flow model has been developed based on solving the breadth-integrated Navier–Stokes equations. Several methods are available to solve the general Navier–Stokes equations, which could also be applied to the breadth-integrated equations. Direct Numerical Simulation numerically resolves all scales of the turbulent spectrum. This method is the least approximate but requires the most computational effort. The other two methods discussed here ignore the small scale physics. With Large eddy simulation the range of length scales of the solution is reduced, leading to a saving in computational cost. The third method, which is applied here, involves solving a time averaged (Reynolds-averaged) version of the Navier–Stokes equations. This method is the least computationally intensive but also the most approximate (Congedo et al., 2012). Due to the benefits of a relatively high computational speed while providing sufficient accuracy, a breadth-integrated version of the Reynolds averaged Navier–Stokes equations is derived in this chapter. The high flow velocities over the embankment in combination with the limited flow distance give a characteristic flow time of the order of seconds. In the case of overflow the characteristic time scale of the upstream boundary conditions

is minutes or hours. The characteristic time scale of erosion is also minutes or hours. The larger order in the time scale of the erosion and the change in boundary conditions for the flow therefore justify a quasi-steady approach, and hence justify the choice for a time/Reynolds-averaged approach for solving the Navier–Stokes equations. Besides the negligible horizontal momentum exchange normal to the main flow direction, the curvature in water level is small. Hence the flow can be accurately simulated using a combination of the breadth-integrated Reynolds-averaged Navier–Stokes momentum equations, a breadth-averaged equation to account for the description of turbulent viscosity, a breadth-integrated pressure Poisson equation, and a depth- and breadth integrated mass balance equation.

The bottom boundary is assumed to consist of a solid surface. Hence the model does not account for the formation of free nappes. Because the incorporation of effects of entrapped air under the free nappe on the flow would complicate the calculations that need to be performed. The time dependent behaviour of these physical processes effects on the run-time of the model would render the model useless for modelling long duration breach events. Future research could extend the present work to include the analysis of nappe flows provided sufficient computational resources are available.

Section 4.1 deals with the integration of the mass balance equation, Section 4.2 with the integration of the momentum equations, Section 4.3 with the description of the turbulent viscosity, and Section 4.4 with the breadth-integrated pressure Poisson equation. Throughout the derivation of each of the equations, water is assumed to be incompressible, and its density unaffected by the transport of sediment. Although this assumption permits the elimination of density from the equations, density is retained in the equations in order to describe accurately the change in density at the free surface and bed when numerically approaching the solution of the equations. Three types of

averaging are employed as given by

$$\begin{aligned} \text{breadth-averaging}: &\quad \tilde{\cdot} \\ \text{depth-averaging}: &\quad \bar{\cdot} \\ \text{time-averaging}: &\quad \langle\cdot\rangle \end{aligned} \tag{4.1}$$

4.1 Mass balance equation

The three dimensional mass balance equation is (see e.g.Falconer (1993))

$$\frac{\partial \rho}{\partial t} + \frac{\partial \rho u}{\partial x} + \frac{\partial \rho v}{\partial y} + \frac{\partial \rho w}{\partial z} = 0, \tag{4.2}$$

where ρ is the density, and u, v, and w are the velocity components in Cartesian coordinates (see Figure (4.1)). Integration of Equation (4.2) over the breadth in the $\hat{y}$-direction gives

$$\int_{y_1}^{y_2} \frac{\partial \rho}{\partial t} dy + \int_{y_1}^{y_2} \frac{\partial \rho u}{\partial x} dy + \int_{y_1}^{y_2} \frac{\partial \rho v}{\partial y} dy + \int_{y_1}^{y_2} \frac{\partial \rho w}{\partial z} dy = 0, \tag{4.3}$$

where y_1 is the right hand lateral boundary and y_2 is the left hand lateral boundary

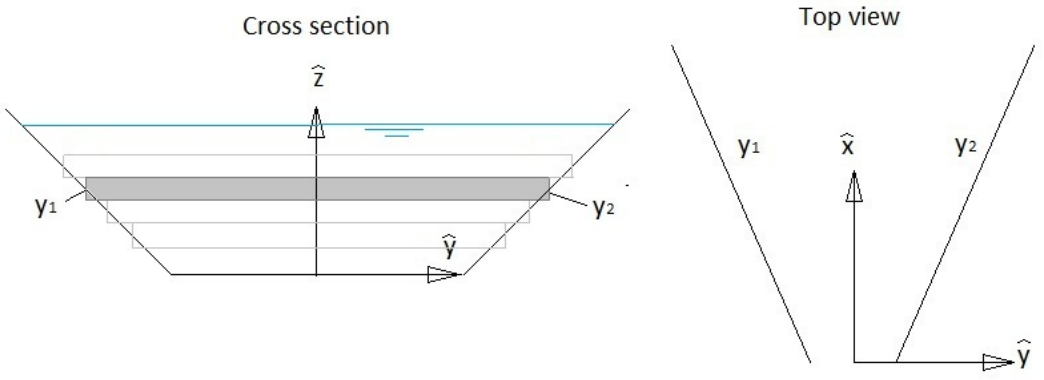

Figure 4.1: Coordinate system used for breadth-integration.

as depicted in Figure (4.1). The integral terms are worked out by applying the Leibniz

rule giving

$$\frac{\partial}{\partial t}\int_{y_1}^{y_2}\rho dy - \rho|_{y_2}\frac{\partial y_2}{\partial t}|_{y_2} + \rho|_{y_1}\frac{\partial y_1}{\partial t}|_{y_1} + \frac{\partial}{\partial x}\int_{y_1}^{y_2}\rho u dy - \rho u|_{y_2}\frac{\partial y_2}{\partial x}|_{y_2} + \rho u|_{y_1}\frac{\partial y_1}{\partial x}|_{y_1}$$
$$+\frac{\partial}{\partial z}\int_{y_1}^{y_2}\rho w dy - \rho w|_{y_2}\frac{\partial y_2}{\partial z}|_{y_2} + \rho w|_{y_1}\frac{\partial y_1}{\partial z}|_{y_1} + \rho v|_{y_2} - \rho v|_{y_1} = 0. \tag{4.4}$$

For no-slip boundary conditions at the walls $u|_{y_1} = u|_{y_2} = w|_{y_1} = w|_{y_2} = 0$. Erosion of the wall in the $\hat{y}$-direction leads to the following boundary conditions for v

$$v|_{y_1} = \frac{dy_1}{dt}|_{y_1} = \left(\frac{\partial y_1}{\partial t} + u\frac{\partial y_1}{\partial x} + w\frac{\partial y_1}{\partial z}\right)|_{y_1} = \frac{\partial y_1}{\partial t}|_{y_1} \tag{4.5}$$

,and

$$v|_{y_2} = \frac{dy_2}{dt}|_{y_2} = \left(\frac{\partial y_2}{\partial t} + u\frac{\partial y_2}{\partial x} + w\frac{\partial y_2}{\partial z}\right)|_{y_2} = \frac{\partial y_2}{\partial t}|_{y_2}.$$

Hence, Equation (4.4) becomes

$$\frac{\partial \widetilde{\rho} b}{\partial t} - \rho|_{y_2}\frac{\partial y_2}{\partial t}|_{y_2} + \rho|_{y_1}\frac{\partial y_1}{\partial t}|_{y_1} + \frac{\partial \widetilde{\rho u} b}{\partial x} + \frac{\partial \widetilde{\rho w} b}{\partial z} \tag{4.6}$$

$$+\rho|_{y_2}\frac{\partial y_2}{\partial t}|_{y_2} - \rho|_{y_1}\frac{\partial y_1}{\partial t}|_{y_1} = 0,$$

where $b = y_2 - y_1$ and $\widetilde{.}$ denotes the breadth-average. Hence

$$\begin{aligned} \tilde{\rho} &= \frac{1}{b}\int_{y_1}^{y_2}\rho dy, \\ \widetilde{\rho u} &= \frac{1}{b}\int_{y_1}^{y_2}\rho u dy, \\ \text{and} \qquad \widetilde{\rho w} &= \frac{1}{b}\int_{y_1}^{y_2}\rho w dy. \end{aligned} \tag{4.7}$$

Hence Equation (4.6) gives

$$\frac{\partial \tilde{\rho} b}{\partial t} + \frac{\partial \widetilde{\rho u} b}{\partial x} + \frac{\partial \widetilde{\rho w} b}{\partial z} = 0. \tag{4.8}$$

Assuming (i) small curvature of the free surface and (ii) solid bottom boundary condition, Equation (4.8) can be integrated over the depth to give

$$\int_{z_1}^{z_2} \frac{\partial \tilde{\rho} b}{\partial t} dz + \int_{z_1}^{z_2} \frac{\partial \widetilde{\rho u} b}{\partial x} dz + \int_{z_1}^{z_2} \frac{\partial \widetilde{\rho w} b}{\partial z} dz = 0, \tag{4.9}$$

which after applying the Leibniz rule becomes

$$\begin{aligned} &\frac{\partial}{\partial t} \int_{z_1}^{z_2} \tilde{\rho} b dz - \tilde{\rho} b|_{z_2} \frac{\partial z_2}{\partial t}|_{z_2} + \tilde{\rho} b|_{z_1} \frac{\partial z_1}{\partial t}|_{z_1} \\ +&\frac{\partial}{\partial x} \int_{z_1}^{z_2} \widetilde{\rho u} b dz - \widetilde{\rho u} b|_{z_2} \frac{\partial z_2}{\partial x}|_{z_2} + \widetilde{\rho u} b|_{z_1} \frac{\partial z_1}{\partial x}|_{z_1} + \widetilde{\rho w} b|_{z_2} - \widetilde{\rho w} b|_{z_1}. \end{aligned} \tag{4.10}$$

The boundary conditions at the free surface and the embankment surface are

$$\begin{aligned} \widetilde{\rho w} b|_{z_2} =& \tilde{\rho} b|_{z_2} \frac{\partial z_2}{\partial t}|_{z_2} + \widetilde{\rho u} b \frac{\partial z_2}{\partial x}|_{z_2} \\ \text{,and} \qquad \widetilde{\rho w} b|_{z_1} =& \tilde{\rho} b|_{z_1} \frac{\partial z_1}{\partial t}|_{z_1} + \widetilde{\rho u} b \frac{\partial z_1}{\partial x}|_{z_1}. \end{aligned} \tag{4.11}$$

Substituting the expressions for $\widetilde{\rho w} b|_{z_2}$ and $\widetilde{\rho w} b|_{z_1}$ in Equation (4.10) results in

$$\frac{\partial \overline{\tilde{\rho}} \bar{b} h}{\partial t} + \frac{\partial \overline{\widetilde{\rho u}} \bar{b} h}{\partial x} = 0, \tag{4.12}$$

where h is the water depth given by $z_2 - z_1$,

$$\begin{aligned} \overline{\tilde{\rho} b} &= \int_{z_1}^{z_2} \tilde{\rho} b dz, \\ \text{and} \qquad \overline{\widetilde{\rho u} b} &= \int_{z_2}^{z_2} \widetilde{\rho u} b dz. \end{aligned} \tag{4.13}$$

The overbar denotes depth-averaging. Equation (4.12) can be extended to

$$\overline{\tilde{\rho} b} \frac{\partial h}{\partial t} + \bar{\tilde{\rho}} h \frac{\partial \bar{b}}{\partial t} + \overline{\tilde{\rho}} \bar{b} \frac{\partial \overline{\tilde{u}_x} h}{\partial x} + \overline{\widetilde{\rho u_x}} h \frac{\partial \bar{b}}{\partial x} = 0. \tag{4.14}$$

The local rate of breach widening due to erosion of both banks is

$$E_w = \frac{\partial b}{\partial t}. \tag{4.15}$$

After depth-averaging,

$$\overline{E_w} = \frac{\partial \bar{b}}{\partial t}, \tag{4.16}$$

where

$$\bar{b} = \frac{1}{h}\int_{z_1}^{z_2} b dh. \tag{4.17}$$

Substituting Equation (4.15) into Equation (4.14) gives the final depth and breadth integrated mass balance equation

$$\overline{\tilde{\rho} b}\frac{\partial h}{\partial t} + \overline{\tilde{\rho} E_w} h + \bar{\tilde{\rho}}\frac{\partial \overline{q_x} h}{\partial x} = 0, \tag{4.18}$$

where $q_x = b\widetilde{u_x}$.

4.2 Breadth-integrated momentum equations

This section describes the derivation of the breadth-averaged Reynolds-averaged Navier–Stokes equations. Applying Newton's law to an elemental fluid volume of size Δx, Δy, and Δz and taking their limits to 0 gives the original Navier–Stokes momentum equations

$$\frac{\partial \rho u}{\partial t} + u\frac{\partial \rho u}{\partial x} + v\frac{\partial \rho u}{\partial y} + w\frac{\partial \rho u}{\partial z} = X + \frac{\partial \sigma_{xx}}{\partial x} + \frac{\partial \tau_{yx}}{\partial y} + \frac{\partial \tau_{zx}}{\partial z}, \tag{4.19}$$

$$\frac{\partial \rho v}{\partial t} + u\frac{\partial \rho v}{\partial x} + v\frac{\partial \rho v}{\partial y} + w\frac{\partial \rho v}{\partial z} = Y + \frac{\partial \sigma_{yy}}{\partial y} + \frac{\partial \tau_{xy}}{\partial x} + \frac{\partial \tau_{zy}}{\partial z}, \tag{4.20}$$

and

$$\frac{\partial \rho w}{\partial t} + u\frac{\partial \rho w}{\partial x} + v\frac{\partial \rho w}{\partial y} + w\frac{\partial \rho w}{\partial z} = Z + \frac{\partial \sigma_{zz}}{\partial z} + \frac{\partial \tau_{yz}}{\partial y} + \frac{\partial \tau_{xz}}{\partial x}, \tag{4.21}$$

where X, Y, and Z represent the body forces on the flow element with dimensions dx, dy and dz, σ_{ii} $(i = x, y, z)$ indicates the normal stress components acting on the surface of the element, and τ_{ij} for $(j = x, y, z)$ and $i \neq j$ indicates the shear stress components acting on the surface of the element. The normal stress is divided into a mean and fluctuating component (Schlichting and Gersten, 1979) as

$$\begin{aligned} \sigma_{xx} &= \widehat{\sigma} + \sigma'_{xx}, \\ \sigma_{yy} &= \widehat{\sigma} + \sigma'_{yy}, \\ \sigma_{zz} &= \widehat{\sigma} + \sigma'_{zz}, \end{aligned} \tag{4.22}$$

where $\widehat{\sigma} = \frac{1}{3}(\sigma_{xx} + \sigma_{yy} + \sigma_{zz}) = -P$ (Falconer, 1993), where P is the pressure. The Stokes relations and Stokes hypothesis (Schlichting and Gersten, 1979) give the rate of strain as a function of the velocity gradients. Stokes hypothesised that the sum of the normal stresses add up to 0 leading to a coefficient of $-2/3\mu$. Using the Stokes equations, and Stokes hypthesis, the fluctuating components of the normal stresses and shear stresses are written as a function of velocity gradients and the dynamic molecular

viscosity μ, giving

$$\frac{\partial \rho u}{\partial t} + u\frac{\partial \rho u}{\partial x} + v\frac{\partial \rho u}{\partial y} + w\frac{\partial \rho u}{\partial z} = X - \frac{\partial P}{\partial x} + \frac{\partial}{\partial x}\mu\left[2\frac{\partial u}{\partial x} - \frac{2}{3}\left(\frac{\partial u}{\partial x} + \frac{\partial v}{\partial y} + \frac{\partial w}{\partial z}\right)\right] + \frac{\partial}{\partial y}\mu\left(\frac{\partial v}{\partial x} + \frac{\partial u}{\partial y}\right) + \frac{\partial}{\partial z}\mu\left(\frac{\partial w}{\partial x} + \frac{\partial u}{\partial z}\right), \tag{4.23}$$

$$\frac{\partial \rho v}{\partial t} + u\frac{\partial \rho v}{\partial x} + v\frac{\partial \rho v}{\partial y} + w\frac{\partial \rho v}{\partial z} = Y - \frac{\partial P}{\partial y} + \frac{\partial}{\partial y}\mu\left[2\frac{\partial v}{\partial y} - \frac{2}{3}\left(\frac{\partial u}{\partial x} + \frac{\partial v}{\partial y} + \frac{\partial w}{\partial z}\right)\right] + \frac{\partial}{\partial x}\mu\left(\frac{\partial v}{\partial x} + \frac{\partial u}{\partial y}\right) + \frac{\partial}{\partial z}\mu\left(\frac{\partial w}{\partial y} + \frac{\partial v}{\partial z}\right), \tag{4.24}$$

and

$$\frac{\partial \rho w}{\partial t} + u\frac{\partial \rho w}{\partial x} + v\frac{\partial \rho w}{\partial y} + w\frac{\partial \rho w}{\partial z} = Z - \frac{\partial P}{\partial z} + \frac{\partial}{\partial z}\mu\left[2\frac{\partial w}{\partial z} - \frac{2}{3}\left(\frac{\partial u}{\partial x} + \frac{\partial v}{\partial y} + \frac{\partial w}{\partial z}\right)\right] + \frac{\partial}{\partial y}\mu\left(\frac{\partial w}{\partial y} + \frac{\partial v}{\partial z}\right) + \frac{\partial}{\partial x}\mu\left(\frac{\partial u}{\partial z} + \frac{\partial w}{\partial x}\right). \tag{4.25}$$

The assumed incompressibility of the flow gives that the flow field is divergence free, or $\nabla \cdot \mathbf{u} = 0$, where ∇ is the divergence operator, and $\mathbf{u} = (u, v, w)$. Application of the

incompressibility assumption gives for an assumed constant molecular viscosity μ

$$\frac{\partial \rho u}{\partial t} + u\frac{\partial \rho u}{\partial x} + v\frac{\partial \rho u}{\partial y} + w\frac{\partial \rho u}{\partial z} = X - \frac{\partial P}{\partial x} + \mu\left(\frac{\partial^2 u}{\partial x^2} + \frac{\partial^2 u}{\partial y^2} + \frac{\partial^2 u}{\partial z^2}\right), \tag{4.26}$$

$$\frac{\partial \rho u}{\partial t} + u\frac{\partial \rho u}{\partial x} + v\frac{\partial \rho u}{\partial y} + w\frac{\partial \rho u}{\partial z} = Y - \frac{\partial P}{\partial z} + \mu\left(\frac{\partial^2 v}{\partial x^2} + \frac{\partial^2 v}{\partial y^2} + \frac{\partial^2 v}{\partial z^2}\right), \tag{4.27}$$

and

$$\frac{\partial \rho u}{\partial t} + u\frac{\partial \rho u}{\partial x} + v\frac{\partial \rho u}{\partial y} + w\frac{\partial \rho u}{\partial z} = Z - \frac{\partial P}{\partial z} + \mu\left(\frac{\partial^2 w}{\partial x^2} + \frac{\partial^2 w}{\partial y^2} + \frac{\partial^2 w}{\partial z^2}\right). \tag{4.28}$$

A Reynolds decomposition is applied whereby the velocity vector $\mathbf{u} = \mathrm{iu} + \mathrm{jv} + \mathrm{kw}$ is split into a mean velocity vector and a fluctuating velocity vector, such that $\mathbf{u} = \langle \mathbf{u} \rangle + \mathbf{u}' = (\langle \mathrm{u} \rangle, \langle \mathrm{v} \rangle, \langle \mathrm{w} \rangle) + (\mathrm{u}', \mathrm{v}', \mathrm{w}')$, where $\langle . \rangle$ denotes the time average. The mean velocity vector is given by

$$\langle \mathbf{u} \rangle = \frac{1}{\Delta t}\int_t^{t+\Delta t} \mathbf{u} dt. \tag{4.29}$$

The fluctuating part is given by $\mathbf{u}' = (u', v', w')$, with the condition

$$\langle \mathbf{u}' \rangle = \frac{1}{\Delta t}\int_t^{t+\Delta t} \mathbf{u}' dt = 0. \tag{4.30}$$

The time integral of the velocity vector $\mathbf{u}$ is now given by

$$\langle \mathbf{u} \rangle = \frac{1}{\Delta t}\int_t^{t+\Delta t} \langle \mathbf{u} \rangle + \mathbf{u}' dt. \tag{4.31}$$

Splitting of the pressure term gives $P = \langle P \rangle + P'$ whereby

$$\langle P \rangle = \frac{1}{\Delta t}\int_t^{t+\Delta t} \langle P \rangle + P' dt. \tag{4.32}$$

Adding the divergence of the velocity components to the momentum equations and rewriting them in terms of mean and fluctuating components, gives

$$\frac{\partial \rho\langle u\rangle}{\partial t} + \frac{\partial \rho\langle u\rangle\langle u\rangle}{\partial x} + \frac{\partial \rho\langle u\rangle\langle v\rangle}{\partial y} + \frac{\partial \rho\langle u\rangle\langle w\rangle}{\partial z} = \langle X\rangle - \frac{\partial\langle P\rangle}{\partial x} + \mu\left(\frac{\partial^2\langle u\rangle}{\partial x^2} + \frac{\partial^2\langle u\rangle}{\partial y^2} + \frac{\partial^2\langle u\rangle}{\partial z^2}\right) - \left(\frac{\partial \rho\langle u'u'\rangle}{\partial x} + \frac{\partial \rho\langle u'v'\rangle}{\partial y} + \frac{\partial \rho\langle u'w'\rangle}{\partial z}\right), \tag{4.33}$$

$$\frac{\partial \rho\langle v\rangle}{\partial t} + \frac{\partial \rho\langle v\rangle\langle u\rangle}{\partial x} + \frac{\partial \rho\langle v\rangle\langle v\rangle}{\partial y} + \frac{\partial \rho\langle v\rangle\langle w\rangle}{\partial z} = \langle Y\rangle - \frac{\partial\langle P\rangle}{\partial y} + \mu\left(\frac{\partial^2\langle v\rangle}{\partial x^2} + \frac{\partial^2\langle v\rangle}{\partial y^2} + \frac{\partial^2\langle v\rangle}{\partial z^2}\right) - \left(\frac{\partial \rho\langle v'u'\rangle}{\partial x} + \frac{\partial \rho\langle v'v'\rangle}{\partial y} + \frac{\partial \rho\langle v'w'\rangle}{\partial z}\right) \tag{4.34}$$

and

$$\frac{\partial \rho\langle w\rangle}{\partial t} + \frac{\partial \rho\langle w\rangle\langle u\rangle}{\partial x} + \frac{\partial \rho\langle w\rangle\langle v\rangle}{\partial y} + \frac{\partial \rho\langle w\rangle\langle w\rangle}{\partial z} = \langle Z\rangle - \frac{\partial\langle P\rangle}{\partial z} + \mu\left(\frac{\partial^2\langle w\rangle}{\partial x^2} + \frac{\partial^2\langle w\rangle}{\partial y^2} + \frac{\partial^2\langle w\rangle}{\partial z^2}\right) - \left(\frac{\partial \rho\langle w'u'\rangle}{\partial x} + \frac{\partial \rho\langle w'v'\rangle}{\partial y} + \frac{\partial \rho\langle w'w'\rangle}{\partial z}\right). \tag{4.35}$$

To close the equations in terms of mean velocity components, the fluctuating components, representing the Reynolds stresses, are expressed by the Boussinesq approxima-

tion as a function of the mean velocity gradients, such that

$$\begin{aligned}
-\rho\langle u'u'\rangle &= \eta\left(\frac{\partial\langle u\rangle}{\partial x}+\frac{\partial\langle u\rangle}{\partial x}\right)-\frac{2}{3}\rho k,\\
-\rho\langle v'v'\rangle &= \eta\left(\frac{\partial\langle v\rangle}{\partial y}+\frac{\partial\langle v\rangle}{\partial y}\right)-\frac{2}{3}\rho k,\\
-\rho\langle w'w'\rangle &= \eta\left(\frac{\partial\langle w\rangle}{\partial z}+\frac{\partial\langle w\rangle}{\partial z}\right)-\frac{2}{3}\rho k,\\
-\rho\langle u'v'\rangle &= \eta\left(\frac{\partial\langle u\rangle}{\partial y}+\frac{\partial\langle v\rangle}{\partial x}\right),\\
-\rho\langle u'w'\rangle &= \eta\left(\frac{\partial\langle u\rangle}{\partial z}+\frac{\partial\langle w\rangle}{\partial x}\right),\\
\text{and}\qquad -\rho\langle v'w'\rangle &= \eta\left(\frac{\partial\langle v\rangle}{\partial z}+\frac{\partial\langle w\rangle}{\partial y}\right),
\end{aligned} \tag{4.36}$$

where k represents the turbulent kinetic energy and η the eddy viscosity (Schlichting and Gersten, 1979). Section (4.3) provides further information on the calculation of value of the the eddy viscosity η. Due to the small spatial scale the Coriolis effects are neglected. When it is furthermore assumed that at the air-water interface the shear and normal stresses are zero, and that the effects of surface tension are negligible due to the small water level curvature, the body forces $\langle X\rangle$, $\langle Y\rangle$, and $\langle Z\rangle$ in Equations (4.33), (4.34), and (4.35) become

$$\begin{aligned}
\langle X\rangle &= 0,\\
\langle Y\rangle &= 0,\\
\text{and}\qquad \langle Z\rangle &= -\rho g.
\end{aligned} \tag{4.37}$$

The expressions containing the fluctuating velocity terms in Equations (4.33), (4.34), and (4.35) are replaced with the expressions for the Reynolds stresses given in Equation (4.36). Furthermore, throughout the main flow domain, the effect of the eddy viscosity (η) is assumed to be much larger than that of the molecular viscosity (μ) and hence the terms preceded by (μ) can be neglected. This gives the three-dimensional momentum equations for incompressible flow in terms of mean velocity components as follows,

$$\begin{aligned}&\frac{\partial\rho\langle u\rangle}{\partial t}+\frac{\partial\rho\langle u\rangle\langle u\rangle}{\partial x}+\frac{\partial\rho\langle u\rangle\langle v\rangle}{\partial y}+\frac{\partial\rho\langle u\rangle\langle w\rangle}{\partial z}=\\&-\frac{\partial\langle P\rangle}{\partial x}+\frac{\partial}{\partial x}\left[2\eta\left(\frac{\partial\langle u\rangle}{\partial x}\right)-\frac{2}{3}\rho k\right]\\&+\frac{\partial}{\partial y}\left[\eta\left(\frac{\partial\langle u\rangle}{\partial y}+\frac{\partial\langle v\rangle}{\partial x}\right)\right]+\frac{\partial}{\partial z}\left[\eta\left(\frac{\partial\langle u\rangle}{\partial z}+\frac{\partial\langle w\rangle}{\partial x}\right)\right],\end{aligned}\tag{4.38}$$

$$\begin{aligned}&\frac{\partial\rho\langle v\rangle}{\partial t}+\frac{\partial\rho\langle v\rangle\langle u\rangle}{\partial x}+\frac{\partial\rho\langle v\rangle\langle v\rangle}{\partial y}+\frac{\partial\rho\langle v\rangle\langle w\rangle}{\partial z}=\\&-\frac{\partial\langle P\rangle}{\partial y}+\frac{\partial}{\partial x}\left[\eta\left(\frac{\partial\langle u\rangle}{\partial y}+\frac{\partial\langle v\rangle}{\partial x}\right)\right]\\&+\frac{\partial}{\partial y}\langle 2\eta\left(\frac{\partial\langle v\rangle}{\partial y}\right)-\frac{2}{3}\rho k+\frac{\partial}{\partial z}\left[\eta\left(\frac{\partial\langle v\rangle}{\partial z}+\frac{\partial\langle w\rangle}{\partial y}\right)\right],\end{aligned}\tag{4.39}$$

and

$$\begin{aligned}&\frac{\partial\rho\langle w\rangle}{\partial t}+\frac{\partial\rho\langle w\rangle\langle u\rangle}{\partial x}+\frac{\partial\rho\langle w\rangle\langle v\rangle}{\partial y}+\frac{\partial\rho\langle w\rangle\langle w\rangle}{\partial z}=-\rho g\\&-\frac{\partial\langle P\rangle}{\partial z}+\frac{\partial}{\partial x}\left[\eta\left(\frac{\partial\langle u\rangle}{\partial z}+\frac{\partial\langle w\rangle}{\partial x}\right)\right]\\&+\frac{\partial}{\partial y}\left[\eta\left(\frac{\partial\langle w\rangle}{\partial y}+\frac{\partial\langle v\rangle}{\partial z}\right)\right]+\frac{\partial}{\partial z}\left[2\eta\left(\frac{\partial\langle w\rangle}{\partial z}\right)-\frac{2}{3}\rho k\right].\end{aligned}\tag{4.40}$$

Equations (4.38-4.40) are now integrated over the breadth. The boundary conditions used for integration are given by Equation (4.5) and are summarised as $u|_{y_1}=u|_{y_2}=w|_{y_1}=w|_{y_2}=0$. Integrating Equation (4.38) over the breadth and applying the Leibniz

rule together with the boundary conditions gives for the left hand side:

$$\frac{\partial}{\partial t}\int_{y_1}^{y_2}\rho\langle u\rangle dy+\frac{\partial}{\partial x}\int_{y_1}^{y_2}\left(\rho\langle u\rangle\langle u\rangle\right)dy+\rho\langle u\rangle\langle v\rangle|_{y_2}-\rho\langle u\rangle\langle v\rangle|_{y_1}+\frac{\partial}{\partial z}\int_{y_1}^{y_2}\left(\rho\langle u\rangle\langle w\rangle\right)dy=$$
$$-\int_{y_1}^{y_2}\frac{\partial\langle P\rangle}{\partial x}dy+\int_{y_1}^{y_2}\frac{\partial}{\partial x}\left[2\eta\left(\frac{\partial\langle u\rangle}{\partial x}\right)-\frac{2}{3}\rho k\right]dy$$
$$+\int_{y_1}^{y_2}\frac{\partial}{\partial y}\left[\eta\left(\frac{\partial\langle u\rangle}{\partial y}+\frac{\partial\langle v\rangle}{\partial x}\right)\right]dy+\int_{y_1}^{y_2}\frac{\partial}{\partial z}\left[\eta\left(\frac{\partial\langle u\rangle}{\partial z}+\frac{\partial\langle w\rangle}{\partial x}\right)\right]dy. \tag{4.41}$$

Denoting the breadth average as before by $\widetilde{.}$,

$$\begin{aligned}\widetilde{\rho\langle u\rangle}&=\frac{1}{b}\int_{y_1}^{y_2}\rho\langle u\rangle dy,\\ \widetilde{\langle u\rangle}&=\frac{1}{b}\int_{y_1}^{y_2}\langle u\rangle dy,\\ \widetilde{\langle v\rangle}&=\frac{1}{b}\int_{y_1}^{y_2}\langle v\rangle dy,\\ \text{and}\qquad\widetilde{\langle w\rangle}&=\frac{1}{b}\int_{y_1}^{y_2}\langle w\rangle dy.\end{aligned} \tag{4.42}$$

Hence:

$$\begin{aligned}&\frac{\partial\widetilde{\rho\langle u\rangle}b}{\partial t}+\frac{\partial\widetilde{\rho\langle u\rangle}\widetilde{\langle u\rangle}b}{\partial x}+\frac{\partial\widetilde{\rho\langle u\rangle}\widetilde{\langle w\rangle}b}{\partial z}=\\ &-\int_{y_1}^{y_2}\frac{\partial\langle P\rangle}{\partial x}dy+\int_{y_1}^{y_2}\frac{\partial}{\partial x}\left[2\eta\left(\frac{\partial\langle u\rangle}{\partial x}\right)-\frac{2}{3}\rho k\right]dy\\ &+\int_{y_1}^{y_2}\frac{\partial}{\partial y}\left[\eta\left(\frac{\partial\langle u\rangle}{\partial y}+\frac{\partial\langle v\rangle}{\partial x}\right)\right]dy+\int_{y_1}^{y_2}\frac{\partial}{\partial z}\left[\eta\left(\frac{\partial\langle u\rangle}{\partial z}+\frac{\partial\langle w\rangle}{\partial x}\right)\right]dy.\end{aligned} \tag{4.43}$$

The effective stresses originate from a velocity gradient and not a discharge gradient. Hence applying the Leibniz rule to the effective stress terms results in

$$\begin{aligned}\int_{y_1}^{y_2}\frac{\partial}{\partial x}\left[2\eta\left(\frac{\partial\langle u\rangle}{\partial x}\right)-\frac{2}{3}\rho k\right]dy&=\frac{\partial}{\partial x}\int_{y_1}^{y_2}\left[2\eta\left(\frac{\partial\langle u\rangle}{\partial x}\right)-\frac{2}{3}\rho k\right]dy-a_1+a_2\\ &=\frac{\partial}{\partial x}2b\eta\frac{\partial\widetilde{\langle u\rangle}}{\partial x}-\frac{2}{3}\frac{\partial\rho kb}{\partial x}-a_1+a_2.\end{aligned} \tag{4.44}$$

where a_1 and a_2 are defined by

$$a_1 = \left(2\eta\frac{\partial\langle u\rangle}{\partial x} - \frac{2}{3}\rho k\right)|_{y_2}\frac{\partial y_2}{\partial x}|_{y_2}, \tag{4.45}$$

$$\text{and} \qquad a_2 = \left(2\eta\frac{\partial\langle u\rangle}{\partial x} - \frac{2}{3}\rho k\right)|_{y_1}\frac{\partial y_1}{\partial x}|_{y_1}.$$

Applying the same procedure to the other effective stress terms gives

$$\int_{y_1}^{y_2}\frac{\partial}{\partial y}\left[\eta\left(\frac{\partial\langle u\rangle}{\partial y} + \frac{\partial\langle v\rangle}{\partial x}\right)\right]dy = a_3 - a_4, \tag{4.46}$$

where

$$a_3 = \eta\left(\frac{\partial\langle u\rangle}{\partial y} + \frac{\partial\langle v\rangle}{\partial x}\right)|_{y_2}, \tag{4.47}$$

$$a_4 = \eta\left(\frac{\partial\langle u\rangle}{\partial y} + \frac{\partial\langle v\rangle}{\partial x}\right)|_{y_1},$$

and

$$\begin{aligned}\int_{y_1}^{y_2}\frac{\partial}{\partial z}\left[\eta\left(\frac{\partial\langle u\rangle}{\partial z} + \frac{\partial\langle w\rangle}{\partial x}\right)\right]dy =& \frac{\partial}{\partial z}\int_{y_1}^{y_2}\left[\eta\left(\frac{\partial\langle u\rangle}{\partial z} + \frac{\partial\langle w\rangle}{\partial x}\right)\right]dy - a_5 + a_6 \\ =& \frac{\partial}{\partial z}\left[b\eta\left(\frac{\partial\widetilde{\langle u\rangle}}{\partial z} + \frac{\partial\widetilde{\langle w\rangle}}{\partial x}\right)\right] - a_5 + a_6\end{aligned} \tag{4.48}$$

where

$$a_5 = \eta\left(\frac{\partial\langle u\rangle}{\partial z} + \frac{\partial\langle w\rangle}{\partial x}\right)|_{y_2}\frac{\partial y_2}{\partial z}|_{y_2}, \tag{4.49}$$

$$\text{and} \qquad a_6 = \eta\left(\frac{\partial\langle u\rangle}{\partial z} + \frac{\partial\langle w\rangle}{\partial x}\right)|_{y_1}\frac{\partial y_1}{\partial z}|_{y_1}.$$

The breadth-integrated pressure gradient terms are derived noting the fact that a breadth gradient by itself may not initiate a flow, hence

$$\begin{aligned}\int_{y_1}^{y_2} \frac{\partial \langle P \rangle}{\partial x} dy &= b \widetilde{\frac{\partial \langle P \rangle}{\partial x}} \\ \int_{y_1}^{y_2} \frac{\partial \langle P \rangle}{\partial z} dy &= b \widetilde{\frac{\partial \langle P \rangle}{\partial z}}.\end{aligned} \tag{4.50}$$

The breadth-integrated Reynolds-averaged momentum equation in the $\hat{x}$-direction is then given by

$$\begin{aligned}&\widetilde{\frac{\partial \rho \langle u \rangle b}{\partial t}} + \widetilde{\frac{\partial \rho \langle u \rangle \langle u \rangle b}{\partial x}} + \widetilde{\frac{\partial \rho \langle u \rangle \langle w \rangle b}{\partial z}} = -b \widetilde{\frac{\partial \langle P \rangle}{\partial x}} \\ &+ \frac{\partial}{\partial x}\left(2b\eta \widetilde{\frac{\partial \langle u \rangle}{\partial x}}\right) - \frac{2}{3}\widetilde{\frac{\partial \rho k b}{\partial x}} - \left(2\eta \frac{\partial \langle u \rangle}{\partial x} - \frac{2}{3}\rho k\right)|_{y_2} \frac{\partial y_2}{\partial x}|_{y_2} + \left(2\eta \frac{\partial \langle u \rangle}{\partial x} - \frac{2}{3}\rho k b\right)|_{y_1} \frac{\partial y_1}{\partial x}|_{y_1} \\ &+ \eta\left(\frac{\partial \langle u \rangle}{\partial y} + \frac{\partial \langle v \rangle}{\partial x}\right)|_{y_2} - \eta\left(\frac{\partial \langle u \rangle}{\partial y} + \frac{\partial \langle v \rangle}{\partial x}\right)|_{y_1} \\ &+ \frac{\partial}{\partial z}\left[b\eta\left(\widetilde{\frac{\partial \langle u \rangle}{\partial z}} + \widetilde{\frac{\partial \langle w \rangle}{\partial x}}\right)\right] - \eta\left(\frac{\partial \langle u \rangle}{\partial z} + \frac{\partial \langle w \rangle}{\partial x}\right)|_{y_2} \frac{\partial y_2}{\partial z}|_{y_2} + \eta\left(\frac{\partial \langle u \rangle}{\partial z} + \frac{\partial \langle w \rangle}{\partial x}\right)|_{y_1} \frac{\partial y_1}{\partial z}|_{y_1}\end{aligned} \tag{4.51}$$

Applying the same procedure to the momentum equation in the $\hat{z}$-direction leads to

$$\begin{aligned}&\widetilde{\frac{\partial \rho \langle w \rangle b}{\partial t}} + \widetilde{\frac{\partial \rho \langle w \rangle \langle u \rangle b}{\partial x}} + \widetilde{\frac{\partial \rho \langle w \rangle \langle w \rangle b}{\partial z}} = -\rho g b - b \widetilde{\frac{\partial \langle P \rangle}{\partial z}} \\ &+ \frac{\partial}{\partial x}\left[b\eta\left(\widetilde{\frac{\partial \langle u \rangle}{\partial z}} + \widetilde{\frac{\partial \langle w \rangle}{\partial x}}\right)\right] - \eta\left(\frac{\partial \langle u \rangle}{\partial z} + \frac{\partial \langle w \rangle}{\partial x}\right)|_{y_2} \frac{\partial y_2}{\partial x}|_{y_2} + \eta\left(\frac{\partial \langle u \rangle}{\partial z} + \frac{\partial \langle w \rangle}{\partial x}\right)|_{y_1} \frac{\partial y_1}{\partial x}|_{y_1} \\ &+ \eta\left(\frac{\partial \langle w \rangle}{\partial y} + \frac{\partial \langle v \rangle}{\partial z}\right)|_{y_2} - \eta\left(\frac{\partial \langle w \rangle}{\partial y} + \frac{\partial \langle v \rangle}{\partial z}\right)|_{y_1} \\ &+ \frac{\partial}{\partial z}\left(2b\eta \widetilde{\frac{\partial \langle w \rangle}{\partial z}}\right) - \frac{2}{3}\widetilde{\frac{\partial \rho k b}{\partial z}} - \left(2\eta \frac{\partial \langle w \rangle}{\partial z} - \frac{2}{3}\rho k\right)|_{y_2} \frac{\partial y_2}{\partial z}|_{y_2} + \left(2\eta \frac{\partial \langle w \rangle}{\partial z} - \frac{2}{3}\rho k\right)|_{y_1} \frac{\partial y_1}{\partial z}|_{y_1}.\end{aligned} \tag{4.52}$$

For mathematical simplicity, it is assumed that the geometry and flow are symmetrical about the centre-line of the channel which allows the following simplifications

$$\left(2\eta\frac{\partial\langle u\rangle}{\partial x}-\frac{2}{3}\rho k\right)|_{y_2}\frac{\partial y_2}{\partial x}|_{y_2}=-\left(2\eta\frac{\partial\langle u\rangle}{\partial x}-\frac{2}{3}\rho k\right)|_{y_1}\frac{\partial y_1}{\partial x}|_{y_1},$$

$$\eta\left(\frac{\partial\langle u\rangle}{\partial z}+\frac{\partial\langle w\rangle}{\partial x}\right)|_{y_2}\frac{\partial y_2}{\partial z}|_{y_2}=-\eta\left(\frac{\partial\langle u\rangle}{\partial z}+\frac{\partial\langle w\rangle}{\partial x}\right)|_{y_1}\frac{\partial y_1}{\partial z}|_{y_1}, \tag{4.53}$$

$$\eta\left(\frac{\partial\langle u\rangle}{\partial z}+\frac{\partial\langle w\rangle}{\partial x}\right)|_{y_2}\frac{\partial y_2}{\partial x}|_{y_2}=-\eta\left(\frac{\partial\langle u\rangle}{\partial z}+\frac{\partial\langle w\rangle}{\partial x}\right)|_{y_1}\frac{\partial y_1}{\partial x}|_{y_1},$$

and $$\left(2\eta\frac{\partial\langle w\rangle}{\partial z}-\frac{2}{3}\rho k\right)|_{y_2}\frac{\partial y_2}{\partial z}|_{y_2}=-\left(2\eta\frac{\partial\langle w\rangle}{\partial z}-\frac{2}{3}\rho k\right)|_{y_1}\frac{\partial y_1}{\partial z}|_{y_1}.$$

The terms in Equation (4.47) denote the shear stresses at the wall. Replacing these with the original expression for the shear stress results in

$$\begin{aligned}
\tau_{yx_{y_2}} &= \eta\left(\frac{\partial\langle u\rangle}{\partial y}+\frac{\partial\langle v\rangle}{\partial x}\right)|_{y_2},\\
\tau_{yx_{y_1}} &= \eta\left(\frac{\partial\langle u\rangle}{\partial y}+\frac{\partial\langle v\rangle}{\partial x}\right)|_{y_1},\\
\tau_{yz_{y_2}} &= \eta\left(\frac{\partial\langle w\rangle}{\partial y}+\frac{\partial\langle v\rangle}{\partial z}\right)|_{y_2},\\
\text{and}\qquad \tau_{yz_{y_1}} &= \eta\left(\frac{\partial\langle w\rangle}{\partial y}+\frac{\partial\langle v\rangle}{\partial z}\right)|_{y_1},
\end{aligned} \tag{4.54}$$

which gives for the momentum equations in the $\hat{x}$, and $\hat{z}$-direction

$$\begin{aligned}
&\frac{\partial\widetilde{\rho\langle u\rangle}b}{\partial t}+\frac{\partial\widetilde{\rho\langle u\rangle}\widetilde{\langle u\rangle}b}{\partial x}+\frac{\partial\widetilde{\rho\langle u\rangle}\widetilde{\langle w\rangle}b}{\partial z}=-b\frac{\partial\widetilde{\langle P\rangle}}{\partial x}\\
&+\frac{\partial}{\partial x}\left(2b\eta\frac{\partial\widetilde{\langle u\rangle}}{\partial x}\right)-\frac{2}{3}\frac{\partial\widetilde{\rho k}b}{\partial x}+\tau_{yx_{y_1}}-\tau_{yx_{y_2}}+\frac{\partial}{\partial z}\left[b\eta\left(\frac{\partial\widetilde{\langle u\rangle}}{\partial z}+\frac{\partial\widetilde{\langle w\rangle}}{\partial x}\right)\right],
\end{aligned} \tag{4.55}$$

and

$$\frac{\partial\widetilde{\rho\langle w\rangle}b}{\partial t}+\frac{\partial\widetilde{\rho\langle w\rangle\langle u\rangle}b}{\partial x}+\frac{\partial\widetilde{\rho\langle w\rangle\langle w\rangle}b}{\partial z}=-\tilde{\rho}gb-b\frac{\partial\widetilde{\langle P\rangle}}{\partial z} \\ +\frac{\partial}{\partial x}\left[b\eta\left(\frac{\partial\widetilde{\langle u\rangle}}{\partial z}+\frac{\partial\widetilde{\langle w\rangle}}{\partial x}\right)\right]+\tau_{yz_{y_1}}-\tau_{yz_{y_2}}+\frac{\partial}{\partial z}\left(2b\eta\frac{\partial\widetilde{\langle w\rangle}}{\partial z}\right)-\frac{2}{3}\frac{\partial\widetilde{\rho k}b}{\partial z}. \tag{4.56}$$

It should be noted that because of symmetry, the velocity gradients in the shear stress terms in Equation (4.54) are of opposite sign. The shear stress terms should therefore be summed in both the $\hat{x}$ and $\hat{z}$-direction momentum equations. The sum of the shear stresses in $\hat{x}$ and $\hat{z}$-direction may be written as

$$\tau_{yx_{y1}}-\tau_{yx_{y2}}=-c_f\rho\widetilde{\langle u\rangle}|\widetilde{\langle\mathbf{u}\rangle}|, \tag{4.57}$$

and

$$\tau_{yz_{y1}}-\tau_{yz_{y2}}=-c_f\rho\widetilde{\langle w\rangle}|\widetilde{\langle\mathbf{u}\rangle}|, \tag{4.58}$$

where c_f is a drag coefficient, and the $(-)$sign on the right hand side follows logically from the negative effect of the shear stress on the flow velocity. Replacing the wall shear stresses with the expressions from Equations 4.57 and 4.58, the final breadth-integrated momentum equations become

$$\frac{\partial\widetilde{\rho\langle u\rangle}b}{\partial t}+\frac{\partial\widetilde{\rho\langle u\rangle\langle u\rangle}b}{\partial x}+\frac{\partial\widetilde{\rho\langle u\rangle\langle w\rangle}b}{\partial z}=-b\frac{\partial\widetilde{\langle P\rangle}}{\partial x} \\ +\frac{\partial}{\partial x}\left(2b\eta\frac{\partial\widetilde{\langle u\rangle}}{\partial x}\right)-\frac{2}{3}\frac{\partial\widetilde{\rho k}b}{\partial x}-c_f\rho\widetilde{\langle u\rangle}|\widetilde{\langle\mathbf{u}\rangle}|+\frac{\partial}{\partial z}\left[b\eta\left(\frac{\partial\widetilde{\langle u\rangle}}{\partial z}+\frac{\partial\widetilde{\langle w\rangle}}{\partial x}\right)\right], \tag{4.59}$$

and

$$\frac{\partial\widetilde{\rho\langle w\rangle}b}{\partial t}+\frac{\partial\widetilde{\rho\langle w\rangle\langle u\rangle}b}{\partial x}+\frac{\partial\widetilde{\rho\langle w\rangle\langle w\rangle}b}{\partial z}=-\tilde{\rho}gb-b\frac{\partial\widetilde{\langle P\rangle}}{\partial z} \\ +\frac{\partial}{\partial x}\left[b\eta\left(\frac{\partial\widetilde{\langle u\rangle}}{\partial z}+\frac{\partial\widetilde{\langle w\rangle}}{\partial x}\right)\right]-c_f\rho\widetilde{\langle w\rangle}|\widetilde{\langle\mathbf{u}\rangle}|+\frac{\partial}{\partial z}\left(2b\eta\frac{\partial\widetilde{\langle w\rangle}}{\partial z}\right)-\frac{2}{3}\frac{\partial\widetilde{\rho k}b}{\partial z}. \tag{4.60}$$

To solve these equations, expressions for η, $\tilde{k}$, b, and $\widetilde{\langle P \rangle}$ are required. The formulation of these expressions is discussed in Sections 4.3 and 4.4.

4.3 Eddy viscosity and turbulent energy

An eddy viscosity is applied in the momentum equations to account for turbulence effects and to prevent unrealistic high flow velocities in the case of flows down a slope. The eddy viscosity is dependent on the required accuracy with which the turbulent motions need to be predicted, and so can be calculated with increasing accuracy ranging from assuming a constant eddy viscosity to using a multiple equation full eddy viscosity model. Constant values for the eddy viscosity are used for model testing. A typical value is approximately 10Pa-s . A parabolic description of the eddy viscosity leads to a small improvement in the accuracy with which the eddy viscosity is predicted. The parabolic description is effective in calculating the horizontal momentum exchange but gives unrealistic values for the vertical momentum exchange (Van Rijn, 1984). Further improvement in accuracy is obtained with a zero-equation model in which the Reynolds stresses are given by

$$\rho \langle u'w' \rangle = \rho \epsilon \frac{\partial u_\varepsilon}{\partial \zeta}, \tag{4.61}$$

where u_ε is the velocity component parallel to the landside embankment slope, ζ is the coordinate in the $\hat{\zeta}$- coordinate direction perpendicular to the landside slope into the embankment, and ϵ is the kinematic eddy viscosity. Zero-equation models are based on the assumption that the kinematic eddy viscosity (ϵ) is of the same order as the fluctuating velocities of the eddies. For a shear flow this results in the relationship

$$\epsilon = -l_{mix}^2 \frac{\partial u_\varepsilon}{\partial \zeta}, \tag{4.62}$$

where l_{mix} is some characteristic mixing-length scale. For a sufficiently high flow velocity over the embankment crest, the flow separates at the end of the crest and reattaches again on the landside slope. Where the flow reattaches with the embankment slope, the

velocity gradient close to the bed is $\partial u_\varepsilon/\partial\zeta = 0$. Hence at the point of reattachment a zero-equation model gives $\nu = 0$, and the theory fails. For a more accurate prediction of the eddy viscosity, without making the breach model computationally much more expensive, the Spalart–Allmaras one-equation model is recommended which gives reasonably accurate predictions for a wide range of flow problems (Deck et al., 2002). The Spalart–Allmaras model is based on empirical observations and dimensional analysis, and requires a numerical solution of the transport equation (Deck et al., 2002)

$$\frac{\partial\hat{\nu}}{\partial t} + u\frac{\partial\hat{\nu}}{\partial x} + v\frac{\partial\hat{\nu}}{\partial y} + w\frac{\partial\hat{\nu}}{\partial z} = \tag{4.63}$$

$$c_{b1}\hat{S}\hat{\nu} + \frac{1}{\sigma}\left\{\frac{\partial}{\partial x}\left[(\nu+\hat{\nu})\frac{\partial\hat{\nu}}{\partial x}\right] + c_{b2}\frac{\partial\hat{\nu}}{\partial x}\frac{\partial\hat{\nu}}{\partial x}\right\}$$
$$+\frac{1}{\sigma}\left\{\frac{\partial}{\partial y}\left[(\nu+\hat{\nu})\frac{\partial\hat{\nu}}{\partial y}\right] + c_{b2}\frac{\partial\hat{\nu}}{\partial y}\frac{\partial\hat{\nu}}{\partial y}\right\} + \frac{1}{\sigma}\left\{\frac{\partial}{\partial z}\left[(\nu+\hat{\nu})\frac{\partial\hat{\nu}}{\partial z}\right] + c_{b2}\frac{\partial\hat{\nu}}{\partial z}\frac{\partial\hat{\nu}}{\partial z}\right\}$$
$$-c_{w1}f_w\left(\frac{\hat{\nu}}{d}\right)^2, \tag{4.64}$$

where $\hat{\nu}$ is the preserved Spalart–Allmaras quantity in m^2/s. The first term on the right hand side denotes the production term, whose magnitude depends on the vorticity of the flow. The terms starting with $1/\sigma$ denote the diffusion of the Spalart–Allmaras variable, and the last term is a sink term of the Spalart–Allmaras quantity and denotes the destruction of kinetic energy (Deck et al., 2002). Spalart and Allmaras also defined a damping function to ensure that $\hat{\nu}$ equals $\kappa h u_*$ in the log boundary layer, where κ is the Von Kármán constant, h is the height above the bed in the negative $\hat{\zeta}$-coordinate direction, and u_* is the shear velocity (Deck et al., 2002),and (Van Rijn, 1993). The damping function f_{v1} is

$$f_{v1} = \frac{\chi^3}{\chi^3 + c_{\nu1}^3}, \tag{4.65}$$

with

$$\chi = \frac{\hat{\nu}}{\nu} \tag{4.66}$$

The vorticity magnitude of $\hat{S}$ is defined such that it maintains its log-layer behaviour (Deck et al., 2002), and is given by

$$\hat{S} = \sqrt{2\Omega_{ij}\Omega_{ij}} f_{\nu 3} + \frac{\hat{\nu}}{\kappa^2 d_{fs}^2} f_{\nu 2}, \tag{4.67}$$

where d_{fs} is the distance to the free surface,

$$f_{v_2} = \left(1 + \frac{\chi}{c_{\nu 2}}\right)^{-3}, \tag{4.68}$$

$$f_{v_3} = \frac{(1 + \chi f_{\nu_1})(1 - f_{\nu 2})}{\chi}, \tag{4.69}$$

and $\sqrt{2\Omega_{ij}\Omega_{ij}}$ denotes the magnitude of the vorticity of the flow, where

$$\Omega_{ij} = \frac{1}{2}\left(\frac{\partial u}{\partial y} - \frac{\partial v}{\partial x} + \frac{\partial u}{\partial z} - \frac{\partial w}{\partial x} + \frac{\partial v}{\partial z} - \frac{\partial w}{\partial y}\right). \tag{4.70}$$

Spalart and Allmaras proposed the following model constants (Deck et al., 2002): $c_{b1} = 0.1355$, $c_{b2} = 0.622$, $\sigma = 2/3$, $\kappa = 0.41$, $c_{w1} = \frac{c_{b1}}{\kappa^2} + \frac{1+c_{b2}}{\sigma}$, $c_{w2} = 0.3$, $c_{w3} = 2$, $c_{\nu 1} = 7.1$, and $c_{\nu 2} = 5$. So far the analysis has been for smooth beds for which the boundary conditions are given by $\hat{\nu} = 0$. To mimic the roughness effects of the wall, the Dirichlet boundary condition needs to be replaced by the Von Neumann boundary condition (Aupoix and Spalart, 2003)

$$\frac{\partial \hat{\nu}}{\partial \zeta} = -\frac{\hat{\nu}}{d}, \tag{4.71}$$

where the negative $\hat{\zeta}$-direction is perpendicular to the embankment surface upwards. In Cartesian coordinates this becomes

$$\frac{\partial \hat{\nu}}{\partial x} = \sin\alpha \frac{\hat{\nu}}{d} \tag{4.72}$$

$$\frac{\partial \hat{\nu}}{\partial z} = -\cos\alpha \frac{\hat{\nu}}{d}$$

where d is the depth in the direction normal to the bed, and α is the angle between the $\hat{\zeta}$-coordinate direction and the Cartesian $\hat{z}$-coordinate direction (See Figure 2.1). To account for roughness, the depth d is increased. Aupoix and Spalart (2003) imposed an offset on d given by

$$d = d_{\min} + d_0, \tag{4.73}$$

where $d_{\min}$ is the depth, and d_0 is a function of the Nikuradse roughness coefficient k_s. For rough surfaces, Aupoix and Spalart (2003) and Van Rijn (1993) give

$$d_0 = 0.03k_s, \tag{4.74}$$

where k_s is the Nikuradse roughness coefficient. To predict the eddy viscosity correctly in the case of smaller roughnesses Equation (4.66) becomes (Aupoix and Spalart, 2003).

$$\chi = \frac{\hat{\nu}}{\nu} + c_{R1}\frac{k_s}{d}, \tag{4.75}$$

with $c_{R1} = 0.5$.

For mathematical consistency with respect to breadth-integrating the quadratic gradient terms in Equation (4.63), the boundary conditions for Equation (4.63) are given by $\hat{\nu}|_{y_1} = \hat{\nu}|_{y_2} = \widetilde{\hat{\nu}}$ at the side walls. For small time steps, the sideways erosion rate v becomes negligible and hence the boundary conditions for the velocity components have been assumed to be 0 at the walls, or $\mathbf{u_{y_1}} = \mathbf{u_{y_2}} = 0$. Integrating the Spalart–Allmaras equation over the breadth gives for the local and advective terms

$$b\frac{\partial\tilde{\hat{\nu}}}{\partial t} + \frac{\partial\widetilde{\langle u\rangle}\tilde{\hat{\nu}}b}{\partial x} + \frac{\partial\widetilde{\langle w\rangle}\tilde{\hat{\nu}}b}{\partial z}. \tag{4.76}$$

Assuming that $\hat{\nu}$ is constant over the breadth, the breadth integrated production term is determined from integrating $\hat{S}$ over y, and is given by

$$c_{b1}\widetilde{\hat{S}\hat{\nu}} \tag{4.77}$$

where

$$\tilde{\hat{S}} = f_{\nu 3}\sqrt{2\widetilde{\Omega_{ij}}\widetilde{\Omega_{ij}}} + \frac{\tilde{\hat{\nu}}b}{\kappa^2 d^2} f_{\nu 2}, \tag{4.78}$$

with $\widetilde{\Omega_{ij}}$ denoting the breadth-integrated vorticity terms, and $f_{\nu 2}$ given by

$$f_{\nu 2} = \left(1 + \frac{\chi}{c_{\nu 2}}\right)^{-3}, \tag{4.79}$$

with $c_{\nu 2} = 5$ (Deck et al., 2002). The vorticity is caused by a gradient in velocity and not a gradient in discharge. With $\int_{y_1}^{y_2} v dy = 0$, the breadth-integrated vorticity terms are

$$\widetilde{\Omega_{ij}} = \frac{1}{2}\left(b\frac{\partial\widetilde{\langle u\rangle}}{\partial z} - b\frac{\partial\widetilde{\langle w\rangle}}{\partial x}\right). \tag{4.80}$$

Finally,

$$f_{\nu 3} = \frac{(1 + \chi f_{\nu 1})(1 - f_{\nu 2})}{\chi}, \tag{4.81}$$

with χ given by

$$\chi = \frac{\tilde{\hat{\nu}}}{\nu}. \tag{4.82}$$

Integrating the diffusive terms of the Spalart–Allmaras equation (see Equation 4.63) gives

$$\frac{b}{\sigma}\left\{\frac{\partial}{\partial x}\left[\left(\nu + \tilde{\hat{\nu}}\right)\frac{\partial\tilde{\hat{\nu}}}{\partial x}\right] + c_{b2}\widetilde{\frac{\partial\hat{\nu}}{\partial x}\frac{\partial\hat{\nu}}{\partial x}}\right\} + \frac{b}{\sigma}\left\{\frac{\partial}{\partial z}\left[\left(\nu + \tilde{\hat{\nu}}\right)\frac{\partial\tilde{\hat{\nu}}}{\partial z}\right] + c_{b2}b\widetilde{\frac{\partial\hat{\nu}}{\partial z}\frac{\partial\hat{\nu}}{\partial z}}\right\}. \tag{4.83}$$

Breadth-integration of the dissipation term leads to

$$-c_{w1}bf_w\widetilde{\left(\frac{\hat{\nu}}{d}\right)^2}, \tag{4.84}$$

where

$$f_w = \gamma\left(\frac{1 + c_{w3}^6}{g^6 + c_{w3}^6}\right)^{1/6}, \tag{4.85}$$

in which

$$\gamma = r + c_{w2}\left(r^6 - r\right), \tag{4.86}$$

where

$$r = \frac{\tilde{\hat{\nu}} b}{\tilde{\hat{S}} \kappa^2 d^2}. \tag{4.87}$$

Here κ denotes the Von Kármán constant with a value of 0.41 (Van Rijn, 1993), and d is the local depth. Hence for a constant molecular kinematic viscosity ν the breadth-integrated equation for the conserved Spalart–Allmaras quantity $\tilde{\hat{\nu}}$ is given by

$$\begin{aligned} b\frac{\partial \tilde{\hat{\nu}}}{\partial t} + \frac{\partial \widetilde{\langle u \rangle} \tilde{\hat{\nu}} b}{\partial x} + \frac{\partial \widetilde{\langle w \rangle} \tilde{\hat{\nu}} b}{\partial z} &= c_{b1} \widetilde{\hat{S}\hat{\nu}} - c_{w1} b f_w \widetilde{\left(\frac{\hat{\nu}}{d}\right)^2} \\ + \frac{b}{\sigma}\left[\left(\nu + \tilde{\hat{\nu}}\right)\frac{\partial^2 \tilde{\hat{\nu}}}{\partial x^2} + (1 + c_{b2})\widetilde{\frac{\partial \hat{\nu}}{\partial x}\frac{\partial \hat{\nu}}{\partial x}}\right] &+ \frac{b}{\sigma}\left[\left(\nu + \tilde{\hat{\nu}}\right)\frac{\partial^2 \tilde{\hat{\nu}}}{\partial z^2} + (1 + c_{b2})\widetilde{\frac{\partial \hat{\nu}}{\partial z}\frac{\partial \hat{\nu}}{\partial z}}\right]. \end{aligned} \tag{4.88}$$

After solving the breadth-integrated Spalart–Allmaras equation, the eddy viscosity η is found by

$$\eta = \tilde{\rho} \tilde{\hat{\nu}} f_{\nu 1}. \tag{4.89}$$

Although the Spalart–Allmaras equation gives a value for the eddy viscosity, the value of the kinetic energy term k in Equations (4.59) and (4.60) still needs to be determined. To estimate k without having to solve an additional differential equation the following relationship between the kinetic energy and the eddy viscosity was used, as given by Prandtl (Schlichting and Gersten, 1979)

$$\eta = \rho k^{\frac{1}{2}} l_{mix} \tag{4.90}$$

where k denotes the kinetic energy. The turbulent length scale l_{mix} is approximated with the Prandtl mixing-length L, for $L \neq 0$, such that

$$L = \kappa \left| \frac{\partial \widetilde{\langle u \rangle}_{\varepsilon}}{\partial \zeta} \Big/ \frac{\partial^2 \widetilde{\langle u \rangle}_{\varepsilon}}{\partial \zeta^2} \right|, \tag{4.91}$$

where (ε, ζ) is the 2D coordinate system with ζ perpendicular to the wall. Hence for more complicated geometries, the calculation of the mixing-length becomes cumbersome. Prandtl assumed that $\eta \sim \widetilde{\langle u \rangle}_i L$, where $\widetilde{\langle u \rangle}$ is here a turbulent velocity scale,

and L a mixing-length. Prandtl furthermore postulated that

$$\widetilde{\langle u \rangle}_i \sim L \left| \frac{\partial \widetilde{\langle u \rangle}_i}{\partial x_j} \right|, \tag{4.92}$$

leading to the mixing-length model given by (CHAM Limited, 2013)

$$\eta = \rho L^2 \left[\frac{\partial \widetilde{\langle u \rangle}_i}{\partial x_j} \left(\frac{\partial \widetilde{\langle u \rangle}_i}{\partial x_j} + \frac{\partial \widetilde{\langle u \rangle}_j}{\partial x_i} \right) \right]. \tag{4.93}$$

The breath-integrated form of Equation (4.93) is

$$\eta = \rho L^2 \left[2 \left(\frac{\partial \widetilde{\langle u \rangle}}{\partial x} \right)^2 + 2 \left(\frac{\partial \widetilde{\langle w \rangle}}{\partial z} \right)^2 + \left(\frac{\partial \widetilde{\langle u \rangle}}{\partial z} + \frac{\partial \widetilde{\langle w \rangle}}{\partial x} \right)^2 \right]^{\frac{1}{2}}, \tag{4.94}$$

from which follows that

$$L = \left\{ \frac{\tilde{\tilde{\nu}} f_{\nu 1}}{\left[2 \left(\frac{\partial \widetilde{\langle u \rangle}}{\partial x} \right)^2 + 2 \left(\frac{\partial \widetilde{\langle w \rangle}}{\partial z} \right)^2 + \left(\frac{\partial \widetilde{\langle u \rangle}}{\partial z} + \frac{\partial \widetilde{\langle w \rangle}}{\partial x} \right)^2 \right]^{\frac{1}{2}}} \right\}^{\frac{1}{2}}, \tag{4.95}$$

where $\tilde{\tilde{\nu}}$ and $f_{\nu 1}$ are obtained from the Spalart–Allmaras model. Using the eddy viscosity from the Spalart–Allmaras model in combination with the Prandtl mixing-length relationship for η leads to a value for the mixing-length which can also be applied in more complicated flow geometries. The breadth-averaged kinetic energy $\widetilde{k}$ follows from

$$\widetilde{k} = \tilde{\tilde{\nu}} f_{\nu 1} \left[2 \left(\frac{\partial \widetilde{\langle u \rangle}}{\partial x} \right)^2 + 2 \left(\frac{\partial \widetilde{\langle w \rangle}}{\partial z} \right)^2 + \left(\frac{\partial \widetilde{\langle u \rangle}}{\partial z} + \frac{\partial \widetilde{\langle w \rangle}}{\partial x} \right)^2 \right]^{\frac{1}{2}}, \tag{4.96}$$

hence no additional differential equation for k needs to be solved.

4.4 Pressure equation

The advantage of modelling the flow using a non-depth-averaged model is that the non-hydrostatic pressure distribution is used to calculate accurately the flow field when vertical accelerations occur. The expression for the pressure is derived from taking the divergence of the momentum equations. The breadth-integrated Reynolds-averaged momentum equations are given by

$$\begin{aligned}&\frac{\partial\widetilde{\rho\langle u\rangle}b}{\partial t}+\frac{\partial\widetilde{\rho\langle u\rangle}\widetilde{\langle u\rangle}b}{\partial x}+\frac{\partial\widetilde{\rho\langle u\rangle}\widetilde{\langle w\rangle}b}{\partial z}=-b\frac{\partial\widetilde{\langle P\rangle}}{\partial x}\\&+\frac{\partial}{\partial x}\left(2b\eta\frac{\partial\widetilde{\langle u\rangle}}{\partial x}\right)-\frac{2}{3}\frac{\partial\widetilde{\rho k}b}{\partial x}-c_f\rho\widetilde{\langle u\rangle}|\widetilde{\langle\mathbf{u}\rangle}|+\frac{\partial}{\partial z}\left[b\eta\left(\frac{\partial\widetilde{\langle u\rangle}}{\partial z}+\frac{\partial\widetilde{\langle w\rangle}}{\partial x}\right)\right],\end{aligned}\tag{4.97}$$

and

$$\begin{aligned}&\frac{\partial\widetilde{\rho\langle w\rangle}b}{\partial t}+\frac{\partial\widetilde{\rho\langle w\rangle}\widetilde{\langle u\rangle}b}{\partial x}+\frac{\partial\widetilde{\rho\langle w\rangle}\widetilde{\langle w\rangle}b}{\partial z}=-\tilde{\rho}gb-b\frac{\partial\widetilde{\langle P\rangle}}{\partial z}\\&+\frac{\partial}{\partial x}\left[b\eta\left(\frac{\partial\widetilde{\langle u\rangle}}{\partial z}+\frac{\partial\widetilde{\langle w\rangle}}{\partial x}\right)\right]-c_f\rho\widetilde{\langle w\rangle}|\widetilde{\langle\mathbf{u}\rangle}|+\frac{\partial}{\partial z}\left(2b\eta\frac{\partial\widetilde{\langle w\rangle}}{\partial z}\right)-\frac{2}{3}\frac{\partial\widetilde{\rho k}b}{\partial z}.\end{aligned}\tag{4.98}$$

Due to the assumed negligibly small flow accelerations in the $\hat{y}$-direction, any pressure gradient in the $\hat{y}$-direction is neglected. The divergence of the momentum equations in

the $\hat{x}$ and $\hat{z}$ direction gives

$$\begin{aligned}
&-b\frac{\partial^2\widetilde{\langle P\rangle}}{\partial x^2} - b\frac{\partial^2\widetilde{\langle P\rangle}}{\partial z^2} = \\
&\frac{\partial}{\partial x}\left(\frac{\partial\widetilde{\rho\langle u\rangle}b}{\partial t} + \frac{\partial\widetilde{\rho\langle u\rangle}\widetilde{\langle u\rangle}b}{\partial x} + \frac{\partial\widetilde{\rho\langle u\rangle}\widetilde{\langle w\rangle}b}{\partial z}\right) \\
&+\frac{\partial}{\partial z}\left(\frac{\partial\widetilde{\rho\langle w\rangle}b}{\partial t} + \frac{\partial\widetilde{\rho\langle w\rangle}\widetilde{\langle u\rangle}b}{\partial x} + \frac{\partial\widetilde{\rho\langle w\rangle}\widetilde{\langle w\rangle}b}{\partial z}\right) \\
&-\frac{\partial}{\partial x}\left(\frac{\partial}{\partial x}\left(2b\eta\frac{\partial\widetilde{\langle u\rangle}}{\partial x}\right) - \frac{2}{3}\frac{\partial\widetilde{\rho k}b}{\partial x} + c_f\rho\widetilde{\langle u\rangle}|\widetilde{\langle \mathbf{u}\rangle}|\right) \\
&-\frac{\partial}{\partial z}\left(\frac{\partial}{\partial z}\left(2b\eta\frac{\partial\widetilde{\langle w\rangle}}{\partial z}\right) - \frac{2}{3}\frac{\partial\widetilde{\rho k}b}{\partial z} + c_f\rho\widetilde{\langle w\rangle}|\widetilde{\langle \mathbf{u}\rangle}|\right) \\
&-\frac{\partial}{\partial x}\left\{\frac{\partial}{\partial z}\left[b\eta\left(\frac{\partial\widetilde{\langle u\rangle}}{\partial z} + \frac{\partial\widetilde{\langle w\rangle}}{\partial x}\right)\right]\right\} \\
&-\frac{\partial}{\partial z}\left\{\frac{\partial}{\partial x}\left[b\eta\left(\frac{\partial\widetilde{\langle u\rangle}}{\partial z} + \frac{\partial\widetilde{\langle w\rangle}}{\partial x}\right)\right]\right\} + b\frac{\partial\rho g}{\partial z}
\end{aligned} \tag{4.99}$$

The breadth term is placed outside the divergence operator when taking the divergence of the breadth multiplied with the pressure gradient terms, given in Equations 4.97 and 4.98. Proof of this follows from integrating the divergence of the pressure gradient terms in three dimensions, as

$$\begin{aligned}
&\int_{y_1}^{y_2}\left(\frac{\partial^2\langle P\rangle}{\partial x^2} + \frac{\partial^2\langle P\rangle}{\partial y^2} + \frac{\partial^2\langle P\rangle}{\partial z^2}\right)dy \\
=&\frac{\partial}{\partial x}\left(\frac{\partial}{\partial x}\int_{y_1}^{y_2}\langle P\rangle dy - \langle P\rangle|_{y_2}\frac{\partial y_2}{\partial x} + \langle P\rangle|_{y_1}\frac{\partial y_1}{\partial x}\right) \\
&-\frac{\partial\langle P\rangle}{\partial x}|_{y_2}\frac{\partial y_2}{\partial x}|_{y_2} + \frac{\partial\langle P\rangle}{\partial x}|_{y_1}\frac{\partial y_1}{\partial x}|_{y_1} \\
&+\frac{\partial}{\partial z}\left(\frac{\partial}{\partial z}\int_{y_1}^{y_2}\langle P\rangle dy - \langle P\rangle|_{y_1}\frac{\partial y_2}{\partial z} + \langle P\rangle|_{y_1}\frac{\partial\langle P\rangle}{\partial z}\right) \\
&-\frac{\partial\langle P\rangle}{\partial z}|_{y_2}\frac{\partial y_2}{\partial z}|_{y_2} + \frac{\partial\langle P\rangle}{\partial z}|_{y_1}\frac{\partial y_1}{\partial z}|_{y_1}.
\end{aligned} \tag{4.100}$$

With the pressure boundary conditions given by

$$\begin{aligned} \langle P\rangle_{y_1} &= \langle P\rangle_{y_2} = \widetilde{\langle P\rangle}, \\ -\langle P\rangle|_{y_2}\frac{\partial y_2}{\partial x} + \langle P\rangle|_{y_1}\frac{\partial y_1}{\partial x} &= -\widetilde{\langle P\rangle}\frac{\partial b}{\partial x}, \\ \text{and} \qquad -\langle P\rangle|_{y_2}\frac{\partial y_2}{\partial z} + \langle P\rangle|_{y_1}\frac{\partial y_1}{\partial z} &= -\widetilde{\langle P\rangle}\frac{\partial b}{\partial z}, \end{aligned} \tag{4.101}$$

the integral on the left hand side of the = sign in Equation 4.100 becomes

$$\begin{aligned} &\int_{y_1}^{y_2}\left(\frac{\partial^2\langle P\rangle}{\partial x^2} + \frac{\partial^2\langle P\rangle}{\partial y^2} + \frac{\partial^2\langle P\rangle}{\partial z^2}\right)dy \\ =&\frac{\partial}{\partial x}\left(b\frac{\partial\langle P\rangle}{\partial x}\right) - \frac{\partial\langle P\rangle}{\partial x}\frac{\partial b}{\partial x} \\ +&\frac{\partial}{\partial z}\left(b\frac{\partial\langle P\rangle}{\partial z}\right) - \frac{\partial\langle P\rangle}{\partial z}\frac{\partial b}{\partial z}. \\ =&b\frac{\partial^2\widetilde{\langle P\rangle}}{\partial x^2} + b\frac{\partial^2\widetilde{\langle P\rangle}}{\partial z^2}. \end{aligned} \tag{4.102}$$

The divergence of the advective terms in the momentum equations are rewritten as

$$\begin{aligned} &\frac{\partial}{\partial t}\left(\frac{\partial\widetilde{\rho\langle u\rangle}b}{\partial x} + \frac{\partial\widetilde{\rho\langle w\rangle}b}{\partial z}\right) + \frac{\partial}{\partial x}\left[\widetilde{\langle u\rangle}\left(\frac{\partial\widetilde{\rho\langle u\rangle}b}{\partial x} + \frac{\partial\widetilde{\rho\langle w\rangle}b}{\partial z}\right) + \widetilde{\rho\langle u\rangle}b\frac{\partial\widetilde{\langle u\rangle}}{\partial x} + \widetilde{\rho\langle w\rangle}b\frac{\partial\widetilde{\langle u\rangle}}{\partial z}\right] \\ &+\frac{\partial}{\partial z}\left[\widetilde{\langle w\rangle}\left(\frac{\partial\widetilde{\rho\langle u\rangle}b}{\partial x} + \frac{\partial\widetilde{\rho\langle w\rangle}b}{\partial z}\right) + \widetilde{\rho\langle u\rangle}b\frac{\partial\widetilde{\langle w\rangle}}{\partial x} + \widetilde{\rho\langle w\rangle}b\frac{\partial\widetilde{\langle w\rangle}}{\partial z}\right]. \end{aligned} \tag{4.103}$$

For an incompressible divergence free flow field

$$\left(\frac{\partial\widetilde{\rho\langle u\rangle}b}{\partial x} + \frac{\partial\widetilde{\rho\langle w\rangle}b}{\partial z}\right) = 0, \tag{4.104}$$

leaving

$$\frac{\partial}{\partial x}\left(\widetilde{\rho\langle u\rangle}b\frac{\partial\widetilde{\langle u\rangle}}{\partial x} + \widetilde{\rho\langle w\rangle}b\frac{\partial\widetilde{\langle u\rangle}}{\partial z}\right) + \frac{\partial}{\partial z}\left(\widetilde{\rho\langle u\rangle}b\frac{\partial\widetilde{\langle w\rangle}}{\partial x} + \widetilde{\rho\langle w\rangle}b\frac{\partial\widetilde{\langle w\rangle}}{\partial z}\right). \tag{4.105}$$

The expression for pressure now becomes

$$
\begin{aligned}
&-b\frac{\partial^2\widetilde{\langle P\rangle}}{\partial x^2} - b\frac{\partial^2\widetilde{\langle P\rangle}}{\partial z^2} = \\
&\frac{\partial}{\partial x}\left(\widetilde{\rho\langle u\rangle}b\frac{\partial\widetilde{\langle u\rangle}}{\partial x} + \widetilde{\rho\langle w\rangle}b\frac{\partial\widetilde{\langle u\rangle}}{\partial z}\right) + \frac{\partial}{\partial z}\left(\widetilde{\rho\langle u\rangle}b\frac{\partial\widetilde{\langle w\rangle}}{\partial x} + \widetilde{\rho\langle w\rangle}b\frac{\partial\widetilde{\langle w\rangle}}{\partial z}\right) \\
&-\frac{\partial^2}{\partial x^2}\left(2b\eta\frac{\partial\widetilde{\langle u\rangle}}{\partial x}\right) + \frac{2}{3}\frac{\partial^2\widetilde{\rho k}b}{\partial x^2} - \frac{c_f\rho\widetilde{\langle u\rangle}|\widetilde{\langle\mathbf{u}\rangle}|}{\partial x} \\
&-\frac{\partial^2}{\partial z^2}\left(2b\eta\frac{\partial\widetilde{\langle w\rangle}}{\partial z}\right) + \frac{2}{3}\frac{\partial^2\widetilde{\rho k}b}{\partial z^2} - \frac{c_f\rho\widetilde{\langle w\rangle}|\widetilde{\langle\mathbf{u}\rangle}|}{\partial z} \\
&-2\frac{\partial}{\partial x}\left\{\frac{\partial}{\partial z}\left[b\eta\left(\frac{\partial\widetilde{\langle u\rangle}}{\partial z} + \frac{\partial\widetilde{\langle w\rangle}}{\partial x}\right)\right]\right\} + b\frac{\partial\rho g}{\partial z}.
\end{aligned}
\tag{4.106}
$$

The breadth term is not included in the divergence of $\rho g b$ since a gradient in breadth would otherwise induce a pressure gradient and hence initiate a flow. Unlike the case for a constant breadth, the diffusive terms may not be neglected in solving the pressure Poisson equation.

4.5 Changes in flow geometry

Due to the continuous accelerating flow over the relatively short distance of the breach no equilibrium sediment transport conditions are obtained. The erosion rate of the embankment soil follows from the erosion equation, and the description of the sediment-laden gravity flows. The effects of sediment transport on the eddying motions and hence the flow shear stresses are assumed to be negligibly small compared to the errors originating from the uncertainty in the values for the soil erodibility , and hence have been disregarded. Due to the constant velocity with which soil saturates near the surface, both the erosion cause by sediment-laden gravity flows, and the erosion caused by the bed shear stresses, are represented by (Nearing et al., 1988)

$$E_\zeta = K\left(\tau - \tau_c\right)^n, \tag{4.107}$$

where E_ζ is the erosion rate in m/s in the $\hat{\zeta}$-coordinate direction (see Figure (2.1)), K is the erodibility in m^3/Ns, n is a coefficient with an expected value somewhere between 1 and 1.5, τ_c is the critical shear stress in N/m^2, and τ is the bed shear stress and follows from the flow model. The embankment erodes in the direction perpendicular to the surface. The erosion rate in the vertical $\hat{z}$-coordinate direction follows from

$$E_z = \frac{E_\zeta}{cos\alpha} \tag{4.108}$$

where α is the angle between the ζ-coordinate direction and the Cartesian $\hat{z}$-coordinate direction (See Figure 2.1). For a low concentration of non-cohesive sediment whereby the sediment does not influence the flow, the three dimensional mass balance equation for the sediment concentration is given by

$$\frac{\partial c}{\partial t} + \frac{\partial}{\partial x}\left(\langle u\rangle c - \epsilon\frac{\partial c}{\partial x}\right) + \frac{\partial}{\partial y}\left(\langle v\rangle c - \epsilon\frac{\partial c}{\partial y}\right) + \frac{\partial}{\partial z}\left(\left(\langle w\rangle - w_s\right)c - \epsilon\frac{\partial c}{\partial z}\right) = 0, \tag{4.109}$$

where c is the sediment concentration, ϵ is the kinematic eddy viscosity $\left(\frac{\eta}{\rho}\right)$, and w_s is the fall velocity of a sediment particle. Integrating over y gives

$$\begin{aligned}&\int_{y_1}^{y_2}\frac{\partial c}{\partial t}dy + \int_{y_1}^{y_2}\frac{\partial}{\partial x}\left(\langle u\rangle c - \epsilon\frac{\partial c}{\partial x}\right)dy \\ &+ \int_{y_1}^{y_2}\frac{\partial}{\partial z}\left(\left(\langle w\rangle - w_s\right)c - \epsilon\frac{\partial c}{\partial z}\right)dy + \left(\langle v\rangle c - \epsilon\frac{\partial c}{\partial y}\right)|_{y_2} - \left(\langle v\rangle c - \epsilon\frac{\partial c}{\partial y}\right)|_{y_1} = 0.\end{aligned} \tag{4.110}$$

Applying the Leibniz rule to the integral terms gives

$$\begin{aligned}&\frac{\partial}{\partial t}\int_{y_1}^{y_2} c dy - c|_{y_2}\frac{\partial y_2}{\partial t}|_{y_2} + c|_{y_1}\frac{\partial y_1}{\partial t}|_{y_1} \\ &+\frac{\partial}{\partial x}\int_{y_1}^{y_2}\left(\langle u\rangle c - \epsilon_x\frac{\partial c}{\partial x}\right)dy - \left(\langle u\rangle c - \epsilon_x\frac{\partial c}{\partial x}\right)|_{y_2}\frac{\partial y_2}{\partial x}|_{y_2} + \left(\langle u\rangle c - \epsilon_x\frac{\partial c}{\partial x}\right)|_{y_1}\frac{\partial y_1}{\partial x}|_{y_1} \\ &+\frac{\partial}{\partial z}\int_{y_1}^{y_2}\left(\left(\langle w\rangle - w_s\right)c - \epsilon_z\frac{\partial c}{\partial z}\right)dy - \left(\left(\langle w\rangle - w_s\right)c - \epsilon_z\frac{\partial c}{\partial z}\right)|_{y_2}\frac{\partial y_2}{\partial z}|_{y_2} \\ &+\left(\left(\langle w\rangle - w_s\right)c - \epsilon_z\frac{\partial c}{\partial z}\right)|_{y_1}\frac{\partial y_1}{\partial z}|_{y_1} + \left(\langle v\rangle c - \epsilon_y\frac{\partial c}{\partial y}\right)|_{y_2} - \left(\langle v\rangle c - \epsilon_y\frac{\partial c}{\partial y}\right)|_{y_1} = 0.\end{aligned} \tag{4.111}$$

Assuming that: $c_{y_1} = c_{y_2} = c_{wall}$, that $\frac{\partial y_2}{\partial t} = -\frac{\partial y_1}{\partial t} = v_{y_2} = -v_{y_1}$, and that $\widetilde{\langle u \rangle}_{y_1} = \widetilde{\langle u \rangle}_{y_2} = \widetilde{\langle w \rangle}_{y_1} = \widetilde{\langle w \rangle}_{y_2} = 0$ gives with $E_w = v_{y1} + v_{y2}$

$$\begin{aligned} &\frac{\partial}{\partial t}\tilde{c}b - c_{wall}E_w + \frac{\partial \widetilde{\langle u \rangle} cb}{\partial x} - \frac{\partial}{\partial x}\left(\epsilon\frac{\partial \tilde{c}b}{\partial x} - \epsilon c_{wall}\frac{\partial b}{\partial x}\right) - \left(-\epsilon\frac{\partial \tilde{c}}{\partial x}\right)|_{wall}\frac{\partial b}{\partial x} \\ &+\frac{\partial}{\partial z}\left[\left(\widetilde{\langle w \rangle} - \widetilde{w_s}\right)b\tilde{c}\right] - \frac{\partial}{\partial z}\left(\epsilon\frac{\partial \tilde{c}b}{\partial z}\right) - \frac{\partial}{\partial z}\epsilon c_{wall}\frac{\partial b}{\partial z} + w_s c|_{wall}\frac{\partial b}{\partial z} + \epsilon\frac{\partial c}{\partial z}|_{wall}\frac{\partial b}{\partial z} \\ &-\epsilon\frac{\partial c}{\partial y}|_{y_2} + \epsilon\frac{\partial c}{\partial y}|_{y_1} = 0. \end{aligned} \tag{4.112}$$

Neglecting the diffusion in the $\hat{y}$-coordinate direction, for $c_{wall} = 1$, and for $E_w = \frac{\partial b}{\partial t}$ the equation becomes

$$b\frac{\partial \tilde{c}}{\partial t} + \frac{\partial \widetilde{\langle u \rangle} cb}{\partial x} + \frac{\partial \widetilde{\langle w \rangle} cb}{\partial z} - b\frac{\partial}{\partial x}\left(\epsilon\frac{\partial c}{\partial x}\right) - b\frac{\partial}{\partial z}\left[\widetilde{w_s} + \epsilon\frac{\partial \tilde{c}}{\partial x}\right] = (1-\tilde{c})E_w, \tag{4.113}$$

where

$$E_w = K\left[c_f\rho\sqrt{\left(\widetilde{\langle u \rangle}|\widetilde{\langle \mathbf{u} \rangle}|\right)^2 + \left(\widetilde{\langle w \rangle}|\widetilde{\langle \mathbf{u} \rangle}|\right)^2} - \tau_c\right]^n. \tag{4.114}$$

The erosion rate of the embankment is perpendicular to the embankment surface in the $\hat{\zeta}$-coordinate direction as defined in Figure 2.1. With the erosion rate parallel to the embankment surface set to zero, this gives the following results

$$\begin{pmatrix} E_x \\ E_z \end{pmatrix} = \begin{pmatrix} -\cos\alpha & -\sin\alpha \\ -\sin\alpha & \cos\alpha \end{pmatrix}\begin{pmatrix} E_\varepsilon \\ E_\zeta \end{pmatrix}. \tag{4.115}$$

With $E_\varepsilon = 0$ this becomes

$$\begin{aligned} E_x &= -\sin\alpha E_\zeta, \\ \text{and} \qquad E_z &= \cos\alpha E_\zeta. \end{aligned} \tag{4.116}$$

With the equations derived in this chapter the flow during Stage 2 can be described accurately. The next chapter describes a way of solving the momentum equations

and pressure Poisson equation numerically. The description of the numerical methods for solving the breadth-integrated Spalart-Allmaras equation, and the testing of the derived relationship between the eddy viscosity and the kinematic energy fall outside the scope of this thesis.

Chapter 5

Solver

This chapter gives the solution method for the breadth-integrated momentum equations. The breadth is thereby allowed to vary in space but is constant in time. To accurately describe embankment erosion during Stage 2, during which the horizontal acceleration in $\hat{y}$-coordinate direction is negligibly small, the equations that need to be solved are:

- The breadth-integrated and depth-integrated mass balance equation,

$$\overline{\tilde{\rho}b}\frac{\partial h}{\partial t} = 0, \tag{5.1}$$

  where $\overline{\tilde{\rho}b}$, in kg/m^2, is the density of water ρ multiplied with the breadth b, h the water depth, and t the time.

- The momentum equations,

$$\begin{aligned} &\frac{\partial \widetilde{\rho\langle u\rangle}b}{\partial t} + \frac{\partial \widetilde{\rho\langle u\rangle}\widetilde{\langle u\rangle}b}{\partial x} + \frac{\partial \widetilde{\rho\langle u\rangle}\widetilde{\langle w\rangle}b}{\partial z} = -b\frac{\partial \widetilde{\langle P\rangle}}{\partial x} \\ &+\frac{\partial}{\partial x}\left(2b\eta\frac{\partial \widetilde{\langle u\rangle}}{\partial x}\right) - \frac{2}{3}\frac{\partial \widetilde{\rho k}b}{\partial x} - c_f\rho\widetilde{\langle u\rangle}|\widetilde{\langle \mathbf{u}\rangle}| + \frac{\partial}{\partial z}\left[b\eta\left(\frac{\partial \widetilde{\langle u\rangle}}{\partial z} + \frac{\partial \widetilde{\langle w\rangle}}{\partial x}\right)\right], \end{aligned} \tag{5.2}$$

and

$$\frac{\partial\widetilde{\rho\langle w\rangle}b}{\partial t}+\frac{\partial\widetilde{\rho\langle w\rangle}\widetilde{\langle u\rangle}b}{\partial x}+\frac{\partial\widetilde{\rho\langle w\rangle}\widetilde{\langle w\rangle}b}{\partial z}=-\tilde{\rho}gb-b\frac{\partial\widetilde{\langle P\rangle}}{\partial z} \tag{5.3}$$
$$+\frac{\partial}{\partial x}\left[b\eta\left(\frac{\partial\widetilde{\langle u\rangle}}{\partial z}+\frac{\partial\widetilde{\langle w\rangle}}{\partial x}\right)\right]-c_f\rho\widetilde{\langle w\rangle}|\widetilde{\langle\mathbf{u}\rangle}|+\frac{\partial}{\partial z}\left(2b\eta\frac{\partial\widetilde{\langle w\rangle}}{\partial z}\right)-\frac{2}{3}\frac{\partial\widetilde{\rho k}b}{\partial z},$$

where $\widetilde{\cdot}$ indicates the breadth-averaging, $\langle u\rangle$ and $\langle w\rangle$ are respectively the Reynolds-averaged flow velocity components in Cartesian $\hat{x}$ and $\hat{z}$-coordinate directions, η is the viscosity in Pa-s, k is the kinetic energy, c_f is a drag coefficient, g the acceleration due to gravity, and $\langle P\rangle$ is the pressure corresponding to the Reynolds-averaged accelerations.

- The breadth integrated pressure Poisson equation

$$-b\frac{\partial^2\widetilde{\langle P\rangle}}{\partial x^2}-b\frac{\partial^2\widetilde{\langle P\rangle}}{\partial z^2}=$$
$$\frac{\partial}{\partial x}\left(\widetilde{\rho\langle u\rangle}b\frac{\partial\widetilde{\langle u\rangle}}{\partial x}+\widetilde{\rho\langle w\rangle}b\frac{\partial\widetilde{\langle u\rangle}}{\partial z}\right)+\frac{\partial}{\partial z}\left(\widetilde{\rho\langle u\rangle}b\frac{\partial\widetilde{\langle w\rangle}}{\partial x}+\widetilde{\rho\langle w\rangle}b\frac{\partial\widetilde{\langle w\rangle}}{\partial z}\right) \tag{5.4}$$
$$-\frac{\partial^2}{\partial x^2}\left(2b\eta\frac{\partial\widetilde{\langle u\rangle}}{\partial x}\right)+\frac{2}{3}\frac{\partial^2\widetilde{\rho k}b}{\partial x^2}-\frac{c_f\rho\widetilde{\langle u\rangle}|\widetilde{\langle\mathbf{u}\rangle}|}{\partial x}$$
$$-\frac{\partial^2}{\partial z^2}\left(2b\eta\frac{\partial\widetilde{\langle w\rangle}}{\partial z}\right)+\frac{2}{3}\frac{\partial^2\widetilde{\rho k}b}{\partial z^2}-\frac{c_f\rho\widetilde{\langle w\rangle}|\widetilde{\langle\mathbf{u}\rangle}|}{\partial z}$$
$$-2\frac{\partial}{\partial x}\left\{\frac{\partial}{\partial z}\left[b\eta\left(\frac{\partial\widetilde{\langle u\rangle}}{\partial z}+\frac{\partial\widetilde{\langle w\rangle}}{\partial x}\right)\right]\right\}+b\frac{\partial\rho g}{\partial z},$$

- The eddy viscosity equation

$$\tilde{\eta}=\tilde{\rho}\tilde{\hat{\nu}}f_{\nu 1}, \tag{5.5}$$

where $f_{\nu 1}$ is a damping function given by

$$f_{\nu 1}=\frac{\xi^3}{\xi^3+c_{\nu 1}^3}. \tag{5.6}$$

Spalart and Allmaras give $c_{\nu 1}=7.1$, and $\xi=\frac{\tilde{\hat{\nu}}}{\nu}$ where ν is the kinematic viscosity of water. $\tilde{\hat{\nu}}$ is the breadth averaged Spalart–Allmaras variable which follows from

the breadth integrated Spalart–Allmaras equation given by

$$b\frac{\partial\tilde{\hat{\nu}}}{\partial t}+\frac{\partial\widetilde{\langle\rangle\tilde{\hat{\nu}}b}}{\partial x}+\frac{\partial\widetilde{\langle w\rangle\tilde{\hat{\nu}}b}}{\partial z}=c_{b1}\widetilde{\hat{S}\hat{\nu}}-c_{w1}bf_w\widetilde{\left(\frac{\hat{\nu}}{d}\right)^2} \tag{5.7}$$
$$+\frac{b}{\sigma}\left[\left(\nu+\tilde{\hat{\nu}}\right)\frac{\partial^2\tilde{\hat{\nu}}}{\partial x^2}+(1+c_{b2})\widetilde{\frac{\partial\hat{\nu}}{\partial x}\frac{\partial\hat{\nu}}{\partial x}}\right]+\frac{b}{\sigma}\left[\left(\nu+\tilde{\hat{\nu}}\right)\frac{\partial^2\tilde{\hat{\nu}}}{\partial z^2}+(1+c_{b2})\widetilde{\frac{\partial\hat{\nu}}{\partial z}\frac{\partial\hat{\nu}}{\partial z}}\right],$$

where the vorticity magnitude $\hat{S}$ is given by Equation 4.67. A full explanation of all the terms and coefficients in the breadth integrated Spalart–Allmaras equation is given in section 4.3.

- The kinetic energy equation

$$k=\tilde{\hat{\nu}}\left(\frac{\eta}{\rho l}\right)^2 f_{\nu1}\left[2\left(\frac{\partial\widetilde{\langle u\rangle}}{\partial x}\right)^2+2\left(\frac{\partial\widetilde{\langle w\rangle}}{\partial z}\right)^2+\left(\frac{\partial\widetilde{\langle u\rangle}}{\partial z}+\frac{\partial\widetilde{\langle w\rangle}}{\partial x}\right)^2\right]^{1/2} \tag{5.8}$$

Commercial codes, like FLUENT, are available that accurately calculate free surface flow in a vertical 2D plane. Some of these codes use pressure correction methods to determine the divergence free solution of the momentum equations. However, thus far the pressure correction methods have been limited to dealing with a constant breadth geometry. This chapter focuses on how the pressure correction methods should be altered to account for a variable breadth geometry. Section 5.1 focuses on the temporal discretization of the equations and the order in which the equations are solved, and Section 5.2 focuses on the spatial discretization. The modelling of the Eddy viscosity, kinetic energy, or free surface fall outside the scope of this chapter. In Chapter 6, the described methodology is tested for a series of laminar flow cases.

5.1 Temporal discretization

Using Einstein's summation convention, the momentum equations are given in matrix vector format by

$$\frac{\tilde{\rho} b^{n+1} \widetilde{\langle u \rangle}_i^{n+1}}{\delta t} + A_p \widetilde{\langle u \rangle}_i^{n+1} + A_f^{\widetilde{\langle u \rangle}_i^{n+1}} \widetilde{\langle u \rangle}_i^{n+1} = -b^{n+1} \frac{\delta \widetilde{\langle P \rangle}^{n+1}}{\delta x_i} + s_i^{n+1} + \frac{\tilde{\rho} \widetilde{\langle u_i \rangle} b^n}{\delta t}, \quad (5.9)$$

with $i = 1, 2$ referring to the Cartesian coordinate directions $\hat{x}$ and $\hat{z}$. A contains the matrix coefficients that follow from the discretized momentum equations, with A_p containing the coefficients from the momentum equations which are independent of the neighbouring velocity nodes, and A_f containing the coefficients of the terms dependent on the neighbouring velocity nodes. Vector s contains the source terms and cross derivative terms. The components of the discretized matrix that make up matrices A_p and A_f, and vector s are given in section 5.1.2. For the solution of the momentum equations to be divergence free, the flow accelerations at $t = n + 1$ need to balance the pressure gradients at $t = n + 1$. However $\widetilde{\langle P \rangle}^{n+1}$ is unknown when calculating $\widetilde{\langle u \rangle}_i^{n+1}$ and cannot be expressed as a function of $\widetilde{\langle u \rangle}_i^{n+1}$. Hence the equations are solved using an iterative method. The increase in breadth per time step is small, and so b^{n+1} is calculated using the solution of the momentum equations at the previous time step, and forms no part of the iteration process. The following section discusses several iterative methods that solve Equation (5.9), and its spatial derivatives expressed as the Poisson equation

$$-b^n \frac{\delta^2 \widetilde{\langle P \rangle}^{n+1}}{\delta x_i^2} = \frac{\delta}{\delta x_i} \frac{\rho b^n \widetilde{\langle u \rangle}_i^{n+1}}{\delta t} + \frac{\delta}{\delta x_i} A_p \widetilde{\langle u \rangle}_i^{n+1} + \frac{\delta}{\delta x_i} A_f^{\widetilde{\langle u \rangle}_i^{n}} \widetilde{\langle u \rangle}_i^{n+1} - \frac{\delta s_i^n}{\delta x_i} + \frac{\delta}{\delta x_i} \frac{\widetilde{\rho \langle u_i \rangle} b^n}{\delta t}, \quad (5.10)$$

5.1.1 Iterative solution methods

For all the Pressure correction methods considered, the first step of the iteration process consists of solving

$$\frac{\rho b^{n+1}\widetilde{\langle u\rangle}_i^{r1}}{\delta t} + A_p\widetilde{\langle u\rangle}_i^{r1} + A_f^{\widetilde{\langle u\rangle}_i^{r0}}\widetilde{\langle u\rangle}_i^{r1} = -b^{n+1}\frac{\delta\widetilde{\langle P\rangle}^{r0}}{\delta x_i} + s_i^{r0} + \frac{\widetilde{\rho\langle u_i\rangle}b^n}{\delta t}, \tag{5.11}$$

where $(^{r1})$ refers to the intermediate velocity, and $(^{r0})$ refers to the result from the previous iteration step. In the first iteration step the pressure gradient term follows from the pressure field at $t = n$. The velocity terms in $A_f^{\widetilde{\langle u\rangle}_i^{r0}}$, derived from linearizing the advective terms and the cross-derivative terms in s_i^{r0}, are updated each iteration step. After solving the momentum equations using the old pressure, a solution is found which is corrected to arrive at a divergence-free solution in keeping with the pressure Poisson equation. The pressure correction iterative methods discussed below each arrive at a divergence-free solution of the momentum equations, though vary in the rate of convergence.

SIMPLE

The SIMPLE method (Semi-Implicit Method for Pressure-Linked Equations) applies a correction to the velocity field, obtained from Equation (5.11), that satisfies (Ferziger and Perić, 2002)

$$\frac{\rho b^{n+1}\widetilde{\langle u\rangle}_i^{r2}}{\delta t} + A_p\widetilde{\langle u\rangle}_i^{r1} + A_f^{\widetilde{\langle u\rangle}_i^{r0}}\widetilde{\langle u\rangle}_i^{r1} = -b^{n+1}\frac{\delta\widetilde{\langle P\rangle}^{r1}}{\delta x_i} + s_i^{r0} + \frac{\widetilde{\rho\langle u_i\rangle}b^n}{\delta t}, \tag{5.12}$$

where ^{r2} refers to the second iteration step, and $\widetilde{\langle P\rangle}^{r1}$ is the unknown pressure field at the first iteration step. Recall that the pressure Poisson equation is derived by taking the divergence of the momentum equation. Subtracting Equation (5.11) from (5.12), and noting from continuity that

$$\frac{\delta\rho b^{n+1}\widetilde{\langle u\rangle}_i^{r2}}{\delta x_i} = 0, \tag{5.13}$$

leads to the velocity-correction equation given by

$$\frac{\rho b^{n+1}}{\delta t}\left(\widetilde{\langle u\rangle}_i^{r2} - \widetilde{\langle u\rangle}_i^{r1}\right) = -b^{n+1}\frac{\delta\left(\widetilde{\langle P\rangle}^{r1} - \widetilde{\langle P\rangle}^{r0}\right)}{\delta x_i}. \tag{5.14}$$

The Poisson equation for the velocity correction now follows from taking the divergence of Equation 5.14 and is given by

$$b^{n+1}\frac{\delta^2\left(\widetilde{\langle P\rangle}^{r1} - \widetilde{\langle P\rangle}^{r0}\right)}{\delta x_i^2} = \frac{\delta}{\delta x_i}\left(\frac{\rho b^{n+1}\widetilde{\langle u\rangle}_i^{r1}}{\delta t}\right). \tag{5.15}$$

Equation (5.15) is solved with the known velocity field $\widetilde{\langle u\rangle}_i^{r1}$ and used to correct the velocity field with Equation (5.14) until a divergence-free velocity field is obtained. Pressure increment values given by $\widetilde{\langle P\rangle}^{r1} - \widetilde{\langle P\rangle}^{r0}$ are added to the known pressure field $\widetilde{\langle P\rangle}^{r0}$, from the previous iteration, to arrive at a new estimate of the pressure field $\widetilde{\langle P\rangle}^{r1}$ used for the next iteration. It should be noted that in order to arrive at a correct answer for the velocity field and pressure field at time step $(n+1)$, the initial pressure field given by $\widetilde{\langle P\rangle}^{n}$ should correspond to the initial velocity field. Since A_p, and $A_f^{\widetilde{\langle u\rangle}_i^{r0}}$ are still multiplied by the initial estimate $\widetilde{\langle u\rangle}^{r1}$, the corrected velocity field could differ considerably from the solution of the momentum equations and hence the rate of convergence is small. A minor improvement could be made by updating the velocity field to satisfy

$$\frac{\rho b^{n+1}\widetilde{\langle u\rangle}_i^{r2}}{\delta t} + A_p\widetilde{\langle u\rangle}_i^{r2} + A_f^{\widetilde{\langle u\rangle}_i^{r0}}\widetilde{\langle u\rangle}_i^{r1} = -b^{n+1}\frac{\delta\widetilde{\langle P\rangle}^{r1}}{\delta x_i} + s_i^{r0} + \frac{\widetilde{\rho\langle u_i\rangle}b^n}{\delta t}, \tag{5.16}$$

in which A_p is a diagonal matrix. Hence a minor computational cost is incurred per iteration while the solution converges slightly faster to an answer that abides by the momentum equations and is divergence-free. The velocity-correction equation is now given by

$$\left(\frac{\rho b^{n+1}}{\delta t} + A_p\right)\left(\widetilde{\langle u\rangle}_i^{r2} - \widetilde{\langle u\rangle}_i^{r1}\right) = -b^{n+1}\frac{\delta\left(\widetilde{\langle P\rangle}^{r1} - \widetilde{\langle P\rangle}^{r0}\right)}{\delta x_i}, \tag{5.17}$$

and the Poisson equation is given by

$$b^{n+1}\frac{\delta}{\delta x_i}\left[\left(\frac{1}{\delta t}+\frac{A_p}{\rho b^{n+1}}\right)^{-1}\frac{\delta\left(\widetilde{\langle P\rangle}^{r1}-\widetilde{\langle P\rangle}^{r0}\right)}{\delta x_i}\right]=\frac{\delta\rho b^{n+1}\widetilde{\langle u\rangle_i^{r1}}}{\delta x_i}. \tag{5.18}$$

SIMPLEC

Van Doormaal and Raithby (1984) increased the rate of convergence towards a divergence-free solution of the momentum equations by incorporating the effects of the neighbour cells in $A_f^{\widetilde{\langle u\rangle}^{r0}}$, leading to the SIMPLEC (SIMPLE consistent) method. In SIMPLEC the effects of ignoring $A_f^{\widetilde{\langle u\rangle}^{r0}}$ in solving the Poisson equation are reduced by using a weighed average of $A_f^{\widetilde{\langle u\rangle}^{r0}}$, here indicated by $\underline{A_f}^{\widetilde{\langle u\rangle}_i^{r0}}$ (Ferziger and Perić, 2002; Van Doormaal and Raithby, 1984). Hence during the velocity correction step SIMPLEC solves

$$\frac{\rho b^{n+1}\widetilde{\langle u\rangle}_i^{r2}}{\delta t}+A_p\widetilde{\langle u\rangle}_i^{r2}+\underline{A_f}^{\widetilde{\langle u\rangle}_i}\widetilde{\langle u\rangle}_i^{r2}=-b^{n+1}\frac{\delta\widetilde{\langle P\rangle}^{r1}}{\delta x_i}+s_i^{r0}+\frac{\widetilde{\rho\langle u_i\rangle}^{n}b^n}{\delta t}. \tag{5.19}$$

Since A_p and $\underline{A_f}^{\widetilde{\langle u\rangle}_i}$ are both leading diagonal matrices, the intermediate solutions converge faster to the solution of Equation (5.9). The velocity-correction equation is now given by

$$\left(\frac{\rho b^{n+1}}{\delta t}+A_p+\underline{A_f}^{\widetilde{\langle u\rangle}_i^{n}}\right)\left(\widetilde{\langle u\rangle}_i^{r2}-\widetilde{\langle u\rangle}_i^{r1}\right)=-b^{n+1}\frac{\delta\left(\widetilde{\langle P\rangle}^{r1}-\widetilde{\langle P\rangle}^{r0}\right)}{\delta x_i}, \tag{5.20}$$

and the Poisson equation by

$$b^{n+1}\frac{\delta}{\delta x_i}\left[\left(\frac{1}{\delta t}+\frac{A_p+\underline{A_f}^{\widetilde{\langle u\rangle}_i^{r0}}}{\rho b^{n+1}}\right)^{-1}\frac{\delta\left(\widetilde{\langle P\rangle}^{r1}-\widetilde{\langle P\rangle}^{n}\right)}{\delta x_i}\right]=\frac{\delta\rho b^{n+1}\widetilde{\langle u\rangle_i^{r1}}}{\delta x_i}. \tag{5.21}$$

Similarly to the SIMPLE method, in SIMPLEC the pressure increment values given by $\widetilde{\langle P\rangle}^{r1}-\widetilde{\langle P\rangle}^{r0}$ are added to the known pressure $\widetilde{\langle P\rangle}^{r0}$ to arrive at a new estimate of the pressure field $\widetilde{\langle P\rangle}^{r1}$ used for the next iteration. Due to the presence of non-linear

terms in the momentum equations, $A_f{}^{\widetilde{\langle u\rangle}_i}$ contains velocity terms. In the case of large velocity gradients $\underline{A_f}{}^{\widetilde{\langle u\rangle}_i^{r0}}$ can become negative. For larger time steps, the influence of $\underline{A_f}{}^{\widetilde{\langle u\rangle}_i^{r0}}$ on the terms between the brackets in (5.20) and (5.21) increases, and this in turn could cause unrealistically high values to be computed for the velocity corrections given by $\widetilde{\langle u\rangle}^{r2} - \widetilde{\langle u\rangle}^{r1}$ and hence induce instabilities in the model.

PISO

The PISO (Pressure Implicit Splitting Operators) method applies two correction steps instead of one (Issa, 1986). The first correction step is identical to that of the SIMPLE method. The second correction step is applied to obtain a closer approximation to the solution of the momentum equations and improve convergence. The second correction step consists of explicitly solving the momentum equations using the corrected velocity as a predictor whereby the matrix coefficients A_p and $A_f^{\widetilde{\langle u\rangle}^r 0}$ has not been updated (Issa, 1986). The second correction step is given by

$$\frac{\rho b^{n+1}\widetilde{\langle u\rangle}_i^{r3}}{\delta t} + A_p\widetilde{\langle u\rangle}_i^{r2} + A_f^{\widetilde{\langle u\rangle}_i^r 0}\widetilde{\langle u\rangle}_i^{r2} = -b^{n+1}\frac{\delta\widetilde{\langle P\rangle}^{r2}}{\delta x_i} + s_i^{r0} + \frac{\widetilde{\rho\langle u_i\rangle}^n b^n}{\delta t}, \tag{5.22}$$

where $(^{r3})$ indicates the result of the second correction step. With

$$\frac{\delta\rho b^{n+1}\widetilde{\langle u\rangle}_i^{r3}}{\delta x_i} = 0, \tag{5.23}$$

the pressure correction equation during the second correction step is

$$-b^{n+1}\frac{\delta^2\widetilde{\langle P\rangle}^{r2}}{\delta x_i^2} = \frac{\delta A_p\widetilde{\langle u\rangle}_i^{r2}}{\delta x_i} + \frac{\delta A_f^{\widetilde{\langle u\rangle}_i^{r0}}\widetilde{\langle u\rangle}_i^{r2}}{\delta x_i} - \frac{\delta S_i^{r0}}{\delta x_i} - \frac{1}{\delta t}\left(\frac{\widetilde{\rho\langle u_i\rangle}^n b^n}{\delta x_i}\right). \tag{5.24}$$

The pressure field $\widetilde{\langle P\rangle}^{r2}$ is used both to calculate the new velocity field explicitly using Equation (5.22), and to calculate the new velocity field implicitly after updating the matrix coefficients of the momentum equations with $\widetilde{\langle u\rangle}_i^{r2}$. When applying the PISO method as described in the paper by Issa (1986), attention should be paid to the

second correction step. When an initial velocity field is chosen with positive values for the velocity components, then coefficients in the matrix A, used in the discretization of the non-linear equations, are also positive. When the first correction step causes components of $\widetilde{\langle u \rangle}^{r2}$ to become negative, then this gives non-physical negative values for the non-linear advective terms in the momentum equations, and a non-physical input for the pressure Poisson equation. Although the method could converge to the overall solution the answers obtained during the intermediate iteration steps would have no physical meaning.

SIMPLER

In the first step of the SIMPLER method (SIMPLE revised) the velocity field is corrected as described in SIMPLE. However instead of using the pressure increment equation to arrive at a new pressure field for the next iteration, $\widetilde{\langle u \rangle}_i^{r2}$ is used to update the matrix coefficients of the momentum equations, and the pressure field for the next iteration step is calculated from (Patankar, 1980; Ferziger and Perić, 2002)

$$-b^n \frac{\delta^2 \widetilde{\langle P \rangle}^{r2}}{\delta x_i^2} = \frac{\delta A_p \widetilde{\langle u \rangle}_i^{r2}}{\delta x_i} + \frac{\delta A_f^{\widetilde{\langle u \rangle}_i^{r2}} \widetilde{\langle u \rangle}_i^{r2}}{\delta x_i} - \frac{\delta s_i^{r2}}{\delta x_i} - \frac{1}{\delta t}\left(\frac{\widetilde{\rho \langle u_i \rangle}^n b^n}{\delta x_i}\right), \tag{5.25}$$

where $\widetilde{\langle u \rangle}_i^{r2}$ is the corrected velocity from the previous iteration round, and $\widetilde{\langle P \rangle}^{r2}$ is the pressure field used in the next iteration. Unlike the PISO method, the matrix coefficients in A_f are updated before calculating the pressure. Hence positive values for the non-linear advective terms are guaranteed and a more realistic representation of the pressure field is obtained. During each iteration step the pressure field is calculated with greater accuracy as would have been the case when correcting the pressure field, and so convergence is improved (Jang et al., 1986). For the solution of the momentum equations, the SIMPLER method was chosen because of its improved convergence rate over the SIMPLE method and its prevention of unrealistic velocity corrections through solving the full pressure Poisson equation using updated velocities for the matrix coefficients. The total flow diagram of the solver is given in Figure 5.1.1.

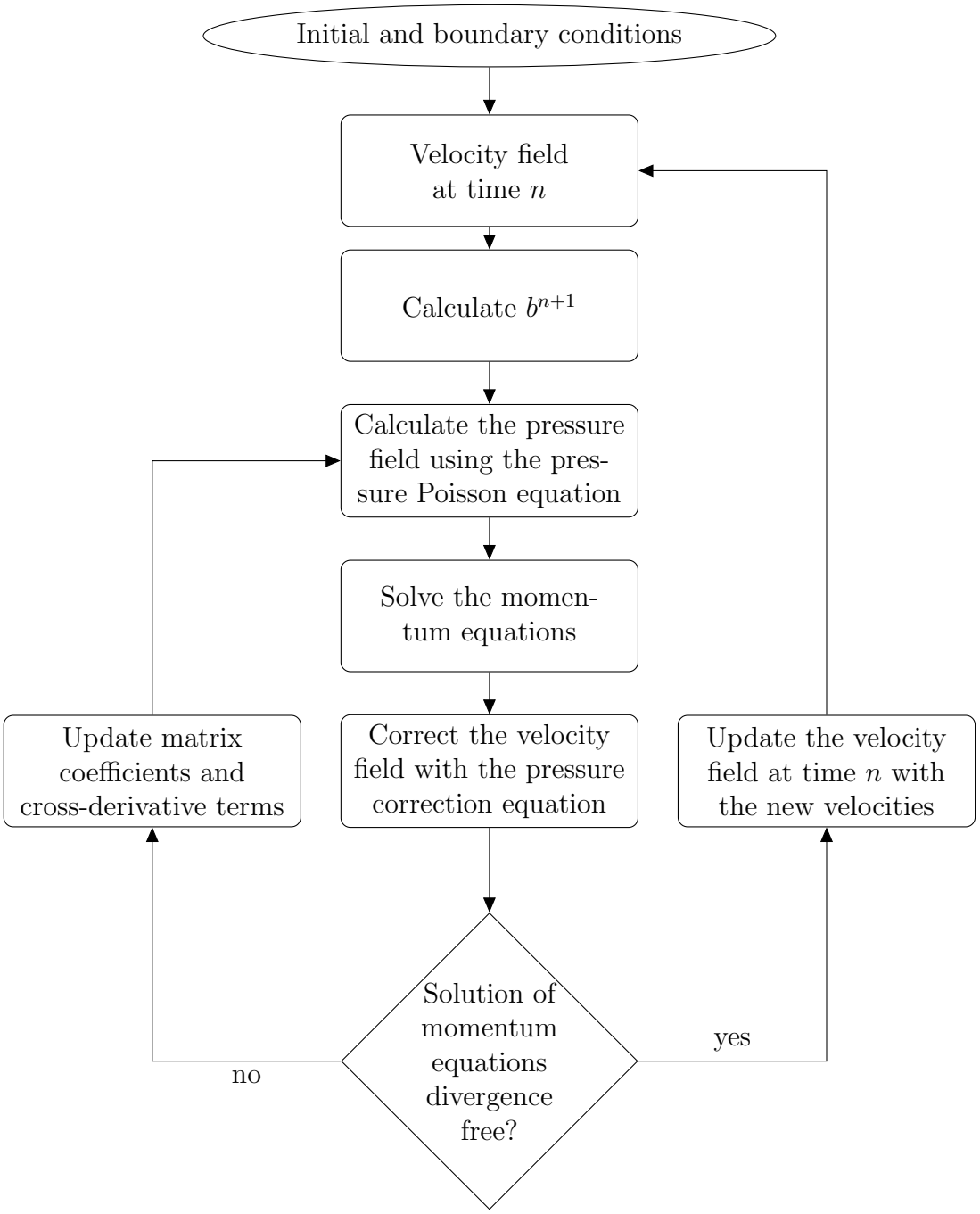

Figure 5.1: Flow chart of the SIMPLER method

5.1.2 Matrix and vector coefficients of the temporally discretized momentum equations

The coefficients of the discretized momentum equations in matrix A_f contain those terms which are dependent on the neighbouring velocity nodes and thus account for the normal stresses, the shear stresses with exclusion of the cross-derivatives, and the advective terms. In order to arrive at a system of linear equations with known matrix coefficients that converges rapidly to the full non-linear solution of the momentum equations, the non-linear advective terms in the momentum equations are linearized by defining (Ferziger and Perić, 2002)

$$\begin{aligned} \widetilde{\langle u\rangle}_i^{r1} &= \widetilde{\langle u\rangle}_i^{r1} + \Delta t\left(\widetilde{\langle u\rangle}_i^{r1} - \widetilde{\langle u\rangle}_i^{r0}\right) \\ \text{and} \qquad b\widetilde{\rho\langle u\rangle}_i^{n+1} &= b\widetilde{\rho\langle u\rangle}_i^{r1} + \Delta t\left(b\widetilde{\rho\langle u\rangle}_i^{r1} - b\widetilde{\rho\langle u\rangle}_i^{r0}\right), \end{aligned} \tag{5.26}$$

where $\widetilde{\rho\langle u\rangle}_i^{r0}$ are the velocity components that follow from the previous iteration step. For the first iteration step $\widetilde{\rho\langle u\rangle}_i^{r0} = \widetilde{\rho\langle u\rangle}_i^{n}$. Using this definition the non-linear terms of $\left(\widetilde{\rho\langle u\rangle}_i\widetilde{\langle u\rangle}_j\right)^{r1}$ are rewritten as (Ferziger and Perić, 2002)

$$b^{n+1}\left(\widetilde{\rho\langle u\rangle}\widetilde{\langle u\rangle}\right)^{r1} = b^{n+1}\left[\widetilde{\rho\langle u\rangle}^{r0}\widetilde{\langle u\rangle}^{r1} + \widetilde{\rho\langle u\rangle}^{r1}\widetilde{\langle u\rangle}^{r0} - \widetilde{\rho\langle u\rangle}^{r0}\widetilde{\langle u\rangle}^{r0} + \delta t^2\widetilde{\rho\Delta\langle u\rangle}\widetilde{\Delta\langle u\rangle}\right],$$

$$b^{n+1}\left(\widetilde{\rho\langle u\rangle}\widetilde{\langle w\rangle}\right)^{r1} = b^{n+1}\left[\widetilde{\rho\langle u\rangle}^{r0}\widetilde{\langle w\rangle}^{r1} + \widetilde{\rho\langle u\rangle}^{r1}\widetilde{\langle w\rangle}^{r0} - \widetilde{\rho\langle u\rangle}^{r0}\widetilde{\langle w\rangle}^{r0} + \delta t^2\widetilde{\rho\Delta\langle u\rangle}\widetilde{\Delta\langle w\rangle}\right], \tag{5.27}$$

$$b^{n+1}\left(\widetilde{\rho\langle w\rangle}\widetilde{\langle u\rangle}\right)^{r1} = b^{n+1}\left[\widetilde{\rho\langle w\rangle}^{r0}\widetilde{\langle u\rangle}^{r1} + \widetilde{\rho\langle w\rangle}^{r1}\widetilde{\langle u\rangle}^{r0} - \widetilde{\rho\langle w\rangle}^{r0}\widetilde{\langle u\rangle}^{r0} + \delta t^2\widetilde{\rho\Delta\langle w\rangle}\widetilde{\Delta\langle u\rangle}\right],$$

$$b^{n+1}\left(\widetilde{\rho\langle w\rangle}\widetilde{\langle w\rangle}\right)^{r1} = b^{n+1}\left[\widetilde{\rho\langle w\rangle}^{r0}\widetilde{\langle w\rangle}^{r1} + \widetilde{\rho\langle w\rangle}^{r1}\widetilde{\langle w\rangle}^{r0} - \widetilde{\rho\langle w\rangle}^{r0}\widetilde{\langle w\rangle}^{r0} + \delta t^2\widetilde{\rho\Delta\langle w\rangle}\widetilde{\Delta\langle w\rangle}\right],$$

with

$$\widetilde{\Delta\langle u\rangle}_i = \left(\widetilde{\langle u\rangle}_i^{r1} - \widetilde{\langle u\rangle}_i^{r0}\right) \tag{5.28}$$

and

$$\widetilde{\rho\Delta\langle u\rangle}_i = \left(\widetilde{\rho\langle u\rangle}_i^{r1} - \widetilde{\rho\langle u\rangle}_i^{r0}\right).$$

The terms in Equation (5.27) containing δt^2 are neglected because their order is equal to that of the error made in the time discretization in the ADI method (Ferziger and Perić, 2002), used to solve the momentum equations. When solving the $\hat{x}$-direction momentum equation, $\widetilde{\langle w\rangle}^{r1}$ is unknown. However, $\widetilde{\langle u\rangle}^{r1}$ is known when calculating $\widetilde{\langle w\rangle}^{r1}$ but is uncorrected. Hence for linearization of respectively $\left(\widetilde{\rho\langle u\rangle\langle w\rangle}\right)^{r1}$ and $\left(\widetilde{\rho\langle w\rangle\langle u\rangle}\right)^{r1}$, it is assumed that

$$\left(\widetilde{\rho\langle u\rangle\langle w\rangle}\right)^{r1} = \widetilde{\rho\langle u\rangle}^{r1}\widetilde{\langle w\rangle}^{r0}, \tag{5.29}$$

and

$$\left(\widetilde{\rho\langle w\rangle\langle u\rangle}\right)^{r1} = \widetilde{\rho\langle w\rangle}^{r1}\widetilde{\langle u\rangle}^{r0}.$$

For $\widetilde{\rho u_i}$ simplified as $\widetilde{\rho}\widetilde{u_i}$, the terms in the temporally discretized momentum equations, implicitly accounted for in A_f, are given in Table 5.1.2. A_p is a diagonal matrix that contains

terms in the momentum equations in $\hat{x}$-direction	terms in the momentum equations in $\hat{z}$-direction
$2\frac{\delta\tilde{\rho}\widetilde{\langle u\rangle}^{r0}\widetilde{\langle u\rangle}^{r1}b^{n+1}}{\delta x}$	$2\frac{\delta\tilde{\rho}\widetilde{\langle w\rangle}^{r0}\widetilde{\langle w\rangle}^{r1}b^{n+1}}{\delta z}$
$\frac{\delta\tilde{\rho}\widetilde{\langle u\rangle}^{r1}\widetilde{\langle w\rangle}^{r0}b^{n+1}}{\delta z}$	$\frac{\delta\tilde{\rho}\widetilde{\langle w\rangle}^{r1}\widetilde{\langle u\rangle}^{r0}b^{n+1}}{\delta x}$
$-\frac{\delta}{\partial x}\left(2b^{n+1}\eta\frac{\delta\widetilde{\langle u\rangle}^{r1}}{\delta x}\right)$	$-\frac{\delta}{\delta z}\left(2b^{n+1}\eta\frac{\delta\widetilde{\langle w\rangle}^{r1}}{\delta z}\right)$
$-\frac{\delta}{\delta z}\left(b^{n+1}\eta\frac{\delta\widetilde{\langle u\rangle}^{r1}}{\delta z}\right)$	$-\frac{\delta}{\delta x}\left(b^{n+1}\eta\frac{\delta\widetilde{\langle w\rangle}^{r1}}{\delta x}\right)$

Table 5.1: Terms in the momentum equations accounted for in the matrix A_f

the contribution of the drag coefficient. Just as for the advective terms, the side wall drag is non-linear. However due to the relatively small contribution of the side wall drag on the

convergence rate of the overall solution of the momentum equations, the side wall drag is linearised as

$$c_f \left(\rho\widetilde{\langle u\rangle}_i|\widetilde{\langle \mathbf{u}\rangle}|\right)^{r1} = c_f\rho\widetilde{\langle u\rangle}_i^{r1}|\widetilde{\langle \mathbf{u}\rangle}|^{r0}. \tag{5.30}$$

The coefficients on the main diagonal of A_p are given by

$$A_p = c_f\tilde{\rho}|\widetilde{\langle \mathbf{u}\rangle}|^{r0}, \tag{5.31}$$

where δt is the time step. Finally the source terms consist of the residual terms and are given by

$$s_1 = \frac{\delta}{\delta z}\left[b^{n+1}\eta\frac{\delta\widetilde{\langle w\rangle}^{r0}}{\delta x}\right] - \frac{2}{3}\frac{\delta\widetilde{\rho k}b^{n+1}}{\delta x} + \frac{\delta}{\delta x}\rho\widetilde{\langle u\rangle}^{r0}\widetilde{\langle u\rangle}^{r0}, \tag{5.32}$$

$$s_2 = \frac{\delta}{\delta x}\left[b^{n+1}\eta\frac{\delta\widetilde{\langle u\rangle}^{r0}}{\delta z}\right] - \frac{2}{3}\frac{\delta\widetilde{\rho k}b^{n+1}}{\delta z} + \frac{\delta}{\delta z}\rho\widetilde{\langle w\rangle}^{r0}\widetilde{\langle w\rangle}^{r0} - \rho g b^{n+1}.$$

Now, all the terms in Eqn. (5.9) have been dealt with, except for the local acceleration term and the pressure gradient term. A solution of the momentum equations is found by solving $A\widetilde{\langle u\rangle}_i = RHS$ where A is given by

$$A = \frac{\tilde{\rho}b^{n+1}}{\delta t}I + A_p + A_f, \tag{5.33}$$

I is the identity matrix, and RHS is given by

$$RHS = -b^{n+1}\frac{\delta\widetilde{\langle P\rangle}^{r0}}{\delta x_i} + s_i^{r0} + \frac{\tilde{\rho}\widetilde{\langle u_i\rangle}b^n}{\delta t}. \tag{5.34}$$

5.2 Spatial discretization scheme

The Reynolds-averaged Navier–Stokes equations are solved on a staggered grid as shown in Figure (5.2). The strong coupling between the velocity nodes and pressure nodes is used to prevent convergence problems (Ferziger and Perić, 2002). The location of the pressure $\widetilde{\langle P\rangle}$, breadth b, and Eddy viscosity η are indicated by subscript (i, j), the location of the velocity

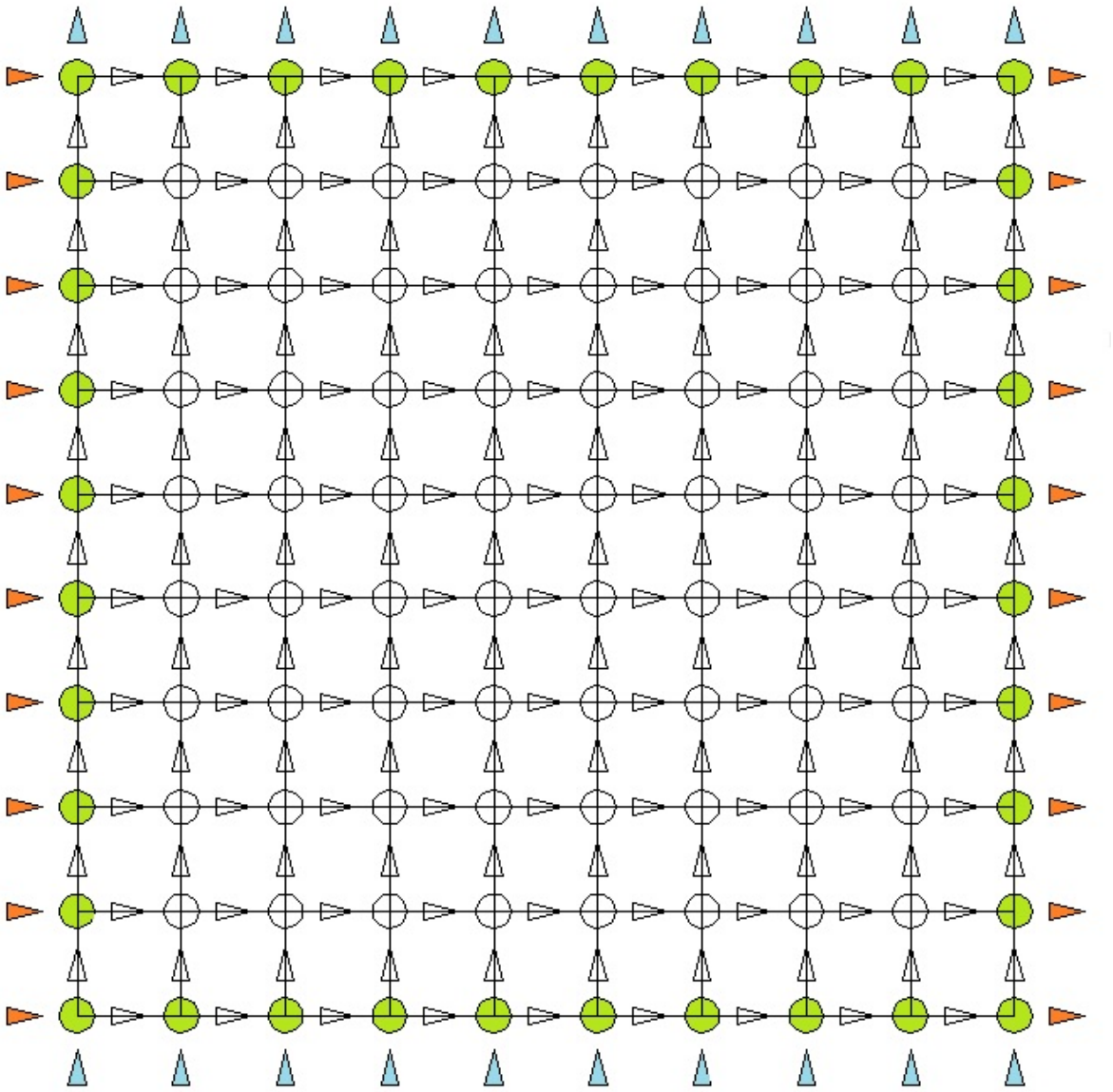

Figure 5.2: 10x10 staggered grid. The right pointing arrows indicate $\widetilde{\langle u \rangle}$, the upward pointing arrows, indicate $\widetilde{\langle w \rangle}$ and the circles indicate the location of the pressures, breadth, and eddy viscosity. The coloured symbols indicate the boundary points.

component $\widetilde{\langle u \rangle}$ by $\left(i - \frac{1}{2}, j\right)$, and the location of the velocity component $\widetilde{\langle w \rangle}$ by $\left(i, j - \frac{1}{2}\right)$. In order to correct the velocity $\widetilde{\langle u \rangle}$ at $\left(\frac{1}{2}, j\right)$, whereby $\left(-\frac{1}{2}, j\right)$, is the Dirichlet velocity boundary condition at the left boundary, the pressure is calculated at $(0, j)$. This requires a right hand side value for the Poisson equation at $(0, j)$. With the right hand side of the Pressure Poisson given by the divergence of the momentum equation, the momentum equation is solved at $\left(-\frac{1}{2}, j\right)$. At the left and bottom boundaries a forward differencing scheme is used to solve the discretized momentum equation in the $\hat{x}$ and $\hat{z}$-directions, and at the right and top boundaries a backward differencing scheme is used. These discretizations are solely used in determining the right hand side of the pressure Poisson equation and do not contribute to solving the momentum equations. The forward differencing schemes in horizontal direction are given by

$$2\Delta x \frac{\partial \phi}{\partial x}|_{-\frac{1}{2}} = -3\phi_{\frac{1}{2}} + 4\phi_{1\frac{1}{2}} - \phi_{2\frac{1}{2}}, \tag{5.35}$$

and

$$(\Delta x)^2 \frac{\partial^2 \phi}{\partial x^2}|_{-\frac{1}{2}} = \phi_{\frac{1}{2}} - 2\phi_{1\frac{1}{2}} + \phi_{2\frac{1}{2}}, \tag{5.36}$$

where ϕ is the value of interest. The backward differencing schemes in the horizontal direction are given by

$$2\Delta x \frac{\partial \phi}{\partial x}|_{bc_{RT}+\frac{1}{2}} = 3\phi_{bc_{RT}+\frac{1}{2}} - 4\phi_{bc_{RT}-\frac{1}{2}} + \phi_{bc_{RT}-1\frac{1}{2}}, \tag{5.37}$$

and

$$(\Delta x)^2 \frac{\partial^2 \phi}{\partial x^2}|_{bc_{RT}+\frac{1}{2}} = \phi_{bc_{RT}+\frac{1}{2}} - 2\phi_{bc_{RT}-\frac{1}{2}} + \phi_{bc_{RT}-1\frac{1}{2}}, \tag{5.38}$$

where bc_{RT} refers to the right boundary location of the pressure field as shown by the uppermost right row of circles in Figure 5.2.

5.2.1 Face addressing finite volume scheme

A face addressing finite volume scheme is used for the spatial discretization. In this scheme the gradient over the centre of the cell is calculated from the difference over the cell faces, divided by the spatial step size. Gradients at the cell faces, needed when solving the diffusive terms, are calculated from the difference in centre cell values. Leonard (1991) developed a high resolution finite volume discretization scheme based on normalized values for regular grids (Jasak et al., 1999; Leonard, 1991). The scheme developed by Leonard (1991) abides

by the convective boundedness criterion given by (Gaskell and Lau, 1988)

> "*Criterion.* Define a continuous increasing function or union of piecewise continuous increasing functions f relating to the modelling normalized value $\hat{\phi}_{i-1/2}$, to the normalized upstream nodal value $\hat{\phi}_{i-1}$, that is, $\hat{\phi}_{i-1/2} = f(\hat{\phi}_{i-1})$. Then a finite difference approximation to $\phi_{i-1/2}$ is bounded if:
>
> 1. for $\hat{\phi}_{i-1} \in [0,1]$, f is bounded below by the function $\hat{\phi}_{i-1/2} = \hat{\phi}_{i-1}$ and above by unity and passes through the points $\langle 0,0 \rangle$ and $\langle 1,1 \rangle$;
> 2. for $\hat{\phi}_{i-1} \notin [0,1]$, f is equal to $\hat{\phi}_{i-1}$."

The scheme uses the numerical diffusion of diagonally dominant first-order spatial discretization schemes to avoid numerical dispersion errors where necessary, and uses a second-order discretization scheme for higher accuracy where possible. The scheme developed by Leonard (1991), is adopted in the flow model to arrive at bounded solutions for the convective terms, and calculates the face values in the following two steps.

1. The direction of the flow is checked and the normalised value calculated from

$$\hat{\phi}_C = \frac{\phi_C - \phi_U}{\phi_D - \phi_U} \tag{5.39}$$

   where $\hat{\phi}$ is the normalised value, ϕ is the variable of interest, and subscripts $_{D,C}$ and $_U$ refer respectively to values in the downstream, centre, or upstream cell.

2. Based on the normalised value $\hat{\phi}_C$, the face values of the downstream cell face are calculated from;

   (a) for $\hat{\phi}_C \leq 0$ or $\hat{\phi}_C \geq 0$

$$\phi_f = \phi_C, \tag{5.40}$$

   (b) for $\beta_m \leq \hat{\phi_C} < 1$

$$\phi_f = \frac{1}{2}\phi_C + \frac{1}{2}\phi_D, \qquad \text{and} \tag{5.41}$$

   (c) for $0 < \hat{\phi}_C < \beta_m$ blending is applied as given by

$$\phi_f = \left(1 - \frac{\hat{\phi}_C}{2k}\right)\phi_C - \left(\frac{\hat{\phi}_D}{2k}\right)\phi_D. \tag{5.42}$$

Here the coefficient β_m is kept as low as possible to ensure good resolution. Jasak et al. (1999) provided the following range for the β_m-value, with the upper limit being a hard condition and the lower limit a recommendation.

$$\frac{1}{10} \leq \beta_m \leq \frac{1}{2}. \tag{5.43}$$

Here β_m is set to 1/10. Due to the staggered grid configuration, at respectively the left and bottom boundaries, the Western and Southern face values are given by the boundary values. Similarly at the right and top boundary, the Eastern and Northern face values are given by the boundary values.

When calculating the face values, ϕ is given by $\widetilde{\langle u \rangle}$ when solving the $\hat{x}$-direction momentum equation, and by $\widetilde{\langle w \rangle}$ when solving the $\hat{z}$-direction momentum equation. Gradients over the cell faces of $\widetilde{\langle u \rangle}$ are calculated from

$$\frac{\partial \widetilde{\langle u \rangle}}{\partial x}|_{i,j} = \frac{\widetilde{\langle u \rangle}_{i+\frac{1}{2},j} - \widetilde{\langle u \rangle}_{i-\frac{1}{2},j}}{\Delta x}, \tag{5.44}$$

and

$$\frac{\partial \widetilde{\langle u \rangle}}{\partial z}|_{i-\frac{1}{2},j+\frac{1}{2}} = \frac{\widetilde{\langle u \rangle}_{i-\frac{1}{2},j+1} - \widetilde{\langle u \rangle}_{i-\frac{1}{2},j}}{\Delta z}.$$

For $\widetilde{\langle w \rangle}$, gradients over the cell faces follow from

$$\frac{\partial \widetilde{\langle w \rangle}}{\partial x}|_{i+\frac{1}{2},j-\frac{1}{2}} = \frac{\widetilde{\langle w \rangle}_{i+1,j-\frac{1}{2}} - \widetilde{\langle w \rangle}_{i,j-\frac{1}{2}}}{\Delta x}, \tag{5.45}$$

and

$$\frac{\partial \widetilde{\langle w \rangle}}{\partial z}|_{i,j} = \frac{\widetilde{\langle w \rangle}_{i,j+\frac{1}{2}} - \widetilde{\langle w \rangle}_{i,j-\frac{1}{2}}}{\Delta z}.$$

5.2.2 Face values for the breadth, viscosity, and density

As shown in Figure 5.3, the values for the breadth b, and eddy viscosity η, are defined in the staggered grid configuration at the Eastern and Western faces in the case of $\widetilde{\langle u \rangle}$, and at the Northern and Southern faces in the case of $\widetilde{\langle w \rangle}$. For the calculation of the cross derivative terms, η and b have to be defined at the Northern and Southern cell faces when solving for

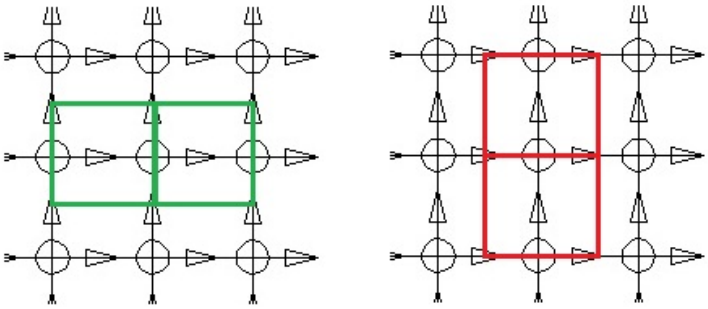

Figure 5.3: cell boundaries for $\widetilde{\langle u \rangle}$ (green) and $\widetilde{\langle w \rangle}$ (red)

$\widetilde{\langle u \rangle}$ and at the Easter and Western cell face when solving for $\widetilde{\langle w \rangle}$. For the calculation of $\widetilde{\langle u \rangle}_{i-\frac{1}{2},j}$, the values for $\eta_{i-\frac{1}{2},j+\frac{1}{2}}$, and $b_{i-\frac{1}{2},j+\frac{1}{2}}$ follow from averaging the values for η and b at the locations (i,j), $(i-1,j)$, $(i,j+1)$, and $(i-1,j+1)$. Similarly, for the calculation of $\widetilde{\langle w \rangle}_{i,j-\frac{1}{2}}$, the values for $\eta_{i+\frac{1}{2},j-\frac{1}{2}}$, and $b_{i+\frac{1}{2},j-\frac{1}{2}}$ follow from averaging the values for η and b at the locations (i,j), $(i+1,j)$, $(i,j-1)$, and $(i+1,j-1)$.

In the main fluid domain, the density in the cell centre and at the cell faces is given by the density of water. At the intersection with the bed, or the free surface, the flux through the cell faces is calculated by accounting only for that fraction of the cell face which is part of flow domain (Ubbink, 1997). Hence the density values at the cell faces near the bed or free surface are altered. For calculation of $\widetilde{\langle u \rangle}$ and $\widetilde{\langle w \rangle}$, the face values for the density follow from density values at the location (i,j). For the first pressure correction step, the discretized right hand side is given by

$$\frac{1}{\delta t}\left[\frac{\left(\widetilde{\rho\langle u\rangle b}\right)|_{i+\frac{1}{2},j}-\left(\widetilde{\rho\langle u\rangle b}\right)|_{i-\frac{1}{2},j}}{\delta x}+\frac{\left(\widetilde{\rho\langle w\rangle b}\right)|_{i,j+\frac{1}{2}}-\left(\widetilde{\rho\langle w\rangle b}\right)|_{i,j-\frac{1}{2}}}{\delta z}\right]. \tag{5.46}$$

Thus for calculation and correction of $\widetilde{\langle u \rangle}$ the density needs to be known at a vertical face at (i,j), and $(i+\frac{1}{2},j)$, and at a horizontal face at $(i-\frac{1}{2},j+\frac{1}{2})$. For calculation of $\widetilde{\langle w \rangle}$ the density needs to be known at the horizontal faces at (i,j) and $(i,j+\frac{1}{2})$, and at the vertical face at $(i,j-\frac{1}{2})$. Both the water level and bed level are calculated in one-dimension and then converted into a 2D representation using density fractions according to the method given below.

Figure (5.4) shows the transition between the bed and water over three cells, indicated by

the solid thick horizontal lines per vertical column of cells. The face value for the bed level

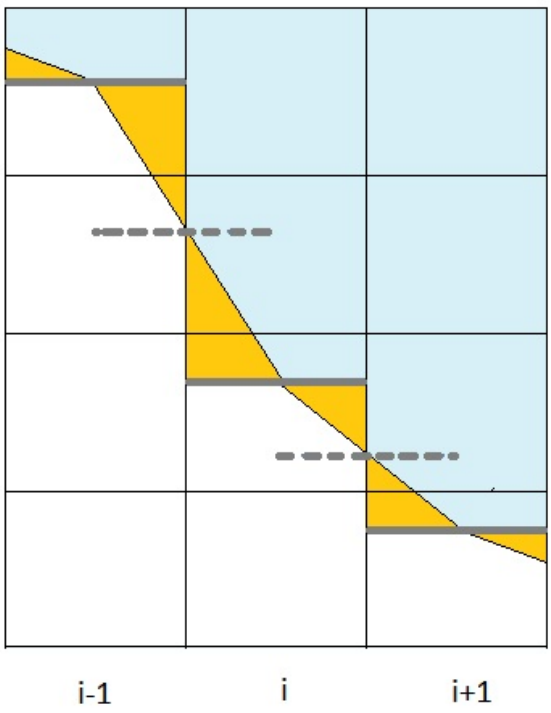

Figure 5.4: Density fractions in the case of a flow down a slope

h_{bed} at location $\left(i+\frac{1}{2}\right)$ follows from linearly interpolating between $h_{bed}(i)$ and $h_{bed}(i+1)$. The difference in shapes between the trangles above and below the thick solid lines in Figure 5.4 indicate the volumetric error introduced per cell due to linear interpolation. Hence after calculating the bed levels at $(i+\frac{1}{2})$, the bed level at (i) is corrected for the volume error using

$$\Delta h^*_{bed}(i) = h_{bed}(i) - \left[\frac{1}{8}\left(h_{i+1}-h_i\right) - \frac{1}{8}\left(h_i - h_{i-1}\right)\right], \tag{5.47}$$

where h^*_{bed} refers to the bed level, corrected for the calculation of density at centre of the cell. The fractions over the vertical faces at the locations (i) and $(i+\frac{1}{2})$ follow from dividing the bed height at those locations by the vertical grid spacing distance, leaving a real value in the form of $aa.bb$. The integer aa refers to the number of cells with density 0 below the bed level. The density at the vertical face at $aa+1$, at for example i, is given by

$$\rho(i, aa+1) = \rho_w\left(1-bb\right), \tag{5.48}$$

When applying the technique to the cells below the water level the integer aa refers to the

number of cells with density equal to ρ_w, and the density fraction at $aa+1$ is given by

$$\rho(i, aa+1) = \rho_w\,(bb)\,. \tag{5.49}$$

After some simple geometric calculations, the gradients in bed level at $(i \pm \frac{1}{2})$ together with the corrected bed levels at (i) provide the locations of the horizontal cell faces with a density fraction other than ρ_w or 0, and their corresponding density fractions per half a spatial step. The total process of density calculations in the case of a free surface and a bed level is given by the following steps

1. Use linear interpolation to calculate the face values for the water levels.
2. Correct the value for the water level at i in order to satisfy the volume balance
3. Using Equation (5.49) calculate the density over the vertical faces at i, and $i + \frac{1}{2}$.
4. Calculate the density over the horizontal faces at j and $j + \frac{1}{2}$.
5. Use linear interpolation to calculate the face values for the bed levels.
6. Correct the value of the bed level at i to satisfy the volume balance.
7. Using Equation (5.48) calculate the density over the vertical faces at i, and $i + \frac{1}{2}$.
8. Calculate the density over the horizontal faces at j and $j + \frac{1}{2}$

5.2.3 Pressure calculations with a free surface

When solving the momentum equations in $\hat{z}$-direction, the spatial discretization presents a challenge when a free surface is present. Figure 5.5 shows three possible density configurations near the free surface. In the case of a still water level the pressure distribution is hydrostatic. In all three cases depicted in Figure 5.5 the hydrostatic pressure at the second cell from the top is 0. The locations of $\widetilde{\langle w \rangle}$ are indicated by the upward pointing triangles. In each of the cases depicted, the density at the centre triangle is equal to the density of water. However, the values for the hydrostatic pressure at the locations below the centre triangle are different in each case. When the momentum equation in $\hat{z}$-direction is solved for a horizontal water

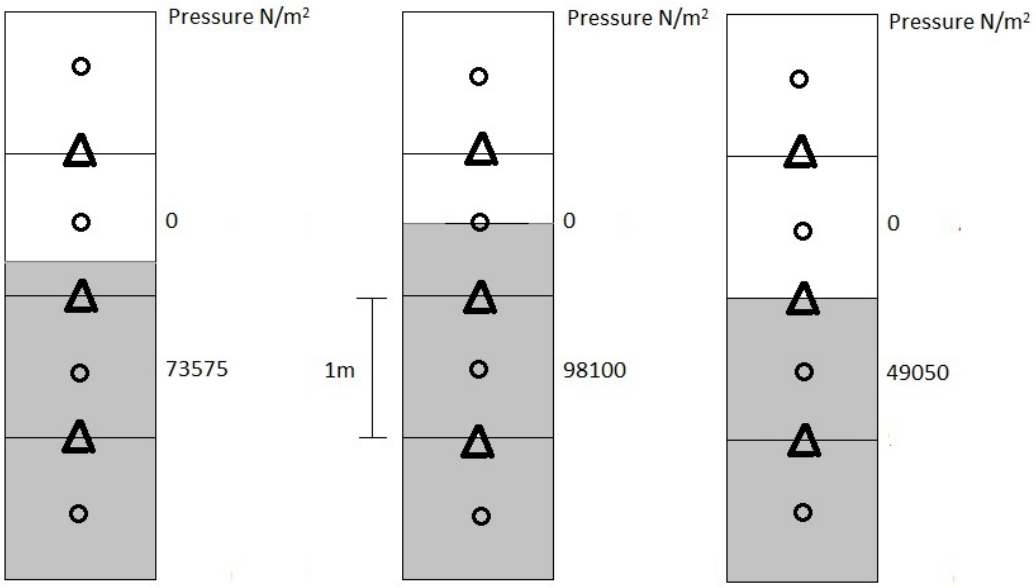

Figure 5.5: Pressure gradients at the free surface

level, then for the left and the right case in Figure 5.5, a non-zero value is found for

$$-b\rho g - b\frac{\partial P}{\partial z}, \tag{5.50}$$

and a vertical flow initiates. To induce a sharp gradient over the free surface, the terms in Equation 5.50 have been rewritten as

$$b\frac{\partial \rho_w g d_{fs}}{\partial z} - b\frac{\partial P}{\partial z}, \tag{5.51}$$

where ρ_w is the density of water, and d_{fs} is the distance below the free surface given at the locations (i, j) and easily follows from the known location of the water level. Above the free surface $d_{fs} = 0$. Similarly the pressure Poisson equation for a still water level becomes

$$b\left(\frac{\partial^2 P}{\partial x^2} + \frac{\partial^2 P}{\partial z^2}\right) = b\frac{\partial^2 \left(\rho_w g d_{fs}\right)}{\partial z^2} \tag{5.52}$$

Using this approximation, flows in $\hat{z}$-direction are prevented for any free surface configuration.

5.2.4 Boundary conditions

The iterative solver should be able to account for Dirichlet and Von Neumann boundary conditions for the velocity and pressure, and account for the free surface. The type of boundary conditions applied for the Poisson equation is determined by the correction step of the scheme and the type of velocity boundary conditions. In the first two sections below the boundary conditions for the Poisson equation are discussed for the Dirichlet and Von Neumann velocity boundary condition cases. The third section discusses how the free surface is accounted for when solving the momentum equations and Poisson equation for the velocity correction.

Dirichlet boundary conditions for the velocity

In the first correction step a Poisson equation is solved to correct the velocity. According to Gresho and Sani (1987), the Von Neumann boundary condition follows logically from the velocity-correction equation and is always appropriate. The velocity field is corrected according to

$$\frac{\rho b^n}{\delta t}\left(\widetilde{\langle u\rangle}_i^{r2} - \widetilde{\langle u\rangle}_i^{r1}\right) = -\frac{\delta\left(\widetilde{\langle P\rangle}^{r1}\right)}{\delta x_i}. \tag{5.53}$$

A Dirichlet boundary condition for the velocity

$$\frac{\tilde{\rho} b}{\Delta t}\left(\widetilde{\langle \mathbf{u}\rangle}^{r2} - \widetilde{\langle \mathbf{u}\rangle}^{r1}\right) = 0, \tag{5.54}$$

leads to the boundary condition for the pressure Poisson equation given by

$$\frac{\partial\widetilde{\langle P\rangle}}{\partial n} = 0, \tag{5.55}$$

where n is the normal direction to the boundary. In the second step of SIMPLER the Poisson equation is solved to obtain a new pressure field. The right hand side of the pressure Poisson equation now consists of the divergence of the momentum equations. In the case of a Dirichlet boundary condition for the velocity, the local acceleration term in the momentum equations

is 0 at the boundary, and the pressure gradients at the boundary follow from

$$b\frac{\partial\widetilde{\langle P\rangle}}{\partial x} = -\frac{\partial\widetilde{\rho\langle u\rangle}^{r2}\widetilde{\langle u\rangle}^{r2}b^{n+1}}{\partial x} - \frac{\partial\widetilde{\rho\langle u\rangle}^{r2}\widetilde{\langle w\rangle}^{r2}b^{n+1}}{\partial z} + \frac{\partial}{\partial x}\left(2b^{n+1}\eta\frac{\partial\widetilde{\langle u\rangle}^{r2}}{\partial x}\right) \tag{5.56}$$
$$-\frac{2}{3}\frac{\partial\widetilde{\rho k}b^{n+1}}{\partial x} - c_f\rho\widetilde{\langle u\rangle}^{r2}|\widetilde{\langle\mathbf{u}\rangle}^{r2}| + \frac{\partial}{\partial z}\left[b^{n+1}\eta\left(\frac{\partial\widetilde{\langle u\rangle}^{r2}}{\partial z} + \frac{\partial\widetilde{\langle w\rangle}^{r2}}{\partial x}\right)\right],$$

for the left and right boundaries, and

$$b\frac{\partial\widetilde{\langle P\rangle}}{\partial z} = -\frac{\partial\widetilde{\rho\langle w\rangle}^{r2}\widetilde{\langle u\rangle}^{r2}b^{n+1}}{\partial x} - \frac{\partial\widetilde{\rho\langle w\rangle}^{r2}\widetilde{\langle w\rangle}^{r2}b^{n+1}}{\partial z} - \tilde{\rho}gb^{n+1} + \frac{\partial}{\partial z}\left(2b^{n+1}\eta\frac{\partial\widetilde{\langle w\rangle}^{r2}}{\partial z}\right) \tag{5.57}$$
$$-c_f\rho\widetilde{\langle w\rangle}^{r2}|\widetilde{\langle\mathbf{u}\rangle}^{r2}|\frac{2}{3}\frac{\partial\widetilde{\rho k}b^{n+1}}{\partial z} + \frac{\partial}{\partial x}\left[b^{n+1}\eta\left(\frac{\partial\widetilde{\langle u\rangle}^{r2}}{\partial z} + \frac{\partial\widetilde{\langle w\rangle}^{r2}}{\partial x}\right)\right],$$

for the top and bottom boundaries.

Von Neumann boundary conditions for the velocity

In the case of Von Neumann boundary conditions for both velocity components, the left hand side of Equation (5.53) is no longer equal to 0 and it is therefore no longer possible to assume a zero pressure gradient for the first correction step. Similarly the local acceleration term is no longer zero at the boundary, and hence the pressure is defined at the boundary in order to solve the pressure Poisson equation. A relationship for the pressure at the boundary follows from integrating one of the momentum equations. However this requires one of the velocity components to be defined at the boundary. With $\widetilde{\langle w\rangle}$ defined at the boundary, $\frac{\partial\widetilde{\langle w\rangle}}{\partial z}$ is known, and so $\frac{\partial\widetilde{\langle u\rangle}}{\partial x}$ follows from the condition of a divergence-free flow. With $\widetilde{\langle w\rangle}$, $\frac{\partial\widetilde{\langle u\rangle}}{\partial x}$, and $\frac{\partial b}{\partial x}$ defined at the left or right hand side boundary, an expression for the pressure is derived by integrating the $\hat{z}$-direction momentum equation. For example, in the case of an unidirectional flow and boundary conditions $\frac{\partial b}{\partial x} = 0$, and $\widetilde{\langle w\rangle} = 0$, the expression for the pressure becomes

$$\widetilde{\langle P\rangle} = \eta\frac{\partial\widetilde{\langle u\rangle}}{\partial x} + C, \tag{5.58}$$

where C is the hydrostatic pressure distribution given by

$$C = \max\left(\rho_w g d - \rho_w g z, 0\right), \tag{5.59}$$

in which d is the depth. With the pressure defined, the system of equations can be solved.

Free surface boundary conditions for the velocity

At the free surface it is assumed that the shear stresses are 0. Using $\tau = b\eta\frac{\partial u_{e_1}}{\partial e_3}$ the velocity boundary condition at the free surface is given by

$$\frac{\partial u_{e_1}}{\partial e_3} = 0, \tag{5.60}$$

where e_1 is a coordinate in the $\hat{e_1}$-coordinate direction tangential to the free surface and e_3 is a coordinate in the $\hat{e_3}$-coordinate direction perpendicular to the free surface. The right hand side of the Poisson equation for the velocity correction during the first step in SIMPLER consists of the continuity equation. The free surface boundary conditions in the continuity equation are accounted for in two steps;

1. Calculate the velocity gradients at the free surface in the Cartesian coordinate system, and convert them to the $\hat{e_1}, \hat{e_3}$ coordinate system with

$$\begin{pmatrix} \widetilde{\frac{\partial\langle u_{e1}\rangle}{\partial e_1}} \\ \widetilde{\frac{\partial\langle u_{e3}\rangle}{\partial e_3}} \end{pmatrix} = \begin{pmatrix} \cos\phi & \sin\phi \\ -\sin\phi & \cos\phi \end{pmatrix} \begin{pmatrix} \cos\phi & \sin\phi \\ -\sin\phi & \cos\phi \end{pmatrix} \begin{pmatrix} \widetilde{\frac{\partial\langle u\rangle}{\partial x}} \\ \widetilde{\frac{\partial\langle w\rangle}{\partial z}} \end{pmatrix}. \tag{5.61}$$

2. Set the value for $\widetilde{\frac{\partial\langle u\rangle_{e3}}{\partial e_3}} = 0$ and convert the system back into a Cartesian coordinate system with

$$\begin{pmatrix} \widetilde{\frac{\partial\langle u\rangle}{\partial x}} \\ \widetilde{\frac{\partial\langle w\rangle}{\partial z}} \end{pmatrix} = \begin{pmatrix} \cos\phi & -\sin\phi \\ \sin\phi & \cos\phi \end{pmatrix} \begin{pmatrix} \cos\phi & -\sin\phi \\ \sin\phi & \cos\phi \end{pmatrix} \begin{pmatrix} \widetilde{\frac{\partial\langle u_{e1}\rangle}{\partial e_1}} \\ 0 \end{pmatrix}. \tag{5.62}$$

When solving the discretized momentum equations, the density fractions are used to identify the location of the free surface. In the case of zero density at the face of a cell which is part of the free surface, the velocity gradients become 0 over that face.

5.2.5 Solution method of the equations

Momentum equations

The momentum equations are solved with the Alternate Direction Implicit (ADI) method, in which the solution is obtained by splitting the discretized momentum equations in terms of directional derivatives, and by iterating the solutions of the unidirectional components. The ADI method does not allow for cross-derivative terms to be accounted for implicitly and hence these are accounted for explicitly and updated every outer iteration step. The right hand sides f_x and f_z of the discretized $\hat{x}$ and $\hat{z}$- direction momentum equations, with exception of the time derivative, are given by

$$f_x = \frac{\partial}{\partial z} b^{n+1} \eta \frac{\partial \widetilde{\langle w \rangle}^{r0}}{\partial x} - b^{n+1} \frac{\partial \widetilde{\langle P \rangle}^{r0}}{\partial x} - \frac{2}{3} \frac{\partial \widetilde{\rho k} b^{n+1}}{\partial x}, \tag{5.63}$$

and

$$f_z = \frac{\partial}{\partial x} b^{n+1} \eta \frac{\partial \widetilde{\langle u \rangle}^{r0}}{\partial z} - \tilde{\rho} g b^{n+1} - b^{n+1} \frac{\partial \widetilde{\langle P \rangle}^{r0}}{\partial z} - \frac{2}{3} \frac{\partial \widetilde{\rho k} b^{n+1}}{\partial z}, \tag{5.64}$$

Time discretization based on the Crank-Nickelson method leads to an unconditionally stable solver of the momentum equations (In 't Hout and Welfert, 2007), which is given in terms of matrix vector operations by

$$\begin{aligned} \frac{\tilde{\rho} b}{\delta t} \left(\widetilde{\langle u \rangle}^{r1} - \widetilde{\langle u \rangle}^{n} \right) + \frac{1}{2} \left(A_p \widetilde{\langle u \rangle}^{r1} + A_{fx}^{\widetilde{\langle u \rangle}^{r0}} \widetilde{\langle u \rangle}^{r1} + A_{fz}^{\widetilde{\langle u \rangle}^{r0}} \widetilde{\langle u \rangle}^{r1} \right) \\ + \frac{1}{2} \left(A_p \widetilde{\langle u \rangle}^{n} + A_{fx}^{\widetilde{\langle u \rangle}^{r0}} \widetilde{\langle u \rangle}^{n} + A_{fz}^{\widetilde{\langle u \rangle}^{r0}} \widetilde{\langle u \rangle}^{n} \right) = f_x, \end{aligned} \tag{5.65}$$

and

$$\begin{aligned} \frac{\tilde{\rho} b}{\delta t} \left(\widetilde{\langle w \rangle}^{r1} - \widetilde{\langle w \rangle}^{n} \right) + \frac{1}{2} \left(A_p \widetilde{\langle w \rangle}^{r1} + A_{fx}^{\widetilde{\langle w \rangle}^{r0}} \widetilde{\langle w \rangle}^{r1} + A_{fz}^{\widetilde{\langle w \rangle}^{r0}} \widetilde{\langle w \rangle}^{r1} \right) \\ + \frac{1}{2} \left(A_p \widetilde{\langle w \rangle}^{n} + A_{fx}^{\widetilde{\langle w \rangle}^{r0}} \widetilde{\langle w \rangle}^{n} + A_{fz}^{\widetilde{\langle w \rangle}^{r0}} \widetilde{\langle w \rangle}^{n} \right) = f_z, \end{aligned} \tag{5.66}$$

where A contains the coefficients of the discretized momentum equation in respectively the $\hat{x}$-direction, and $\hat{z}$-direction, and $_p$ and $_f$ are used to refer to those matrix coefficients which are respectively independent and dependent on the neighbouring velocity nodes, and given in section 5.1.2. Subscripts $_x$ and $_z$ refer to components of A_f with respectively gradients in

$\hat{x}$-direction, and $\hat{z}$-direction. Given that

$$A2_x = \frac{\delta t}{2\tilde{\rho}b}\left(\frac{1}{2}A_p + A_{fx}^{\widetilde{\langle u\rangle}^{r0}}\right), \tag{5.67}$$

$$A2_z = \frac{\delta t}{2\tilde{\rho}b}\left(\frac{1}{2}A_p + A_{fz}^{\widetilde{\langle u\rangle}^{r0}}\right),$$

$$B2_x = \frac{\delta t}{2\tilde{\rho}b}\left(\frac{1}{2}A_p + A_{fx}^{\widetilde{\langle w\rangle}^{r0}}\right), \tag{5.68}$$

$$\text{and} \qquad B2_z = \frac{\delta t}{2\tilde{\rho}b}\left(\frac{1}{2}A_p + A_{fz}^{\widetilde{\langle w\rangle}^{r0}}\right),$$

Equations (5.65) and (5.66) become

$$\left(I + A2_x + A2_z\right)\widetilde{\langle u\rangle}^{r1} = \left(I - A2_x - A2_z\right)\widetilde{\langle u\rangle}^{n} + \frac{\delta t}{\tilde{\rho}b}f_x, \tag{5.69}$$

and

$$\left(I + B2_x + B2_z\right)\widetilde{\langle w\rangle}^{r1} = \left(I + B2_x + B2_z\right)\widetilde{\langle w\rangle}^{n} + \frac{\delta t}{\tilde{\rho}b}f_z \tag{5.70}$$

These equations are split as

$$\left(I + A2_x\right)\left(I + A2_z\right)\widetilde{\langle u\rangle}^{r1} = \left(I - A2_x\right)\left(I - A2_z\right)\widetilde{\langle u\rangle}^{n} + \frac{\delta t}{\tilde{\rho}b}f_x, \tag{5.71}$$

and

$$\left(I + B2_x\right)\left(I + B2_z\right)\widetilde{\langle w\rangle}^{r1} = \left(I + B2_x\right)\left(+B2_z\right)\widetilde{\langle w\rangle}^{n} + \frac{\delta t}{\tilde{\rho}b}f_z, \tag{5.72}$$

leaving a residual error of respectively

$$\frac{\delta t^2}{4\tilde{\rho}b}\left(\frac{1}{2}A_p + A_{fx}\right)\left(\frac{1}{2}A_p + A_{fz}\right), \tag{5.73}$$

and

$$\frac{\delta t^2}{4\tilde{\rho}b}\left(\frac{1}{2}B_p + B_{fx}\right)\left(\frac{1}{2}B_p + B_{fz}\right). \tag{5.74}$$

These errors are of $O(\delta t^2)$ and thereby of the same order as the discretization error of the Crank-Nickelson scheme, and hence are neglected. Peaceman and Rachford Jr (1955); Douglas and Peaceman (1955) proposed an iterative method of solving the equations. After

replacing $A2$ and $B2$ with their original expressions, the method is given by.

$$\left(\frac{2\tilde{\rho b}}{\delta T}+\frac{1}{2}A_p+A_{fx}^{\widetilde{\langle u\rangle}^{r0}}\right)\widetilde{\langle u\rangle}^{it+\frac{1}{2}}=\left(-\frac{1}{2}A_p-A_{fz}^{\widetilde{\langle u\rangle}^{r0}}\right)\widetilde{\langle u\rangle}^{it}+\frac{2\tilde{\rho b}}{\delta t}\widetilde{\langle u\rangle}^{n}+f_x \tag{5.75}$$
$$\left(\frac{2\tilde{\rho b}}{\delta T}+\frac{1}{2}A_p+A_{fz}^{\widetilde{\langle u\rangle}^{r0}}\right)\widetilde{\langle u\rangle}^{it+1}=\left(-\frac{1}{2}A_p-A_{fx}^{\widetilde{\langle u\rangle}^{r0}}\right)\widetilde{\langle u\rangle}^{it+\frac{1}{2}}+\frac{2\tilde{\rho b}}{\delta t}\widetilde{\langle u\rangle}^{n}+f_x$$

in which $(^n)$ refers to the velocity field at the previous time step, and $(^{it})$ refers to the iteration round whereby for $r=1$, $\widetilde{\langle u\rangle}^{it}=\widetilde{\langle u\rangle}^{n}$. After completion of the iteration process $\widetilde{\langle u\rangle}^{r1}=\widetilde{\langle u\rangle}^{it+1}$. Similarly for the $\hat{z}$-direction momentum equations this becomes.

$$\left(\frac{2\tilde{\rho b}}{\delta T}+\frac{1}{2}A_p+A_{fx}^{\widetilde{\langle w\rangle}^{r0}}\right)\widetilde{\langle w\rangle}^{it+\frac{1}{2}}=\left(-\frac{1}{2}A_p-A_{fz}^{\widetilde{\langle w\rangle}^{r0}}\right)\widetilde{\langle w\rangle}^{it}+\frac{2\tilde{\rho b}}{\delta t}\widetilde{\langle w\rangle}^{n}+f_z \tag{5.76}$$

and

$$\left(\frac{2\tilde{\rho b}}{\delta T}+\frac{1}{2}A_p+A_{fz}^{\widetilde{\langle w\rangle}^{r0}}\right)\widetilde{\langle w\rangle}^{it+1}=\left(-\frac{1}{2}A_p-A_{fx}^{\widetilde{\langle w\rangle}^{r0}}\right)\widetilde{\langle w\rangle}^{it+\frac{1}{2}}+\frac{2\tilde{\rho b}}{\delta t}\widetilde{\langle w\rangle}^{n}+f_z.$$

At each iteration step the values of $\widetilde{\langle u\rangle^{it}}$ and $\widetilde{\langle w\rangle^{it}}$ are replaced by the solution of the previous iteration given by $\widetilde{\langle u\rangle^{it+1}}$ and $\widetilde{\langle u\rangle^{it+1}}$.

Pressure Poisson equation

When applying Dirichlet boundary conditions for the velocity, the Poisson equation is solved with four Von Neumann boundary conditions. In theory this gives an infinite number of solutions for the pressure. However the gradient field for every solution is the same, and so any solution suffices. Ferziger and Perić (2002) proposed to solve the matrix by anchoring the solution. This involves replacing the Von Neumann boundary condition with a Dirichlet one at a single cell in the computational domain. However instead of inverting the matrix, the system of equations is rapidly solved using a Fourier transform method at the cost of $10(N^2)\log_2 N$ operations for a grid of size of $N\times N$ cells (Averbuch et al., 1998). The discretized Poisson equation is given by

$$(P_{i-1,j}+P_{i+1,j}+P_{i,j+1}+P_{i,j-1}-4P_{i,j})=f\Delta^2 \tag{5.77}$$

where the subscripts indicate the locations in the five point stencil given in Figure 5.6, Δ^2 refers to the spatial step size for a square grid, P refers to the matrix locations of the pressure, and f is the right hand side. Defining the Fourier series

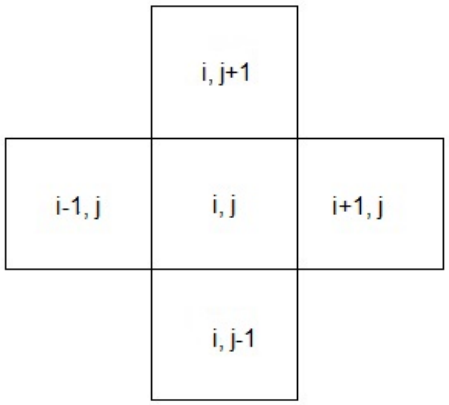

Figure 5.6: Five point stensil

$$P_{i,j} = \frac{1}{IJ} \sum_{m=0}^{I-1} \sum_{n=0}^{J-1} \hat{P}_{mn} e^{-2\pi kim/I} e^{-2\pi kjn/J}, \tag{5.78}$$

and

$$f_{i,j} = \frac{1}{IJ} \sum_{m=0}^{I-1} \sum_{n=0}^{J-1} \hat{f}_{mn} e^{-2\pi kim/I} e^{-2\pi kjn/J}, \tag{5.79}$$

where i and j are the spectral frequencies. The number of spectral frequencies accounted for is given by the grid size and indicated by I and J. $\hat{P}_{mn}$ and $\hat{f}_{mn}$ contain the Fourier coefficients. Equation (5.77) is rewritten as (Press et al., 1992)

$$\hat{P}_{mn} \left(e^{2\pi km/I} + e^{-2\pi km/I} + e^{2\pi kn/J} + e^{-2\pi kn/J} - 4 \right) = \hat{f}_{mn} \Delta^2. \tag{5.80}$$

After some manipulation this leads to

$$\hat{P}_{mn} = \frac{\hat{f}_{mn} \Delta^2}{2 \left(cos \frac{2\pi m}{J} + cos \frac{2\pi n}{L} - 2 \right)}. \tag{5.81}$$

For all Von Neumann boundary conditions, the Fourier Transform method reduces to the Discrete Cosine Transform method whereby (Press et al., 1992; Agrawal et al., 2005, 2006)

$$P_{i,j} = \frac{4}{IJ} \sum_{m=0}^{I} \sum_{n=0}^{J} \hat{P}_{mn} \cos \frac{\pi im}{I} \cos \frac{\pi jn}{J}, \tag{5.82}$$

and

$$f_{i,j} = \frac{4}{IJ} \sum_{m=0}^{I} \sum_{n=0}^{J} \hat{f}_{mn} \cos\frac{\pi i m}{I} \cos\frac{\pi j n}{J}. \tag{5.83}$$

Hence the numerical solver consists of the steps;

1. Adapt the right hand side f to account for the gradients at the boundaries
2. Calculate the Discrete Cosine Transform of f to obtain $\hat{f}$
3. Compute $\hat{P}_{mn}$ from Equation (5.81)
4. Compute the inverse Discrete Cosine Transform to get $P_{i,j}$

Disadvantages of the Discrete Cosine method are that all the boundary conditions have to be given by Von Neumann boundary conditions, and that in its original form it is only applicable on square grids. In the case of all Dirichlet boundary conditions, the solution can be rapidly obtained from the Discrete sine transform instead. In the case of one or more open boundary conditions for the velocity, some of the Pressure boundary conditions are of the Dirichlet type and the equation is solved using Matlab built-in backslash solver. It is recommended to further develop the Fourier Transform solver towards dealing with varying boundary conditions and irregular grids, and towards expediting the solver using cyclic reduction methods (Press et al., 1992).

Special attention should be paid to solving the Poisson equation when solving the breadth averaged momentum equations for a variable breadth geometry. Integration of the pressure term in the $\hat{x}$-direction momentum equations over the breadth gives

$$\int \frac{\partial \langle P \rangle}{\partial x} dy = \frac{\partial}{\partial x} \int \langle P \rangle dy - P|_{y_2} \frac{\partial y_2}{\partial x} + P|_{y_1} \frac{\partial y_1}{\partial x}. \tag{5.84}$$

Since a gradient in breadth does not initiate a flow,

$$-P \frac{\partial b}{\partial x} = -P|_{y_2} \frac{\partial y_2}{\partial x} + P|_{y_1} \frac{\partial y_1}{\partial x}, \tag{5.85}$$

and

$$\int \frac{\partial \langle P \rangle}{\partial x} dy = b \widetilde{\frac{\partial \langle P \rangle}{\partial x}}. \tag{5.86}$$

Similarly

$$\frac{\partial}{\partial x}\left(b\frac{\partial\widetilde{\langle P\rangle}}{\partial x}\right) = b\frac{\partial^2\widetilde{\langle P\rangle}}{\partial x^2}. \tag{5.87}$$

A discrepancy arises when applying these equations to the physical problem illustrated by the following example. Consider a flow through a duct with a length L of 30 m, a height H of 1 m, and a variable breadth geometry $b(x)$ depicted in Figure 5.7, and given by

$$\begin{aligned} &b(x) = 2 \text{ m} \qquad \text{for } x < 3 \text{ m}, \\ &b(x) = 1.5 + 0.5\cos\left(\frac{\pi x}{L}\right) \qquad \text{for } 3 \text{ m} \geq x \leq 13\text{m} \\ &, b(x) = 1 \text{ m} \qquad \text{for } 13 \text{ m} < x < 17\text{m}, \\ &b(x) = 1.5 - 0.5\cos\left(\frac{\pi x}{L}\right) \qquad \text{for } 17 \text{ m} \geq x \leq 27\text{m} \\ &, b(x) = 2 \text{ m} \qquad \text{for } 27 \text{ m} < x < 30 \text{ m}, \end{aligned} \tag{5.88}$$

(5.89)

where $L = 10$ m and the domain of $x = [0, 30]$. The flow velocity in the duct follows from

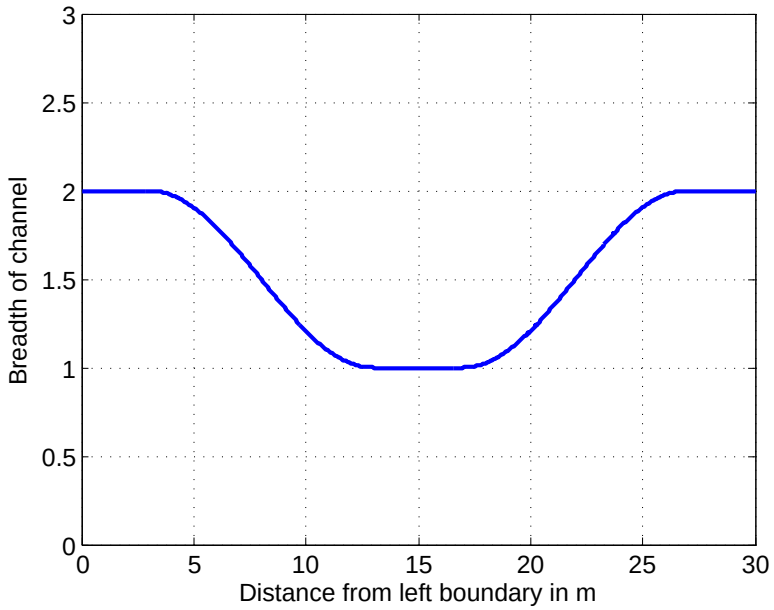

Figure 5.7: Breadth profile along the length of the channel

the mass balance for an incompressible flow and is given by

$$\widetilde{\langle u\rangle}(x,z) = \frac{q}{b(x)}, \tag{5.90}$$

where q is the discharge in m^2/s. For a steady state inviscid flow with $\widetilde{\langle w \rangle} = 0$, the $\hat{x}$-direction momentum equation reduces to

$$\rho \widetilde{\langle u \rangle} b \frac{\partial \widetilde{\langle u \rangle}}{\partial x} = -b \frac{\partial \widetilde{\langle P \rangle}}{\partial x}. \tag{5.91}$$

In those sections of the duct where the breadth is constant, there are no flow accelerations and the advective acceleration terms are zero. Analytical expressions for the different terms of the momentum equation follow from substituting Equation (5.90) in Equation 5.91. In the section where the duct narrows, the analytical expression of the advective term is given by

$$\rho \widetilde{\langle u \rangle} b \frac{\partial \widetilde{\langle u \rangle}}{\partial x} = \frac{2\rho q^2 \sin\left(\frac{\pi x}{L}\right)}{L\left(\cos\left(\frac{\pi x}{L}\right) + 3\right)^2}, \tag{5.92}$$

and for the widening section this is

$$\rho \widetilde{\langle u \rangle} b \frac{\partial \widetilde{\langle u \rangle}}{\partial x} = -\frac{2\rho q^2 \sin\left(\frac{\pi x}{L}\right)}{L\left(\cos\left(\frac{\pi x}{L}\right) - 3\right)^2}. \tag{5.93}$$

Both b, and $\widetilde{\langle P \rangle}$ are continuous functions in x and z. For an inviscid flow, $\frac{\partial^2 P}{\partial x^2}$ follows from dividing the advective terms of the momentum equations by b, differentiating by x, and then multiplying by b again as is given for the narrowing section by

$$b \frac{\partial}{\partial x}\left(\rho \widetilde{\langle u \rangle} \frac{\partial \widetilde{\langle u \rangle}}{\partial x}\right) = 2\pi^2 q^2 \rho \left[\frac{\cos\left(\frac{\pi x}{L}\right)\left(\cos\left(\frac{\pi x}{L}\right) + 3\right) + 3\sin^2\left(\frac{\pi x}{L}\right)}{L^2\left(\cos\left(\frac{\pi x}{L}\right) + 3\right)^3}\right], \tag{5.94}$$

and for the widening section by

$$b \frac{\partial}{\partial x}\left(\rho \widetilde{\langle u \rangle} \frac{\partial \widetilde{\langle u \rangle}}{\partial x}\right) = -2\pi^2 q^2 \rho \left[\frac{\cos\left(\frac{\pi x}{L}\right)\left(3 - \cos\left(\frac{\pi x}{L}\right)\right) - 3\sin^2\left(\frac{\pi x}{L}\right)}{L^2\left(3 - \cos\left(\frac{\pi x}{L}\right)\right)^3}\right]. \tag{5.95}$$

According to the physical assumptions $\frac{\partial}{\partial x}\left(b \frac{\partial \widetilde{\langle P \rangle}}{\partial x}\right) = b\left(\frac{\partial^2 \widetilde{\langle P \rangle}}{\partial x^2}\right)$ and hence these equations should match the answers obtained from directly differentiating the advective terms as given for the narrowing section by

$$\frac{\partial}{\partial x}\left(\rho \widetilde{\langle u \rangle} b \frac{\partial \widetilde{\langle u \rangle}}{\partial x}\right) = 2\pi^2 q^2 \rho \left[\frac{\cos\left(\frac{\pi x}{L}\right)\left(\cos\left(\frac{\pi x}{L}\right) + 3\right) + 2\sin^2\left(\frac{\pi x}{L}\right)}{L^2\left(\cos\left(\frac{\pi x}{L}\right) + 3\right)^3}\right], \tag{5.96}$$

and for the widening section by

$$\frac{\partial}{\partial x}\left(\rho\widetilde{\langle u\rangle}b\frac{\partial\widetilde{\langle u\rangle}}{\partial x}\right)=-2\pi^2q^2\rho\left[\frac{\cos\left(\frac{\pi x}{L}\right)\left(3-\cos\left(\frac{\pi x}{L}\right)\right)-2\sin^2\left(\frac{\pi x}{L}\right)}{L^2\left(3-\cos\left(\frac{\pi x}{L}\right)\right)^3}\right]. \tag{5.97}$$

The difference is given by $\frac{\partial b}{\partial x}\frac{\partial P}{\partial x}$ and since this is not equal to zero. Different results are found when calculating the pressure field from

$$\frac{\partial^2\widetilde{\langle P\rangle}}{\partial x_i^2}=RHS, \tag{5.98}$$

where RHS either follows from dividing Equations (5.94) and (5.95) by b, or from dividing Equations (5.96) and (5.97) by b. When the right hand side of the pressure Poisson equation is obtained from Equations (5.94) and (5.95), then the Poisson equation for the velocity correction becomes

$$\frac{\partial^2\widetilde{\langle P\rangle}}{\partial x_i^2}=\frac{1}{\delta t}\frac{\partial\tilde{\rho}\widetilde{\langle u\rangle}_i^{r1}}{\partial x_i}, \tag{5.99}$$

which does not satisfy mass continuity. However when the right hand side follows from Equations (5.94) and (5.95), then the Poisson equation for the velocity correction is given by

$$\frac{\partial}{\partial x}b\frac{\partial\widetilde{\langle P\rangle}}{\partial x}=\frac{1}{\delta t}\frac{\tilde{\rho}\widetilde{\langle u\rangle}_i^{r1}b}{\partial x_i}, \tag{5.100}$$

and continuity is preserved. Since, mathematically speaking, $\frac{\partial}{\partial x}\left(b\frac{\partial\widetilde{\langle P\rangle}}{\partial x}\right)\neq b\left(\frac{\partial^2\widetilde{\langle P\rangle}}{\partial x^2}\right)$ and $\frac{\partial\widetilde{\langle P\rangle}}{\partial x}$ is unknown for accelerating flows it is not possible to arrive at a Poisson equation of the form

$$\frac{\partial^2\widetilde{\langle P\rangle}}{\partial x_i^2}=RHS. \tag{5.101}$$

Hence a new way of solving the Poisson equation is used that satisfies continuity. It is given that b and $\widetilde{\langle P\rangle}$ are both continuous functions in x and z. A function $F(x,z)$ is now defined such that

$$\frac{\partial F(x,z)}{\partial x}=b\frac{\partial\widetilde{\langle P\rangle}}{\partial x}, \tag{5.102}$$

and

$$\frac{\partial F(x,z)}{\partial z}=b\frac{\partial\widetilde{\langle P\rangle}}{\partial z}. \tag{5.103}$$

The Poisson equation is now given by

$$\frac{\partial^2 F}{\partial x^2} + \frac{\partial^2 F}{\partial z^2} = \nabla \cdot M_i \tag{5.104}$$

where ∇ is the divergence operator, M_i contains the advective terms, shear stress terms, and normal stress terms from respectively the $\hat{x}$-direction momentum equation ($i = 1$), and $\hat{z}$-direction momentum equation ($i = 2$). Since $F(x, z)$ is an arbitrary function, the result of the Poisson equation has no physical meaning. However the gradients in F give the pressure gradients multiplied with the breadth required to solve the momentum equations. Since the $F(x, z)$ has no physical meaning, it is not possible to derive Dirichlet boundary conditions for the pressure Poisson equation. Hence the boundary conditions have to be given by $b\frac{\partial\widetilde{\langle P\rangle}}{\partial x_i}$. The velocity boundary conditions therefore have to be of the Dirichlet type. As a preliminary test, the equations have been solved for

$$b = \cos\left(\frac{2\pi}{L}(x+z)\right), \tag{5.105}$$

and

$$\widetilde{\langle P\rangle} = e^{(2x+z)},$$

where l is the length of the computational domain, and is 1 m for the test case considered. Hence

$$\frac{\partial F}{\partial x} = b\frac{\partial\widetilde{\langle P\rangle}}{\partial x} = \frac{2e^{(2x+z)}}{L}\left[L\cos\left(\frac{2\pi\,(x+z)}{L}\right) - \pi\sin\left(\frac{2\pi\,(x+z)}{L}\right)\right], \tag{5.106}$$

and

$$\frac{\partial F}{\partial z} = b\frac{\partial\widetilde{\langle P\rangle}}{\partial z} = \frac{e^{(2x+z)}}{L}\left[L\cos\left(\frac{2\pi\,(x+z)}{L}\right) - 2\pi\sin\left(\frac{2\pi\,(x+z)}{L}\right)\right]. \tag{5.107}$$

Now the Poisson equation is solved whereby the right hand side follows from the divergence of Equations (5.106) and (5.107). Figure 5.8 shows the comparison between the gradient field given by Equation 5.106 and the gradient field obtained from differentiating the numerical results for F. For a clear comparison the results have been manually offset by 80 N/m^2. The close agreement between the two gradient fields shows that a divergence-free solution of the momentum equations can be obtained.

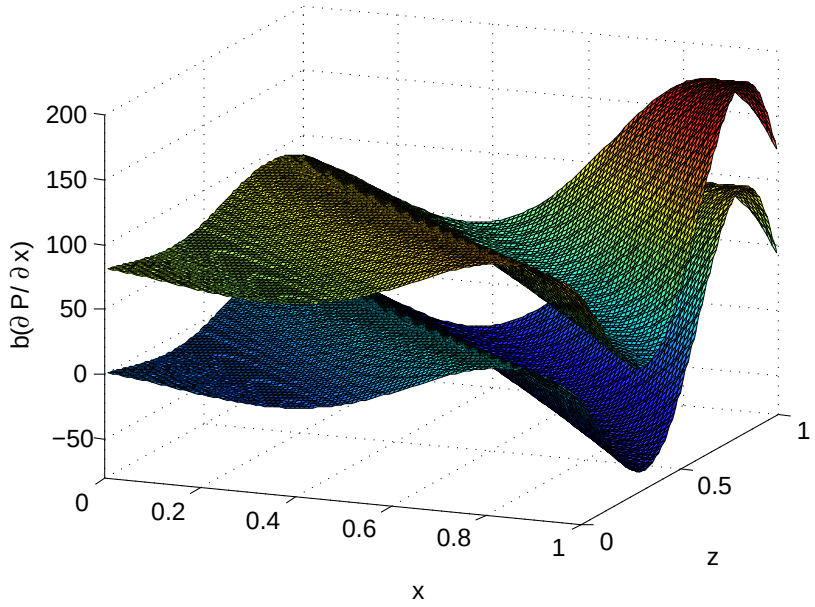

Figure 5.8: The top figure shows the result of Equation 5.106. The bottom figure shows $\frac{\partial F}{\partial x}$ after differentiation of the solution of the Poisson equation. The figures have been offset by 80 N/m^2 for clarity.

The analysis of the different pressure correction methods, given in this chapter, has led to the choice of the SIMPLER method for solving the momentum equations. In each iteration step the velocity field is calculated with the unconditionally stable Alternate Direction Implicit method. The velocity field is then corrected by solving the Poisson equation, and after updating of the matrix coefficients, the pressure field is updated. For all Von Neumann boundary conditions for the pressure, the Poisson equation is rapidly solved with the Discrete Cosine Transform solver. Tests used for validating the solver are given in the Chapter 6.

Chapter 6

Validation of the 2D flow model

This chapter describes the test cases used to verify, and validate the numerical solver of the breadth integrated Navier-Stokes equations for an incompressible flow and varying breadth geometry. The test cases include a fully developed laminar flows in an inclined duct, a flow in a duct containing a hump, a flow over a backward facing step, and a lid driven laminar flow in a square cavity. In discussing the validation tests, the terminology used to describe the location of the boundaries is:

- The left boundary ($x = 0$)
- The right boundary ($x = L$)
- The bottom boundary ($z = 0$)
- The top boundary ($z = H$)
- The near wall boundary ($y = 0$)
- The far wall boundary ($y = B$)

The x-axis is always taken along the center line of the channel from left to right, the z axis perpendicular to the x-axis pointing upwards, and the y-axis perpendicular to both the x and z axis pointing from the near wall to the far wall, also see Figure (4.1). In discussing the pressure boundary condition, for clarity, purely the non-hydrostatic contribution is mentioned indicated by $\widetilde{\langle P \rangle}_{NH}$.

6.1 Test cases for a constant breadth

6.1.1 Gravity driven laminar flow in an inclined duct with slip boundary conditions at the near and far wall

The first test case is a gravity driven laminar flow in an inclined duct under a gradient of 1/100. The duct has a uniform breadth b of 1 m. The boundary conditions consist of open boundaries in the $\hat{x}$-direction, an impenetrable no slip boundary conditions along the top and bottom wall of the duct, and slip boundary conditions at the near and far wall of the duct. The computational domain has a length L of 1 m and height H of 1 m, and is subdivided into a grid of 101×101 grid points, giving a spatial step of 1 cm. The number of grid points were determined via grid convergence tests with a grid of 20×20. Similar results were found. The pressure gradient along the duct is given by

$$\frac{\widetilde{\partial \langle P \rangle}}{\partial x} = \frac{\widetilde{\partial \langle P \rangle_p}}{\partial x} + \frac{\widetilde{\partial \langle P \rangle_i}}{\partial x}, \tag{6.1}$$

where the first gradient term on the right hand side follows from the calculation of the Poisson equation with the non-hydrostatic contribution to the pressure boundary conditions given by $\widetilde{\langle P \rangle}_{NH}|_{x=0} = \widetilde{\langle P \rangle}_{NH}|_{x=L} = 0$, corresponding with $\widetilde{\langle w \rangle}|_{x=0} = \widetilde{\langle w \rangle}|_{x=L} = 0$, and $\frac{\partial \widetilde{\langle u \rangle}}{\partial x}|_{x=0} = \frac{\partial \widetilde{\langle u \rangle}}{\partial x}|_{x=L} = 0$. The second gradient term on the right hand side of Equation (6.1) is the pressure that follows from the gradient of the duct i_p, and is given by $\rho_w g i_p$. The fluid's dynamic viscosity $\eta = 10$ Pa-s, and the flow has zero turbulent kinetic energy. The initial conditions are given by $\widetilde{\langle u \rangle} = \widetilde{\langle w \rangle} = \widetilde{\langle P \rangle}_{NH} = 0$, and the test was run until a steady state condition was obtained. For the flow described in this test case, the Reynolds-Averaged Navier-Stokes equations reduce to the Navier-Stokes equations for laminar flow. The analytical steady state solution is derived from the $\hat{x}$-direction momentum equation. With $\widetilde{\langle w \rangle} = 0$, $\frac{\partial \widetilde{\langle u \rangle}}{\partial x} = 0$, and constant values for both η and b, the $\hat{x}$-direction momentum equation reduces to

$$-\frac{\partial \langle P \rangle}{\partial x} = \eta \frac{\partial^2 \widetilde{\langle u \rangle}}{\partial z^2}. \tag{6.2}$$

With $-\frac{\partial\langle P\rangle}{\partial x} = \rho_w g i_p$, the analytical velocity profile is given by

$$\widetilde{\langle u\rangle}(z) = \frac{1}{2}\frac{\rho_w g i_p}{\eta} z\,(z - D) \tag{6.3}$$

where D is the height of the duct, i_p the slope gradient of the duct, which is negative for a flow going right, and z is the distance above the duct invert level. Figure (6.1) shows the excellent agreement between the analytical and numerical solution. This confirms that the $\hat{x}$-direction momentum equation accounts for the viscous effects correctly, and that the SIMPLER method converges nicely to a steady state solution.

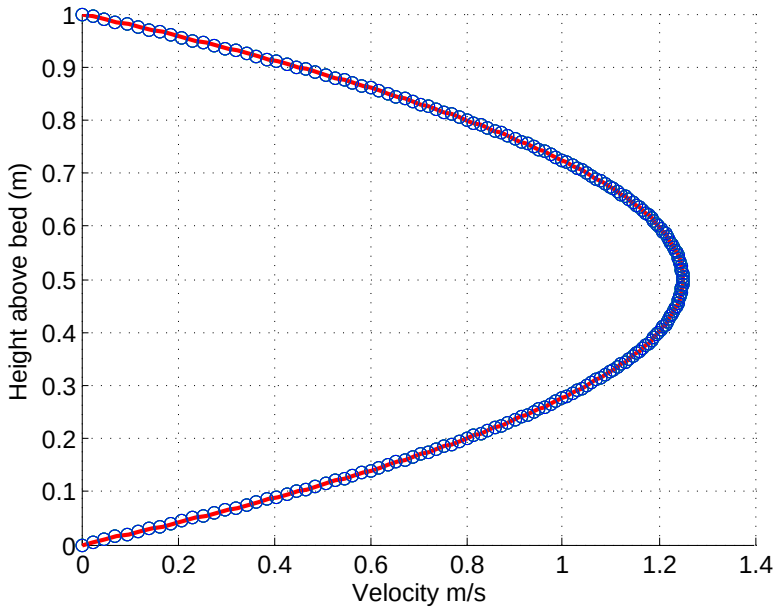

Figure 6.1: Analytical solution (red line) and numerical solution (blue dots) of a pipe flow.

6.1.2 Gravity driven laminar flow in an inclined duct with drag boundary conditions at the near and far walls

The second test only differs from the first test by accounting for drag at the side walls. For a drag coefficient c_f of 0.015 at the near and far wall boundaries, the steady state parabolic velocity profile is given in Figure 6.2. The effect of the drag coefficient on the flow is indicated by the difference between the numerical result, and the analytical result for a laminar flow in an inclined duct without sidewall drag, given by Equation (6.3). The additional wall shear stress at the near and far wall extract energy from the flow leading to an overall reduction in

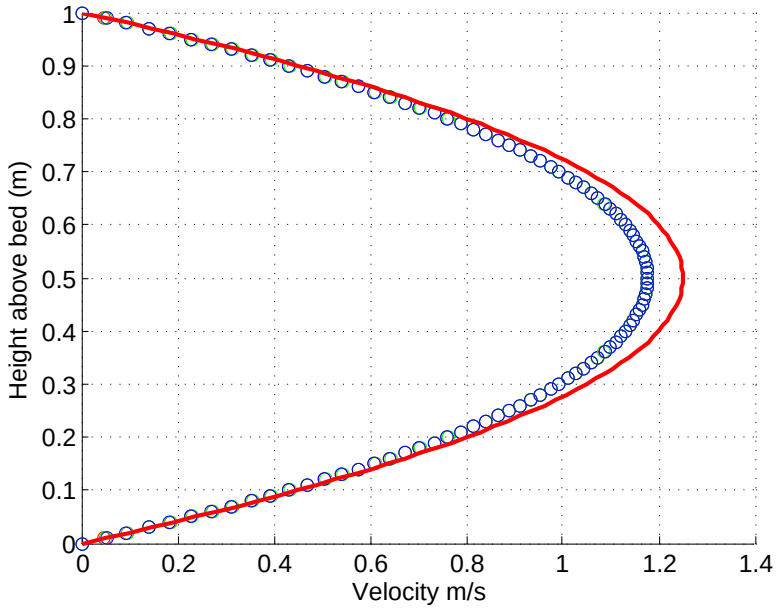

Figure 6.2: Analytical solution of pipe flow with no side wall drag(red line), and numerical solution of pipe flow with side wall drag (blue dots).

momentum transfer and hence a reduction in flow velocity over the height of the duct. The effects of the side wall drag increases with the flow velocity which behaviour is represented correctly by the numerical result in Figure 6.2.

6.1.3 Flow down a hump in a duct

To illustrate the density fraction method, the flow field was calculated for a laminar flow down a hump in a duct with constant breadth. The computational domain has a height H of 1 m and a constant breadth of 1 m. The length of the computational domain was set to 30 m to allow for the boundary layer to fully develop. The computational domain was split up in a grid with 1501×50 grid points giving a spatial step size of 0.02 m. Tests with a finer grid size gave similar results. The height of the hump above a horizontal reference level is given by the bed height (See Figure 6.3) expressed as

$$h_{bed} = 0.5 \text{ m for } x \leq 3 \text{ m}, \tag{6.4}$$

$$h_{bed} = 0.25 + 0.25\cos(\pi(x-3)/12) \text{ for } 3 \text{ m} < x \leq 15 \text{ m},$$

$$h_{bed} = 0 \text{ for } x > 15 \text{ m},$$

The velocity boundary conditions upstream are given by

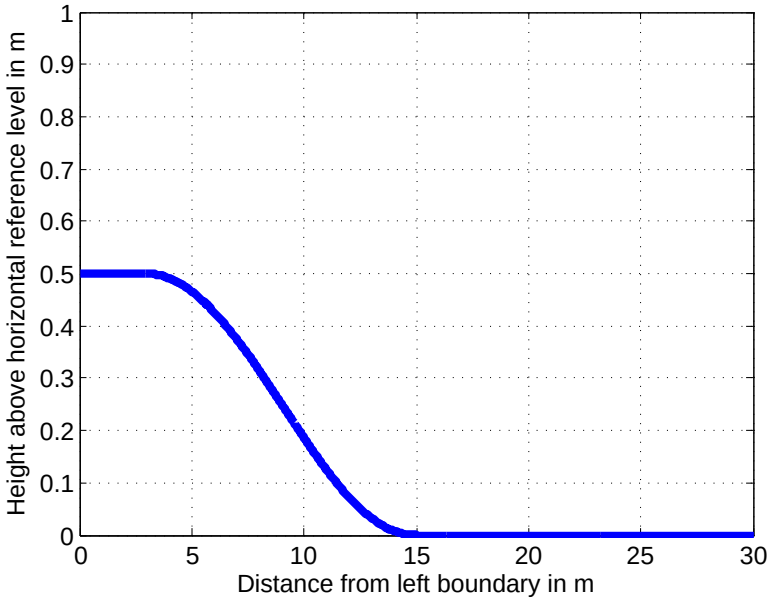

Figure 6.3: Depth profile for the flow down a hump test

$$u(z)|_{x=0} = -48(0.5 - z)(1 - z) \text{ m/s for } 0.5 \text{ m} \leq z \leq 1 \text{ m} \tag{6.5}$$
$$u(z)|_{x=0} = 0 \text{ for } 0 \leq z < 0.5 \text{ m}$$

and downstream by

$$u(z)|_{x=L} = 6(z - z^2) \text{ m/s} \tag{6.6}$$

At the near and far wall slip boundary conditions are assumed. The no-slip boundary conditions at the top and bottom walls are given by $\widetilde{\langle u \rangle} = \widetilde{\langle w \rangle} = 0$. The results for the first 18 m of the flow domain are depicted in Figure 6.4. Although neither comparative tests, nor analytical results are available for this test case, the results show that even under a shallow slope with gradual changes in bed gradient, a flow with $\eta = 10$ Pa-s separates from the slope. Falconer (1993) mentions that in the case of very simple eddy viscosity models a constant eddy viscosity is used with a typical value of $\eta = 10$ Pa-s. Hence this test case for a laminar flow with $\eta = 10$ Pa-s indicates the necessity of using a 2D flow representation instead of a 1D representation when simulating flows over beds which significantly change in level.

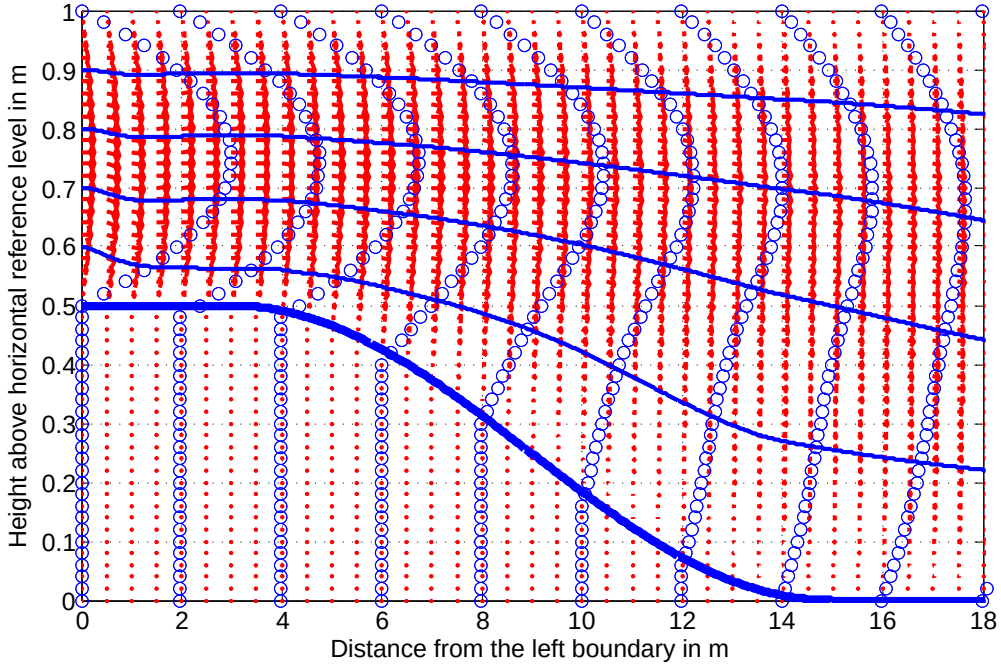

Figure 6.4: Velocity field for a flow down a hump

6.1.4 Laminar versus turbulent steady state free surface flow over an inclined bed with constant depth

To show the model's ability to deal with impenetrable surfaces, free surfaces, and variable eddy viscosities within the computational domain, both the laminar and turbulent velocity profiles are given for a gravity driven free surface flow over a 0.1 m high bed. The computational domain has a length L of 1 m, a height H of 1 m, and has been subdivided into 101×101 gridpoints giving a spatial step size of 0.01 m. Increase in spatial step sizes gave the same results. The average flow velocity is 1 m/s, the breadth constant, the flow depth 0.7 m, and the slope gradient 1/100. The boundary conditions are given by $\frac{\partial \widetilde{\langle u \rangle}}{\partial x} = 0$ and $\widetilde{\langle w \rangle} = 0$ at $x = 0$ and $x = L$, a $\widetilde{\langle u \rangle} = \widetilde{\langle w \rangle} = 0$ at $z = 0$, $\frac{\partial \widetilde{\langle u \rangle}}{\partial z} = 0$ at the free surface, and slip boundary conditions at $y = 0$ and $y = B$. The non-hydrostatic contribution to the pressure boundary conditions is given by $\widetilde{\langle P \rangle}_{NH}|_{x=0} = \widetilde{\langle P \rangle}_{NH}|_{x=L} = 0$. The viscosity required for an average flow velocity of 1 m/s is calculated from

$$\tau = -\rho_w g \, (h - z) \, i_b, \tag{6.7}$$

and

$$\tau = \eta \frac{\partial \widetilde{\langle u \rangle}}{\partial z}, \tag{6.8}$$

where τ is the shear stress, i_b is the bed gradient, η is the viscosity in Pa-s, h is the water depth, and z is the distance above the raised bed. After some manipulation this gives

$$\eta = \frac{\rho_w g i_b h^2}{3\overline{\widetilde{\langle u \rangle}}}, \tag{6.9}$$

where $\overline{\widetilde{\langle u \rangle}}$ is the breadth and depth-averaged velocity. For a breadth- and depth-averaged velocity of 1 m/s, $\eta = 16.33$ Pa-s. This leads to the parabolic shaped laminar velocity profile indicated in red in Figure 6.5. A logarithmic velocity profile was created using the

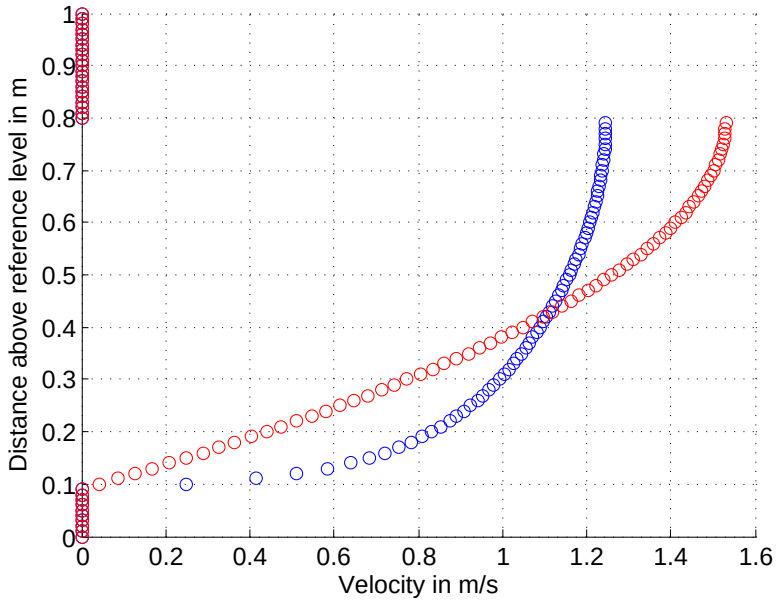

Figure 6.5: Turbulent (blue) and Laminar (red) velocity profiles for a free surface flow over a horizontal plane

parabolic-constant eddy viscosity description for η given by (Van Rijn, 1984)

$$\eta = 4\frac{z}{h}\left(1 - \frac{z}{h}\right)\eta_{max} \text{ for } \quad \frac{z}{h} \leq \frac{1}{2}, \tag{6.10}$$

$$\text{and} \quad \eta = \eta_{max} \text{ for } \quad \frac{z}{h} > \frac{1}{2}.$$

Because of open boundaries in $\hat{x}$-direction, and no flow in $\hat{z}$-direction $\frac{\partial \widetilde{\rho k b}}{\partial x} = \frac{\partial \widetilde{\rho k b}}{\partial z} = 0$. Hence the turbulent kinetic energy k was ignored. Through numerical experimentation was found that for a breadth and depth-averaged velocity of 1 m/s, $\eta_{\max} = 50$Pa-s, leading to the blue logarithmic velocity profile depicted in Figure 6.5. Both velocity profiles clearly show that

the results of the model are consistent with the free surface boundary of a zero shear stress over the free surface given by $\frac{\partial \widetilde{\langle u \rangle}}{\partial z} = 0$. The test case also shows that the model is able to account correctly for a variable free eddy viscosity over the depth

6.1.5 Laminar flow over a backward facing step in a duct with a constant breadth

The first test case for simulating rotating flows is that of a flow over a backward facing step for an inflow Reynolds number of 100 (η = 10Pa-s) and an inflow Reynolds number of 8 (η = 125 Pa-s). For this test case the inflow Reynolds number is defined as

$$Re = \frac{\rho_w V D}{\eta}, \tag{6.11}$$

where D is the height of the inlet channel, and V is the average inlet velocity which for a laminar flow corresponds with two-thirds of the maximum inlet velocity (O' Leary and Mueller, 1969). The step height, and the height of the inlet region, are both equal to $H/2$, the downstream channel has a unit height H and a constant breadth b. A channel length of $30H$ is used to allow the boundary layer to develop fully before reaching the downstream boundary with as boundary condition $\frac{\partial \widetilde{\langle u \rangle}}{\partial x} = 0$, and $\widetilde{\langle w \rangle} = 0$ (Gartling, 1990). The non-hydrostatic contribution to the downstream pressure boundary condition is 0. The mean flow velocity over the height of the computational domain is 1 m/s in both cases. The computational domain for this test case is given by $L = 30$ m, $H = 1$ m, and $B = 1$ m. The computational has been spit up in a grid of 1501×51 grid points giving a grid size of 0.02 m. Grid refinement tests were performed and gave similar results. The boundary conditions along the channel are given by a no-slip boundary condition at the top and bottom with $\widetilde{\langle u \rangle} = \widetilde{\langle w \rangle} = 0$, and slip boundary conditions for the side walls at $y = 0$ and $y = B$. The left velocity boundary conditions consist of $\widetilde{\langle w \rangle} = 0$ everywhere, and $\widetilde{\langle u \rangle} = 0$ over the height of the step. At the inlet, $\widetilde{\langle u \rangle}$ is given by the parabolic velocity distribution

$$u(z)|_{x=0} = -48(0.5 - z)(1 - z) \text{ m/s for } 0.5 \text{ m} \leq z \leq 1 \text{ m}. \tag{6.12}$$

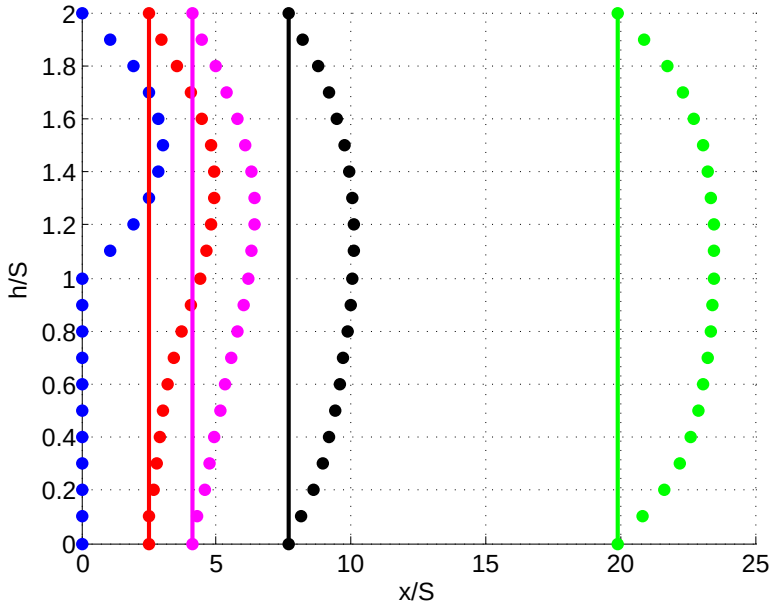

Figure 6.6: Velocity profiles for a laminar flow over a backward facing step $Re = 100$

The predicted reattachment length for $Re = 100$ is validated against experimental data by Armaly et al. (1983). Armaly et al. (1983) measured the reattachment length and velocity distribution for Reynolds numbers in the range between 70 and 8000 to cover the laminar, transitional and turbulent flow regime. Figure 6.6 shows how the flow profile over the depth changes with location for a steady state flow over a backward facing step for $Re = 100$. The obtained flow profiles match closely the experimental data by Armaly et al. (1983). The results for $Re = 8$ were compared against the reattachment length found experimentally by O' Leary and Mueller (1969) and numerically by Rogers (2001)Rogers (2001). O' Leary and Mueller (1969) found a reattachment length of $1.5S$, where S is the step height for a flow with a Reynolds no of 7.9. Rogers (2001) found a reattachment length of $1.29S$ trying to reproduce the experimental results by O' Leary and Mueller (1969) using a flow model with adaptive quadtree grids. The present numerical results are shown in Figures 6.7 and 6.8; Figure 6.7 shows a reattachment length of S, which is smaller than the values given by O' Leary and Mueller (1969) or Rogers (2001). Convergence tests performed with a smaller grid size give identical results. The vector plots in Figure 6.8, and Figure 6.7 show that the velocity is very small near the bed at $x = S$. Between $x = S$ and $x = 1.3S$ the magnitude of the velocity is of the order or an order smaller than the spatial discretization error, which could account for the discrepancy found with the results by Rogers (2001). Hence the comparison obtained from the model was deemed sufficient.

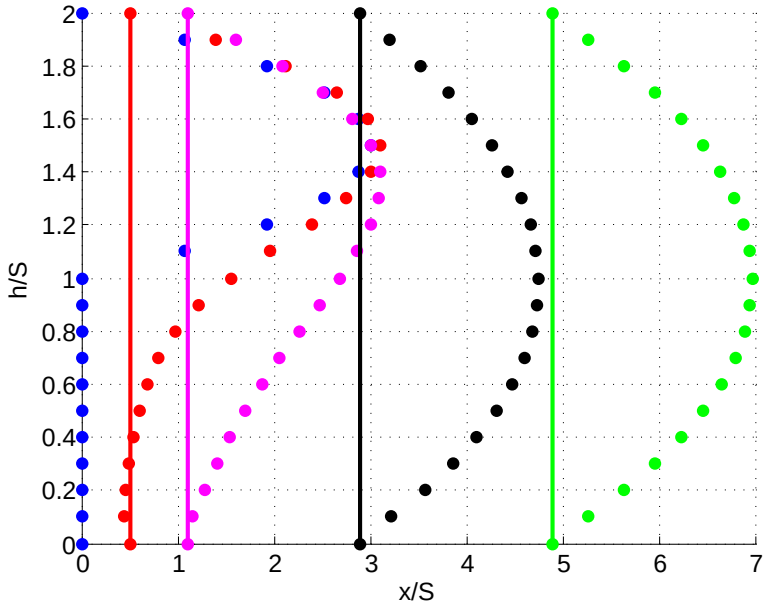

Figure 6.7: Velocity profiles for a laminar flow over a backward facing step $Re = 8$

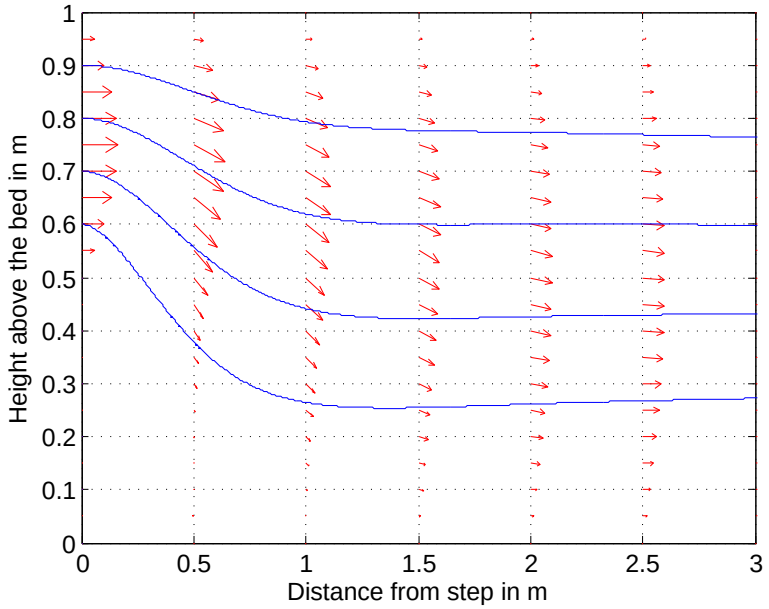

Figure 6.8: Vectorplot of a laminar flow over a backward facing step $Re = 8$

6.1.6 Lid driven cavity flow

The second test case for rotational flows is the lid driven cavity flow case. The problem is described by a closed box, filled with fluid, whose lid moves to the right with a velocity of 1 m/s. The dimensions of the computational domain are 1×1 m and the spatial step following from grid convergence tests is 1 cm. The experiment was performed for $Re = 100$ and $Re = 400$, whereby by the Reynolds number Re is defined as

$$Re = \frac{\rho_w u_{lid} H}{\eta}, \tag{6.13}$$

where H is the height of the box and u_{lid} the velocity with which the lid moves to the right. The velocity boundary conditions are given by $\widetilde{\langle u \rangle}|_{x=0} = \widetilde{\langle u \rangle}|_{x=L} = \widetilde{\langle u \rangle}|_{z=0} = \widetilde{\langle w \rangle}|_{x=0} = \widetilde{\langle w \rangle}|_{x=L} = \widetilde{\langle w \rangle}|_{z=0} = \widetilde{\langle w \rangle}|_{z=H} = 0$, and $\widetilde{\langle u \rangle}|_{z=H} = 1$ m/s. The results for the validation test are compared against the model results from Ghia et al. (1982), who solved the 2D Navier-Stokes equations using a stream-function vorticity-model. Figures 6.9 and 6.10 show the velocity profiles through respectively the horizontal and vertical centerline of computational domain together with the results given by Ghia et al. (1982) for $Re = 100$. Figures 6.11 and 6.12 show the comparisons for $Re = 400$. Figure 6.13 presents the with the velocity profiles corresponding pressure distribution after subtracting the hydrostatic pressure distribution, for $Re = 100$. Comparison of the velocity profiles with the velocity profiles from Ghia

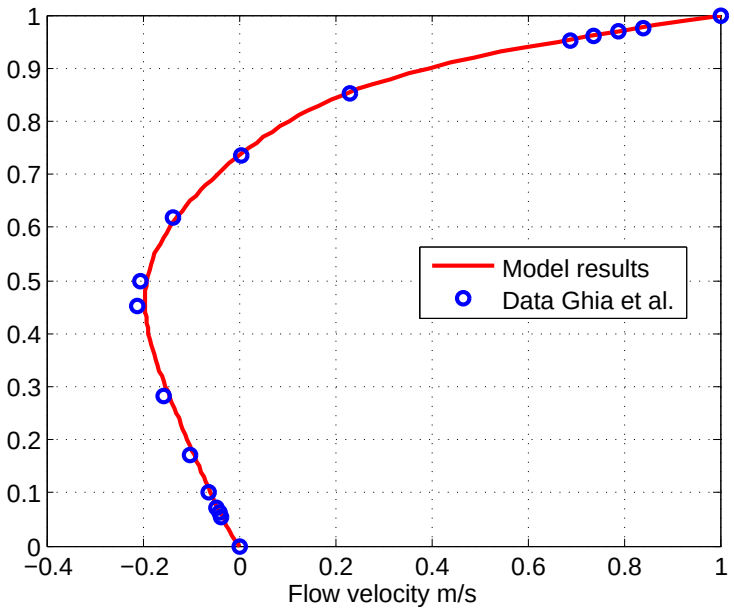

Figure 6.9: Horizontal flow velocity through the vertical center line for a lid driven cavity flow of Re=100

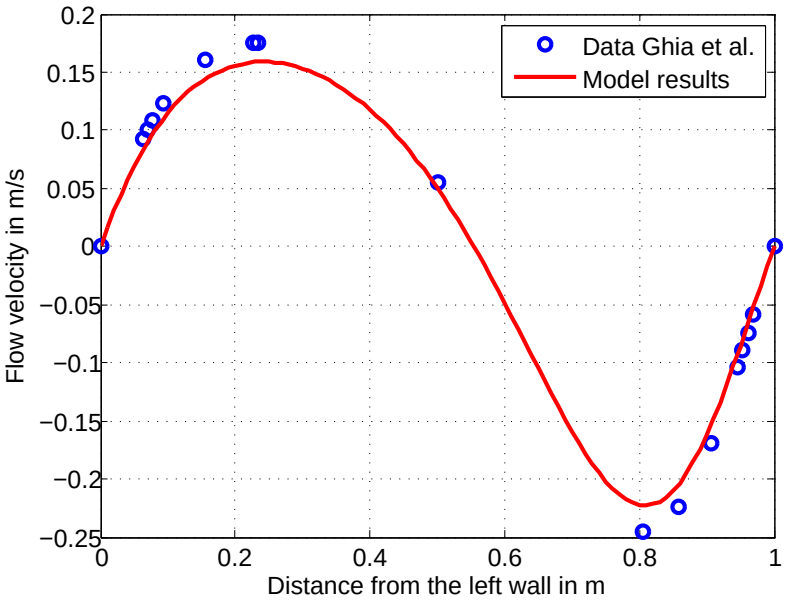

Figure 6.10: Vertical flow velocity through the horizontal center line for a lid driven cavity flow of Re=100

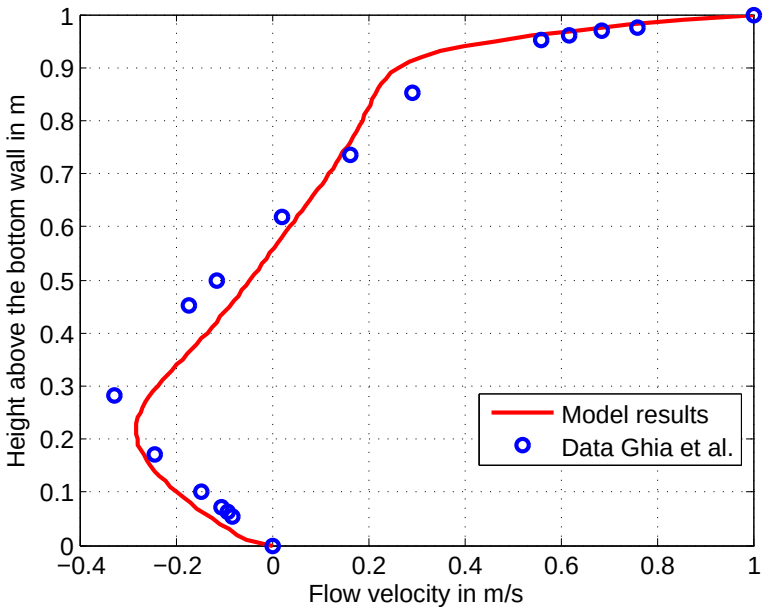

Figure 6.11: Horizontal flow velocity through the vertical center line for a lid driven cavity flow of Re=400

et al. (1982) shows that, for both $Re = 100$ and $Re = 400$, the $\hat{x}$-direction and $\hat{z}$-direction momentum equations are solved correctly using the Alternate Direction Implicit solver, that the Discrete Cosine Transform solver for the Poisson equation accurately calculates correct pressure profiles for the case of all Von Neumann boundary conditions for the pressure, and that the SIMPLER algorithm gives good convergence towards the overall steady state solution for a constant breadth.

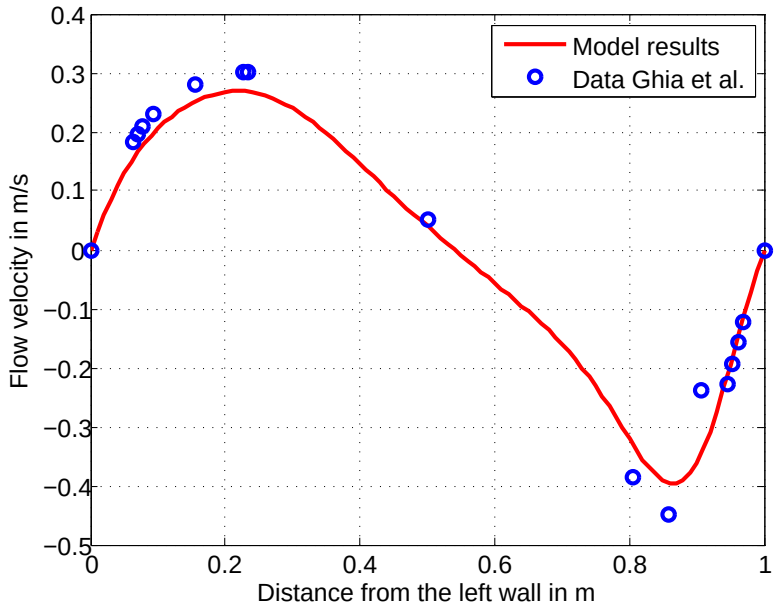

Figure 6.12: Vertical flow velocity through the horizontal center line for a lid driven cavity flow of Re=400

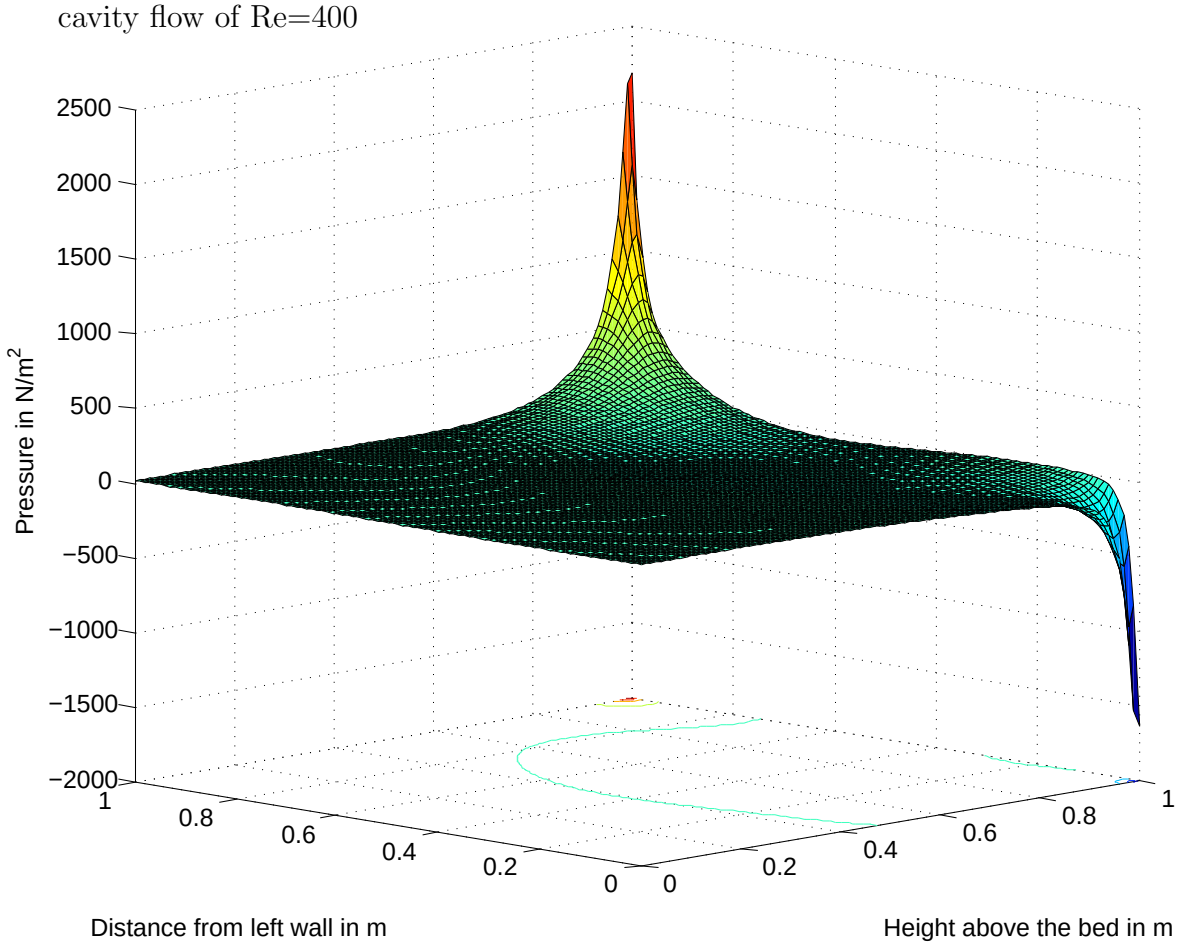

Figure 6.13: Pressure profile minus the hydrostatic pressure for a lid driven cavity flow of Re=100

The results presented here show the ability of the model to solve accurately a variety of test problems involving a constant breadth with or without accounting for side wall drag. The solvers of the momentum equations and Poisson equations have been extensively tested and the results are in acceptable agreement with the solutions. The following section discusses the ability of the model to account for a variable breadth geometry.

6.2 Test cases for a variable breadth geometry

6.2.1 Couette flow in a horizontal duct with a breadth varying over the height

To show how the variation in breadth influences the velocity distribution in the $\hat{z}$-direction, the results of Couette flow in a duct with variable breadth geometry are compared against their analytical solution. For a Couette flow the momentum equations reduce to

$$\frac{\partial}{\partial z} b\eta \frac{\partial \widetilde{\langle u \rangle}}{\partial z} = 0 \tag{6.14}$$

The test flow depth in the duct is $H = 1$ m and is confined at the bottom and the top by impenetrable no slip boundary conditions. The top boundary moves in the $\hat{x}$-direction with a velocity of 1 m/s. The computational domain has a length $L = 1$ m and height H of 1 m and is subdivided into a grid of 50×50 grid points, which gave similar results to a grid of 20×20 grid points. The boundary conditions are given by $\frac{\partial \widetilde{\langle u \rangle}}{\partial x} = 0$, and $\widetilde{\langle w \rangle} = 0$ at $x = 0$ and $x = L$, $\widetilde{\langle u \rangle} = \widetilde{\langle w \rangle} = 0$ at $z = 0$, $\widetilde{\langle u \rangle} = 1$ m/s and $\widetilde{\langle w \rangle} = 0$ at $z = H$, and slip boundary conditions at $y = 0$ and $y = B$. The non-hydrostatic contribution to the pressure boundary conditions are given by $\widetilde{\langle P \rangle}_{NH}|_{x=0} = \widetilde{\langle P \rangle}_{NH}|_{x=L} = 0$. The initial flow velocities are $\widetilde{\langle u \rangle} = \widetilde{\langle w \rangle} = 0$. Two cases were tested for.

1. In the first test case the breadth increases linearly with the distance above the bed such that $b|_{z=0} = 1$ m, and $\frac{\partial b}{\partial z} = 0.1$. The analytical steady state solution of the flow profile follows from

$$\frac{\partial}{\partial z} b\eta \frac{\partial \widetilde{\langle u \rangle}}{\partial z} = 0, \tag{6.15}$$

or

$$b\eta\frac{\partial\widetilde{\langle u\rangle}}{\partial z} = C, \tag{6.16}$$

where C is an arbitrary constant. For $b = 1 + 0.1z$, and $\eta = 10$Pa-s,

$$\frac{\partial\widetilde{\langle u\rangle}}{\partial z} = \frac{C}{10 + 10z}. \tag{6.17}$$

With $\widetilde{\langle u\rangle}|_{z=H} = 1$ m/s

$$\widetilde{\langle u\rangle} = 1.4427 \cdot \ln(1 + z) \tag{6.18}$$

The analytical solution for a duct with a breadth linearly increasing over the height is given together with the numerical solution in Figure 6.14.

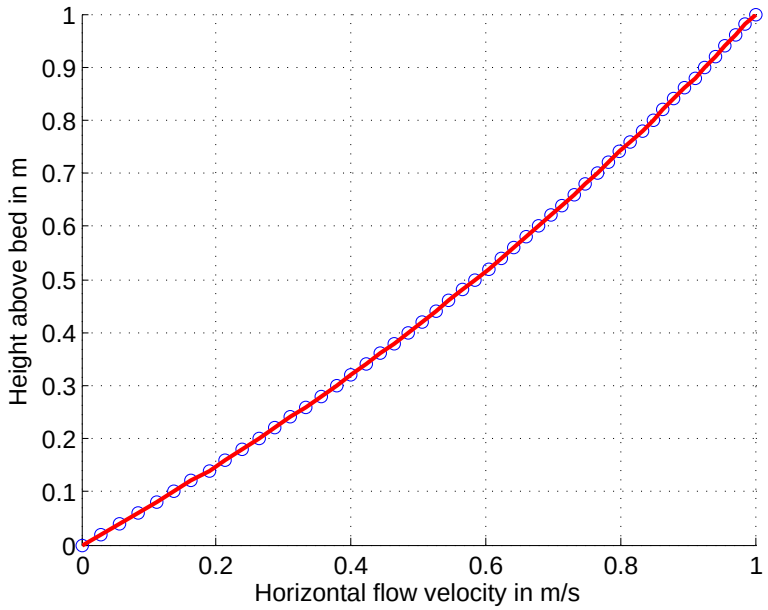

Figure 6.14: Analytical solution (red line) and numerical solution (blue dots) of a Couette flow with a linearly increasing breadth geometry over the height.

2. In the second test case the breadth changes over the height according to

$$b(z) = 1 + 0.5\cos\left(\frac{2\pi}{z/H}\right) \tag{6.19}$$

Solving Equation (6.14) for a breadth profile given by Equation 6.19 gives the analytical solution

$$y = 0.0184 \cdot 17.32 \cdot \text{atan}(0.57735 \cdot \tan(\pi(z - 0.5)/L)) + 0.5. \tag{6.20}$$

The analytical solution is given with the numerical solutions in Figure (6.15)

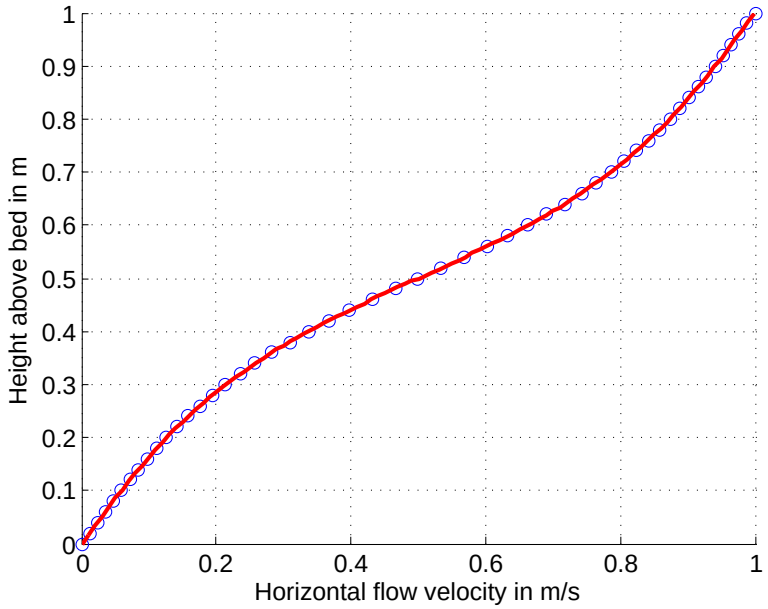

Figure 6.15: Analytical solution (red line) and numerical solution (blue dots) of a Couette flow with a breadth geometry changing over the height according to Equation (6.19).

Both figures show a close approximation between the analytical and numerical results. Hence the momentum equations account correctly for a linear increase in the breadth over the height of a duct. However, since the breadth changes in the direction perpendicular to the main flow direction, no conclusive statements can yet be made about how the Poisson equation deals with the change in breadth. Hence an additional test is described in Section 6.2.2 whereby the breadth changes in the main flow direction.

6.2.2 Laminar flow in a duct with a varying breadth geometry in $\hat{x}$-direction and slip boundary conditions at the near and far walls

To test whether the pressure Poisson equation gives accurate results for a variable breadth geometry in the main flow direction ($\hat{x}$-direction), consider a duct of a length $L = 30$ m,

height $H = 1$ m, and variable breadth geometry $b(x)$ given by

$$\begin{aligned} b(x) &= 2 \text{ m} \qquad \text{for } x < 3 \text{ m}, \\ b(x) &= 1.5 + 0.5\cos\left(\frac{\pi x}{L}\right) \qquad \text{for } 3 \text{ m} \geq x \leq 13 \text{ m} \\ , b(x) &= 1 \text{ m} \qquad \text{for } 13 \text{ m} < x < 17\text{m}, \\ b(x) &= 1.5 - 0.5\cos\left(\frac{\pi x}{L}\right) \qquad \text{for } 17 \text{ m} \geq x \leq 27 \text{ m} \\ , b(x) &= 2 \text{ m} \qquad \text{for } 27 \text{ m} < x < 30 \text{ m}, \end{aligned} \tag{6.21}$$

as depicted in Figure 6.16. The computational domain is subdivided into a square grid with

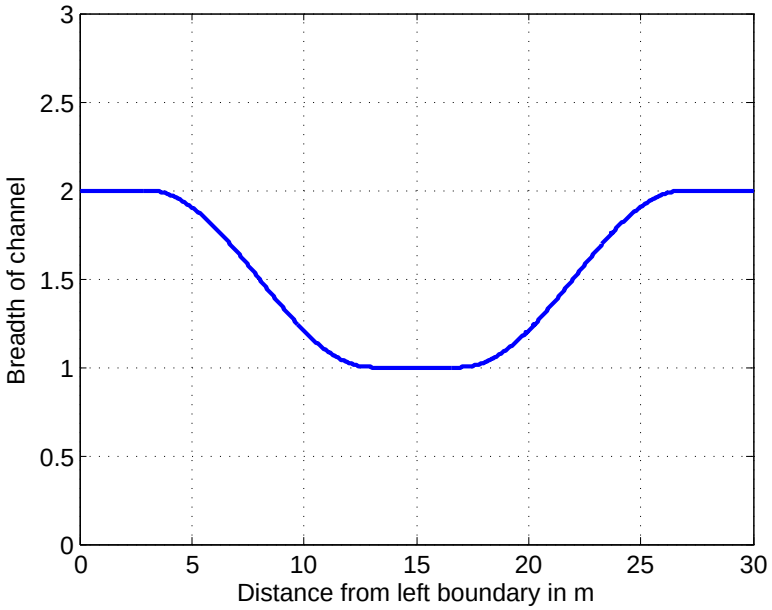

Figure 6.16: Breadth profile along the length of the channel

601×21 grid points with a spatial step of 0.02 m. A convergence test with a grid of 1501×51 gave matching results. For stability reasons the time step is set at 1 s. The flow and pressure profile are obtained for Dirichlet boundary conditions at $x = 0$, and $x = L$. The initial conditions are given by $\widetilde{\langle w \rangle} = 0$, and

$$\widetilde{\langle u \rangle}(z) = \frac{q}{b}, \tag{6.22}$$

where q is the breadth integrated velocity $\widetilde{\langle u \rangle}$. The first run was made for an inviscid flow. The flow boundary conditions at the left and right boundary are given by $q|_{x=0} = q|_{x=L} = 2$ m^2/s. Since the test case concerns a steady state solution, the pressure gradients following from the

momentum equations should match the outcome of the Poisson equation. For an inviscid flow with a mean inflow velocity of 1 m/s the results of the pressure gradient multiplied by the breadth are presented in Figure 6.17 as follows from the momentum equations, and Figure 6.18 as follows from the Poisson equation. An identical match was found for the pressure

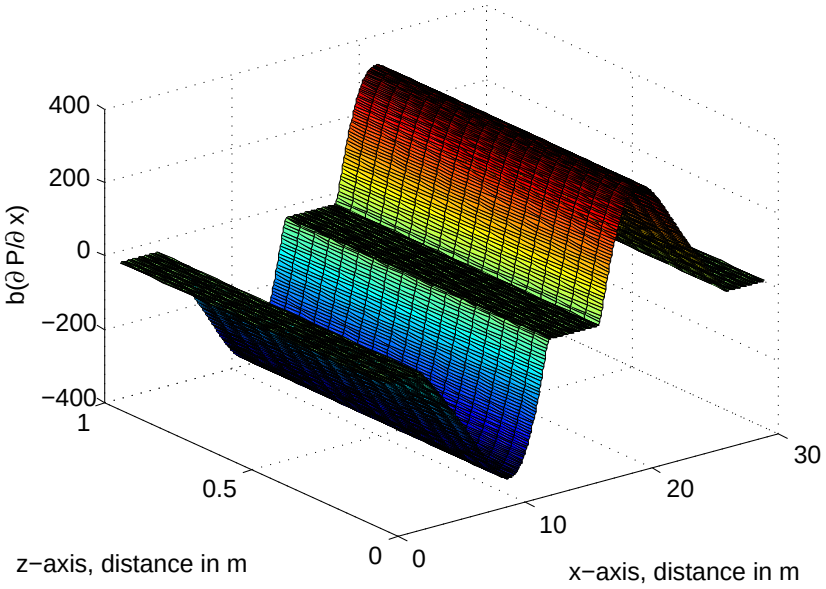

Figure 6.17: Pressure gradients $b\widetilde{\frac{\partial\langle P\rangle}{\partial x}}$ following from the solution of the x-direction momentum equation

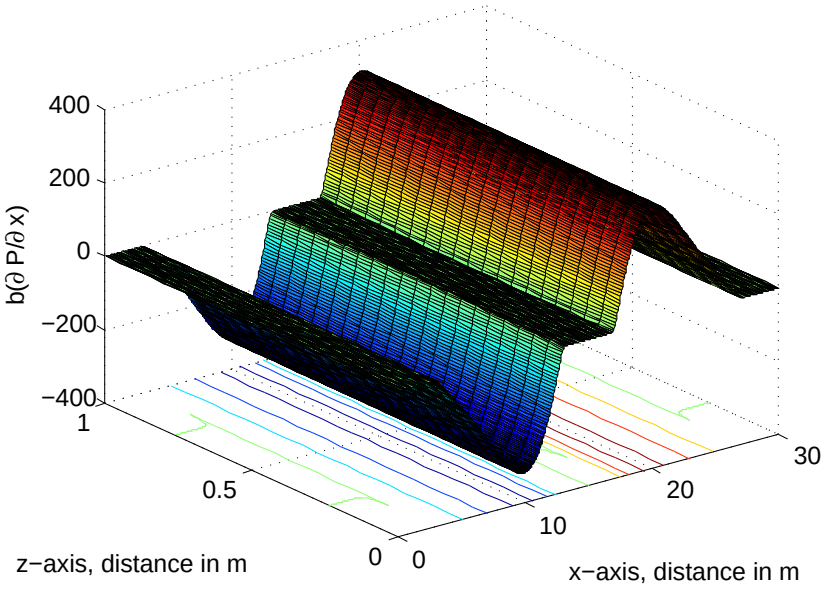

Figure 6.18: Pressure gradients $b\widetilde{\frac{\partial\langle P\rangle}{\partial x}}$ following from the solution of the Poisson equation

indicating that the Poisson equation leads to an accurate pressure profile for an inviscid flow. The second test case was similar to the first test case, except that here a viscous flow was

used. The boundary conditions are given by $\widetilde{\langle w \rangle}|_{x=0} = \widetilde{\langle w \rangle}|_{x=L} = 0$, furthermore

$$q = 10z\,(z - D)\,, \tag{6.23}$$

and the initial condition follows from $\widetilde{\langle w \rangle} = 0$ and $\widetilde{\langle u \rangle} = \frac{q}{b}$. The solution for $b\frac{\partial \widetilde{\langle P \rangle}}{\partial x}$ as given by the $\hat{x}$-direction momentum equation solver, is shown in Figure 6.19. The increasingly

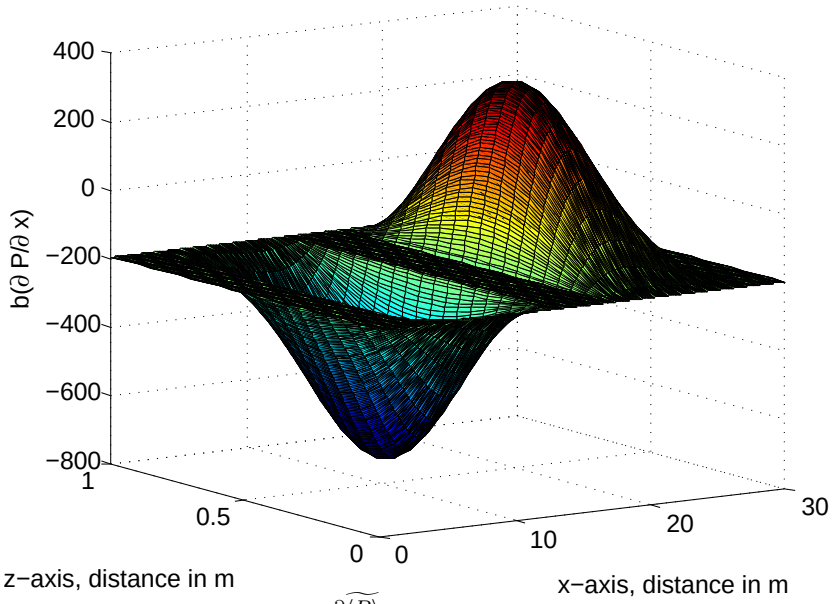

Figure 6.19: Pressure gradients $b\frac{\partial \widetilde{\langle P \rangle}}{\partial x}$ following from the $\hat{x}$-direction momentum equation

high flow velocity closer to the center of the channel, combined with the changing breadth give higher values for the pressure gradient closer to the centre of the channel than near the bottom and top wall (see Figure 6.19). If the parabolic velocity distribution is to be maintained then the pressure gradients will induce a flow in the vertical direction. However, the initial conditions do not account for a vertical flow. Hence the pressure gradients at the bottom and top boundary are solely given by $\frac{\partial}{\partial x} b\eta \frac{\partial \widetilde{\langle u \rangle}}{\partial z}$ and are negligibly small compared to the pressure gradients following from the advective terms. The pressure gradients in the $\hat{x}$-direction multiplied by the breadth that follow from the pressure Poisson equation are presented in Figure 6.20. The pressure gradients following from the Poisson equation clearly do not match the pressure profile shown in Figure 6.19. The calculated pressure profile leads to incorrect flow velocities for $\widetilde{\langle u \rangle}$, and gives $\widetilde{\langle w \rangle} = 0$. A possible reason for this problem is that the initial pressure profile does not match the initial velocity profile. The pressure gradient in the $\hat{z}$-direction should instigate a flow in the $\hat{z}$-direction which has to be accounted

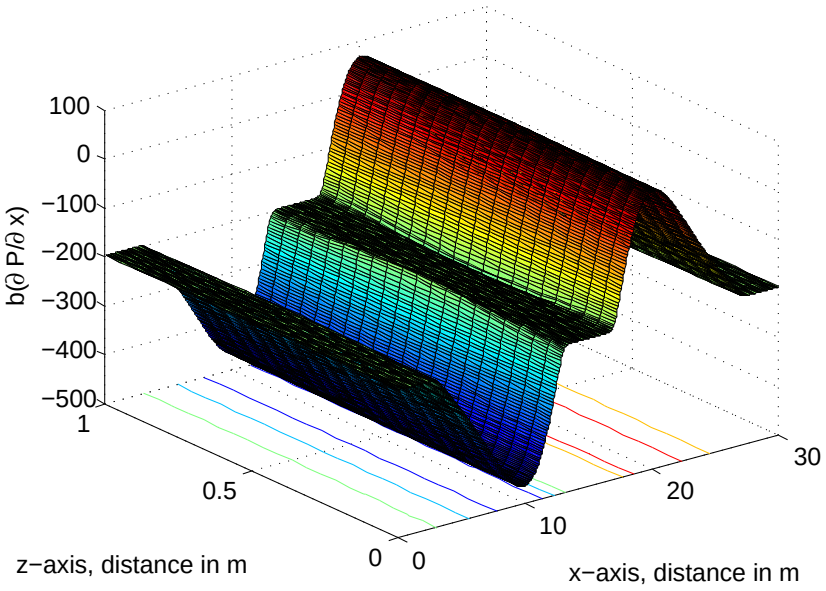

Figure 6.20: Pressure gradients $b\frac{\partial\widetilde{\langle P\rangle}}{\partial x}$ following from the solution of the pressure Poisson equation

for. Hence changes in the breadth in the main flow direction make defining the initial flow velocity profile and a matching pressure profile more of a challenge.

The tests shown in this chapter show that the model converges to a divergent free solution of the momentum equations for several test cases with and without a varying breadth under the condition that the initial pressure profile matches the initial velocity profile.

Chapter 7

Discussion

State-of-the-art embankment breach models use a simplified and incomplete description of the physical processes involved, and the errors induced require additional empirically-based assumptions in order to improve the accuracy of their simulations. The reason for the incomplete and simplified description lies in a lack of understanding of the physical processes, and the need for a high modelling speed. In modelling the surface erosion process, pre-defined breach shapes are often used to prevent the landside or side slope(s) of the embankment developing unrealistically high gradients. The choice of pre-defined breach shape is based on an overly simplified description of the geotechnical processes, whereby no distinction is made between the behaviour of unsaturated soils and saturated soils. Also, the contribution of possible groundwater flows is ignored and hence an incomplete description of the physical processes is used. In AREBA (the model described in Chapter 3), a 1D soil stability analysis forms the basis of the assumption that the steepness of the landside slope remains equal to its initial value. The 1D slope stability analysis in Chapter 2 was performed to test the hypothesis that unsaturated soil mechanics is responsible for limiting the landside embankment slope gradient in the case of surface erosion. The analysis proves that sediment-laden gravity flows prevent the landside embankment slope from steepening, and thereby contributes to a better understanding of the surface erosion processes. The effects of the underlying assumptions made in the 1D soil stability analysis are in line with the theory that a steepening of the landside embankment slope does not occur for slopes steeper than 15 °. However embankments with an infinitely long embankment slope and groundwater flows parallel to the

landside slope do not exist in reality. A flow over the embankment causes the embankment soil to saturate from the top as well as from the landside slope. Hence the soil is more likely to fail over a greater depth near the top than further down the landside slope. This leads to diffusion of the cross-sectional embankment profile where the crest and landside slope meet. In contrast, the higher flow velocities near the toe of the landside embankment slope suggest a larger failure depth near the toe than near the top. However, this leads to an increase of the landside slope gradient, and hence to failure of the slope above. The 1D slope stability analysis proves the hypothesis that sediment-laden gravity flows contribute to embankment erosion. However the 1D analysis in itself is insufficient to serve as the basis for an accurate formulation of a pre-defined breach shape. The application of higher dimensional unsaturated flow models for breach prediction is therefore recommended.

In AREBA, the erosion equation accounts for both the erosion processes of the soil, and the artificial erosion due to sediment-laden gravity flows. The erosion rate is averaged over the landside slope to prevent steepening. Another approach might have been to use the derived shear stress relationship to calculate the bed shear stress at the bottom of the landside slope under the assumption that any steepening of the landside slope is prevented by the sediment-laden gravity flows. From the model runs, the difference between averaging the shear stress and taking the maximum values was found to be small compared to the accuracy with which the soil erodibility can be predicted. By averaging the shear stress the assumptions used in AREBA were closer to those in HR BREACH, allowing for easier comparisons in the benchmarking tests. The benchmark tests show that AREBA and HR BREACH agree on the time at which the peak discharge occurs, though they differ in the peak discharge prediction due to differences in assumptions with respect to limiting the landside slope steepness. However correspondence between AREBA and HR BREACH on the time of the peak discharge does mean that AREBA and HR BREACH agree on the estimate of the flood volume through the breach. Figures 3.7 and 3.8 show that the hydrograph and final breach widths obtained from field measurements are within the bounds of uncertainty arising from possible variations in the input parameters. Since AREBA is volume conservative, it is able to reproduce the outcome of the field data. However the degree of accuracy of the model remains unknown as long as the true input values for the Manning coefficient and Erodibility remain unknown. As with other breach models, the low quality of the limited number of

datasets available makes it impossible to make a conclusive statement regarding the ability of the AREBA model to simulate the physical processes of an embankment failure accurately.

Figures 3.9, 3.10, and 3.11 show the correspondence between the outcome from AREBA's headcut description and the EU IMPACT project experiments for a maximum cohesive embankment. The actual breach occurs around $t = 15000$ s where there is a jump in the hydrograph. The hydrograph before the breach in Figure 3.9 and the stronger decrease in water depth before the breach, shown in Figure 3.10, indicate that before the breach the increase in discharge was higher in the experiments than was predicted by AREBA. The differences illustrate the effect of assuming a non-downward eroding crest. The erodibility of the clay used in the IMPACT experiments was relatively high, yet despite this the jump in water level found during the experiments still falls within the bounds of uncertainty. The final breach width found during the experiments also lies within the bounds of uncertainty used in the model. This indicates that AREBA is able to reproduce the experimentally measured hydrograph reasonably well. Since incorporation of downward crest erosion in the headcut mode would affect the empirical relationships for the headcut retreat in an unquantifiable way, it was decided not to change the headcut modelling method, though further study is recommended to investigate the influence of downward erosion on the headcut process. The larger difference between the lower bound and lower bound half than between the upper bound and upper bound half, shown in Figures 3.10 and 3.11, can be explained by the non-linear dependencies in the erosion equations.

The headcut mode of AREBA was also validated against the USDA-ARS field test data. Figure 3.12 shows an experimental peak outflow which is higher than the predicted peak outflow by AREBA. Despite the mismatch in peak discharge, the time at which the peak outflow occurs is predicted reasonably well by AREBA. The higher peak value in the field data is expected to have been caused by geotechnical failures which are not simulated by AREBA. The hydrodynamic and hydrostatic forces exerted by the flow on the embankment could cause part of the embankment to fail suddenly instead of being eroded gradually, giving the sudden increase in discharge. Accurately predicting when this failure occurs is very difficult to achieve in a simplified manner and has therefore not been incorporated in AREBA. Figure 3.15 shows a close match between the second USDA-ARS data and the prediction obtained from AREBA. In the second USDA-ARS experiment, the erosion resistance of the

soil prevented failure from occurring. Hence the results of the experiment simply reflect an overflow, which is simulated correctly by AREBA as shown by the close match between the upper and lower bounds. As with the surface erosion mode, no conclusive remark can be made regarding the ability of AREBA to model the headcut process accurately since input parameters, such as the erodibility, still need to be estimated. However the analysis has shown that the AREBA model is capable of reproducing the overall breach hydrograph shape and change in water levels within the bounds of uncertainty following from the input parameters.

AREBA was developed to improve on the calculation method used in the UK national flood risk assessment (NaFRA) and the modelling and decision support framework (MDSF2) for the calculation of flood volume through a breach. The volume predictions from AREBA are a close approximation to those of HR BREACH, which was selected by the dam safety interest group (Wahl et al., 2008) as a model with the potential for further development. Hence it can be concluded that with AREBA the prediction of flood volumes is improved. However breach models remain the least accurate component within system risk models. Besides errors in input parameters, breach model accuracy is influenced by the underlying assumptions concerning erosion behaviour. For example, the shear stress is quadratically dependent on the flow velocity. The impact of assuming 1D flow behaviour is therefore quadratically amplified in the calculation of the shear stress. A summary is provided below of all assumptions that are likely to influence the accuracy of the flow and erosion rate calculations.

- Negligible horizontal flow accelerations perpendicular to the main flow direction during the entire breach event.
- Negligible vertical flow accelerations (hydrostatic pressure distribution)
- Horizontal flow contraction commences only when the landside slope retreat has reached the waterside slope.
- Flow velocities in the reservoir are negligible.
- The breach width is spatially constant.
- The flow depth on top of the landside slope is equal to the critical depth.
- The bed roughness is spatially constant .

- The critical shear stress is spatially constant.

Other assumptions that could have an impact on the time of occurrence of the peak discharge are:

- Grass protection fails instantaneously.
- No downward erosion of the crest in the case of headcut erosion due to flow over the crest.

The assumptions listed above mostly originate from the objective to ensure a low model runtime. This allows the user to use the model for statistical analyses for which numerous runs are required. However like all breach models the assumptions do limit the ability of AREBA to accurately simulate the underlying physics. The effect of the assumptions remains unknown as long as highly accurate datasets are not available. The physics behind breaching is in itself still relatively poorly understood which contributes to the inaccuracy of breach models. The question as to how to change the assumptions for a more accurate description of the physics is difficult to answer. For example, the Manning coefficient is known to vary along the breach, but it is unknown where and by how much it varies, and is consequently assumed as constant. Use of a vertical 2D model would eliminate the need for describing the roughness using a Manning coefficient, though in this case the roughness needs to be incorporated in the calculation of the eddy viscosity and so the problem repeats itself.

Another difficulty is that the soil parameters are often poorly known, and have to be estimated with considerable uncertainty. In certain cases even the type of construction material is unknown. The influence of soil parameters on modelling the breach process of an embankment is therefore uncertain. In order to state that a breach model properly represents reality, accurate data from numerous field tests have to be available to validate the model. Accurate modelling of unsaturated soil processes in combination with soil erosion require full-scale experiments and hence the number of controlled experiments is likely to remain small. Another approach would be to combine accurate flow models with accurate geotechnical models to arrive at a breach model. The run time of such a breach model would be long compared with the simpler models. However accurate modelling of the individual processes will provide renewed insight into the impact of assumptions in the simpler models.

One of the assumptions used in most breach models is that the flow can be adequately described with a depth-averaged flow model. This assumption is inconsistent with the rapid vertical flow accelerations at the transition between the crest and the landside slope, as can be seen from Figure (6.4). Hence besides the need for a vertical 2D model to simulate the unsaturated soil processes with greater accuracy, the flow over the embankment needs to be modelled in the vertical plane to obtain an accurate description of the stresses exerted on the embankment. During Stage 2 (see Figure 1.8a), horizontal contraction of the flow is negligible and hence a vertical 2D model suffices. However commercially available vertical 2D models do not account for a variable breadth geometry. In order to model the flow correctly in the vertical 2D plane in the case of a variable breadth geometry, a new set of breadth-integrated mass, momentum, and pressure equations has been derived in Chapter 4. The chapter also gives guidelines on how to calculate the eddy viscosity for a variable breadth geometry, and how to obtain the kinetic energy from the eddy viscosity model using mixing-length theory.

Solution methods for the 2D Navier–Stokes equations with variable breadth geometry are given in Chapter 5. The SIMPLER method has been applied in the model and was tested against several laminar flow test cases in Chapter 6. Tests for a constant breadth and slip conditions at the near and far walls allowed comparison with datasets available for testing 2D solutions of the Navier–Stokes equations for incompressible flow. These test cases included a laminar duct flow, flow over a backward facing step inside a duct, and lid-driven cavity flow. The predicted results for laminar duct flow showed a perfect match with the analytical solution, and those for flow over a backward facing step compared well with the test results by Armaly et al. (1983). As can be seen in Figures 6.12 and 6.11, an identical match is not obtained between the flow model and the results from Ghia et al. (1982) for the lid driven cavity flow. The discrepancies between the results may be due to the difference between using a vorticity-driven model and a pressure-correction-based model. In a vorticity-driven model, the vorticity defined at the boundary follows from a numerical approximation, since physically the value for vorticity at the boundary is 0 (Ghia et al., 1982). The approximation used in vorticity–stream function models could explain the differences in results observed.

In comparison with the 2D Navier–Stokes equations often solved in commercial models, the first enhancement considered in Chapter 4 is the incorporation of drag at the near and far walls. The predicted laminar flow through a duct with drag at the side walls has a lower

mean velocity and lower peak velocity than the same flow through a duct without drag (see Figure 6.2). The effects of the side wall drag are higher at the centre of the duct than near the sides due to the higher flow velocities, and are associated with the flow velocity-dependent expression for the side wall drag. The second enhancement is the ability of the equations to deal with a variable breadth. Herein a duct flow with a variable breadth, and Dirichlet boundaries on either side of the duct were used to test whether the equations and solution method account for a variable breadth correctly. Horizontal Couette flows through a duct with a variable breadth in the $\hat{z}$-direction show that the momentum equations are able to account correctly for the change in breadth. When the breadth is changed in the main flow direction, the higher values for the advective terms in the narrow part of the duct than in the wider part were correctly accounted for under conditions of inviscid flow. For viscous flow, the higher flow velocities in the centre of the duct, give higher pressure gradients in the centre of the duct than near the walls. These pressure gradients induce a secondary flow which is not accounted for in the initial conditions. Hence the initial velocity field does not match the initial pressure field. This results in divergence from the solution of the momentum equations. Further study is therefore recommended of the boundary conditions of the Poisson equation for solving the Navier–Stokes equations with a variable breadth geometry.

Finally Chapter 4 provides a method for solving the eddy viscosity with the breadth-integrated Spalart–Allmaras model, and gives a suggestion for calculating the kinetic energy from the eddy viscosity by means of Prandtl's mixing-length hypothesis. Validation of the derived eddy viscosity model under variable breadth geometries against experimental data is recommended. Studying the impact of deriving the turbulent kinetic energy from the eddy viscosity instead of solving the energy balance equations is also recommended.

The work performed in this thesis shows that the processes behind embankment breach formation are poorly understood. Breach models often contain too many simplifications to arrive at an accurate prediction, yet the impact of the simplifications cannot be assessed due to the limited amount of accurate experimental data available. The only way to arrive at more accurate breach growth predictions is by focussing on correct modelling of all the physical processes that contribute to a breach event. The insights into the physical processes obtained from such accurate models could then be used to test and develop new rapid breach modelling techniques.

Chapter 8

Conclusions and Future Work

8.1 General conclusions

This thesis provides an overview of the physical processes involved in embankment breach formation due to overflow, and discusses current limitations and uncertainties involved in modelling these processes.

A 1D slope stability analysis has been performed for an infinitely long slope overflowing with water. An analytical solution of the Richards equations has been derived for an exponential relationship between the moisture content and the degree of matric suction, and used to explain how the depth at which a slope fails increases and how this depth relates to the shear stress on the slope, the slope angle, and the rate of saturation of the slope. With this analysis a contribution is made to the understanding of surface erosion processes by providing a physical explanation of the processes that limit the steepness of the landside embankment slope.

A fast breach model AREBA (A Rapid Embankment Breach Assessment) has been developed to predict the breach hydrograph for embankment failure due to piping or overflow. In the case of failure due to overflow, the model distinguishes between breach formation due to surface erosion, and breach formation due to headcut erosion. Analytical functions have been derived for the shear stress along the landside slope, with which the erosion rate can rapidly be calculated. AREBA produces a breach hydrograph which, in the timing of the peak discharge, is in agreement with the breach model HR BREACH, the EU IMPACT field

datasets, and the USDA-ARS field datasets. Given the volume-conservative nature of the equations, and the correspondence between the predicted timing of the peak discharge and observed values from field data and other breach models, the AREBA model improves on the flood volume calculation method currently used in the UK National Flood Risk Assessment and the Modelling and Decision Framework MDSF2.

For accurate simulation of breach formation, the shear stresses on the embankment need to be calculated accurately. Based on standard allowable flow assumptions, a new set of breadth-integrated Reynolds-averaged Navier–Stokes equations, pressure Poisson equation, and a one-equation eddy viscosity model have been derived, which account for drag on the side walls, and a variable-breadth geometry. A pressure-correction-based method has been derived for solving the breadth-integrated Reynolds-averaged Navier–Stokes equations under a free surface, which has been validated for laminar flows in a duct, with and without side wall drag, laminar Couette flow for a variable breadth geometry, flow over a backward facing step, flow down a hump, and a lid-driven cavity flow.

8.2 Detailed conclusions

8.2.1 Slope stability analysis on unsaturated soils

A shear stress needs to be defined on a slope surface to determine the depth at which the soil material fails. In deriving the conditions for sediment-laden gravity flows, it is often assumed that the flow exerts a shear stress and normal stress on the slope surface, and transports any failed material. However conditions for sediment-laden gravity flows have only been derived for fully saturated conditions and hence only exist for steady-state situations.

In this thesis, an unsteady analysis of the initiation of sediment-laden gravity flows has been used to explain how such flows limit the steepness of the landside slope in the case of surface erosion, and to show the importance of accounting for sediment-laden gravity flows in embankment breach formation. The 1D analysis predicts a constant rate of saturation of the soil, which gives a linear increase in failure depth with time. In the analysis, the progressive failure of the slope itself has not been accounted for in calculation of the rate of saturation of the soil. A further increase in the rate of saturation can be expected when accounting

for slope failure. For the purpose of obtaining rapid breach model predictions, the effects of sediment-laden gravity flows can be described by means of a modified erosion equation when assuming one-sided infiltration. For accurate modelling of breach formation, water infiltrating the embankment from the crest as well as the landside slope, the normal and shear stress on the embankment crest by the slope, and the increase in shear stresses along the landside slope due to the accelerating flow may not be neglected. Hence a multi-dimensional analysis would be necessary in order to describe better how sediment-laden gravity flows influence breach formation.

8.2.2 The Simplified breach model AREBA

The current UK National Flood Risk Assessment (NaFRA), and the Modelling and Decision Support Framework (MDFS2) use very coarse assumptions in the calculation of flood volumes. The AREBA model has been developed to improve the accuracy with which flood volumes are predicted. The results calculated with AREBA correspond well with the results from more physically-based models, like HR BREACH, in the calculation of flood volumes and hence an improvement is made. Moreover the low run-time of AREBA allows it to perform statistical analysis for which numerous runs are required. Nevertheless no statements can be made about the degree of accuracy of AREBA and other breach models, since a perfect match against the field data could be obtained by means of different combinations of input parameters. For the same reason, empirical relationships describing breach are highly inaccurate. The dependence of breach formation on soil parameters like hydraulic conductivity, and erodibility, and the shear stresses and normal stresses induced by the flow over the embankment, make it difficult to scale the problem down and hence large-scale experiments are required against which to validate models. Accurate modelling of each of the physical processes contributing to breach formation would give more insight into the allowable assumptions with respect to modelling breach formation, while validation of each of the individual processes would partially eliminate the requirement for numerous large scale experiments.

8.2.3 Modelling breach flow

The time to the peak discharge, defined by Stage 2 of the breach formation, is the most influential on the final shape of the breach hydrograph and the volume of flood water predicted by the breach model. Breach models developed in the past used either 1D or depth-integrated 2D models to simulate breach flow during Stage 2. The rapid flow acceleration in the vertical direction where the crest and the landside slope meet, and along the landside slope, do not permit the vertical accelerations to be ignored.

In this thesis a new set of breadth-integrated Reynolds-averaged Navier–Stokes equations is presented by which the breach flow during Stage 2 can be accurately modelled. When solving the pressure field from the pressure Poisson equation in the case of a variable breadth geometry, the viscous terms in the right hand side of the Poisson equation may no longer be ignored. An analysis of the analytical solution of the Poisson equations for an inviscid flow through a channel which varies in breadth along the channel axis, showed that the Poisson equation can only be solved with Von Neumann boundary conditions. Modifications to the pressure Poisson equation have been made to arrive at pressure gradients which satisfy the mass-balance equation in the case of a variable breadth geometry. Numerical results compared well against the analytical solution for an inviscid flow down a channel which varies in breadth in the main flow direction. A good comparison was also found with analytical pressure solutions for a Couette flow in a channel with a varying breadth over the height.

8.3 Future Work

The following recommendations follow from the research carried out for this thesis:

1. **Field studies for an improved insight into breaching**

   A major challenge in embankment breach modelling is that the physcial processes involved in breach formation are still poorly understood. Furthermore, information on the design and construction materials of embankments is often lacking. Hence for a better forensic understanding, field studies concerned with identifying the mechanisms of breach initiation are recommended after embankment failures have occurred. Also, improved documentation of embankment design and the properties of construction materials are recommended.

2. **Study to the impact of assumptions in simplified breach models**

   Field data from the EU IMPACT experiments show that some downward erosion of the crest occurs while the landside slope retreats towards the waterside slope. The shear stresses induced by the high flow velocities at the crest are also expected to induce some degree of erosion. However, in accordance with the empirical equations used to describe the rate at which the headcut progresses through the embankment, it is assumed in AREBA that no downward crest erosion occurs. Studies are recommended on the impact of ignoring the downward crest erosion when modelling headcut formation.

3. **Modelling of the failure of surface protection on embankments**

   Surface protections on an embankment are often assumed to fail everywhere instantaneously once a certain overflow condition is reached. The conditions for failure are found experimentally. The large variety in grass quality and embankment soil lead to a large range of uncertainty associated with the empirical relationships describing the condition for failure of a grass cover. Furthermore, the higher stress levels over the landside embankment slope than over the crest would suggest a more rapid failure on the landside slope than at the crest. Further study on the failure mechanisms of protection layers is strongly recommended in order to improve the accuracy to which breach formation is modelled.

4. **Study of the role of sediment-laden gravity flows**

   Slope stability analyses indicate that sediment-laden gravity flows play an important role in surface erosion. A multidimensional groundwater flow model for unsaturated soils is necessary to account accurately for the role sediment-laden gravity flows play in breach formation. Hence development of such a multidimensional model with an application to breaching is recommended. The multidimensional model could in turn be used to define conditions under which headcut erosion would occur, and be used in the development of a rapid and accurate method for limiting the steepness of the landside slope when undertaking surface erosion modelling. Experimental studies are recommended, not only for validation of the groundwater flow model, but also for validation of the hypothesis that sediment-laden gravity flows play a role in breach formation. Large-scale experiments, in which erosion of the soil is prevented by a

geotextile but the bed shear stress is transferred to the subsoil directly under the geotextile, could provide further insight into the role of sediment-laden gravity flows in embankment breach formation, and hence are recommended.

5. **Calculation of the kinetic energy in one-equation turbulence models**

   Chapter 4 of this thesis proposes a new method for calculating kinetic energy directly from the eddy viscosity. This method is especially useful when applying a one-equation eddy viscosity model because no additional balance equation for the kinetic energy needs to be solved. Validation of this proposed method against a k-ϵ turbulence model is recommended.

6. **Research on solving the pressure Poisson equation**

   It was shown that the momentum equations for a variable breadth can only be solved for Dirichlet boundary conditions for the velocity, and hence Von Neumann boundary conditions for the pressure Poisson equation. However, when extending the method to account for a variable free surface, it becomes more difficult to define the velocity at the downstream boundary, and hence a Von Neumann boundary condition for the velocity is required. Further study is therefore recommended on how to solve the pressure Poisson equation with Von Neumann boundary conditions. Since the Poisson equation needs to be solved twice per iteration, the solver speed is of importance to the performance of the overall flow model. Further development of the discrete cosine transform solver for the Poisson equation is therefore recommended.

Bibliography

ABC news (2011, Jan). Flood costs tipped to top $30b.

Ackers, P., W. White, J. Perkins, and A. Harrison (1978). *Weirs and flumes for flow measurement*. John Wiley and Sons.

Agrawal, A., R. Chellappa, and R. Raskar (2005). An algebraic approach to surface reconstructions from gradient fields. In *10th IEEE International Conference on Computer Vision (ICCV 2005)*, Volume 1, pp. 174–181.

Agrawal, A., R. Raskar, and R. Chellappa (2006). What is the range of surface reconstructions from a gradient field? 9th European Conference on Computer Vision, pp. 578–591.

Alyamani, S. and Z. Sen (1993, Jul). Hydraulic conductivity from grain size curves. *Ground water 31*(4), 551–555.

Armaly, B. F., F. Durst, J. C. F. Pereira, and B. Schönung (1983). Experimental and theoretical investigation of backward-facing step flow. *Journal of Fluid Mechanics 127*, 473–496.

Aupoix, B. and P. R. Spalart (2003). Extensions of the Spalart–Allmaras turbulence model to account for wall roughness. *International Journal of Heat and Fluid Flow 24*(4), 454–462.

Averbuch, A., M. Israeli, and L. Vozovoi (1998, May). A fast Poisson solver of arbitrary order accuracy in rectangular regions. *SIAM Journal on Scientific Computing 19*(3), 933–952.

Bagnold, R. A. (1966). An approach to the sediment transport problem from general physics. *Geological survey professional paper*.

Barends, F. B. J. and G. J. M. Uffink (2003, Jul). *Groundwatermechanics flow and transport*. TU Delft.

Battjes, J. A. (2002, Apr). *Vloeistofmechanica*. CT2100. Delft University of Technology.

Broich, K. (1996). *Computergestützte Analyse des Dammererosionbruchs*. Ph. D. thesis, Universität der bundeswehr München institut für Wasserwesen.

Broich, K. (1998). An overview of breach modelling. Technical report, University of the Federal Armed Forces Munich.

Butt, T., R. P., and I. Turner (2001). The influence of swash infiltration–exfiltration on beach face sediment transport: onshore or offshore? *Journal of Coastal Engineering 42*, 35–52.

CHAM Limited (2013, Feb). Phoenics encyclopaedia.

Congedo, P., C. Duprat, G. Balarac, and C. Corre (2012). Numerical prediction of turbulent flows using Reynolds-averaged NavierStokes and large-eddy simulation with uncertain inflow conditions. *Numerical methods in fluids*.

De Moel, H. (2012, Jul). *Uncertainty in FLood Risk*. Ph. D. thesis, VU University Amsterdam.

Deck, S., P. Duveau, P. d'Espiney, and P. Guillen (2002). Development and application of Sparart–Allmaras one equation turbulence model to three dimensional supersonic complex configurations. *Aerospace Science and Technology 6*, 171–183.

Douglas, J. j. and D. W. Peaceman (1955, Dec). Numerical solution of two-dimensional heat-flow problems. *AIChE Journal 1*(4), 505–512.

Environment Agency (2009). Flooding in England - A national assessment of flood risk. Technical report, Environment Agency.

European Environment Agency (2010). Mapping the impacts of natural hazards and technological accidents in europe, an overview of the last decade. Technical report, European Environment Agency.

Falconer, R. A. (1993). *Coastal, Estuarial and Harbour Engineer's Reference Book*, Chapter An introduction to nearly-horizontal flows. E & FN Spon.

Ferziger, J. H. and M. Perić (2002). *Computational methods for Fluid Dynamics* (3 ed.). Springer.

Fox, A. G., G. V. Wilson, and A. Simon (2007). Measuring streambank erosion due to ground water seepage: correlation to bank pore water pressure, precipitation and stream stage. *Journal of Earth Surface Processes and Landforms 32*, 1558–1573.

Fredlund, D. G. and A. Xing (1994). Equations for the soil water characteristic curve. *Canadian Geotechnical Journal 31*, 521–532.

Gartling, D. K. (1990). A test problem for outflow boundary conditions-flow over backward facing step. *International Journal for Numerical Methods in Fluids 11*, 953–967.

Gaskell, P. H. and A. K. C. Lau (1988). Curvature-compensated convective transport: smart, a new boundedness-preserving transport algorithm. *International Journal for Numerical Methods in Fluids 8*, 617–641.

Ghia, U., K. N. Ghia, and C. T. Shin (1982, Jan). High-Re solutions for incompressible flow using the Navier–Stokes equations and a multigrid method. *Journal of Computational Physics 48*, 387–411.

Gouldby, B. P., P. B. Sayers, M. Panzeri, and J. Lanyon (2010). Development and application of efficient methods for the forward propagation of epistemic uncertainty and sensitivity analysis within complex broad-scale flood risk system models. *Canadian Journal of Civil Engineering 37*(7), 955–967.

Govindaraju, R. S. and M. L. Kavvas (1991). Modelling the erosion process over steep slopes: approximate analytical solutions. *Journal of Hydrology 127*, 279–305.

Gresho, P. M. and R. L. Sani (1987). On pressure boundary conditions for the incompressible Navier–Stokes equations. *International Journal for Numerical Methods in Fluids 7*, 1111–1145.

Hall, J. W., I. C. Meadowcroft, P. Sayers, and M. Bramley (2003, Aug). Integrated flood risk management in England and Wales. *Natural Hazards Review 4*(3), 126–135.

Hanson, G. J. (2012, Nov). Personal correspondence on grass failure in SIMBA.

Hassan, M. and M. Morris (2009, Feb). IMPACT project field tests data analysis. Technical Report T04-08-04, HR Wallingford.

HR, Wallingford and University of Bristol (2004, Nov). Defra/Environment Agency flood and coastal defence R&D programme: Risk assessment for flood and coastal defence for strategic planning (RASP), a summary. Technical Report W5B-030/TR, Defra.

IMPACT project (2005). Investigation of extreme flood processes & uncertainty (IMPACT), breach formation (WP2), technical report: Section 4. Technical report, HR Wallingford.

In 't Hout, K. J. and B. D. Welfert (2007). Stability of ADI schemes applied to convection–diffusion equations with mixed derivative terms. *Applied Numerical Mathematics 57*(1), 19–35.

Issa, R. I. (1986). Solution of the implicitly discretized fluid flow equations by operator-splitting. *Journal of Computational Physics 62*, 40–65.

Iverson, R. M. (2000, Jul). Landslide triggering by rain infiltration. *Water Resources Research 36*(7), 1897–1910.

Iverson, R. M., M. Reid, and R. LaHusen (1997). Debris-flow mobilization from landslides. *Annual Review of Earth and Planetary Sciences*, 85–138.

Jang, D. S., R. Jetli, and S. Acharya (1986). Comparison of the PISO, SIMPLER, and SIMPLEC algorithms for the treatment of the pressure-velocity coupling in steady flow problems. *Numerical Heat Transfer, Part A: Applications 10*(3), 209–228.

Jasak, H., H. Weller, and A. Gosman (1999). High resolution NVD differencing scheme for arbitrarily unstructured meshes. *International Journal for Numerical Methods in Fluids 31*, 431–449.

Leonard, B. (1991, Jun). The ultimate conservative differencing scheme applied to unsteady one-dimensional advection. *Computer Methods in Applied Mechanics and Engineering 88*(1), 17–74.

Mc. Gahey, C., B. Gouldby, and P. Sayers (2011, Mar). MDSF2 technical report. Technical report, Environment Agency.

McKee, C. R. and A. C. Bumb (1984, Mar). *National Conference on Management of Uncontrolled Hazardous Waste Sites*, Chapter The importance of unsaturated flow parameters in the designing a monitoring system for hazardous wastes and environmental emergencies, pp. 50–58. Hazardous Materials Control Research Institute.

Mohamed, M. A. A. (2002). *Embankment Breach Formation and Modelling Methods*. Ph. D. thesis, Open University, UK.

Morris, M., G. J. Hanson, and M. Hassan (2008). Improving the accuracy of breach modelling: Why are we not progressing faster? *Journal of Flood Risk Management 1*(3), 150–161.

Morris, M., M. Hassan, A. Kortenhaus, P. Geisenhainer, P. J. Visser, and Y. Zhu (2009). Modelling breach initiation and growth. *Floodsite T06_08_02*.

Morris, M., M. Hassan, A. Kortenhaus, and P. Visser (2009). Breaching processes, a state of the art review. Technical report, HR Wallingford.

Morris, M. W. (2010, Oct). *Breaching of Earth Embankments and Dams*. Ph. D. thesis, Open University.

Muijs, J. A. (1999). Grass cover as a dike revetment. Technical report, Technical Advisory Committee for Flood Defence TAW.

Nearing, M. A., L. T. West, and L. C. Brown (1988). A consolidation model for estimating changes in rill erodibility. *ASAE 31*(3), 696–700.

Nezu, I. and T. Okamoto (2010). Simultaneous measurements of ,velocity and plant motion in open-channel flows with flexible vegetations. In *Environmental Hydraulics Volume 2*, pp. 209–214.

Nortier, I. W. and P. De Koning (1991). *Toegepaste Vloeistofmechanics, hydraulica voor waterbouwkundigen*. Stam Techniek.

O' Leary, R. A. and T. J. Mueller (1969). Correlation of physical and numerical experiments for incompressible laminar separated flows. Technical report, Notre Dame University - College of Engineering.

Parliament, E. (2007, Oct). on the assessment and management of flood risk. *Official Journal of the European Union*, 27–34. Directive 2007/60/EC of the European Parliament and of the council.

Patankar, S. (1980). *Numerical heat transfer and fluid flow*. Taylor & Francis.

Peaceman, D. W. and H. H. Rachford Jr (1955). The numerical solution of parabolic and elliptic differential equations. *Journal of the Society for Industrial & Applied Mathematics 3*(1), 28–41.

Pollen, N. (2006). Temporal and spatial variability in root reinforcement of streambanks accounting for soil shear strength and moisture. *Elsevier Catena 69*, 197–205.

Press, W. H., S. A. Teukolsky, W. T. Vetterling, and B. P. Flannery (1992). *Numerical Recipes in C, The Art of Scientific Computing* (2 ed.). Cambridge University Press.

Richards, L. A. (1931). Capillary conduction of liquids through porous mediums. *Journal of Physics 1*, 318–333.

Rinaldi, M. and N. Casagli (1999). Stability of streambanks formed in partially saturated soils and effects of negative pore water pressures: The Sieve river (italy). *Journal of Geomorphology 26*, 253–277.

Rogers, B. (2001). *Refined Localised Modelling of Coastal Flow Features using Adaptive Quadtree Grids*. Ph. D. thesis, University of Oxford, St Edmund Hall.

Sametz, L. (1981). *Beitrag zur Frage der Flutwellenbildung bei progressiven Dammbrüchen infolge von Überströmung.* Ph. D. thesis, Technischen Universität Graz.

Schlichting, J. and K. Gersten (1979). *Boundary Layer Theory.* Springer.

Seed, R., R. Bea, R. Abdelmalak, A. Anthanasopoulos, G. Boutwell, and B. J.D. (2006, July). Investigation of the Performance of the New Orleans Flood Protection Systems in Hurricane Kartina on august 29, 2005. Technical report.

Sellmeijer, J. B. (1988, Oct). *On the mechanism of piping under impervious structures.* Ph. D. thesis, Defft University of Technology.

Sidorchuk, A. (2002). Stochastic modelling of soil erosion and deposition. pp. 136–142. ISCO Conference.

Smith, K. R. (2006, Aug). Flood hazard evaluation and foundation recommendations. Technical Report 2418, TerraCosta Consulting group.

Takahashi, T. (1981). Debris flow. *Annual Review of Fluid Mechanics 13*, 57–77.

Takahashi, T. (2009). A review of japanese debris flow research. *International Journal of Erosion Control Engineering 2*(1).

Temple, D. M., G. J. Hanson, M. L. Nielsen, and K. R. Cook (2005, Jun). Simplified breach analysis model for homogeneous embankments: Part 1, background and model components. In *USSD Proceedings: Technologies to Enhance Dam Safety and the Environment*, pp. 151–161.

Ubbink, O. (1997). *Numerical prediction of two fluid systems with sharp interfaces.* Ph. D. thesis, University of London.

Van Damme, M., M. W. Morris, and M. Hassan (2012, Jun). FRMRC2 WP4.4: A new approach to rapid assessment of breach driven embankment failures. Technical report, University of Oxford and HR Wallingford.

Van Doormaal, J. P. and G. D. Raithby (1984). Enhancement of the SIMPLE method for predicting incompressible fluid flows. *Numerical Heat Transfer: An international Journal of Computation and Methodology 7*(2), 147–163.

Van Rijn, L. C. (1984, Nov). Sediment transport, part II: Suspended load transport. *Journal of Hydraulic Engineering 110*(11), 1613–1641.

Van Rijn, L. C. (1993). *Principles of Sediment transport in Rivers Estuaries and Coastal Seas, Part 1.* Aque Publications.

Verheij, H. J. and F. C. M. Van der Knaap (2002). Modification breach growth model in HIS-OM. *WL— Delft Hydraulics Q 3299*, 2002.

Verruijt (2001). *Soil Mechanics.* Delft University of Technology.

Visser, P. J. (1998). *Breach growth in sand-dikes.* Ph. D. thesis, Delft University of Technology, Netherlands.

Wahl, T., G. Hanson, J.-R. Courivaud, M. Morris, R. Kahawita, R. McClenethan, and D. Gee (2008). Development of next-generation embankment dam breach models. In *The Sustainability of Experience Investing in the Human Factor*.

Wahl, T. L. (2007). Laboratory investigation of embankment dam erosion and breach processes. Technical Report T0327000-0207A, CEA Technologies Inc.

Whitehead, E., W. Bull, and M. Schiele (1976). A guide to the use of grass in hydraulic engineering practice. Technical report, Construction and Industry Research and Information Association (CIRIA).

Yang, C. T. (1979). Unit stream power equations for total load. *Journal of Hydrology 40*, 123–138.

Yang, C. T. (2006, Nov). *Reclamation, Managing water in the West, Erosion and Sedimentation Manual*, Chapter Non-cohesive sediment transport. US Department of Interior, Bureau of Reclamation.

Zhu, Y., P. Visser, J. K. Vrijling, and G. Wang (2011). Experimental investigation on breaching of embankments. *Science China 54*(1), 148–155.

Zhu, Y.-H., P. J. Visser, and J. K. Vrijling (2008). Soil headcut erosion: process and mathematical modeling. In *Sediment and Ecohydraulics: INTERCOH 2005*, pp. 125–137.

Appendix A

Piping in AREBA

Piping is defined here as the internal erosion of embankment material by seepage flow. Sellmeijer (1988) reports that piping may stop once some erosion has taken place due to the larger permeability of the embankment where the soil has eroded compared with the surrounding soil. The increase in permeability reduces the hydraulic gradient that initiates the piping process. Besides a hydraulic head over the embankment structure, burrowing animals may also initiate pipe formation. Once an open connection between both sides of the embankment is formed, erosion along the perimeter of the pipe causes the pipe diameter to increase to the point that the soil above the pipe fails and slumps downs into the pipe (Mohamed, 2002). Depending upon flow velocities through the pipe and the volume of soil slumping down, the slumping material could either be transported instantaneously or could cause the pipe flow to stop and the embankment crest to lower initiating an overflow failure. Soil properties like cohesion, matric suction and internal friction angle determine when the material above the pipe fails. Positive arching of the soil above the pipe, whereby part of the load above the pipe is transferred to other soil prisms, reduces the load on the pipe.

A.1 Piping modelling methodology

AREBA models piping failure according to the method proposed by Mohamed (2002) and applied in HR BREACH. An open pipe connection is assumed between both sides of the embankment, and the discharge through the pipe follows from multiplying the flow velocity through the pipe u with the wet cross sectional area of the pipe A. The flow velocity follows from Bernoulli's energy equation is given by

$$\frac{u^2}{2g} + 0.05\frac{u^2}{2g} + f\frac{L}{D}\frac{u^2}{2g} = \Delta H, \tag{A.1}$$

where the terms on the left hand side are respectively the energy height, the contraction losses, and the friction losses. ΔH is the head difference over the pipe. After some manipulation the discharge follows from (Mohamed, 2002)

$$Q_b = A\sqrt{\frac{2g\Delta H}{h_f}}, \tag{A.2}$$

where h_f is a head loss factor representing contraction and friction losses given by

$$h_f = 1.05 + \frac{fL}{D_p} \tag{A.3}$$

where L is the pipe length in m, and D_p is the pipe diameter in m. f is a friction coefficient determined from

$$f = 0.2162\left(\frac{D_{50}}{D_p}\right)^{\frac{1}{6}} \tag{A.4}$$

where D_{50} , is the grain diameter in m exceeded by 50% of the soil mass. Due to the long straight pipe geometry, the energy losses are dominated by the wall friction and hence the losses due to outflow from the pipe are neglected (Mohamed, 2002). The cross sectional area of the pipe A is calculated assuming a circular shaped pipe that does not grow beyond the embankment's foundation level. Once the pipe bottom reaches the embankment's foundation, the pipe shape becomes that of a truncated circle. The surface area of the pipe then follows from

$$A = \frac{1}{4}\pi D_p^2 - \frac{\alpha}{4}D_p^2 + h_p^2 \tan\alpha \tag{A.5}$$

with

$$\alpha = \frac{\arccos\left(2h_p\right)}{D_p} \tag{A.6}$$

where h_p is the distance between the centerline of the pipe and the foundation level of the embankment. The pipe is assumed to grow uniformly along its length according to

$$E = K_e\left(\tau - \tau_c\right)^n \tag{A.7}$$

where K_e is the soil erodibility in m^3/Ns (for $n = 1$), τ the wall shear stress in , τ_c the critical shear stress in, and ^{n} a coefficient of efficiency. The wall shear stress τ in the pipe is given by

$$\tau = \rho_w g R i_w \tag{A.8}$$

where ρ_w is the density of water, and R the hydraulic radius of the pipe, which for a submerged circular pipe is equal to $D_p/4$, with D_p representing the pipe diameter (Nortier and

De Koning, 1991). i_w is the gradient in water level over the pipe and follows from

$$i_w = f\frac{u^2}{2gD_p} \tag{A.9}$$

In AREBA the assumption has been adopted from Mohamed (2002) that the soil mass above the pipe fails when the weight of the soil above the pipe exceeds the frictional forces in the soil. AREBA accounts for soil cohesion in determining the frictional forces inside the soil, and for arching in determining the weight of the soil above the pipe. Mohamed (2002) gives the following relationship for the factor of safety (FOS).

$$FOS = \frac{cA_c}{W} \tag{A.10}$$

where c is the cohesion of the soil in N/m^2, and A_c is the cross sectional area of the embankment above the center line of the pipe in m^2. For simplicity the weight of the soil W, is purely determined for the soil above the top of the pipe from.

$$W = f_a \rho g D_p A_s \tag{A.11}$$

where A_s is the cross sectional area of the embankment above the top of the pipe. Mohamed (2002) uses an empirically based reduction factor to account for the effects of arching of the soil, given by

$$f_a = 0.0003759 + 0.0000986r^2 - 0.0002918r \tag{A.12}$$

where r represents the ratio of the distance from the top of the pipe to the crest, and the pipe diameter. The ratio r has a lower limit of 0.1 and an upper limit of 1.6. For $FOS < 1$, the pipe collapses, and the embankment crest is assumed to lower with a distance equal to the height needed to fill the volume of the pipe. At the moment of failure, the grass protection is assumed to have failed. From this time onwards the embankment's failure mechanism transfers to that of a surface erosion process as described in section 3.1.1

A.2 validation against the EU IMPACT piping test

Figure A.1 gives an overview of the test setup of the Piping field experiment performed under the EU IMPACT project. Figure A.2 shows the inflow into the reservoir, outflow from the pipe and the water level in the reservoir. Figure A.2 shows the inflow, and outflow hydrograph from the piping experiment as undertaken in IMPACT (IMPACT project, 2005). The technical report describing the experiments (IMPACT project, 2005) mentions a rapid pipe failure after approximately 20 minutes. The moment of opening the pipe is estimated

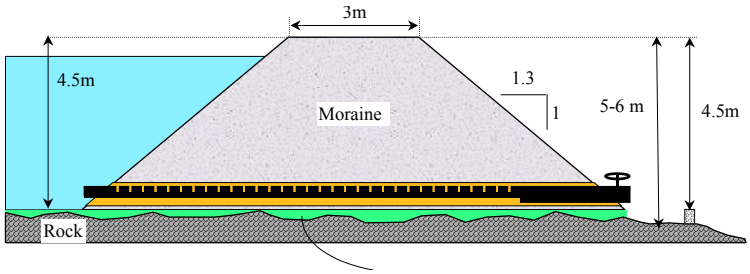

Figure A.1: Test setup EU IMPACT piping experiment (IMPACT project, 2005)

from Figure A.2 and coincides with a sudden drop in water level. The exact moment at which the pipe was opened, relative to the start time of the given inflow hydrograph, is however unknown. Before the drop in water level the reservoir was filled slowly. The discharge into the reservoir before opening of the pipe was estimated at 0.6 m^3/s from curve fitting. During

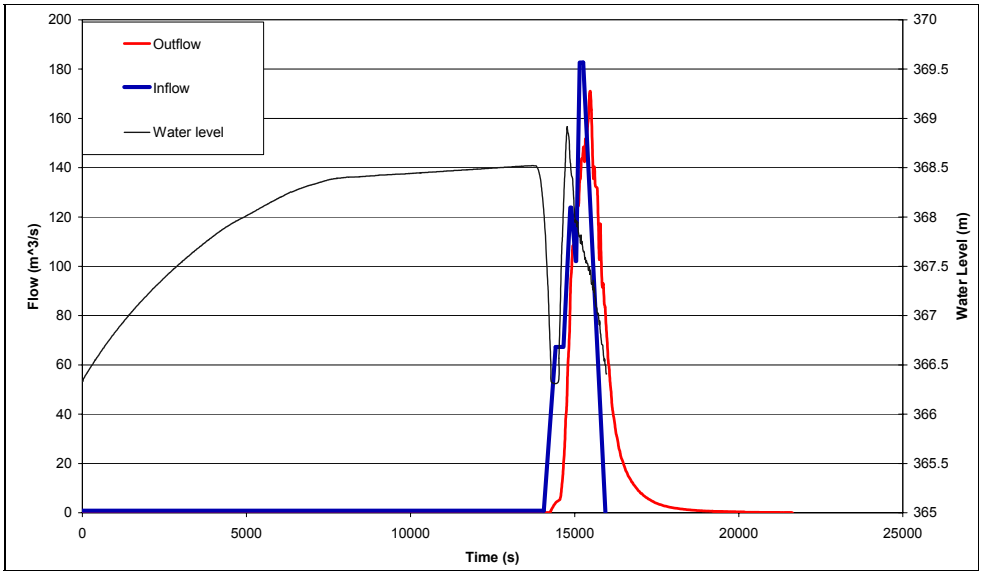

Figure A.2: Water level, inflow and outflow for EU IMPACT piping experiment (IMPACT project, 2005)

the experiment it was attempted to keep the upstream water level constant irrespective of the outflow. The ability to control the upstream water level by accounting for the effects of the outflow from the pipe had strongly been underestimated and caused for a rapid increase of inflow into the reservoir. According to Figure A.2 the blue line represents the inflow. However the drop in water level should be correlated with an increase in outflow from the reservoir. The behaviour described in Figure A.2 can only be explained if the red line represents the inflow and the blue line the outflow. AREBA was run for this situation. The range of input parameters, given in Table A.2, was obtained from the available documentation on the

experiment. Validation of AREBA against the field data was complicated due to the unknown opening time of the pipe relative to the given inflow hydrograph, the unknown discharge into the reservoir before opening the pipe, and the sudden increase in discharge into the reservoir just after opening the pipe. Treating the relative opening time of the pipe as a statistical variable in the analysis resulted in a very large uncertainty bounds since the sudden increase in discharge just after opening the pipe resulted in widely varying outcomes in water level in the reservoir for different initiation times. A similar problem was encountered with specifying a wide range for the erodibility. The only solution was to limit the range for the erodibility, the inflow before the pipe was opened, and the time at which the pipe opened by fitting the data slightly to the found outcome. The range in erodibility is given in Table A.2, the inflow before the pipe was opened was estimated at 0.6 m^3/s. The opening time of the pipe used in the model runs presented by Figures A.3 and A.4 was 13450 s. Due to the small statistical range of the variables the piping case was only run for the wide range in data.

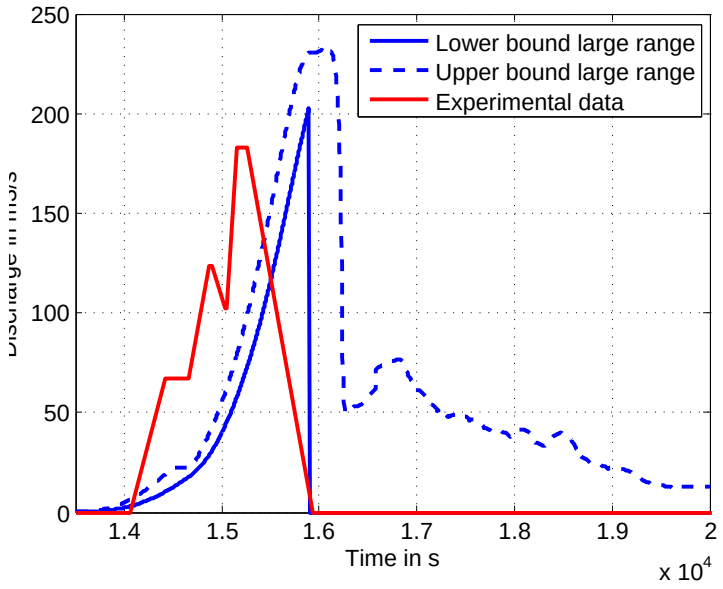

Figure A.3: Outflow hydrograph wide range AREBA compared to data from the EU IMPACT piping experiment.

Both Figures A.3 and A.4 show a second spike in the model outcomes which results from the assumption that when the pipe fails the body of soil above the pipe fills up the volume of the pipe. During the experiment the soil that slumped in the pipe was washed away instantly. However since the instantaneous removal of slumped material is case dependent the description of the physics by the model has not been changed.

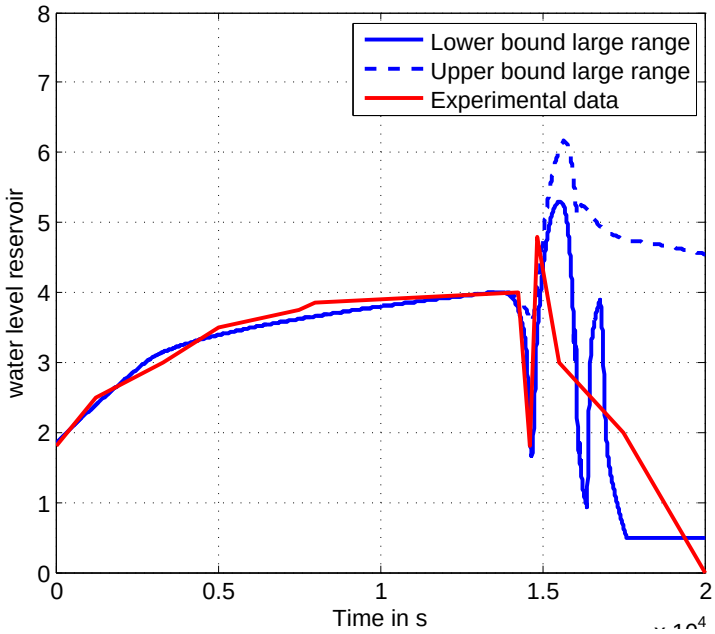

Figure A.4: Modelled water level in the reservoir following from AREBA compared to data from the EU IMPACT piping experiment.

-	**Lower bound**	**Lower bound half**	**Mean**	**Upper bound half**	**Upper bound**
Manning coefficient ($s/m^{1/3}$)	0.025	0.03	0.035	0.04	0.045
Cohesion (kN/m^2)	18	19	20	21	22
Dry density (kg/m^3)	2000	2050	2100	2150	2200
Critical shear stress (N/m^2)	0	2.5	5	7.5	10
Erodibility coefficient (m^3/Ns)	9×10^{-6}	9.5×10^{-6}	1×10^{-5}	1.05×10^{-5}	1.1×10^{-5}
D_{50} (mm)	5.5	6.25	7	7.75	8.5
Weir coefficient 1	0.9	0.95	1	1.05	1.1
Weir coefficient 2	1	1.1	1.2	1.3	1.4
Waterside slope gradient	1/1.3	1/1.325	1/1.35	1/1.375	1/1.4
Landside slope gradient	1/1.3	1/1.325	1/1.35	1/1.375	1/1.4
Pipe level above ref. (m)	0.29	0.295	0.3	0.305	0.31
Crest height (m)	4.3	4.35	4.4	4.45	4.5
Crest width (m)	2.8	2.85	2.9	2.95	3

Table A.1: Range of input parameters AREBA for testing against the EU IMPACT piping experiment

Nomenclature

Latin Letters

$\langle . \rangle$	Time-averaging	
$\bar{.}$	Depth-averaging	
$\tilde{.}$	Breadth-averaging	
$\underline{A_f}$	Diagonal matrix where the terms on the diagonal are a weighed average of the coefficients in A_f	kg/m^{2}s
A_c	cross sectional area of the embankment above the center line of the pipe	m^2
A_f	Matrix containing the coefficients following from the discretized momentum equations which are dependent on the neighbouring nodes	kg/m^{2}s
a_l	depth at which the slope will fail as defined by Takahashi (1981)	m
A_p	Matrix containing the the coefficients following from the discretized momentum equations which are independent on the neighbouring nodes	kg/m^{2}s
A_s	Cross sectional area of embankment above the top of the pipe	m^2
A_{ca}	Size of the catchment area upstream of the asset	km^2
b	Breadth of the flow	m
C	Headcut coefficient	s$^{-2/3}$
c	Soil Cohesion	N/m^2
c_*	Grain concentration	
c_f	Drag coefficient	1/m
c_w	Weir coefficient	
c_{R1}	Model coefficient in the Spalart–Allmaras model	
Δd	Difference between the normal depth and the local water depth	m
Δd_0	Difference between the critical depth and the normal depth	m
d	Local water depth measured normal to the bed	m
d_c	Critical depth	m
d_n	Normal depth	m

D_p	Pipe diameter	m
d_0	Depth offset as a function of the Nikuradse roughness coefficient	m
D_{10}	The grain diameter, which is exceeded by 90% of the grain sizes in the grain distribution	m
D_{50}	Median grain diameter	m
$d_{\min}$	Depth measured normal to the bed	m
d_{fs}	distance to the free surface	m
d_{ph}	Distance below the landside slope at which the phreatic surface is located	m
$\hat{e_1}$	Coordinate direction tangential to the free surface	
$\hat{e_3}$	Coordinate direction perpendicular to the free surface	
$\overline{E}$	numerical averaged erosion rate of the landside slope	m/s
E	Erosion rate	m/s
e	Base of the natural logarithm	
E_w	Breach widening rate	m/s
E_z	Erosion rate in the $\hat{z}$-coordinate direction	m/s
E_ζ	Erosion rate in $\hat{\zeta}$-coordinate direction	m/s
F_s	Slope stability factor	
f_S	Factor accounting for the reduction in the rate with which the crest width reduces due to downward erosion of the invert level	
f_{v1}	Damping function	
g	Acceleration due to gravity	m/s^2
H	Height difference between the upstream water level and the crest level	m
h	Height above the bed, measured perpendicular to the bed	m
h_2	Water level over the crest	m
h_{hc}	Step height of the headcut	m
$Hydmult$	Hydrograph multiplier used in the national flood risk assessment	
I	Identity matrix	
i_{bi}	Landside slope gradient embankment	
i_{bo}	Waterside slope gradient	
K	Hydraulic conductivity of the soil	m/s
k	Turbulent kinetic energy	m^2/s^2
K_e	Erodibility coefficient	m^3/Ns
k_s	Nikuradse roughness coefficient	m
L	Adaptation length, length along the slope where Δd is equal to $\Delta d_0/e$	m
L_x	Ratio between the return period of the extreme event and the standard of protection of the asset	
L_{def}	Defence length	m
L_{mix}	Prandtl mixing-length	m

l_{mix}	Characteristic mixing-length	m
n	Manning coefficient	$s/m^{1/3}$
$\langle P \rangle$	Time-averaged pressure	N/m^2
P	Pressure	N/m^2
P_p	Local pore pressure	N/m^2
$\overline{q}$	breadth-averaged overflow discharge	m^2/s
$\widetilde{q}$	breadth-averaged discharge over the embankment	m^2/s
Q_b	Breach discharge	m^3/s
R_c	Rate at which the crest width reduces	m/s
RP	Return period of the loading event	years
$\hat{S}$	Magnitude of the vorticity of the flow	rad/s
cl	Crest level	m
S	*Sine* of the angle of the landside slope with the horizontal	rad
s_i	vector containing the the cross derivative terms following from the discretized momentum equations, the contribution from the turbulent kinetic energy, and the explicit terms that follow from linearization of the advective terms	N/m^2
SoP	Standard of protection of the asset	years
swl	Still water level	m
δt	Numerical time step	s
T	Time	hours
t	Time	s
$\langle \mathbf{u} \rangle$	Vector of the time-averaged velocity components, $(\langle u \rangle, \langle v \rangle, \langle w \rangle)$	m/s
$\mathbf{u}$	Velocity vector (u, v, w)	m/s
$\mathbf{u}'$	Vector of the fluctuating velocity components, (u', v', w')	m/s
$\lvert\widetilde{\langle \mathbf{u} \rangle}\rvert$	Modulus of the velocity vector $\widetilde{\langle \mathbf{u} \rangle}$	m/s
$\overline{\widetilde{u}}_n$	Breadth-averaged and depth-averaged flow velocity corresponding with the normal depth	m/s
$\overline{\widetilde{u}}_{gi}$	Critical flow velocity for grass failure of quality i	m/s
$\widetilde{\langle \mathbf{u} \rangle}$	Vector of breadth-averaged and time-averaged velocity components, $(\widetilde{\langle u \rangle}, \widetilde{\langle v \rangle}, \widetilde{\langle w \rangle})$	m/s
$\widetilde{\langle u \rangle}_i$	Velocity vector $(\widetilde{\langle u \rangle}, \widetilde{\langle w \rangle})$	m/s
u	Velocity component in the Cartesian $\hat{x}$-direction	m/s
u_*	Shear velocity	m/s
u_c	Breadth-averaged and depth-averaged flow velocity corresponding to the critical depth	m/s
u_ε	Flow velocity in the $\hat{\varepsilon}$-direction	m/s
V	Volume of water entering the floodplain	m^3
v	Velocity component in the Cartesian $\hat{y}$-direction	m/s

W	Weight of the soil above the pipe	N
w	Velocity component in the Cartesian $\hat{z}$-direction	m/s
w_ζ	Flow velocity in the $\hat{\zeta}$-direction	m/s
$\hat{x}$	Horizontal Cartesian coordinate direction in line with the main flow	
$\hat{x}$	Horizontal coordinate direction from left to right	
X	Body forces in the Cartesian $\hat{x}$-direction	N/m^3
x	Coordinate in horizontal direction	m
$\hat{y}$	Horizontal Cartesian coordinate direction perpendicular to the main flow	
Y	Body forces in the Cartesian $\hat{y}$-direction	N/m^3
y_1	Location of the near wall	
y_2	Location of the far wall	
$\hat{z}$	Vertical Cartesian coordinate direction perpendicular to x and y	
$\hat{z}$	Vertical coordinate direction upwards	
Z	Body forces in the Cartesian $\hat{z}$-direction	N/m^3
z	Coordinate in vertical upwards direction	m

Greek Letters

α	Angle between the $\hat{z}$ coordinate direction and the $\hat{\zeta}$-coordinate direction	rad
ϵ	Kinematic eddy viscosity	m^2/s
$\hat{\varepsilon}$	Coordinate direction parallel to the landside slope in downwards direction	
ε	Coordinate in the coordinate direction parallel to the landside slope in downwards direction	m
ε_0	Offset from the origin located where the crest and landside slope meet	m
Φ	Internal friction angle of soil	rad
γ_s	Specific weight of the soil	N/m^3
γ_w	Specific weight of water	N/m^3
η	Eddy viscosity	Pa-s
$\hat{\kappa}$	Von Kármán constant	
μ	Dynamic molecular viscosity	Pa-s
$\hat{\nu}$	Preserved Spalart–Allmaras quantity	m^2/s
∇	Divergence operator	1/m
Ψ	Matric suction	N/m^2
Ψ_m	matric suction following from a modified water content suction relationship	N/m^2
ρ_w	density of water	kg/m^3
σ	variable in the Spalart–Allmaras equation related to diffusion or the Spalart–Allmaras quantity	
σ'	Effective normal stresses	N/m^2

$\sigma'_{\varepsilon\varepsilon}$	Effective normal stresses in the $\hat{\zeta}$ coordinate direction	N/m^2
$\sigma'_{\zeta\zeta}$	Effective normal stresses in the $\hat{\zeta}$-coordinate direction	N/m^2
$\sigma_{\varepsilon\varepsilon}$	Normal soil pressure in the $\hat{\zeta}$ coordinate direction	N/m^2
$\sigma_{\zeta\zeta}$	Normal soil pressure in the $\hat{\zeta}$-coordinate direction	N/m^2
τ'	Effective shear stresses	N/m^2
Θ	Normalised pore water concentration	
θ	Pore water concentration	
Θ_0	Initial normalised water content	
θ_r	Residual pore water concentration	
θ_s	Pore water concentration saturated soil	
τ	bed shear stress	N/m^2
τ_c	Critical shear stress needed for initiation of erosion	N/m^2
τ_f	Critical shear stress for initiation of shear failure	N/m^2
$\hat{\zeta}$	Coordinate direction normal to the landside slope into the soil	
ζ	Coordinate in the coordinate direction normal to the landside slope into the soil	m

Superscripts

$.^{n+1}$	New time step
$.^{r1}$	First iteration step
$.^{r2}$	Second iteration step